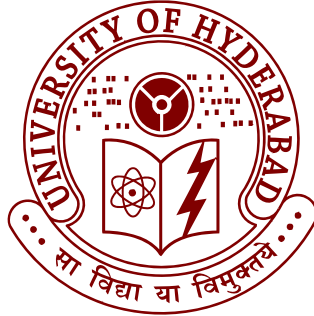


Ph.D Thesis

Computational Study of Energetic Materials under Hydrostatic Compression

Neelam Yedukondalu



ACRHEM, School of Physics
University of Hyderabad
Hyderabad - 500 046
Telangana, India

Computational Study of Energetic Materials under Hydrostatic Compression

A Thesis submitted to University of Hyderabad for the award of
the degree of

Doctor of Philosophy

in Physics

by

Neelam Yedukondalu
(10ACPP03)



ACRHEM, School of Physics

University of Hyderabad

Hyderabad-500 046

February 2016

Dedicated to

My Mother

(She is the best gift of my life)

Declaration

I, Neelam Yedukondalu hereby declare that this thesis entitled “**Computational Study of Energetic Materials under Hydrostatic Compression**” submitted by me under the supervision of Dr. G. S. Vaitheeswaran, ACRHEM, University of Hyderabad, Hyderabad, India, is a bonafide research work which is also free from plagiarism. I also declare that it has not been submitted previously in part or in full to this University or any other University or Institution for the award of any degree or diploma. I hereby agree that my thesis can be deposited in Shodhganga/INFLIBNET.

A report on plagiarism statistics from the University Librarian is enclosed

Date

Neelam Yedukondalu
Reg. No: 10ACPP03.

Dr. G. S. Vaitheeswaran,
Thesis Supervisor,
ACRHEM,
University of Hyderabad.

Certificate

This is to certify that the thesis entitled “*Computational Study of Energetic Materials under Hydrostatic Compression*” being submitted to the University of Hyderabad by **Neelam Yedukondalu** (Reg. No. 10ACPP03), for the award of the degree of Doctor of Philosophy in Physics, is a record of *bonafide* work carried out by him under my supervision and is free of plagiarism.

The matter embodied in this report has not been submitted to any other University or Institution for the award of any degree or diploma.

Dr. G. S. Vaitheeswaran,
Thesis Supervisor,
ACRHEM,
University of Hyderabad.

Director,
ACRHEM,
University of Hyderabad.

Dean,
School of Physics,
University of Hyderabad.

A word of Gratitude

There are numerous people that I would like to thank for their kind support and encouragement without which the last five and half years would not have been so successful or enjoyable.

First and foremost I would like to thank my research advisor **Dr. G. S. Vaitheeswaran** for introducing me to the world of modelling and simulations using Density Functional Theory and his constant guidance throughout the research work. This dissertation would not have been possible without his assistance, allowed me to discuss through user forums and experts in this field of research. I knew thanks itself is not sufficient but I don't have words to express my gratitude and it is a matter of pride to have association with him. I am always grateful to him through bottom of my heart. I would like to extend my sincere thank to **Dr. V. Kanchana**, Indian Institute of Technology, Hyderabad, India, for providing me the computational facilities, language and technical correction of my scientific reports related to my thesis as well as other works.

I also would like to thank my doctoral committee members **Prof. C. S. Sunandana**, **Dr. V. Ashoka** and **Prof. Ashok Chatterjee**, University of Hyderabad, India, for their valuable suggestions and comments towards completion of my doctoral research work. Especially, **Prof. C. S. Sunandana** who has corrected all my manuscripts and including the current thesis. A special thanks to **Prof. M. C. Valsakumar**, IIT Palkkad, India, for showing his interest on my research work, fruitful discussions and being always ready to clarify all my doubts at the fundamental level. I extend my gratitude to **Dr. S. Lebègue**, Université de Lorraine, France and **Dr. T. R. Ravindran**, Indira Gandhi Centre for Atomic Research, Kalpakkam, India, for their fruitful suggestions during their visit to ACRHEM. I also would like to thank the **anonymous reviewers** for reviewing my publications to improve the quality of the research work. I am extremely thankful to **faculty members of ACRHEM** for teaching me the concepts of high energy materials, MATLAB and research methodology. My sincere thanks to **Dr. Vikas D. Ghule**, NIT kurukshetra, and **Mr. P. Anees**, Kalpakkam, India for sharing their valuable ideas and collaboration work. I also thank **non-teaching staff of ACRHEM** as well as **school of physics** for their help in office related work.

It has been a very pleasant experience to work in the warm and friendly atmosphere of my group members **Dr. S. Appalakondaiah**, **Dr. K. Ramesh Babu**, **Dr. Ch. Bheemalingam**, **E. Narsimha Rao**, **S. Mondal**, **B. M. Abraham**, **J. Prathap Kumar**, **J. Adivaiah** & **M. V. Jyothirmai**. Thank you as well to all members of the Dr. V. Kanchana's group present (**G. Shwetha**, **G. Vikaykumar**, **P. V. Sreenivasa Reddy** and **P. C. Sreeparvathy**) and past (**Dr. Swetarekha Ram**) for making the time during this period so enjoyable. I think we have learnt many

things from each other during our interesting discussions, good times we have spent together. I would like to thank all my **ACRHEM** and **School of Physics friends** for their help and support whenever I needed. I also would like to thank **Dr. Athar Parveen** for her suggestions. I have to mention my special and sincere thanks to my best and family friends **S. C. Rakesh Roshan** and his wife **K. Lavanya** for their encouragement and moral support.

My deepest gratitude goes to **B. Somi Reddy sir & family members, J. Katam Raju & family members, M. Yadagiri Reddy & family members, S. Naga Raju & family members, V. Pratap & family members, respected family well wishers Rajeswara Rao sir, Sangeetha Rao sir & their family members** and all my **well wishers** for their invaluable support. Most importantly, none of this would have been possible without my family members, my dear lovable mother (**N. Parvathamma**), wife (**V. Hyndavi**) and son (**N. Venkata Karthikeya**), thank you all for your unflagging love, guidance and support even in the critical situations.

Last but not least I would like to thank **CMSD**, University of Hyderabad for providing me the computational facilities and **DRDO**, India through **ACRHEM** for their financial support, present and former directors of **ACRHEM** for administrative support.

Neelam Yedukondalu

List of Publications

Publications included in the thesis

- [1] N. Yedukondalu and G. Vaitheeswaran, "Structural, electronic and optical properties of well-known primary explosive: Mercury fulminate", *J. Chem. Phys.*, **143**, 204704 (2015).
- [2] N. Yedukondalu, G. Vaitheeswaran, P. Anees and M. C. Valsakumar, "Phase stability and lattice dynamics of ammonium azide under hydrostatic compression", *Phys. Chem. Chem. Phys.*, **17**, 29210 (2015).
- [3] N. Yedukondalu and G. Vaitheeswaran, "Structural stability, vibrational and bonding properties of potassium 1,1-dinitramino-5,5-bistetrazolate: An emerging green primary explosive", *J. Chem. Phys.*, **143**, 064508 (2015).
- [4] N. Yedukondalu and G. Vaitheeswaran, "First principles study of pressure induced polymorphic phase transition in KNO_3 ", *AIP Conf. Proc.*, **1665**, 030002 (2015).
- [5] N. Yedukondalu and G. Vaitheeswaran, "Polymorphism and thermodynamic ground state of silver fulminate studied from van der Waals density functional calculations", *J. Chem. Phys.*, **140**, 224705 (2014).
- [6] G. Vaitheeswaran, K. Ramesh Babu, N. Yedukondalu and S. Appalakondiah, "Structural properties of solid energetic materials: A van der Waals density functional study", *Curr. Sci.*, **106**, 1219 (2014).
- [7] N. Yedukondalu, Vikas D. Ghule and G. Vaitheeswaran, "Pressure induced structural phase transition in solid oxidizer KClO_3 : A first principles study", *J. Chem. Phys.*, **138**, 174701 (2013).
- [8] N. Yedukondalu, Vikas D. Ghule and G. Vaitheeswaran, "Computational study of structural, electronic and optical properties of crystalline NH_4N_3 ", *J. Phys. Chem. C*, **116**, 16910 (2012).
- [9] N. Yedukondalu and G. Vaitheeswaran, "Structural stability of energetic oxidizers under high pressure", *Proceedings of 10th International High Energy Material Conference and Exhibit (HEMCE-2016)*, Vol. I, 407 (2016).
- [10] N. Yedukondalu and G. Vaitheeswaran, "Ab-initio study of structural, vibrational and optical properties of solid oxidizers", *Submitted to journal*.

- [11] **N. Yedukondalu**, Vikas D. Ghule and G. Vaitheeswaran, “High pressure structural, mechanical, IR spectra and detonation properties of green energetic oxidizer: Ammonium dinitramide”, *to be communicated*.

Publications not included in the thesis

- [1] G. Shwetha, V. Kanchana, **N. Yedukondalu** and G. Vaitheeswaran, “Ab initio study of scintillating lanthanide oxyhalide host materials”, *Mat. Res. Express*, **2**, 105901 (2015).
- [2] V. Kanchana, **N. Yedukondalu** and G. Vaitheeswaran, “Lattice dynamics and electronic structure of mixed halofluoride scintillators under high pressure”, *AIP Conf. Proc.*, **1665**, 090009 (2015).
- [3] E. Narsimaha Rao, S. Appalakondaiah, **N. Yedukondalu** and G. Vaitheeswaran, “Structural, electronic and optical properties of novel carbonate fluorides $ABCO_3F$ (A=K, Rb,Cs; B=Ca, Sr)”, *J. Solid State Chem.*, **212**, 179 (2014).
- [4] J. Ramanna, **N. Yedukondalu**, K. Ramesh Babu and G. Vaitheeswaran, “Ab initio study of electronic structure, elastic and optical properties of anti-perovskite type alkali oxyhalides”, *J. Solid State Sci.*, **20**, 120 (2013).
- [5] V. Kanchana, **N. Yedukondalu** and G. Vaitheeswaran, “Structural, elastic, electronic and optical properties of layered alkaline-earth halofluoride scintillators”, *Philo. Mag.*, **26**, 3563 (2013).
- [6] **N. Yedukondalu** and G. Vaitheeswaran, “Vibrational properties of BaClF, BaBrF and BaIF under high pressure”, *J. Phys.: Conf. Ser.*, **377**, 012070 (2012).
- [7] **N. Yedukondalu**, K. Ramesh Babu, Ch. Bheemalingam, David J. Singh, G. Vaitheeswaran and V. Kanchana, “Electronic structure, optical properties, and bonding in alkaline-earth halofluoride scintillators: BaClF, BaBrF and BaIF”, *Phys. Rev. B*, **83**, 165117 (2011).

Abstract

In order to have fundamental knowledge about the macroscopic behavior of energetic materials under operational conditions, it is essential to understand the crystal structure and bonding environment at high pressures and/or temperatures. Computational studies are particularly suited for studying the energetic materials at extreme conditions since these studies allow for tuning of wide range of pressures and temperatures easily. These studies also provide a valuable information to avoid accidents during experimentation and manufacturing process.

In the present thesis, we have focused on understanding the high pressure behavior of a spectrum of energetic materials namely primary explosives, oxidizers and gas generator. All the investigated energetic materials are either layered and/or molecular crystalline solids and hence weak intermolecular interactions play a significant role in describing their structure and stability. Therefore, we have calculated the ground state properties at ambient as well as at moderate pressures using the recently developed additive pair-wise and non-local correction methods which are in good agreement with the recent experimental results.

Silver fulminate (SF) exists in two polymorphic ($Cmcm$ and $R\bar{3}$) phases, we predict $Cmcm$ phase to be the thermodynamic ground state of SF under the studied pressure and temperature range within DFT-D2 method. Hence $Cmcm$ and $R\bar{3}$ polymorphic phases represented as α -SF and β -SF, respectively. We have seen a polymorphic phase transition using standard DFT functionals and the same was not observed using DFT-D2 method. Crystal structure, equation of state and compressibility of SF polymorphs and mercury fulminate (MF) are discussed. Investigation of green primary explosives becomes an emerging field of research during the last half a decade. We have investigated the structural stability, bonding and vibrational properties of a green primary explosive, potassium 1,1'-dinitoamino 5,5'-bistetrazolate (K_2 DNABT) and compared its physical properties with well-known primary explosives. We found that K_2 DNABT is a soft material and it is dynamically stable at the center of Brillouin zone up to 10 GPa.

We then turn our attention to understand the high pressure behavior of potassium and ammonium based oxidizers. We find polymorphic structural phase transitions in both potassium chlorate (PC) and potassium nitrate (PN). PC (PN) undergoes a first order structural phase transition from monoclinic (orthorhombic) to rhombohedral structure at 2.26 (0.27) GPa. The calculated zone centre lattice modes are found to soften for PC while B_{1g} and B_{1u} lattice modes drive an instability at 3.5 GPa for PN due to change in the orientation of nitrate group. In the case of ammonium based oxidizers, we observe a discontinuity in the lattice constants as a function of pressure. In addition, pressure dependent IR spectra disclose the weakening of hydrogen bonding. These two effects may suggest

possible structural phase transitions in Ammonium Perchlorate (AP) and Ammonium DiNitramide (ADN) under high pressure. Also, ADN is found to be a powerful energetic oxidizer when compared to ammonium nitrate and AP from the calculated detonation characteristics.

Ammonium Azide (AA) is a nitrogen rich energetic inorganic azide and it is found to be the thermodynamic ground state of hydro-nitrogen solids (HNS). AA undergoes a phase transition to Trans Tetrazene (TTZ) at around $\sim 39\text{-}43$ GPa followed by TTZ to HNS-1 at around $\sim 80\text{-}90$ GPa under the studied temperature range 0-650 K. The calculated elastic moduli and lattice dynamics under high pressure suggest that AA undergoes a first order structural phase transition and the high pressure crystal structure of AA is still an open challenge. The weakening of hydrogen bonding due to red and blue-shift of N-H stretching bands reveal that AA encounters a structural phase transition around ~ 4 GPa. AA exhibits moderate explosive performance as inferred from the calculated detonation properties.

Finally, we have calculated the electronic structure and optical properties of SF polymorphs, MF, K_2DNABT and AA compounds explicitly using recently developed Tran-Blaha modified Becke Johnson potential (spin-orbit effects are included for heavy metals namely Ag and Hg). Electronic structure, band gap, chemical bonding and optical spectra of the above mentioned compounds are discussed extensively.

Contents

List of publications	i
Abstract	iii
Contents	v
List of figures	vii
List of tables	xiv
1 Introduction	1
1.1 Pressure and its effects	1
1.2 High pressure research	1
1.3 High pressure induced polymorphism	3
1.4 Implications on energetic materials	4
1.5 Classification of energetic materials	5
1.6 Perspective of the thesis	10
2 Theoretical background	23
2.1 The many body problem	23
2.2 Density functional theory	25
2.2.1 The Hohenberg-Kohn theorems	26
2.2.2 The Kohn-Sham equations	26
2.3 Exchange-Correlation functionals	29
2.3.1 Local density approximation	29
2.3.2 Generalized gradient approximation	30
2.4 Full-, Pseudo- and PAW approaches	30
2.5 Limitations of DFT	32
2.6 Dispersion correction methods	34
2.6.1 Additive pair-wise correction methods	34
2.6.2 Non-local correction methods	37

2.7	Tran-Blaha modified Becke Johnson Potential	37
2.8	Density functional perturbation theory	38
2.9	Gibbs free energy of polymorphs	39
3	Heavy metal based fulminates	45
3.1	Introduction	45
3.2	Methodology of calculation	50
3.3	Results and discussion	52
3.3.1	Crystal structure and ground state properties	52
3.3.2	Pressure and temperature effects on the phase stability of SF polymorphs	56
3.3.3	Equation of state and compressibility	61
3.3.4	Electronic structure and chemical bonding	63
3.3.5	Optical properties	70
3.4	Conclusions	74
4	Potassium based green primary explosive	81
4.1	Introduction	81
4.2	Method of computation	84
4.3	Results and discussion	86
4.3.1	Crystal structure and equation of state	86
4.3.2	Zone centre IR and Raman spectra at ambient and under high pressure	90
4.3.3	Electronic structure and absorption spectra	97
4.4	Conclusions	102
5	Potassium based oxidizers	107
5.1	Introduction	107
5.2	Methodology of calculations	112
5.3	Results and discussion	113
5.3.1	Pressure induced polymorphic phase transitions in PC	113
5.3.2	Pressure induced polymorphic phase transitions in PN	117
5.3.3	Zone center phonon frequencies at ambient pressure	119
5.3.4	Zone center phonon frequencies under high pressure	127
5.4	Conclusions	129
6	Ammonium based oxidizers	135
6.1	Introduction	135
6.2	Computational details	140

6.3	Results and discussion	142
6.3.1	Crystal structure and equation of state	142
6.3.2	Hydrogen bonding under pressure	153
6.3.3	Elastic constants and mechanical stability	154
6.3.4	Zone center phonons at ambient pressure	158
6.3.5	IR spectra under high pressure	159
6.3.6	Detonation properties	163
6.4	Conclusions	164
7	Ammonium azide	171
7.1	Introduction	171
7.2	Method of computation	175
7.3	Results and discussion	177
7.3.1	Phase stability of N_4H_4 compounds	177
7.3.2	Structural properties of AA under high pressure	186
7.3.3	Mechanical properties of AA under high pressure	187
7.3.4	Hydrogen bonding in AA under pressure	189
7.3.5	Zone centre phonons of AA at ambient pressure	195
7.3.6	IR spectra of AA under pressure	198
7.3.7	Phonon dispersion curves of AA under high pressure	200
7.3.8	Electronic structure and chemical bonding	201
7.3.9	Optical properties	206
7.3.10	Detonation properties	209
7.4	Conclusions	209
8	Summary & Future scope	217
	Similarity index	221

List of Figures

3.1	Crystal structures of (a, b) layered α -SF, (c) β -SF ($2 \times 2 \times 2$ super cell) and (d) single molecule of β -SF.	46
3.2	Crystal structures of (a, b) unit cell of MF, (c, d) layered structure of MF.	47
3.3	Calculated enthalpy as a function of pressure for α - and β - polymorphic phases of SF with (DFT-D2) and without (DFT within PBE-GGA) dispersion correction method.	48
3.4	Calculated total energy as a function of pressure for α - and β - polymorphic phases of SF within DFT-D2 method.	49
3.5	Calculated Gibbs free energy as a function of temperature for α - and β - polymorphic phases of SF within DFT-D2 method.	50
3.6	Calculated volume as a function of pressure for α - and β - polymorphic phases of SF within DFT-D2 method.	51
3.7	Calculated volume as a function of pressure for MF within optB88-vdW method.	52
3.8	Calculated normalized lattice parameters of a) α - and b) β - polymorphic phases of SF as a function of pressure within DFT-D2 method.	53
3.9	Calculated normalized a) lattice parameters b) bond lengths and c) bond angles of MF as a function of pressure within optB88-vdW method.	54
3.10	Calculated normalized bond lengths of a) α - and b) β - polymorphic phases of SF as a function of pressure within DFT-D2 method.	57
3.11	Calculated normalized bond angles of a) α - and b) β - polymorphic phases of SF as a function of pressure within DFT-D2 method.	58
3.12	Calculated electronic band structures of a) α - and b) β - phases of SF using TB-mBJ potential at the experimental crystal structures [24, 25].	58

3.13	Calculated electronic band structures of a) α -SF and b) MF with (solid red lines) and without (dotted black lines) inclusion of SO coupling using the TB-mBJ functional at the optimized fractional co-ordinates. Influence of SO coupling is given in the inset for both of the compounds.	62
3.14	Calculated total and PDOS of a) α - and b) β - phases of SF using TB-mBJ potential at the experimental crystal structures [24, 25].	64
3.15	Calculated total and PDOS of a) α -SF and b) MF with (solid lines) and without (dotted lines) inclusion of spin-orbit coupling using the TB-mBJ potential at the optimized fractional co-ordinates [24, 34].	66
3.16	Calculated electronic charge densities along (100), (010), (001) planes for α -SF (top) and along (100), (001) planes for β -SF (bottom).	68
3.17	Calculated electronic charge densities of MF along crystallographic (100), (010) and (001) planes.	69
3.18	Calculated real (top) and imaginary (bottom) parts of dielectric function of α - (left) and β - (right) phases of SF using TB-mBJ potential at the experimental crystal structures [24, 25].	69
3.19	Calculated real (top) and imaginary (bottom) parts of complex dielectric function of MF without (dotted black lines) and with (solid red lines) inclusion of spin-orbit interaction (SOI) using the TB-mBJ potential at the experimental lattice constants [34].	71
3.20	Calculated absorption (top) and photoconductivity (bottom) of α - (left) and β - (right) phases of SF using TB-mBJ potential at the experimental crystal structures [24, 25].	72
3.21	Calculated absorption (top) and photoconductivity (bottom) of MF without (dotted black lines) and with (solid red lines) inclusion of spin-orbit interaction (SOI) using the TB-mBJ potential at the experimental lattice constants [34].	73
4.1	(a) Triclinic ($P\bar{1}$) unit cell, (b) Puckered layered structure viewed along xy-plane, (c) Single molecular geometry of tetrazole molecule of K_2 DNABT crystal. Ash, blue, red and violet colour balls represent carbon, nitrogen, oxygen and potassium atoms, respectively.	83
4.2	Calculated (a) lattice constants (a, b and c), (b) normalized lattice constants (a/a_0 , b/b_0 and c/c_0), (c) lattice angles (α , β and γ), (d) normalized lattice angles (α/α_0 , β/β_0 and γ/γ_0) (e) volume (V) and (f) normalized volume (V/V_0) of K_2 DNABT as a function of pressure.	85

4.3	Calculated normalized (a, b) bond lengths and (c) torsion angles of K_2DNABT as a function of pressure. X = bond parameter at any instant of pressure and X_0 = bond parameter at ambient pressure.	87
4.4	Calculated IR spectra (a) 40-500 cm^{-1} , (b) 600-900 cm^{-1} and (c) 900-1500 cm^{-1} of K_2DNABT as a function of pressure.	91
4.5	Calculated Raman spectra (a) 40-350 cm^{-1} , (b) 900-1450 cm^{-1} and (c,d) 1500-1625 cm^{-1} of K_2DNABT as a function of pressure. Black and red solid lines represent standard Ar (514.5 nm) and Nd:YAG (1064 nm) lasers respectively. The lasers used as an incident light while calculating the Raman spectra of K_2DNABT with Gaussian brodening of 2.5 cm^{-1}	92
4.6	The few simulated lattice and internal eigenvectors of K_2DNABT . Here R and IR denote Raman and IR active modes, respectively.	94
4.7	Calculated (a) electronic band structure, (b) partial density of states, (c) electron charge density of K_2DNABT using TB-mBJ potential.	99
4.8	Calculated absorption spectra of K_2DNABT as function of photon energy using TB-mBJ potential.	102
5.1	Crystal structures of a) phase I (monoclinic, $P2_1/m$) and b) phase II (rhombohedral, $R3m$) of $KClO_3$	108
5.2	Crystal structures of a) phase II (Orthorhombic, $Pmcn$) and b) phase III (rhombohedral, $R3m$) of KNO_3	108
5.3	Calculated enthalpy difference of phase I ($P2_1/m$, black solid line) and phase II ($R3m$, red dotted line) of $KClO_3$ as a function of pressure using dispersion corrected DFT-D2 method. The lower and upper inset figures correspond to LDA and PBE-GGA functionals, respectively.	109
5.4	Calculated a) lattice constants b) volume of phase I and II of PC as a function of pressure using dispersion corrected DFT-D2 method. The experimental data points are taken from Ref. [31] for the phase II ($R3m$).	110
5.5	Calculated enthalpy difference of phase II and III of PN polymorphs as a function of pressure.	111
5.6	Calculated (a) lattice constants and (b) volume as a function of pressure for both polymorphic phases II and III of PN.	114
5.7	Calculated phonon density of states (PhDOS) for phase I and phase II of a) PC and b) PN, respectively using DFT-D2 method.	116

5.8	Calculated Raman (top) and IR (bottom) active (a) lattice and (b) internal modes of phase I of PC as a function of pressure using DFT-D2 method.	118
5.9	Calculated a) Raman and b) IR active lattice modes of phase II of PN as a function of pressure using DFT-D2 method.	120
5.10	Calculated (a) Raman and (b) IR active internal modes of phase II of PN as a function of pressure using DFT-D2 method.	128
6.1	Two dimensional hydrogen bonding network in AN as viewed along ab-plane. White, blue and red color balls represent hydrogen, nitrogen and oxygen atoms, respectively.	136
6.2	Periodic wave type hydrogen bonding network in AP as viewed along ab-plane. White, blue, red and light green color balls represent hydrogen, nitrogen, oxygen and chlorine atoms, respectively.	138
6.3	Three dimensional hydrogen bonding network in ADN as viewed along bc (top) and ab (bottom)-planes. White, blue and red color balls represent hydrogen, nitrogen and oxygen atoms, respectively.	141
6.4	Crystal structures of a) AN b) AP and c) ADN.	142
6.5	Calculated lattice constants of AN as a function of pressure up to 45 GPa using various dispersion correction methods. Experimental data is taken from the Ref. [24]	144
6.6	Calculated lattice constants of AP as a function of pressure up to 4 GPa using various dispersion correction methods. Inset figures show the obtained lattice constants under pressure up to 5 GPa using TS-SCS method. Experimental data is taken from the Ref. [26].	146
6.7	Calculated lattice constants of ADN as a function of pressure up to 5 GPa using various dispersion correction methods. Inset figures show the obtained lattice constants under pressure up to 10 GPa using DFT-D2 method. Experimental data is taken from the Ref. [28].	148
6.8	Calculated normalized lattice constants of (a) AN (0-45 GPa), (b) AP (0-5 GPa) (c) (0-5 GPa) ADN as a function of pressure. Experimental data is taken from the Ref. [28]. Here T and E represent theory and experiment, respectively.	150

6.9	Calculated volume of (a) AN (0-45 GPa), (b) AP (0-5 GPa) (c) (0-5 GPa) ADN as a function of pressure. Inset shows the obtained volume under pressure up to 5 and 10 GPa using TS-SCS and DFT-D2 method for AP and ADN, respectively. Experimental data is taken from the Refs. [24, 26, 28].	151
6.10	Calculated intermolecular hydrogen bond lengths (a, c, e) and angles (b, d, f) of (a,b) AN, (c,d) AP and (e,f) ADN as a function of pressure. Where X_0 and X represent obtained bond parameters at ambient and as a function of pressure, respectively.	155
6.11	Calculated elastic constants of a) AN (0-45 GPa) b) AP (0-5 GPa) and c) ADN (0-10 GPa) as a function of pressure.	157
6.12	Calculated IR spectra of AP and ADN in the near IR region at ambient pressure.	159
6.13	Calculated IR spectra (a) lattice modes (b) torsional and bending modes of NH_4 and ClO_4 ions (c) N-H wagging, rocking and scissoring modes (d) ClO_4 asymmetric modes (e, f) N-H symmetric and asymmetric stretching modes of AP as a function of pressure.	160
6.14	Calculated IR spectra (a) lattice modes (b) torsional and bending modes of NH_4 and $\text{N}(\text{NO}_2)_2$ ions (c) N-H wagging, rocking and scissoring modes (d) $\text{N}(\text{NO}_2)_2$ asymmetric modes (e, f) N-H symmetric and asymmetric stretching modes of ADN as a function of pressure.	162
7.1	Crystal structure of AA viewed in a-c (left) b-c (right) planes. Azide (N_3) ion parallel and perpendicular to a-axis named as Type I and Type-II, respectively. Angle θ is defined as orientation of Type-II azides w.r.t. to c-axis.	173
7.2	Crystal structures of hydro-nitrogen solids; (a) AA, (b) T'TZ, (c) HNS-1 (super cell) and (d) HNS-2.	174
7.3	Calculated relative enthalpies of T'TZ and HNS-1 with respect to AA using NCPP approach as a function of pressure.	176
7.4	Calculated phase diagram (G, P, T) of (a) AA and T'TZ (b) viewed in P-T plane for AA and T'TZ using NCPP approach.	178
7.5	Calculated phase diagram (G, P, T) of (a) T'TZ and HNS-1 (b) viewed in P-T plane for T'TZ and HNS-1 using NCPP approach.	179
7.6	Calculated (a, b) lattice constants a, b and c; (c) relative compressibility of unit cell parameters a, b and c; (d) volume of AA as a function of pressure up to 2.5 GPa (except figure 7.6b which is up to 50 GPa). The experimental data is taken from Refs.[1, 19, 38]	181

7.7	Calculated (a) elastic constants (C_{ij}) (b) mechanical stability criteria of AA as a function of pressure up to 20 GPa.	183
7.8	Calculated angle θ that a Type-II azide ion makes with c-axis (see figure 7.1) in AA up to (a) 0-2.5 GPa and (b) 0-50 GPa. The optimized structures of AA are given in inset at 0, 12 and 50 GPa pressures (from left to right) in order to show change in the orientation of azide ions with c-axis in figure (b) as highlighted in ellipse for one Type-II azide and it is also applicable for Type-II azides which are aligned along c-axis. The experimental data is taken from Ref. [1].	185
7.9	Calculated hydrogen bond angles (N-H...N) as a function of pressure up to 50 GPa. Atomic labels are given in figure 7.1.	188
7.10	Calculated (bottom, solid black line) and experimental (top, solid red line) Raman spectra of AA at ambient pressure. The experimental data is taken from Ref. [17]	190
7.11	Calculated IR spectra (a, b) lattice modes (c) torsional and bending modes of NH_4 and N_3 ions (d) N-H wagging, rocking and scissoring modes of NH_4 ions (e) N_3 asymmetric modes of AA as a function of pressure. Calculated lattice, N-H torsional + N_3 bending and azide stretching modes show blue shift with pressure.	191
7.12	Calculated IR spectra (a, b) N-H symmetric and asymmetric stretching modes of AA as a function of pressure. Calculated N-H stretching modes show red shift with pressure. In particular the N-H stretching modes show red shift up to 4 GPa thereafter show blue-shift between 5-12 GPa.	193
7.13	Calculated phonon dispersion curves in the low frequency region ($< 700 \text{ cm}^{-1}$) of AA at 0 GPa (left) as well as at 6 GPa (right) along high symmetry directions $\Gamma (0.0, 0.0, 0.0) \rightarrow Z (0.0, 0.0, 0.5) \rightarrow T (0.0, 0.5, 0.5) \rightarrow Y (0.0, 0.5, 0.0) \rightarrow S (0.5, 0.5, 0.0) \rightarrow X (0.5, 0.0, 0.0) \rightarrow U (0.5, 0.0, 0.5) \rightarrow R (0.5, 0.5, 0.5)$ in the Brillouin zone.	194
7.14	Calculated phonon dispersion curves in the high frequency region ($> 700 \text{ cm}^{-1}$) of AA at 0 GPa (left) as well as at 6 GPa (right) along high symmetry directions (notations have same representation as in figure 7.13) in the Brillouin zone.	196
7.15	Calculated electronic band structure along high symmetry directions in the Brillouin zone (notations have same representation as in figure 7.13) and PDOS of AA using the TB-mBJ potential at the experimental crystal structure. N(M) and N(T) represent middle and terminal nitrogen atoms of azide anions, respectively.	202

-
- 7.16 Calculated electronic charge densities of AA plotted along (200), (101) and (010) planes. 203
- 7.17 The real $\epsilon_1(\omega)$ and imaginary $\epsilon_2(\omega)$ parts of dielectric function of AA along three crystallographic axes as a function of photon energy at ambient conditions. Black solid line (along [100]), red dotted line (along [010]) and green thick dotted line (along [001]). 205
- 7.18 The calculated absorption spectra $\alpha(\omega)$, refractive index $n(\omega)$, reflectivity $R(\omega)$ and loss function $L(\omega)$ of AA as a function of photon energy at ambient conditions. Black solid line (along [100]), red dotted line (along [010]) and green thick dotted line (along [001]). 207

List of Tables

3.1	Calculated ground state lattice parameters (a, b, c, in Å), crystallographic angle (α , in $^\circ$), volume (V, in Å ³) and density (ρ , in gr/cc) of α - and β - polymorphic phases of SF using different dispersion corrected DFT-D2, vdW-TS and OBS methods along with the experimental data.	55
3.2	Calculated ground state lattice parameters (a, b, c, in Å), volume (V, in Å ³), density (ρ , in gr/cc) of orthorhombic MF using standard PBE and various non-local correction methods along with the experimental data.	57
4.1	Calculated ground state lattice constants (a, b, c, α , β , γ), volume (V) and density (ρ) of K ₂ DNABT using standard DFT functionals (LDA, PBE-GGA) and dispersion corrected (DFT-D2) method. Experimental data have been taken from Ref.[10] and the relative errors were given in parenthesis with respect to experimental data.	86
4.2	Calculated bond lengths (in, Å) and torsion angles (in, $^\circ$) of K ₂ DNABT using standard DFT functionals (LDA, PBE-GGA) and dispersion corrected (DFT-D2) method. Experimental data have been taken from Ref.[10]	88
4.3	Calculated lattice, rotational, translational and liberational modes of K ₂ DNABT at the DFT-D2 equilibrium volume.	96
4.4	Calculated liberational and internal modes of K ₂ DNABT at the DFT-D2 equilibrium volume.	98
4.5	Optimized fractional co-ordinates of K ₂ DNABT using FP-LAPW method within PBE-GGA functional at the experimental lattice constants. Experimental data have been taken from Ref. [10].	100
5.1	Calculated lattice parameter (a), rhombohedral angle (α), volume (V) and fractional coordinates for phase II of PC at 3.0 GPa using DFT-D2 method along with the experimental data [29, 31].	117

5.2	Calculated Raman and IR active lattice modes (in cm^{-1}) of phase I of PC at ambient pressure using LDA, PBE-GGA functionals and dispersion corrected DFT-D2 method along with experimental data [21, 24, 25]. (T = Translational and R = Rotational). . .	121
5.3	Calculated Raman and IR active internal modes (in cm^{-1}) of phase I of PC at ambient pressure using LDA, PBE-GGA functionals and dispersion corrected DFT-D2 method along with experimental data [21, 24, 25].	123
5.4	Calculated asymmetric (ν_{Asym}), symmetric (ν_{Sym}) stretching and bending (ν_{Bend}) vibrational frequencies (in cm^{-1}) of PN using DFT-D2 method. Experimental data is taken from the Refs. [62, 63]. .	124
5.5	Calculated lattice modes and their vibrational assignment of PN using DFT-D2 method. The letters T, Tw, R, Roc correspond to Translational, Rotational, Twisting, Rocking modes, respectively. The experimental data in parenthesis is taken from Ref. [62].	126
6.1	Calculated structural properties volume (V_0 , in \AA^3), bulk modulus (B_0 , in GPa) and its pressure derivative (B'_0) of AN, AP and ADN using standard PBE-GGA functional and various dispersion corrected DFT-D methods.	152
6.2	Calculated elastic constants (C_{ij} , in GPa) of AN, AP and ADN using TS, TS-SCS and D2 equilibrium volume, respectively. Experimental data is taken from Refs. [56, 57] for AP.	158
6.3	Calculated heat of formation (HOF, in kJ/mol), density (ρ , in gr/cc), detonation velocity (D_{CJ} , in km/s) and pressure (P_{CJ} , in GPa) of AN, AP and ADN.	164
7.1	Calculated and experimental ground state lattice parameters (a, b, c, in \AA), crystallographic angles (α , β , γ , in $^\circ$), volume (V, in \AA^3) and total energy (E_0 , in eV/atom) of N_4H_4 compounds. USPP and NCPP were used in the vdW-TS calculations implemented in CASTEP package and PAW pseudo potentials were used within dispersion corrected TS-SCS method incorporated through VASP package.	182

Introduction

1.1 Pressure and its effects

Pressure (is defined as the force per unit area) is an important fundamental thermodynamic variable, which influences the physical and chemical processes in materials significantly. In physical processes, it induces phase transitions and affects their kinetics. In chemical processes, it changes the chemical equilibria and reaction rates [1]. The effect of pressure on materials can be broadly classified into two categories: (i) lattice and (ii) electronic effects; however, these two effects are related. In the first one, with increasing pressure, the inter-ionic distances decrease, the lattice becomes denser leading to hardening of phonon spectra associated with changes in the thermo-physical properties. In addition, Gibb's free energy increases with pressure and the material no longer remains with global minimum energy structure. Hence, the material may undergo a first or second order structural phase transition to a structure satisfying the minimum free energy criterion [1]. In the second one, the ions are brought together by the application of pressure resulting in the overlap of outer electron orbitals leading to insulator/semiconductor to metal transition (metallization) and vice versa.

1.2 High pressure research

There are three general methods for studying materials at high pressure (HP): (i) direct static compression, (ii) dynamic shock-wave studies and (iii) computational studies. First one has been of significant interest for over a century in the field of HP research. In 1905, P. W. Bridgman developed a pressure cell for compressing

solids, which accelerates significant increase in the pressure attainable in the HP static experiments [2]. Initially, very low pressures between ~ 0.7 -2 GPa were achieved and his tireless efforts lead to invention and development of opposed-anvil devices which had the capability of reaching pressures between 5-10 GPa. For his pioneering work in the field of HP research, Bridgman received the Nobel Prize in Physics in 1946. The most important breakthrough from Bridgman's work has been the invention of the diamond-anvil cell which can generate the pressures in the range 100-300 GPa [3-5]. With the current nanodiamond-anvil technology, the highest pressures attainable are above 600 GPa [6]. An alternative second method used in high pressure studies is dynamic compression where the material are compressed by means of a shock wave. Recently, terapascal (1 TPa = 1000 GPa) regime has been achieved using laser shock compression studies [7, 8]. The last one, computational studies got much attention to investigate materials under ultra high pressures, since such extreme conditions can be obtained very easily when compared to the static and dynamic compression experiments. This approach may provide a fundamental knowledge prior to performing the actual experiments so that experimentalists can be prepared better for making observations.

The recent developments in crystal structure prediction at high pressures [9-12] is a revolution in the field of computational studies. Without any input from the experiments, this approach can predict the crystal structures at ambient as well as at high pressures just by knowing the chemical composition using genetic algorithms. For instance, ionic elemental boron [13] and transparent dense sodium [14] are predicted at high pressures using the crystal structure prediction packages. HP research was started with simple elements [15] of the periodic table, an excellent review [16] on elemental metals which covers high pressure studies of 51 elements and non-metals namely iodine [17] and oxygen [18]. Minerals [19, 20], inorganic compounds, as an examples, carbon dioxide [21, 22] and B-C-N-O based composition [23] can be used as a precursors for synthesis of super hard materials under high pressures and nano-materials [24]. HP tool is also used in the designing and synthesizing novel phases of Nobel gases [25]. For instance, inert gas elements namely He, Ne and Ar form a peculiar compounds with hydro-

gen, nitrogen and fluorine at high pressures [26–31]. Now a days, the interests of researchers have been shifted to complicated metal-organic frameworks [22, 32], organic & molecular crystals [33, 34], aperiodic crystals, quasi crystals, proteins and viruses [34]. HP research is just not limited to the area of physics, chemistry and materials science but also has spread its wings to biotechnology, food science and pharmaceuticals [24, 35, 36].

1.3 High pressure induced polymorphism

Moreover, HP is a powerful tool for studying polymorphism which has significant implications in molecular crystals. Polymorphism (Greek: poly = many, morph = form) is the property of crystalline solid, which can adopt distinct crystalline forms (known as polymorphs) [37–39]. A common example of polymorphism is elemental carbon. Carbon can exist in numerous crystalline forms and the details can be found elsewhere [1, 35, 36]. Among them, most familiar forms are diamond and graphite. The differences in the crystal structures create dramatic changes in their physical and chemical properties. Diamond is the hardest naturally occurring material and it is electrically insulating, optically transparent and chemically inert whereas graphite is very soft, electrically conducting and chemically reactive. The remarkable differences in properties of the above polymorphs can manifest much research on the effects of polymorphism in the field of physics, chemistry, materials science and pharmaceuticals. In deed comments like “*in general the number of forms for a given compound is proportional to the time and money spent in research on that compound*”[40] suggest that polymorphism is a rule, rather than the exception [35]. The physical properties that are mainly affected by the polymorphism are melting, sublimation temperature, heat capacity, conductivity, color, hygroscopicity, stability and density. Energetic materials are an important class of molecular crystalline solids which exhibit rich polymorphism. Therefore, HP studies are vital to understand polymorphic phase stability, structural phase transitions and thermo-physical properties at extreme conditions.

1.4 Implications of high pressure and polymorphism on energetic materials

HP crystallographic studies on energetic materials provide a significant information about the processes occurring in crystalline material during the explosion. The operating conditions when a shock wave propagates through an explosive material can reach pressures and temperatures up to 50 GPa and 5500 K, respectively [34, 36]. Indeed, such extreme conditions could induce structural changes or even initiate chemical reactions in the solid energetic materials. Therefore, understanding the structural phase transitions and polymorphism may have significant consequences for the development & applications of these materials. For example, the stability order of the energetic polymorphs is as follows: $\beta > \alpha > \gamma > \delta$ for HMX and $\epsilon > \beta > \gamma > \alpha$.H₂O for CL-20. Hence, β -HMX and ϵ -CL-20 polymorphs are permitted in the munitions because of relatively more stable nature of these two polymorphs. HP studies of RDX and CL-20 polymorphs were carried out using diamond-anvil cell in combination with X-ray diffraction and spectroscopic techniques, it is found that the HP behavior of these materials depends markedly on the starting polymorph [35]. Moreover, density (ρ) of a polymorph plays a crucial role in determining the performance of the energetic material since detonation velocity $\propto \rho$ and detonation pressure $\propto \rho^2$ from Kamlet-Jacobs (K-J) empirical equations [41].

On the other hand, synthesis of polymeric nitrogen from molecular nitrogen ($\text{N}\equiv\text{N}$ is the strongest bond with energy 954 KJ/mol) has been achieved [42–44]. It consists of individual nitrogen atoms connected by single bonded (N-N) networks, which is a green high energy density material (HEDM) known till date [42, 44]. The metal azides consist of linear-rod-shaped N_3^- ions with quasi double bonds ($\text{N}=\text{N}$ is weaker bond than $\text{N}\equiv\text{N}$ with energy 418 KJ/mol). Hence, it can be expected that the $(\text{N}=\text{N}=\text{N})^-$ ions of metal azides may form polymeric nitrogen networks more readily than molecular nitrogen ($\text{N}\equiv\text{N}$) [45]. Therefore, the inorganic azides have been used as precursors to synthesize polymeric nitrogen. During the last decade, several experimental [46–50] and theoretical [51–56] studies have been reported to understand the high pressure behavior of

inorganic azides. In addition, extensive studies have been devoted to understand structural, mechanical and dynamical stability of polymeric nitrogen at extreme conditions [57–62]. Using crystal structure prediction [9–12] in combination with density functional theory (DFT), a series of polymeric nitrogen structures have been predicted by considering the alkali metal azides as precursors [63–69]. These studies also reveal that metal atom Cs has the bigger radius among the alkali metals and possesses the strongest chemical preload among the alkali metal azides, which will greatly reduce the synthesis pressure and temperature of polymeric nitrogen [63–70]. But the predicted structures transform back into molecular phase of nitrogen which indicates that these phases are unstable at ambient conditions. Very recently, high pressure and temperature study [71] on ammonium azide provided a new insight to synthesize/predict polymeric nitrogen (hydrogen atoms play an important role in the formation of the polymeric networks) which might be preserved under ambient conditions and it is still awaiting experimental confirmation. Therefore, HP and polymorphic phase transition studies of energetic materials play a crucial role in the development of novel and green energetic materials. A brief summary of the classification of energetic materials and their recent developments towards green energetic formulations is given in the following section.

1.5 Classification of energetic materials

Energetic material is “a meta-stable compound or mixture capable of the rapid release of stored potential energy” [72]. The entirety of energetic materials is defined by the American Society for Testing and Material as “a compound or mixture of substances which contains both fuel and oxidizer and reacts readily with the release of energy and gas” [73]. Energetic materials are broadly classified into three categories: explosives, propellants and pyrotechnics. Explosives are further classified into primary and secondary based up on their sensitivity to the external stimuli such as heat, shock, light and electric charge etc. Explosives involve fast detonation giving rise to shock wave accompanied by rapid release of a large amount of energy. Propellants undergo more rapid combustion which leads to

deflagration but they do not detonate and pyrotechnics undergo combustion at visibly observable rates, usually generating colored smoke and light followed by crackling noise and flames. Now a days, the energetic materials are not only used for military purpose but also they are utilized for civilian applications, in mining, construction, demolition and safety equipment such as airbags, signal flares and fire extinguishing systems.

Primary explosives are very sensitive and they can be easily ignited by small external stimuli [74]. The initiation of primary explosives leads to a very fast deflagration to detonation transition by generating a shock wave that is capable of triggering an insensitive secondary explosive. Milligrams of primary explosive is sufficient to set off the large quantity of secondary explosive. The main requirements for the primary explosives are sensitivity within useful limits, high initiating efficiency, reasonable fluidity, resistance to dead pressing and chemical stability for a long time [75]. Primary explosives are used in detonators, primers, blasting caps and initiators. Mercury fulminate is the first and widely used primary explosive and later on this was replaced by the most commonly used primary explosives lead azide and lead (barium) styphanate. The basic disadvantage of the existing primaries is toxicity of heavy metal which can cause damage to human health and environment [76, 77]. Therefore, there is a considerable interest on the investigation of environmentally benign replacements for the commonly used toxic primary explosives. The green primary explosives should follow the criterion proposed by Los Alamos National Laboratory (LANL) [74, 76–78]. The proposed seven “*green*” primary criteria are as follows: (1) insensitivity to moisture and light (2) sensitivity to initiation but not too sensitive to handle and transport (3) thermally stable at least up to 200 °C (4) chemically stable for extended periods (5) devoid of toxic metals such as lead, mercury, barium and antimony (6) free from perchlorate which may acts as a teratogen and has adverse effects on function of the thyroid gland and (7) ease and safety of synthesis. This can be achieved by replacing the heavy (Hg, Pb) metal primary explosives with less toxic alkali, NH₄, Ag, Fe, Co, Zn and Cu based metal complexes [74, 79–83]. Very recently employed idea is to replace the heavy metal with eco-friendly potassium metal in primary explosives. Some of the green primary explosives synthesized by

replacing the heavy metal with alkali metal potassium during the last 5 years (especially in the last one year) are 4,6-dinitro-7-hydroxybenzofuroxan (KDNP) [84], potassium 1,1-dinitramino 5,5-bistetrazolate (K_2 DNABT) [85], dipotassium 3,4-bis(3-dinitromethylfuran-4-oxo)furan (K_2 BDFOF) [86], dipotassium 3,4-bis(3-dinitromethyl) furoxanate (K_2 BDF) [87], potassium salt of 1,5-(dinitroamino) tetrazole (K_2 DNAT) [88]. In general, the detonation velocities for primary explosives are in the range of 3.5-5.5 km/s [89]. However, the detonation characteristics of advanced green primary explosives are in the range of secondary explosives. The calculated detonation velocity (D_v) and pressure (D_p) for recently synthesized green primary explosives are: K_2 DNABT ($D_v = 8.33$ km/s, $D_p = 31.7$ GPa) [85], K_2 BDFOF ($D_v = 8.43$ km/s, $D_p = 32.93$ GPa) [86], K_2 BDF ($D_v = 7.759$ km/s, $D_p = 27.3$ GPa) [87] and K_2 DNAT ($D_v = 10.01$ km/s, $D_p = 52.2$ GPa) [88] and the last one is found to be the superior green primary explosive known till date [88].

Secondary explosives cannot be initiated simply through heat or shock like primary explosives due to their insensitivity. In order to initiate secondary explosives, primary explosives have to be used, which generate a detonated shockwave and it promotes the reaction front through the unreacted material. The important characteristics for secondary explosives are brisance (shattering power of an explosive), strength, detonation velocity and pressure. The explosive characteristics of secondary explosive determines its applications either as projectiles or in warheads. Picric acid or Trinitrotoluene (TNT) was used as the standard explosive during the 1st world war. But, it has substantial drawbacks like the formation of highly sensitive heavy metal complexes. Research on high performing explosives lead to investigation of Hexahydro-1,3,5-trinitro-1,3,5-triazine (Hexagon, RDX), Octahydro-1,3,5,7-tetranitro-1,3,5,7-tetrazocine (Octogen, HMX) and pentaerythritol tetranitrate (PETN) during the 2nd world war. RDX has been extensively used due to its low sensitivity and high performance than PETN. Recently, Klapötke and co-workers synthesized the pentaerythritol tetranitrocarbamate (PETNC) and tetraammonium salt which are thermally stable and less sensitive than PETN [90]. The two main motivations in the development of modern secondary explosives are (i) improving explosive power and (ii) reducing the

sensitivity to accidental detonation. The first one can be achieved by having both fuel and oxidizer within a molecule, if the molecule possesses ring or cage strain structure and high heat of formation by introducing the nitrogen atoms. When a caged or cyclic explosive compound possesses bond strain resulting from the geometry of the compound, this stored energy contributes to the energy released upon detonation. Hexanitroisowurtzitan (CL-20) and Octanitrocubane (ONC) are cage strained modern explosives with high performance characteristics than HMX but they are sensitive to accidental initiation.

Recent efforts have been made to improve the explosive power as well as reducing the sensitivity of explosives. Two excellent explosives Dihydroxylammonium salts of 5,5-bistetrazole-1,1-diolate (TKX-50) and 3,3-dinitro-5,5-bis-1,2,4-triazole-1,1'-diol (MAD-XI) were synthesized by Klapötke et al [91–93] with superior insensitivity and higher performance than RDX. Also, the heterocyclic compound Nitro-1,2,4-triazole-3-one (NTO) and 1,1-diamino-2,2-dinitroethane (FOX-7) display high energy output comparable to RDX but with dramatically reduced sensitivity which is attributed to high degree of conjugation and hydrogen bonding within the crystal structure [94]. The latest advances in the synthesis of novel and recent green energetic materials are discussed elsewhere [95–100]. An alternative method to achieve high power explosives with reduced sensitivity is co-crystallization which provides the opportunity to tune properties of existing energetics to create superior materials. It provides a complementary alternative to traditional methods that focus primarily on the synthesis of new compounds and/or discovery of polymorphs with the most attractive properties. This approach has been used extensively within the pharmaceutical industry in order to enhance desirable properties, e.g. solubility and bio-availability. To date, however, there has been very little research on the co-crystallisation of energetic materials. Examples include TNT with pyrene, naphthalene and CL-20 [101–104] as well as HMX with CL-20 [105].

Unlike primary and secondary explosives, **propellants** do not detonate but their prime objective is to burn or deflagrate. By deflagrating, propellants build up relatively high pressures without the presence of a high velocity shock wave. Black powder (mixture of 75 % potassium nitrate, 10 % sulfur and 15 % char-

coal) is the first energetic material. Propellants are primarily classified into gun and rocket propellants. A gun propellant consists of both oxidizer and fuel, black powder was the first propellant which is used in both large caliber guns and hand-guns. Later on, it has been largely replaced by the single based propellant nitrocellulose due to the low efficiency of black powder. Further, to improve the performance of propellants, double and triple based (or composite) propellants are developed based on nitrocellulose and nitroglycerine compositions. They possess an enhanced performance, unfortunately these compositions accompanied by a higher erosion of the gun barrel due to their higher combustion temperature. In order to decrease the erosion, triple based propellants which consist of nitrocellulose, nitroglycerine and nitroguanidine were developed [106]. The single based propellant nitrocellulose is sufficient for ammunition of guns and pistols whereas the double and triple based propellants are used in tank and naval artillery ammunition. Modern composite propellants consist of a high explosive like RDX (around 20-60 %). On the other hand, the rocket propellants are either solid or liquid and they act as a propulsion system. The main difference between these two propellants is best described by the isochoric and isobaric combustion for gun and rocket propellants, respectively [107]. Usually solid propellants consist of Ammonium perchlorate (AP) as oxidizer and aluminium powder as fuel and hydroxyl-terminated polybutadine (HTPB) as binder. In the modern solid propellants, toxic AP is replaced by a green energetic oxidizer, ammonium dinitramide (ADN). Liquid propellants are divided into mono (e.g. hydrazine) and bipropellants which are mixtures of an oxidizer and fuel (e.g. HNO_3 and hydrazine/monomethyl-hydrazine) [107]. The liquid propellants find applications in space exploration and technology.

Pyrotechnics means the art of fire (from greek *pyro* “fire” and *tekhnikos* “made by art”) and they can be divided into three categories: heat generating, smoke generating and light emitting pyrotechnics. The heat generating pyrotechnics are used for priming charges, detonators, incendiary compositions or matches. Smoke generating pyrotechnics are used for camouflage and signaling purposes. The light emitting pyrotechnics are used either for illumination (visible and infrared), fireworks or decoy flares [108]. In general every pyrotechnic formula-

tion contains reducing and oxidizing agents. Typical oxidizers are perchlorates and nitrates of potassium and barium, while fuels are boron and silicon or metals of magnesium, titanium and zirconium [109]. Recently, perchlorate and heavy metal (barium) free *i.e.* strontium and periodate based materials [110, 111] got much attention in pyrotechnic formulations due to their eco-friendly nature. A long burning time, low toxicity, bright colors or dense smokes are the major requirements for future pyrotechnic formulations [112].

1.6 Perspective of the thesis

The primary objective of the thesis is to understand the high pressure behavior of diverse classes of energetic materials which are used in primary explosives, propellants and pyrotechnic formulations. Computational studies are particularly suited for studying the energetic materials since these studies allow for tuning of wide range of pressures and temperatures very easily. Also, they provide a detailed information about rates and mechanisms of reactions occurring under such extreme conditions [36]. The ultimate aim of computational studies is to construct models for accurate prediction of performance and characteristics of the existing as well as new energetic materials. In the present thesis, we have investigated the phase stability, possible pressure induced structural phase transitions and lattice dynamical properties of inorganic primary explosives, oxidizers and a gas generator/hydro-nitrogen solid. The energetic materials are layered and/or molecular crystalline solids with complex chemical bonding. It is well-known fact that the intermolecular interactions *i.e.* van der Waals and/or hydrogen bonding play a significant role in determining the stability of the energetic solids. Therefore, various dispersion corrected DFT methods have been employed to capture the weak intermolecular interactions for primary explosives namely silver fulminate (SF), mercury fulminate (MF), K₂DNABT, solid oxidizers such as potassium nitrate (PN) and chlorate (PC), ammonium nitrate (AN), ammonium perchlorate (AP), ammonium dinitramide (ADN) and ammonium azide (AA). In addition, recently developed Tran Blaha-modified Becke Johnson (TB-mBJ) potential [113] has been used to predict reliable electronic band gaps for the investigated ener-

getic solids. The TB-mBJ potential provides band gaps closely comparable with the more sophisticated and computationally demanding methods such as hybrid functionals, GW approximations as well as with the experimental results.

Chapter 2 gives a short description of DFT and its fundamental theorems constructed based on the first principles of quantum mechanics. The thesis includes various quantum mechanical tools using pseudo and full-potential approaches based on DFT which helped in understanding the thermo-physical properties of the examined compounds under hydrostatic compression. This chapter discusses about the successes and failures of the conventional DFT methods. In addition, we also discuss the recent advances in dispersion correction approaches such as pairwise additive and non-local correction methods for treating weak intermolecular interactions. The methodology of semi-local TB-mBJ potential for the calculation of fundamental electronic band gaps thereby carry out the computation of electronic structure and optical properties of the investigated compounds are also discussed.

Chapter 3 presents phase stability of SF polymorphs and MF. Among the dispersion correction methods tested, DFT-D2 and optB88-vdW methods work well for SF polymorphs and MF, respectively. Based on our total energy calculations, the *Cmcm* phase is found to be the preferred thermodynamic ground state of SF polymorphs. Hitherto *Cmcm* and $R\bar{3}$ phases denoted as α and β -forms of SF, respectively. Also a pressure induced polymorphic structural phase transition is visualized using DFT functionals and the same was not observed with DFT-D2 method over the studied pressure and temperature range. The equation of state and compressibility of SF polymorphs and MF were investigated. Spin-Orbit (SO) coupling is found to be more pronounced for MF than α -SF. The calculated electronic structure shows that α , β -phases of SF and MF are indirect band gap insulators. The nature of chemical bonding is analyzed through the calculated charge density maps and partial density of states. Optical anisotropy, electric-dipole transitions and photo sensitivity to light of the SF polymorphs and MF are analyzed from the calculated optical spectra.

Chapter 4 represents the detailed results on structural stability, IR and Raman spectra of layered and molecular K_2DNABT under hydrostatic pressure. We

find anisotropic compressibility behavior ($b < a < c$) from pressure dependent structural properties. The predicted equilibrium bulk modulus value suggest that K_2 DNABT is softer than toxic LA and harder than the most sensitive cyanuric triazide. The calculated zone center IR and Raman frequencies show a blue-shift which leads to hardening of the lattice upon compression. In addition, it is also found that K_2 DNABT is a direct band gap insulator with a band gap of 3.87 eV and the top of the valence band is mainly dominated by $2p$ -states of oxygen and nitrogen atoms. K_2 DNABT exhibits mixed ionic (between potassium and tetrazolate ions) and covalent character within the tetrazolate molecule. The presence of ionic bonding suggests that the investigated compound is relatively stable and insensitive than covalent primaries. From the calculated absorption spectra, the material is found to decompose under ultra-violet light irradiation.

In **chapter 5**, we address the high pressure behavior of the two solid potassium based oxidizers namely PC and PN. The calculated ground state parameters, transition pressure and phonon frequencies using DFT-D2 method are in good agreement with the experimental data. It is found that PC undergoes a pressure induced first order phase transition with an associated volume collapse of 6.4 % from monoclinic ($P2_1/m$) \rightarrow rhombohedral ($R3m$) structure at 2.26 GPa, which is in good accord with experimentally observed transition pressure around 2 GPa. However, the transition pressure was found to underestimate (0.11 GPa) and overestimate (3.57 GPa) using local density approximation and generalized gradient approximation, respectively. Similarly, PN also encounters a polymorphic structural phase transition from orthorhombic ($Pmcn$) \rightarrow rhombohedral ($R3m$) structure at 0.27 GPa with a volume collapse of 4.9%. In addition, the zone center phonon frequencies have been calculated at ambient as well as at high pressure for both of the compounds. The calculated lattice modes are found to soften under pressure between 0.6 to 1.2 GPa for PC while the lattice B_{1g} and B_{1u} modes drive the instability in PN around 3.5 GPa due to a change in the orientation of nitrate group.

In **chapter 6**, we report pressure dependent structural, elastic, IR spectra and detonation properties of ammonium based oxidizers including van der Waals interactions. The calculated ground state lattice parameters and isothermal equation

of state for three investigated compounds are in good agreement with the experimental results. The computed axial compressibility and elastic moduli reveal that AN, ADN and AP are found to be more compressible due to weak intermolecular interactions along **b**- and **a**-axes, respectively. We also observe a discontinuity in the lattice constants as a function of pressure which hints a pressure induced structural phase transition in AP and ADN. In addition, we have also calculated the IR spectra of AP and ADN at ambient as well as at high pressure. ADN is found to have more hygroscopic nature over AP due to strong hydrogen bonding at ambient pressure. Pressure dependent IR spectra disclose weakening of hydrogen bonding which further leads to structural phase transitions in AP and ADN. Red-shift of near and far IR frequencies reveal that the high pressure phase of ADN has stronger hydrogen bonding than the ambient phase. The calculated detonation properties reveal that ADN is a more powerful energetic oxidizer when compared to AN and AP.

In **chapter 7**, we have investigated the effect of hydrostatic pressure and temperature on the phase stability of hydro-nitrogen solids using dispersion corrected DFT-D methods. From our total energy calculations, AA is found to be the thermodynamic ground state of N_4H_4 compounds in preference to trans-tetrazene (TTZ), hydro-nitrogen solid (HNS-1 & 2) phases. We have carried out a detailed study on structure and lattice dynamics of the equilibrium phase. AA undergoes a phase transition to TTZ at around ~ 39 -43 GPa followed by TTZ to HNS-1 at around ~ 80 -90 GPa under the studied temperature range 0-650 K. The accelerated and decelerated compression of *a* and *c* lattice constants response suggests that the ambient phase of AA transforms to a tetragonal phase. It is also noticed that the angle made by type-II azides with the crystallographic *c*-axis shows a rapid decrease and reaches a minimum value at 12 GPa and thereafter increases up to 50 GPa. Softening of the shear elastic moduli is suggestive of a mechanical instability of AA under high pressure. We have made a complete assignment of all the vibrational modes which is in good agreement with the experimental observations at ambient pressure. Moreover, the calculated pressure dependent IR spectra show that the N-H stretching frequencies undergo red and blue-shifts corresponding to strengthening and weakening of hydrogen bonding, respectively, below and

above 4 GPa. The intensity of N-H asymmetric stretching mode B_{2u} is found to diminish gradually and the weak coupling between NH_4 and N_3 ions makes B_{1u} and B_{3u} modes to degenerate with progression of pressure up to 4 GPa which causes weakening of hydrogen bonding and these effects may lead to a structural phase transition in AA around 4 GPa. In addition, we have also calculated the phonon dispersion curves at 0 and 6 GPa and no soft phonon mode is observed under high pressure. Furthermore, we have also calculated the detonation characteristics of AA using the reported heat of formation and calculated crystal density. AA is found to have $D_v = 6.45$ km/s and $D_p = 15.16$ GPa computed by K-J equations.

Finally in **chapter 8**, we summarize conclusions of the present thesis and open up with future scopes and ideas leading to further exploration of energetic solids at extreme conditions.

References

- [1] P. Ch. Sahu, K. Govinda Rajan, N. V. Chandra Shekar and Md. Yousuf, *Proceedings of the conference on Frontiers in Materials Modelling and Design*, p.365-375 (1996).
- [2] P. W. Bridgman, *Physics of High Pressure* (G Bell and Sons, London, 1931), reprinted, Dover, New York, (1970).
- [3] A. Jayaraman, *Rev. Mod. Phys.*, **55**, 65 (1983).
- [4] A. Jayaraman, *Rev. Sci. Instrum.*, **57**, 103 (1986).
- [5] A. L. Ruoff, *Recent Trends in High Pressure Research*, Oxford & IBH, New Delhi, p.769 (1992).
- [6] L. Dubrovinsky, N. Dubrovinskaia, V. B. Prakapenka and A. M. Abakumov, *Nat. Commun.*, **3**, 1163 (2012).
- [7] J. H. Eggert, D. G. Hicks, P. M. Celliers, D. K. Bradley, R. S. McWilliams, R. Jeanloz, J. E. Miller, T. R. Boehly and G. W. Collins, *Nat. Phys.*, **6**, 40 (2010).

-
- [8] H. Nagao, K. G. Nakamura, K. Kondo, N. Ozaki, K. Takamatsu, T. Ono, T. Shiota, D. Ichinose, K. A. Tanaka, K. Wakabayashi, K. Okada, M. Yoshida, M. Nakai, K. Nagai, K. Shigemori, T. Sakaiya and K. Otani, *Phys. Plasma.*, **13**, 052705 (2006).
- [9] A. R. Oganov and C. W. Glass, *J. Chem. Phys.*, **124**, 244704 (2006).
- [10] A. R. Oganov, C. W. Glass and N. Hansen, *Comp. Phys. Comm.*, **175**, 713 (2006).
- [11] Y. Wang, J. Lv, L. Zhu and Y. Ma, *Phys. Rev. B*, **82**, 094116 (2010).
- [12] Y. Wang, J. Lv, L. Zhu and Y. Ma, *Comput. Phys. Commun.*, **183**, 2063 (2012).
- [13] A. R. Oganov, J. Chen, C. Gatti, Y. Ma, Y. Ma, C. W. Glass, Z. Liu, T. Yu, O. O. Kurakevych and V. L. Solozhenko, *Nature*, **457**, 863 (2009).
- [14] Y. Ma, M. Eremets, A. R. Oganov, Y. Xie, I. Trojan, S. Medvedev, A. O. Lyakhov, M. Valle and V. Prakapenka, *Nature*, **458**, 182 (2009).
- [15] E. G. Ponyatovsky and E. Y. Tonkov, *Phase Transformations of Elements Under High Pressure*, CRC Press, Taylor and Francis group (2004).
- [16] M. I. McMahon and R. J. Nelmes, *Chem. Soc. Rev.*, **35**, 943 (2006).
- [17] B. M. Riggleman and H. G. Drickamer, *J. Chem. Phys.*, **38**, 2721 (1963).
- [18] Y. Akahama, H. Kawamura, D. Häusermann, M. Hanfland and O. Shimomura, *Phys. Rev. Lett.*, **74**, 4690 (1995).
- [19] M. H. Manghnani and Y. Syono, *High-Pressure Research in Mineral Physics*, John Wiley & Sons vol. 39, (2013).
- [20] R. J. Hemley, H. K. Mao and S. A. Gramsch, *Mineralogical Magazine*, **64**, 157 (2000).
- [21] Ch. -S. Yoo, *Phys. Chem. Chem. Phys.*, **15**, 7949 (2013).

- [22] Y. Song, *Phys. Chem. Chem. Phys.*, **15**, 14524 (2013).
- [23] A. S. Miguel, *Chem. Soc. Rev.*, **35**, 876 (2006).
- [24] E. V. Boldyreva, *Acta Cryst.*, **A64**, 218 (2008).
- [25] J. S. Schilling, *J. Phys. Chem. Solids*, **59**, 553 (1998).
- [26] W. Grochala, *Chem. Soc. Rev.*, **36**, 163 (2007).
- [27] M. Kim, M. Debessai and C. -S. Yoo, *Nat. Chem.*, **2**, 61 (2010).
- [28] D. Kurzydowski, P. Z. -Ejgierd, W. Grochala and R. Hoffmann, *Inorg. chem.*, **50**, 3832 (2011).
- [29] M. Somayazulu, P. Dera, A. F. Goncharov, S. A. Gramsch, P. Liermann, W. Yang, Z. Liu, H. -K. Mao and R. J. Hemley, *Nat. Chem.*, **2**, 50 (2010).
- [30] Q. Zhu, D. Y. Jung, A. R. Oganov, C. W. Glass, C. Gatti and A. O. Lyakhov, *Nat. Chem.*, **5**, 61 (2013).
- [31] L. Zhu, H. Liu, C. J. Pickard, G. Zou and Y. Ma, *Nat. Chem.*, **6**, 644 (2014).
- [32] L. J. Murray, M. Dinca and J. R. Long, *Chem. Soc. Rev.*, **38**, 1294 (2009).
- [33] R. Lee, J. A. K. Howard, M. R. Probert and J. W. Steed, *Chem. Soc. Rev.*, **43**, 4300 (2014).
- [34] C. Hejny and V. S. Minkov, *IuCrJ*, **2**, 281 (2015).
- [35] D. I. A. Millar, *Energetic materials at extreme conditions*, Springer Theses, Springer-Verlag, Berlin Heideberg, (2011).
- [36] F. A. Fabbiani and C. R. Pulham, *Chem. Soc. Rev.*, **35**, 932 (2006).
- [37] A. Katrusiak, *Acta Cryst.*, **A64**, 135 (2008).
- [38] D. Braga and F. Grepioni, *Chem. Soc. Rev.*, **29**, 229 (2000).
- [39] F. Grepioni, *New J. Chem.*, **32**, 1657 (2008) and references therein.

- [40] W. C. McCrone, *Polymorphism in Physics and Chemistry of the Organic Solid State*, Interscience, New York, vol. II, p.726 (1965).
- [41] M. J. Kamlet and S. J. Jacobs, *J. Chem. Phys.*, **48**, 23 (1968); **48**, 36 (1968).
- [42] M. I. Eremets, A. G. Gavriiliuk, I. A. Trojan, D. A. Dzivenko and R. Boehler, *Nat. Matter.*, **3**, 558 (2004).
- [43] M. I. Eremets, A. G. Gavriiliuk, N. R. Serebryanaya, I. A. Trojan, D. A. Dzivenko, R. Boehler, H. K. Mao and R. J. Hemley, *J. Chem. Phys.*, **121**, 11296 (2004).
- [44] M. I. Eremets, R. J. Hemley, H. K. Mao and E. Gregoryanz, *Nature*, **411**, 170 (2001).
- [45] M. I. Eremets, M. Y. Popov, I. A. Trojan, V. N. Denisov, R. Boehler and R. J. Hemley, *J. Chem. Phys.*, **120**, 10618 (2004).
- [46] S. A. Mededev, I. A. Trojan, M. I. Eremets, T. Palasyuk, T. M. Klapötke and J. Evers, *J. Phys.: Condens. Matter*, **21**, 195404 (2009).
- [47] H. Zhu, F. Zhang, Ch. Ji D. Hou, J. Wu, T. Hannon and Y. Ma, *J. Appl. Phys.*, **113**, 033511 (2013).
- [48] C. Ji, F. Zhang, D. Hou, H. Zhu, J. Wu, M. -C. Chyu, V. I. Levitas and Y. Ma, *J. Phys. Chem. Solids*, **72**, 736 (2011).
- [49] C. Ji, R. Zheng, D. Hou, H. Zhu, J. Wu, M.-C. Chyu and Y. Ma, *J. Appl. Phys.*, **111**, 112613 (2012).
- [50] D. Hou, F. Zhang, C. Ji, T. Hannon, H. Zhu, J. Wu and Y. Ma, *Phys. Rev. B*, **84**, 064127 (2011).
- [51] K. Ramesh Babu, Ch. Bheema Lingam, S.P. Tewari and G. Vaitheeswaran, *J. Phys. Chem. A*, **115**, 4521 (2011).
- [52] M. Zhang, H. Yan, Q. Wei, H. Wang and Z. Wu, *Euro. Phys. Lett.*, **101**, 26004 (2013).

- [53] M. Zhang, K. Yin, X. Zhang, H. Wang, Q. Li and Z. Wu, *Solid State Comm.*, **161**, 13 (2013).
- [54] K. Ramesh Babu and G. Vaitheeswaran, *Chem. Phys. Lett.*, **533**, 35 (2012).
- [55] J. Li, X. Wang, N. Xu, D. Li, D. Wand and L. Chen, *Euro. Phys. Lett.*, **104**, 16005 (2013).
- [56] G. Vaitheeswaran and K. Ramesh Babu, *J. Chem. Sci.*, **124**, 1391 (2012).
- [57] M. I. Eremets, A. G. Gavriliuk and I. A. Trojan, *Appl. Phys. Lett.*, **90**, 171904 (2007).
- [58] A. F. Goncharov, E. Gregoryanz, H. K. Mao, Z. Liu and R. J. Hemley, *Phys. Rev. Lett.*, **85**, 1262 (2007).
- [59] B. Hirshberg, B. Gerber and A. Krylov, *Nat. Chem.*, **6**, 52 (2014).
- [60] X. Wang, Y. Wang, M. Maio, X. Zhong, J. Lv, T. Cui, J. Li, L. Chen, C.J. Pickard and Y. Ma, *Phys. Rev. Lett.*, **109**, 175502 (2012).
- [61] X. Wang, F. Tian, L. Wang, T. Cui, B. Liu and G. Zou, *J. Chem. Phys.*, **132**, 024502 (2010).
- [62] X. Wang, K. Bao, F. Tian, X. Meng, C. Chen, B. Dong, D. Li, B. Liu and T. Cui, *J. Chem. Phys.*, **133** 044512 (2010).
- [63] D. Hou, F. Zhang, C. Ji, T. Hannon, H. Zhu, J. Wu, V. I. Levitas and Y. Ma, *J. Appl. Phys.*, **110**, 023524 (2011).
- [64] D. Li, X. Wu, J. Jiang, X. Wang, J. Zhang, Q. Cui and H. Zhu, *Appl. Phys. Lett.*, **105**, 071903 (2014).
- [65] D. L. V. K. Prasad, N. W. Ashcroft and R. Hoffmann, *J. Phys. Chem. C*, **117**, 20838 (2013).
- [66] X. Wang, J. Li, J. Botana, M. Zhang, H. Zhu, L. Chen, H. Liu, T. Cui and M. Miao, *J. Chem. Phys.*, **139**, 164710 (2013).

- [67] J. Zhang, Z. Zeng, H. -Q. Lin and Y. -L. Li, *Sci. Rep.*, **4**, 4358 (2014).
- [68] X. Wang, J. Li, H. Zhu, N. Xu, H. Zhu, Z. Hu and L. Chen, *Sci. Rep.*, **5**, 16677 (2015).
- [69] X. Wang, J. Li, H. Zhu, L. Chen and H. Lin, *J. Chem. Phys.*, **141**, 044717 (2014).
- [70] D. Plasienka and R. Martonak, *J. Chem. Phys.*, **142**, 094505 (2015).
- [71] H. Yu, D. Duan, F. Tian, H. Liu, D. Li, X. Huang, Y. Liu, B. Liu and T. Cui, *J. Phys. Chem. C*, **119**, 25268 (2015).
- [72] D. Piercey, *Nitrogen-rich energetic materials based on 1,2,4-triazole derivatives*, Dissertation, Rosenheim, p.4, (2013).
- [73] www.astm.org
- [74] M. H. V. Huynh, M. A. Hiskey, T. J. Meyer and M. Wetzler, *PNAS*, **103**, 5409 (2006).
- [75] R. Matyas and J. Pachman, *Primary Explosives*, Springer-Verlag Berlin Heidelberg (2013).
- [76] K. D. Oyler, *Green Energetic Materials*, John Willey & Sons (2014).
- [77] M. A. Ilyushin, I. V. Tselinsky and I. V. Shugalei, *Cent. Eur. J. Energ. Mater.*, **9**, 293 (2012).
- [78] T. M. Klapötke, *Chemistry of High-Energy Materials*, 2nd ed. Walter de Gruyter Berlin, p.19 (2012).
- [79] M. H. V. Huynh, M. D. Coburn, T. J. Meyer and M. Wetzler, *PNAS*, **103**, 10322 (2006).
- [80] H. Delalum, K. Karaghiosoff, T. M. Klapötke and C. M. Sabate, *Cent. Eur. J. Energ. Mater.*, **7**, 197 (2010).

- [81] N. Fischer, M. Joas, T. M. Klapötke and J. Stierstorfer, *Inorg. Chem.*, **52**, 13791 (2013).
- [82] T. Musil, R. Matys, R. Vala, A. Ruzicka and M. Vlcek, *Prop. Explos. Pyrotech.*, **39**, 251 (2014).
- [83] J. W. Fonabarger, M. D. Williams, W. B. Sanborn, J. G. Bragg, D. A. Parrish and M. Bichay, *Prop. Explos. Pyrotech.*, **36**, 541 (2011).
- [84] J. W. Fonabarger, M. D. Williams, W. B. Sanborn, D. A. Parrish and M. Bichay, *Prop. Explos. Pyrotech.*, **36**, 459 (2011).
- [85] D. Fischer, T. M. Klapötke and J. Stierstorfer, *Angew. Chem. Int. Ed.*, **53**, 8172 (2014).
- [86] L. Zhai, X. Fan, B. Wang, F. Bi, Y. Li and Y. Zhu, *RSC Adv.*, **5**, 57833 (2015).
- [87] C. He and J. M. Shreeve, *Angew. Chem. Int. Ed.*, **55**, 772 (2016).
- [88] D. Fischer, T. M. Klapötke and J. Stierstorfer, *Angew. Chem. Int. Ed.*, **54**, 10299 (2015).
- [89] K. Akhavan, *The Chemistry of Explosives* (Royal Society of Chemistry) Cambridge, UK, (2004).
- [90] Q. J. Axthammer, B. Krumm and T. M. Klapötke, *Eur. J. Org. Chem.*, **2015**, 723 (2015).
- [91] D. Fischer, N. Fischer, T. M. klapötke, D. G. Piercey and J. Stierstorfer, *J. Mater. Chem.* **22**, 20418 (2012).
- [92] T. M. Klapötke, N. Fischer, D. Fischer, D. G. Piercey, J. Stierstorfer and M. Reymann, WO201302768A1 (2013).
- [93] A. Dippold, T. M. Klapötke and F. A. Matrin, *Z. Anorg. Allg. Chem.*, **637**, 1181 (2011).

- [94] U. Bemm and H. Ostmark, *Acta Cryst.*, **C54**, 1997 (1998).
- [95] J. P. Agrawal, *Prog. Energy. Cumbust. Sci.*, **24**, 1 (1998).
- [96] P. F. Pagoria, G. S. Lee, A. R. Mitchell and R. D. Schmidt, *Thermochim. Acta.*, **384**, 187 (2002).
- [97] D. M. Badgular, M. B. Talawar, S. N. Astana and P. P. Mahulikar, *J. Hazard. Mater.*, **151**, 289 (2008).
- [98] M. B. Talawar, R. Sivabalan, T. Muthurajan, A. K. Sikder, B. R. Gandhe and A. Subhananda Rao, *J. Hazard. Mater.*, **161**, 589 (2009).
- [99] U. R. Nair, S. N. Asthana, A. Subhananda Rao and B. R. Gandhe, *Defence Science Journal*, **60**, 137 (2010).
- [100] H. H. Krause, *Energetic Materials*, WILEY-VCH Verlag GmbH & Co. KGaA, Weinheim ISBN: 3-527-30240-9 (2005).
- [101] O. Bolton and A. J. Matzger, *Angew. Chem. Int. Ed.*, **50**, 8960 (2011).
- [102] J. C. Barnes and W. Golnazarians, *Acta Cryst. C Cryst. Str. Comm.*, **43**, 549 (1987).
- [103] K. B. Landenberger and A. J. Matzger, *Cryst. Growth & Des.*, **10**, 5341 (2010).
- [104] D. I. A. Millar, H. E. Maynard-Casely, D. R. Allan, A. S. Cumming, A. R. Lennie, A. J. Mackay, I. D. H. Oswald, C. C. Tang and C. R. Pulhama, *Cryst. Eng. Comm.*, **14**, 3742 (2012).
- [105] O. Bolton, L. R. Simke, P. F. Pagoria and A. J. Matzger, *Cryst. Growth & Des.*, **12**, 4311 (2012).
- [106] A. A. Dippold, *Nitrogen rich energetic materials based on 1,2,4-triazole derivative*, Doctoral thesis, Rosenheim (2013).
- [107] D. V. Izsák, *Investigation of the capability of azidotriazoles as primary explosives*, Doctoral Thesis, Budapest, Ungarn, (2015).

-
- [108] M. A. Kettner, *New oxygen-rich materials as high energy dense oxidizers based on polynitro compounds*, Doctoral thesis, München, Deutschland (2015).
- [109] T. M. Klapötke, *Chemistry of high energy materials*, Walter de Gruyter, Berlin New York (2011).
- [110] J. D. Moretti, J. J. Sabatini and G. Chen, *Angew. Chem. Int. Ed.*, **51**, 6981 (2012).
- [111] J. D. Moretti, J. J. Sabatini and J. C. Poret, *Angew. Chem. Int. Ed.*, **20**, 8800 (2014).
- [112] J. A. Conkling, *Chemistry of pyrotechnics: Basic principles and theory*, Taylor & Francis group, New York (1985).
- [113] F. Tran and P. Blaha, *Phys. Rev. Lett.*, **102**, 226401 (2009).

Theoretical background

This chapter presents the theoretical methods which are used to calculate the various physical and chemical properties of the investigated compounds. We also present the basic principles of *density functional theory* (DFT), exchange-correlational functionals namely local density approximation (LDA) and generalized gradient approximation (GGA) along with additive pair-wise and non-local correction methods as implemented through standard DFT description to capture the weak intermolecular interactions. In addition, we give a short description of Tran Blaha-modified Becke Johnson (TB-mBJ) potential to predict reliable energy band gaps for the investigated compounds.

2.1 The many body problem

The many body problem is a general name for a vast category of physical problems pertaining to the properties of microscopic systems made of a large number of interacting particles. To determine the properties of many particle system, one has to solve the Schrödinger equation. The non-relativistic time independent Schrödinger equation is

$$\hat{H}|\psi\rangle = E|\psi\rangle \quad (2.1)$$

where \hat{H} is the Hamiltonian operator and E is the energy eigen value. The Hamiltonian operator for the many particle system is given by

$$\hat{H} = - \sum_{i=1}^{N_e} \frac{\hbar^2}{2m_i} \nabla_i^2 - \sum_{I=1}^{N_n} \frac{\hbar^2}{2M_I} \nabla_I^2 + \frac{e^2}{2} \sum_{I,J=1}^{N_n} \sum_{I \neq J} \frac{Z_I Z_J}{|R_I - R_J|} + \frac{e^2}{2} \sum_{i,j=1}^{N_e} \sum_{i \neq j} \frac{1}{|r_i - r_j|} - \frac{e^2}{2} \sum_{i=1}^{N_e} \sum_{I=1}^{N_n} \frac{Z_I}{|r_i - R_I|} \quad (2.2)$$

where $r = \{r_i/r_j, i/j = 1, 2, \dots, N_e\}$ is a set of N_e electronic coordinates and $R = \{R_I/R_J, I/J = 1, 2, \dots, N_n\}$ is a set of N_n nuclear coordinates. Z_I (or Z_J) and M_I (or M_J) are the nuclear charges and masses, respectively.

The above equation can be simply written as

$$\hat{H} = \hat{T}_e + \hat{T}_n + \hat{V}_{nn} + \hat{V}_{ee} + \hat{V}_{en} \quad (2.3)$$

\hat{T}_e and \hat{T}_n , represent the kinetic energy operators of electrons and nuclei, respectively. While \hat{V}_{nn} , \hat{V}_{ee} and \hat{V}_{en} represent the electrostatic interaction operators between nuclei and electrons. The many body problem is almost impossible to treat within quantum mechanical frame work, except for the hydrogen atom. There are several features that contribute to this difficulty but the most important among them is the multi component many body nature of the system and the two body nature of the Coulomb interaction which makes the above Schrödinger equation inseparable. The usual choice to solve the above complicated equation is to resort to a few reasonable and well-controlled approximations, which encompass a wide variety of problems of interest.

The many body Hamiltonian can be further simplified by taking advantage of the significant differences between the masses of nuclei and electrons. Even the lightest of all nuclei, the proton weighs approximately 1800 times more than an electron. Thus, the nuclei move much slower than the electrons so that the electrons are moving in the field of fixed nuclei. This is the famous Born and Oppenheimer [1] or adiabatic approximation. Of course, if the nuclei are fixed in space and do not move, their kinetic energy is zero and the potential energy

due to nucleus repulsion is merely a constant. Thus, the Hamiltonian given in the equation 2.2 reduces to the so-called electronic Hamiltonian

$$\hat{H} = - \sum_{i=1}^{N_e} \frac{\hbar^2}{2m_i} \nabla_i^2 + \frac{e^2}{2} \sum_{i,j=1}^{N_e} \sum_{i \neq j} \frac{1}{|r_i - r_j|} - \frac{e^2}{2} \sum_{i=1}^{N_e} \sum_{I=1}^{N_n} \frac{Z_I}{|r_i - R_I|} \quad (2.4)$$

and it is simply written as

$$\hat{H} = \hat{T}_e + \hat{V}_{ee} + \hat{V}_{en} \quad (2.5)$$

where \hat{T}_e represents the kinetic energy operator, \hat{V}_{en} represents the external potential (*i.e.* electron-nucleus interaction) and \hat{V}_{ee} represents the electron-electron interaction. Using the Born-Oppenheimer approximation the complexity of the system is significantly reduced. However, the problem is still too difficult to be solved due to the electron-electron interaction. Indeed, the electrons in any of solid systems cannot be treated as like non interacting classical particles and the main difficulty is that electrons interact among themselves via Coulomb two-body forces. For an atom with Z electrons, the probability of finding an electron in space depends on the location of the $(Z-1)$ electrons, so that they can not be considered as individual entities. This phenomenon is known as *correlation*. Therefore, the concept of one-electron wave functions can not be applicable in many cases. The wave function of many-electron system cannot be simply written as the product of the wave functions of individual electrons. Many approaches have been developed starting from Hatree-Fock method to density functional theory (DFT) to solve the many body problem. In the present thesis, we have used the DFT approach, which is explained in the following sections.

2.2 Density functional theory

DFT is made possible by the existence of two ingeniously simple theorems put forward and proven by Hohenberg and Kohn [2] in 1964 based up on Thomas and Fermi approximation [3, 4], which gave a prescription for calculating the energy of an electronic system exclusively in terms of the electronic density.

2.2.1 The Hohenberg-Kohn theorems

Theorem-1: For any system of interacting particles in an external potential $V_{ext}(r)$, the $V_{ext}(r)$ is determined uniquely by the ground-state particle density, $n_0(r)$.

There exists a one-to-one correspondence between the $V_{ext}(r)$ and $n_0(r)$. The ground state expectation value of any observable, thus, is a unique functional of the $n_0(r)$.

$$\langle \psi | A | \psi \rangle = A[n_0(r)] \quad (2.6)$$

Theorem-2: An universal functional for the energy $E[n(r)]$ can be defined in terms of density, the exact ground state is the global minimum value of this functional.

For a particular $V_{ext}(r)$ the ground state energy of the system is the global minimum of $E[n(r)]$. The density $n(r)$ that minimizes $E[n(r)]$ is the ground state density.

$$E[n(r)] = E_{HK}[n(r)] + \int V_{ext}(r)n(r)dr \quad (2.7)$$

where the term $E_{HK}[n(r)]$ includes all internal energies of the interacting particle systems. The global minimum of the functional in above equation is the exact ground-state total energy of the system E_0 and the particle density that minimizes this functional is the exact ground-state density $n_0(r)$, *i.e.*

$$\frac{\partial}{\partial n} E[n(r)]_{n=n_0} = 0, \text{ with } E_0 = E[n_0(r)] \quad (2.8)$$

Based on the above two theorems, Hohenberg and Kohn formulated DFT as an exact theory for solving the many-body systems and it is applicable to any system of interacting particles.

2.2.2 The Kohn-Sham equations

The Hohenberg-Kohn theorems show it is possible to use the ground state density to calculate properties of any system but it doesn't provide a way of finding

the ground state electronic density [5]. The Kohn-Sham (KS) equations offer a practical procedure to obtain ground state electron density. The main idea is to replace the interacting many-body problem by a corresponding non-interacting particle system in an appropriate external potential. It is useful to decouple the kinetic energy, $T[n]$ into two parts (non-interacting system + rest term) as $T[n] = T_s[n] + T_c[n]$, where $T_s[n]$ is the kinetic energy of the non-interacting system and $T_c[n]$ represents the remainder. $T_s[n]$ is not known as a functional of n , but it can be expressed in terms of the single-particle orbitals, $\phi_i(r)$, of a non-interacting system with density n via

$$T_s[n] = -\frac{1}{2} \sum_{\sigma} \sum_{I=1}^N \int dr \phi_i^*(r) \nabla^2 \phi_i(r). \quad (2.9)$$

For a system containing an even number of spin-up and spin-down electrons, the density of the original many-body system can be written in terms of the orbitals as

$$n(r) = \sum_{\sigma} n(r, \sigma) = \sum_{\sigma} \sum_{I=1}^N |\phi_i(r)|^2. \quad (2.10)$$

Thus, all $\phi_i(r)$ are functionals of n and since T_s is an explicit orbital functional it is also an implicit density functional, $T_s[n] = T_s[\phi_i[n]]$. Moreover, the total number of electrons N is a simple functional of the density

$$N = \int n(r) dr \quad (2.11)$$

The classical Coulomb self-interaction energy of the electron density, *i.e.*, Hartree energy is defined as

$$U_H[n] = \frac{1}{2} \int \int dr dr' \frac{n(r)n(r')}{|r-r'|} = \frac{1}{2} \int V_C(r)n(r)dr \quad (2.12)$$

where $V_C(r) = \int dr' \frac{n(r')}{|r-r'|}$ and the energy of the external potential can be written as a functional of the density

$$V_{ext}[n] = \int n(r) V_{ext}(r) dr \quad (2.13)$$

The Kohn-Sham approach [5] is to rewrite the energy functional of the interacting system in the form

$$\begin{aligned} E_{KS}[n] &= T[n] + U[n] + V[n] \\ &= T_s[\phi_i[n]] + U_H[n] + E_{xc}[n] + V_{ext}[n] \\ &= T_s[n] + \int n(r) [V_{ext}(r) + \frac{1}{2} V_C(r)] dr + E_{xc}[n] \\ &= T_s[n] + V_{eff} \end{aligned} \quad (2.14)$$

where $V_{eff} = \int n(r) [V_{ext}(r) + \frac{1}{2} V_C(r)] dr + E_{xc}[n]$, The exchange-correlation energy $E_{xc}[n]$ contains the differences between $T - T_s$ (i.e. T_C) and $U - U_H$. One has to find a good approximation to E_{xc} in order to get good results for real materials. The effective Hamiltonian for a system of non-interacting particles moving in a potential called V_{KS} , constructed so that the total density of the system is the same as for the real system of interacting electrons, which is given by

$$V_{KS}(r) = V_{ext}(r) + V_C(r) + V_{xc}(r) \quad (2.15)$$

with

$$V_{xc} = \frac{\delta E_{xc}}{\delta n} \quad (2.16)$$

is given as

$$H_{KS} = -\frac{1}{2} \nabla^2 + V_{KS}(r). \quad (2.17)$$

This gives rise to the Kohn-Sham Schrödinger-like equation

$$(H_{KS} - \varepsilon_i) \phi_i(r) = 0 \quad (2.18)$$

where ε_i are the eigenvalues of H_{KS} and the orbitals satisfying the above equation, ϕ_i , minimize the Kohn-Sham energy. This yields orbitals that reproduce the density of the original interacting system and the total energy, E_{KS} . These are independent particle equations with a potential that must be found self-consistently with the resulting density. In practice, one starts with an initial guess for $n(r)$ and calculates the resulting $V_{KS}(r)$ and finally solves the Kohn-Sham Schrödinger-like equation for the ϕ_i . The orbitals yield a new density and the process is iteratively repeated until convergence is achieved. In the Kohn-Sham approach [5], finding a good approximation for the exchange-correlation functional, E_{xc} is the main challenge.

2.3 Exchange-Correlation functionals

2.3.1 Local density approximation

The local density approximation (LDA) is the basis of all approximate exchange-correlation functionals. The central idea of this model is a uniform electron gas. The LDA E_{xc} functional can be written as:

$$E_{xc}[n] = \int n(r)\epsilon_{xc}[n(r)]dr \quad (2.19)$$

Here, ϵ_{xc} is the exchange-correlation energy per particle of a uniform electron gas of density $n(r)$. This energy per particle is weighted with the probability $n(r)$ that there is an electron at this position. The quantity ϵ_{xc} can be further split into exchange and correlation contributions,

$$\epsilon_{xc} = \epsilon_x + \epsilon_c \quad (2.20)$$

The exchange part, ϵ_x which represents the exchange energy of an electron in a uniform electron gas of a particular density and it was originally derived by Bloch [6] and Dirac [7],

$$\epsilon_x = -\frac{3}{4} \left(\frac{3n(r)}{\pi} \right)^{\frac{1}{3}} \quad (2.21)$$

no such explicit expression is known for the correlation part, ϵ_c . However, highly accurate numerical quantum Monte-Carlo simulations of the homogeneous electron gas are available [8].

2.3.2 Generalized gradient approximation

The first logical step is to go beyond LDA. Also the idea is to use not only the information about the density $n(\mathbf{r})$ at a particular point \mathbf{r} , but also the gradient of the charge density, $\nabla n(\mathbf{r})$ in order to account for the non-homogeneity of the true electron density [9]. Thus, the generalized gradient approximation (GGA) E_{xc} is given by

$$E_{xc}^{GGA}[n] = \int f(n(\mathbf{r}), \nabla n(\mathbf{r})) d\mathbf{r} \quad (2.22)$$

There are various parameterizations of GGA functionals which differ in the choice of the function $f(n(\mathbf{r}), \nabla n(\mathbf{r}))$. Overall, LDA uses the exchange-correlation density of the uniform electron gas assuming same charge density at every point in the system regardless of the inhomogeneity of the real charge density. The GGA uses the gradient of the charge density to correct for this deviation and therefore thought to be more accurate.

2.4 Full-, Pseudo- and PAW approaches

The *full potential-linearized augmented plane wave* (FP-LAPW) [10] method is the most accurate method for performing electronic structure calculations for bulk crystalline solids. It is constructed by partitioning the unit cell into two parts: spheres around each atom, where the wavefunctions are rapidly varying and atomic-like. The remaining portion is interstitial region, where the wavefunctions are more smoothly varying and not atomic-like. Each basis function is then defined as a planewave in the interstitial region connected smoothly to a linear combination of atomic-like functions in the spheres. The atomic-like nature of the LAPW basis in the vicinity of the atoms leads to an efficient representa-

tion. While the planewave nature in the interstitial region allows for highly accurate solutions for any atomic arrangement: close-packed or open, high-symmetry or low, surfaces or bulk. The full-potential LAPW method is implemented in WIEN2k package, which is used to calculate the electronic structure and optical properties of the investigated materials. However, this method is computationally demanding and complicated for doing the geometry optimization and lattice dynamical calculations for low symmetry crystal systems with large number of atoms (e.g. triclinic, monoclinic and orthorhombic) under high pressure. An alternative and probably the simplest method is the pseudopotential approach.

The plane wave pseudopotential approach has become one of the most widely used methods for calculating ground state properties of extended systems. The electronic states of an atom can be classified into: (1) core states, which are highly localized and not involved in chemical bonding, (2) valence states, which are extended and responsible for chemical bonding and (3) semi-core states, which are localized and polarizable but generally do not contribute directly to chemical bonding. Eventhough, most of the physical and chemical properties of materials depend on the valence electrons, pseudopotentials have to be constructed very carefully in order to reproduce the properties of the all-electron atom accurately. If a pseudoatom, i.e., an atom described by a pseudopotential, reproduces the all-electron behavior accurately for any chemical environment, then the pseudopotential is said to be transferable. Pseudopotentials are frequently denoted as effective core potentials. By eliminating the strongly bound core electrons pseudopotentials reduce the number of occupied electronic orbitals that have to be treated in an electronic structure calculation. In addition, the valence wavefunctions arising from a pseudopotential are much smoother than the all-electron valence wavefunction in the core region, since the orthogonality constraints to the rapidly varying wavefunctions carrying core electrons are missing. Since it is not necessary to describe rapidly varying wavefunctions the size of the basis set used for their representation can be reduced. These two factors lead to a significant reduction of the computational effort of a pseudopotential calculation compared to an all-electron calculation. The distinct pseudopotential approaches are used in the present thesis which are described below.

Norm-conserving [11] pseudopotentials are accurate and the condition of these pseudopotentials requires a relatively large number of plane waves (or large energy cutoff) for “semilocal” orbitals of elements because of their substantial fraction inside the core region and their importance to the bonding. While *ultra-soft* [12] pseudopotentials (for e.g. Vanderbilt type) relax certain requirements and are faster than norm-conserving pseudopotentials, leading to a new pseudo wave function that can be expanded with a much smaller plane wave basis set. The charge deficiency due to the relaxation of the norm-conservation conditions are equilibrated by the introduction of atom-centered augmentation charges to ensure the proper density and potential. These augmentation of charges are defined as the charge difference between the all electron and pseudo wave functions and for convenience they can be treated in a regular grid. The norm-conserving and ultra-soft pseudopotential approaches are implemented in both Cambridge Series of Total Energy Package (CASTEP) [13] and Plane Wave Self-Consistent Field (PWSCF) [14] codes.

Another closely related approach to Vanderbilt’s pseudopotential scheme is the *projector augmented wave* (PAW) method introduced by Blöchl [15]. In the PAW method, a linear transformation is defined to connect the all electron and pseudo wave functions. The total energy is derived in a consistent way by applying this transformation to the Kohn-Sham equations. In contrast to the pseudopotential method, the PAW method retains the all electron wave functions and potentials, avoids the introduction of a pseudopotential and retains all the information on the core states. The PAW approach is incorporated through Vienna Ab-initio Simulation Package (VASP) [16].

2.5 Limitations of DFT

DFT is a well established computational approach with standard and popular exchange-correlation functionals namely LDA and GGA (with various parametrization). It is quite successful in describing the ionic, covalent and metallic systems. On the other hand, DFT has some limitations in explaining the properties such as (i) cohesion of weakly bounded systems (known as van der Waals (vdW) inter-

actions and hydrogen bonding in layered and molecular crystals) (ii) predicting or reproducing the fundamental electronic band gap of the solids (iii) electronic excitations, thereby optical absorption (iv) treating strongly correlated systems (v) too slow for liquids, etc. In fact, the described limitations within the standard DFT methods are not from the basic Kohn-Sham formalism, but arises only due to the approximate functionals. In the present thesis, we have considered the first two limitations and the recent developments & implementations through standard DFT functionals to overcome them.

First one, computational modelling of weakly interacting systems using standard DFT functionals always yields results which are not accurate enough when compared with experiments. This inaccuracy in DFT results is due to insufficiencies in taking account of the asymptotic dependence of the potential for interacting atoms/molecules at large separations which shows non-local nature. Although, dispersive forces are much weaker but they are crucial for the formation of chemical systems such as noble gas solids, layered materials, molecular crystals, biological systems and many more. Particularly, vdW interactions and hydrogen bonding play a vital role in describing the structure and stability of layered and molecular solids (especially for energetic materials). This was known for a long time and many encouraging ideas were proposed to overcome this limitation. Among numerous approaches to treat dispersive interactions, additive pair-wise corrections [17–19] and non-local correction [20, 21] methods were lead to improved results over standard DFT functionals. These methods are well benchmarked and have achieved the desired results for noble gas solids, layered solids such as graphene, h-BN and complex organic molecular solids [21–30].

Second one is predicting the band gap from KS eigenvalues. The KS band gap is defined as the difference between valence band maximum and conduction band minimum of the energy eigen value spectrum. While the experimental band gap is measured from the difference between ionization potential (I) and electron affinity (A) *i.e.* I-A. Unfortunately, the KS calculations strongly underestimate band gaps often by more than a factor of 30-40 % when compared with experiments due to derivative discontinuity of standard LDA/GGA XC-functionals [31]. Several methods such as LDA + U [32], LDA + DMFT [33], hybrid functionals [34],

GW approximation [35, 36] and TB-mBJ [37] potential have been proposed to get reliable energy band gaps compared to experiments. Unfortunately, most of these methods are computationally very demanding. While TB-mBJ potential [37] is computationally inexpensive and it provides reliable energy band gaps as comparable with more sophisticated methods within the frame work of KS formalism. The description of improvements required to overcome the above two limitations are discussed in detailed manner in the upcoming sections.

2.6 Dispersion correction methods

As discussed in the above section, the standard DFT functionals are unable to describe the non-covalent interactions in layered and molecular crystals. In order to capture the weak dispersive interactions, two kinds of dispersion correction methods are used in the present thesis. The first one is the pair-wise additive correction while second one is the non-local correction method. Recently both of these methods have shown remarkable success. These methods are found to improve the results to a great extent when compared to standard LDA/GGA functional for the layered and molecular solids [38].

2.6.1 Additive pair-wise correction methods

The Grimme (DFT-D2) [17] method, Tkatchenko and Scheffler (vdW-TS) [18], self-consistent Tkatchenko and Scheffler (TS-SCS) [19] corrections to PBE [9] and Ortmann, Bechstedt and Schmidt (OBS) [39] correction to PW91 were employed to handle dispersive interactions based on the pair-wise additive correction. The total energy after inclusion of dispersion correction is given by

$$E_{DFT+D} = E_{DFT} + E_{disp} \quad (2.23)$$

where E_{DFT} is the self-consistent Kohn-Sham energy, E_{disp} is empirical dispersion correction energy.

Using the DFT-D2 [17] method the dispersion energy is given by

$$E_{disp} = -S_6 \sum_{i < j} \frac{C_6^{ij}}{R_{ij}^6} f_{damp}(R_{ij}) \quad (2.24)$$

where S_6 is global scaling factor that only depends on the density functional used. C_6^{ij} ($= \sqrt{C_6^i C_6^j}$, where $C_6^i = 0.05 N I_p^i \alpha^i$, where I_p^i and α^i atomic ionization potentials and static dipole polarizabilities, respectively) denotes the dispersion coefficient for the pair of i^{th} and j^{th} atoms that depends on the chemical species and R_{ij} is an inter-atomic distance. $f_{damp} = \frac{1}{1+e^{-d(R_{ij}/R_r-1)}}$ is a damping function which is necessary to avoid divergence for small values of R_{ij} and R_r is the sum of atomic vdW radii.

The vdW-TS method of Tkatchenko and Scheffler [18], which is sensitive to chemical environment of the atoms and corrects for long-range dispersion interactions by adding a correction of the form

$$E_{disp} = -\frac{1}{2} \sum_{A,B} \frac{C_{6AB}}{R_{AB}^6} f_{damp}(R_{AB}, R_{AB}^0), \quad (2.25)$$

where R_{AB} is the distance between atoms A and B, C_{6AB} is the corresponding C_6 coefficient, R_A^0 and R_B^0 are the vdW radii of atoms A and B. In this method, C_{6AB} is obtained from the Casimir-Polder integral [40] which is given by

$$C_{6AB} = \frac{2C_{6AA}C_{6BB}}{\frac{\alpha_0^B}{\alpha_0^A}C_{6AA} + \frac{\alpha_0^A}{\alpha_0^B}C_{6BB}} \quad (2.26)$$

and a Fermi type damping function $f_{damp} = \frac{1}{1+e^{-d(R_{AB}/s_R R_{AB}^0-1)}}$ is used to eliminate spurious interactions at too short distances, where $R_{AB}^0 = R_A^0 + R_B^0$, s_R is free parameters and d adjusts the steepness of damping function. The free-atom reference values of α_0^A and C_{6AA} are taken from the self-interaction corrected Time Dependent (TD)-DFT calculations of Chu and Dalgarno [41]. They take advantage of the relationship between the effective volume and polarizability to calculate dispersion coefficients that depend on the chemical environment of the atom. Hirshfeld partitioning [42] of the electron density of the system is used to

obtain the contribution from each atom to the density. This effective density, and hence the volume, is compared to the density of the free-reference atom to obtain a scaling factor which is used to define the response of the dispersion coefficients to chemical environment. However, the vdW-TS scheme does not include long range electrostatic screening beyond the range of the exponentially decaying atomic densities [19].

Recently, Tkatchenko et al [19] proposed a computationally efficient method (TS-SCS) extension to the vdW-TS method, in which they considered electrodynamic response effects, in particular, the interactions of the atoms with the dynamic electric field due to the surrounding polarizable atoms and also account for many-body effects based on the coupled fluctuating dipole model. In this method, the frequency dependent screened polarizability is obtained by solving self-consistent screening equation 2.27.

$$\alpha_A^{SCS}(i\omega) = \alpha_A^{TS}(i\omega) - \alpha_A^{TS}(i\omega) \sum_{B \neq A} \tau_{A,B} \alpha_B^{SCS}(i\omega). \quad (2.27)$$

The dispersion correction energy using OBS [39] correction to PW91 is given by

$$\epsilon_{ij}^{vdw} = -f_{ij}(R) \frac{C_6^{ij}}{R^6} \quad (2.28)$$

where $f_{ij} (= 1 - \exp(-\lambda x_{ij}^2))$ is the damping function which equals one for large values of R ($= |R_i - R_j|$) and zero for small values of R , where $x_{ij} = \frac{R}{r_{cov}^i + r_{cov}^j}$ and C_6^{ij} is given by

$$C_6^{ij} = \frac{3}{2} \alpha_i \alpha_j \frac{I_i I_j}{I_i + I_j} \quad (2.29)$$

where I_i/I_j is the ionization potential and α_i/α_j the polarizability of the atom at R_i/R_j . London interpreted I_i to be a characteristic energy of the atom i . The resulting dispersion energy $E_{disp} = \frac{1}{2} \sum'_{ij} \epsilon_{ij}^{vdw}$ is added to the total energy functional of the DFT.

2.6.2 Non-local correction methods

In the pair-wise additive correction methods, vdW parameters for heavy metals (Cs, Ba, Hg, Tl, Pb and Bi etc.) *i.e.* 6th and 7th periods of the periodic table are not well optimized whereas the second one, non-local correction methods are employed to study the simple as well as heavy metal based systems and the results show success of this method in treating the vdW interactions for a wide range of materials. Therefore, we have also used the second method or the so-called non-local correction method proposed by Dion et al [20] and further modified by Klimes et al [21] in which the vdW contribution to the total energy is described through modifications to the correlation energy functional within DFT. Specifically, the DFT exchange-correlation functional takes the form:

$$E_{xc} = E_x^{GGA} + E_c^{LDA} + E_c^{nl} \quad (2.30)$$

Here E_x^{GGA} is the exchange energy [9], E_c^{LDA} is the LDA correlation energy [8] and E_c^{nl} is the non-local correction given by

$$E_c^{nl} = \frac{1}{2} \int dr \int dr' n(r) \phi(r, r') n(r') \quad (2.31)$$

where $n(r)$ is the electron density and the kernel $\phi(r, r')$ is a function of $n(r)$, $n(r')$, their gradients, and $r-r'$. However, this method requires a massive computational effort to evaluate the double integral in the above equation using the fast-Fourier-transform grid points, especially for large cells [43].

2.7 Tran-Blaha modified Becke Johnson Potential

The semi local TB-mBJ potential is obtained from simple modification of Becke-Johnson (BJ) potential [44] by the introduction of local parameter c into BJ potential leading to TB-mBJ potential as

$$\nu_{x,\sigma}^{mBJ}(r) = c\nu_{x,\sigma}^{BJ}(r) + (3c - 2) \frac{1}{\pi} \sqrt{\frac{5}{12}} \sqrt{\frac{2t_\sigma(r)}{\rho_\sigma(r)}} \quad (2.32)$$

where $\rho_\sigma = \sum_{i=1}^{N_\sigma} |\psi_{i,\sigma}|^2$ is the electron density, $t_\sigma = \frac{1}{2} \sum_{i=1}^{N_\sigma} \nabla \psi_{i,\sigma}^* \cdot \nabla \psi_{i,\sigma}$ is the kinetic energy density, $\nu_{x,\sigma}^{BR}(r)$ is the Becke-Roussel potential, and $\mathbf{c} = \alpha + \beta \left(\frac{1}{V_{cell}} \int_{cell} \frac{|\nabla \rho(r')|}{\rho(r')} d^3 r' \right)$, where α, β are two free parameters and V_{cell} is volume of the unit cell. Recently, Koller *et al* [45, 46] reported the merits and limitations of the TB-mBJ and also made an attempt to improve the performance of the original TB-mBJ potential by optimizing the local parameter \mathbf{c} in the above equation 2.32. So far, several groups have been using the TB-mBJ potential across the globe for the calculation of electronic structure and optical properties of diverse materials [47–49] and confirmed that TB-mBJ band gaps are improved for a wide range of materials (see Fig. 1 from Ref. [50]) over the standard DFT functionals. The accurate prediction of band gaps using TB-mBJ potential for diverse materials motivated us to use this potential for the energetic materials under investigation.

2.8 Density functional perturbation theory

The basic approximation which allows one to decouple the vibrational from the electronic degrees of freedom in a solid is the adiabatic approximation by Born and Oppenheimer (BO) [1]. The simplified many body Hamiltonian using BO approximation is given by

$$\hat{H}_{BO}(R) = \hat{T}_e + \hat{V}_{ee} + \hat{V}_{en} + \hat{V}_{nn} \quad (2.33)$$

where \hat{T}_e is kinetic energy operator of electrons, $\hat{V}_{ee}, \hat{V}_{en}, \hat{V}_{nn}$ represent electron-electron, electron-nuclei and nuclei-nuclei electrostatic interactions. The equilibrium geometry of the system is given by the condition that the forces acting on individual nuclei vanish:

$$F_I \equiv -\frac{\partial E(R)}{\partial R_I} = 0 \quad (2.34)$$

whereas the vibrational frequencies, ω , are determined by the eigenvalues of the Hessian of the BO energy, scaled by the nuclear masses:

$$\det \left| \frac{1}{\sqrt{M_I M_J}} \frac{\partial^2 E(\mathbf{R})}{\partial R_I \partial R_J} - \omega^2 \right| = 0 \quad (2.35)$$

The calculation of the equilibrium geometry and the vibrational properties of a system thus amounts to computing the first and second derivatives of its BO energy surface. The Hessian of the BO energy surface appearing in the above equation is obtained by differentiating the Hellmann-Feynman forces with respect to nuclear coordinates:

$$\frac{\partial^2 E(\mathbf{R})}{\partial R_I \partial R_J} = \int \frac{\partial n_{\mathbf{R}}(r)}{\partial R_J} \frac{\partial V_{en}(\mathbf{R})}{\partial R_I} dr + \int n_{\mathbf{R}}(r) \frac{\partial^2 V_{en}(\mathbf{R})}{\partial R_I \partial R_J} dr + \frac{\partial^2 V_{nn}(\mathbf{R})}{\partial R_I \partial R_J} \quad (2.36)$$

The calculation of the ground-state electron charge density, $n_{\mathbf{R}}(r)$ as well as of its linear response to a distortion of the nuclear geometry, $\frac{\partial n_{\mathbf{R}}(r)}{\partial R_I}$ is required to calculate the Hessian of the BO energy surface. The Hessian matrix is usually called the matrix of the inter-atomic force constants (IFC) [51]. Once IFC is known, the Fourier transform of IFC resulting in the dynamical matrix in reciprocal space. Therefore, Density Functional Perturbation Theory has become a popular tool for the analysis of the vibrational and spectroscopic properties of materials, routinely providing phonon frequencies and dielectric properties with just a few percent of error with respect to experiment [52].

2.9 Gibbs free energy of polymorphs

The thermodynamic stability was investigated by comparing the free energies of polymorphs. The Gibbs free energy for any material at a given temperature is

$$G(P, T) = F(V, T) + PV = F_{vib} + F_{perfect} + PV \quad (2.37)$$

where F , P , T and V are the Helmholtz free energy, pressure, absolute temperature and volume, respectively. $F(V, T)$ is the sum of vibrational free energy and

perfect lattice energy *i.e.* $F(V, T) = F_{vib} + F_{perfect}$. The vibrational free energy F_{vib} calculated within the harmonic approximation is given by

$$F_{vib} = k_B T \sum_i \left(\frac{\hbar \omega_i}{2k_B T} + \ln \left(1 - e^{-\frac{\hbar \omega_i}{k_B T}} \right) \right) \quad (2.38)$$

where ω_i is the i^{th} phonon frequency, \hbar is the reduced Planck constant and k_B is the Boltzmann constant and $F_{perfect} = E_0 + E_{el} - TS_{el}$. E_0 and $E_{el} - TS_{el}$ are the contributions from the lattice and electronic excitations, respectively. If the electronic excitations are neglected then the Gibbs free energy can be calculated by $G = E_0 + PV + F_{vib} = H_0 + F_{vib}$, where $H_0 = E_0 + PV$ is the enthalpy at $T = 0$ K and E_0 denotes the change in energy of atoms in the unit cell of a perfect crystal with respect to the energy of the isolated atoms.

Using the above discussed theoretical methodologies, we have predicted the thermo-physical properties of the diverse classes of energetic materials and are presented in the upcoming chapters.

References

- [1] M. Born and J. R. Oppenheimer, *Am. J. Phys.*, **84**, 451 (1927).
- [2] P. Hohenberg and W. Kohn, *Phys. Rev.*, **136**, B864 (1964).
- [3] L. H. Thomas, *Proc. Cambridge Phil. Soc.*, **23**, 542 (1927).
- [4] E. Fermi, *Z. Physik*, **48**, 73 (1928).
- [5] W. Kohn and L. Sham, *Phys. Rev.*, **140**, A1133 (1965).
- [6] F. Bloch, *Z. Physik*, **57**, 545 (1929).
- [7] P. A. M. Dirac, *Proc. Roy. Soc. Lond. A*, **123**, 714 (1929).
- [8] D. M. Ceperley and B. J. Alder, *Phys. Rev. Lett.*, **45**, 566 (1980).
- [9] J. P. Perdew, M. Ernzerhof and K. Burke, *J. Chem. Phys.*, **105**, 9982 (1999).

- [10] D. J. Singh and L. Nordstrom, *Planewaves, Pseudopotentials and the LAPW method*, 2nd ed. Springer Verlag, Berlin (2006).
- [11] N. Troullier and J. L. Martins, Phys. Rev. B, **43**, 1993 (1991).
- [12] D. Vanderbilt, Phys. Rev. B, **41**, 7892 (1990).
- [13] M. C. Payne, M. P. Teter, D. C. Allen, T. A. Arias and J. D. Joannopoulos, Rev. Mod. Phys., **64**, 1045 (1992).
- [14] P. Giannozzi et al, J. Phys.: Condens. Matter, **21** 395502 (2009).
- [15] P. E. Blöchl, Phys. Rev. B, **50**, 17953 (1994).
- [16] G. Kresse and D. Joubert, Phys. Rev. B, **54**, 11169 (1996).
- [17] S. Grimme, J. Compu. Chem., **27**, 1787 (2006).
- [18] A. Tkatchenko and M. Scheffler, Phys. Rev. Lett., **102**, 073005 (2009).
- [19] A. Tkatchenko, R. A. Di. Stasio, R. Car and M. Scheffler, Phys. Rev. Lett., **108**, 236402 (2012).
- [20] M. Dion, H. Rydberg, E. Schröder, D. C. Langreth and B. I. Lundqvist, Phys. Rev. Lett., **92**, 246401 (2004).
- [21] J. Klimes and A. Michaelides, J. Chem. Phys., **137**, 120901 (2012).
- [22] T. Bucko, J. Hafner, S. Lebègue and J. G. Ángyán, J. Phys. Chem. A, **114**, 11814 (2010).
- [23] A. O. -D. -L. Roza and E. R. Johnson, J. Chem. Phys., **137**, 054103 (2012).
- [24] T. Risthaus and S. Grimme, J. Chem. Theory Comput., **9**, 1580 (2013).
- [25] T. Bucko, S. Lebègue, J. Hafner and J. G. Ángyán, Phys. Rev. B, **87**, 064110 (2013).
- [26] K. Berland and P. Hyldgaard, Phys. Rev. B, **87**, 205421 (2013).

- [27] T. Bucko, S. Lebègue, J. Hafner and J. G. Ángyán, *J. Chem. Theory Comput.*, **9**, 4293 (2013).
- [28] A. M. Reilly and A. Tkatchenko, *J. Phys. Chem. Lett.*, **4**, 1028 (2013).
- [29] T. Bucko, S. Lebègue, J. Hafner and J. G. Ángyán, *J. Chem. Phys.*, **141**, 034114 (2014).
- [30] J. Moellmann and S. Grimme, *J. Phys. Chem. C*, **118**, 7615 (2014).
- [31] L. J. Sham and M. Schluter, *Phys. Rev. Lett.*, **51**, 1888 (1983).
- [32] V. I. Anisimov, J. Zaanen and O. K. Andersen, *Phys. Rev. B*, **44**, 943 (1991).
- [33] J. Kunes, V. I. Anisimov, S. L. Skornyakov, A.V. Lukoyanov and D. Vollhardt, *Phys. Rev. Lett.*, **99**, 156404 (2007).
- [34] J. Heyd, J. E. Peralta, G. E. Scuseria and R. L. Martin, *J. Chem. Phys.*, **123**, 174101 (2005).
- [35] M. Shishkin and G. Kresse, *Phys. Rev. B*, **75**, 235102 (2007).
- [36] M. Shishkin, M. Marsman and G. Kresse, *Phys. Rev. Lett.*, **99**, 246403 (2007).
- [37] F. Tran and P. Blaha, *Phys. Rev. Lett.*, **102**, 226401 (2009).
- [38] S. Appalakondaiah, *Firrst pricniples study of layered and molecular solids*, Doctoral thesis, Hyderabad (2015).
- [39] F. Ortman, F. Bechstedt and W. G. Schmidt, *Phys. Rev. B*, **73**, 205101 (2006).
- [40] H. B. G. Casimir and B. Polder, *Phys. Rev.*, **73**, 360 (1948).
- [41] X. Chu and A. Dalgarno, *J. Chem. Phys.*, **121**, 4083 (2004).
- [42] F. L. Hirshfeld, *Theo. Chim. Acta.*, **44**, 129 (1977).
- [43] Z. Wu, R. K. Kalia, A. Nakano and P. Vashishta, *J. Chem. Phys.*, **134**, 204509 (2011).

- [44] A. D. Becke and E. R. Johnson, *J. Chem. Phys.*, **124**, 221101 (2006).
- [45] D. Koller, F. Tran and P. Blaha, *Phys. Rev. B*, **85**, 155109 (2012).
- [46] D. Koller, F. Tran and P. Blaha, *Phys. Rev. B*, **83**, 195134 (2011).
- [47] D. J. Singh, *Phys. Rev. B*, **82**, 205102 (2010).
- [48] J. A. Camargo-Mart ez and R. Baquero, *Phys. Rev. B*, **86**, 195106 (2012).
- [49] H. Jiang, *J. Chem. Phys.*, **138**, 134115 (2013).
- [50] H. Dixit, R. Saniz, S. Cottenier, D. Lamoen and B. Partoens, *J. Phys.: Condens. Matter*, **24**, 2055030 (2012).
- [51] S. Baroni, S. D. Gironcoli. A. D. Corso and P. Giannozzi, *Rev. Mod. Phys.*, **73**, 515 (2001).
- [52] M. J. Verstraete and Z. Zanolli, *Lecture Notes of the 45th IFF Spring School “Computing Solids- Models, ab initio methods and supercomputing*, Forschungszentrum Jülich (2014).

Pressure dependent phase stability, electronic structure and optical properties of silver and mercury fulminates

This chapter presents a comprehensive study on thermodynamic ground state of silver fulminate (SF) polymorphs under high pressure and temperature. Apart from this, equation of state, compressibility and bonding properties under high pressure, electronic structure and optical properties are investigated explicitly including spin-orbit (SO) interactions for the α -SF and Mercury Fulminate (MF).

3.1 Introduction

As discussed in chapter 1, explosives are classified into primary and secondary explosives. A typical explosive consists of a main charge of secondary explosive with a high output but low sensitivity to initiation, which is initiated by an adjacent primary explosive, which transmits a sufficiently strong shock to the secondary explosive leading to detonation [1]. Inorganic fulminates are primary explosives and they find applications as initiators for secondary explosives. They are isoelectronic with the corresponding azides, cyanates and cyanamides [2]. SF is an extremely effective detonant and is found to be as efficient as lead azide (LA) in its pure form [3]. It is about 15 times and 30% more efficient than MF for

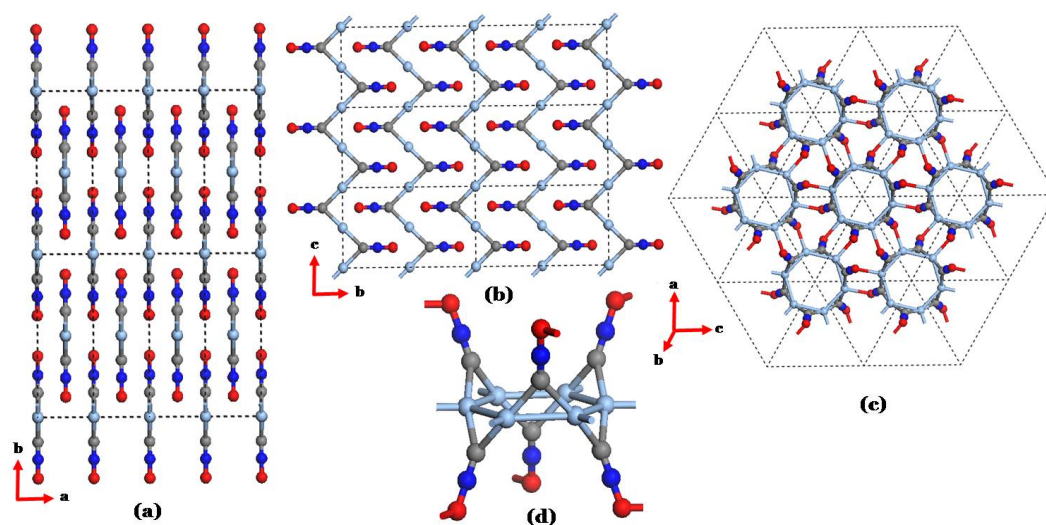


Figure 3.1: Crystal structures of (a, b) layered α -SF, (c) β -SF ($2 \times 2 \times 2$ super cell) and (d) single molecule of β -SF.

exploding 2,4,6-tri-nitro-phenyl-methyl-nitroamine and tri-nitro-xylene, respectively [4]. It is known to be a sensitive explosive for a long time with detonation velocity of 1700 ms^{-1} [5] and its detonators have been used in the Italian Navy [6]. It finds some applications (when used in small quantity) in pyrotechnics, fire works, Christmas crackers [7] and toy pistols [8]. Moreover, the initiating properties of various fulminates were examined by Martin and Wohler [9–11] and they found that the Ag, Cd and Cu fulminates have stronger initiating power than MF. However, MF was the first, widely and long used primary explosive due to its excellent priming power, high performance and it can be easily detonated [12]. MF has rendered invaluable service over many years and this can be clearly seen from its annual production only in Germany which was about 1,00,000 kg per year in the beginning of 20th century [13]. The wide application of dynamite was only possible with the use of MF as initiator which guarantees a safe ignition and hence it is used to initiate dynamite in metal blasting cap detonator [13, 14]. These fulminates detonate after the initiation with external stimuli by producing CO, N₂ and Ag/Hg as the decomposition products: $2\text{AgCNO} \rightarrow 2\text{Ag} + 2\text{CO}$

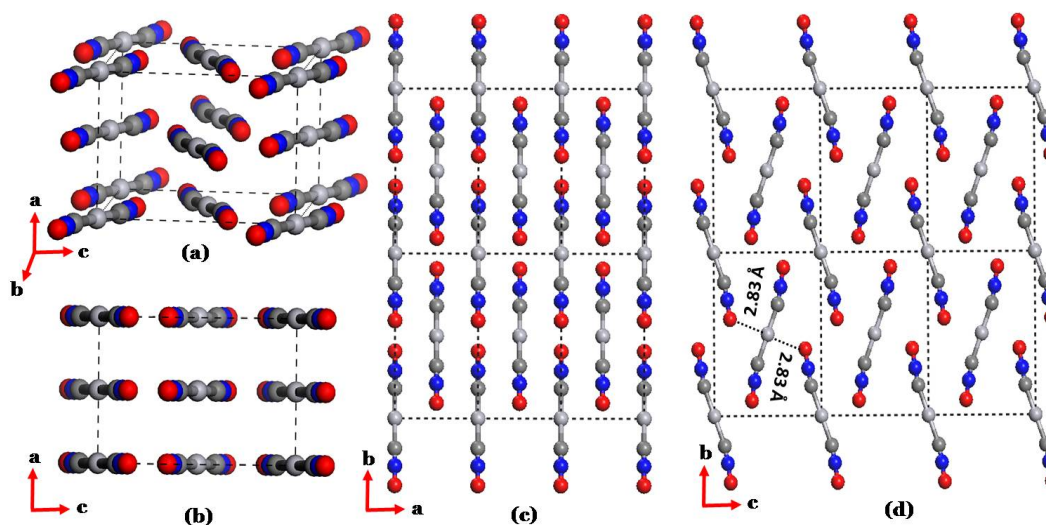


Figure 3.2: Crystal structures of (a, b) unit cell of MF, (c, d) layered structure of MF.

+ N₂ [7]; Hg(CNO)₂ → Hg + 2CO + N₂ [15]. MF is very sensitive to impact, friction and sunlight and is detonated by sparks and flames and also it is desensitized by addition of water. MF is very sensitive to shock, impact, friction and sunlight. MF is detonated by sparks and flames [12] and also it is desensitized by addition of water. Since LA was found to detonate more reliably (detonation velocity 4.25 km/s for MF and 5.3 km/s for LA), less impact sensitivity (1-2 N-m for MF and 2.5-4 N-m for LA) and to have better thermal stability (temperature of ignition 210°C for MF and above 300°C for LA), therefore, MF was largely replaced by LA [3, 16, 17]. The measured figure of insensitiveness (F of I) and temperature of ignition (T of I) for MF (10) < SF (22) < LA (30) and SF (170°C) < MF (210°C) < LA (> 300°C), respectively [Ref. [3] and references therein]. However, it has been reported that SF crystals stored under water about 40 years ago exhibit similar properties like fresh crystals with an exception that the white crystals transform to mouse-gray color due to long exposure to light and these crystals possess non-hygroscopic nature [3, 18].

SF was first prepared by Brugnatelli [19] and later recognised by Gay-Lussac

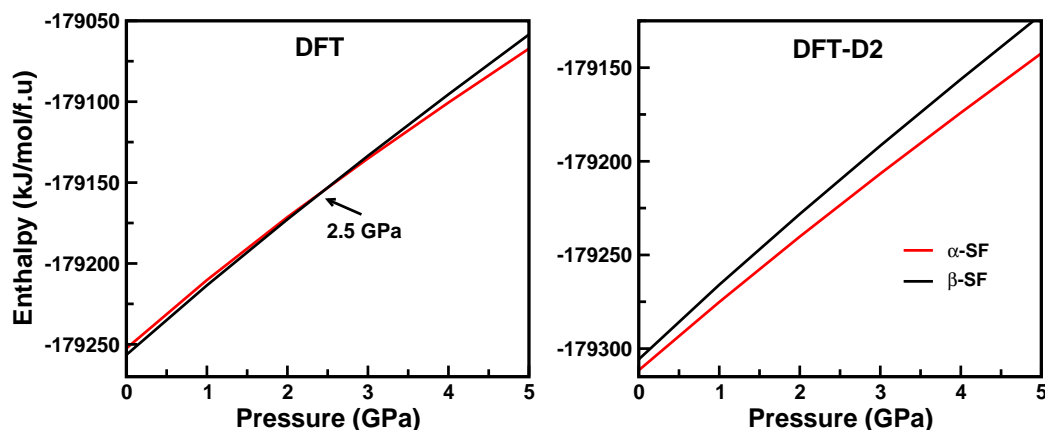


Figure 3.3: Calculated enthalpy as a function of pressure for α - and β - polymorphic phases of SF with (DFT-D2) and without (DFT within PBE-GGA) dispersion correction method.

[20]. Singh [21] reported the crystal structure of SF to be body centred orthorhombic symmetry with space group $Ibam$. The accurate crystal symmetry and formation of two polymorphic phases of SF was first pointed out by Pandey [22] and Britton *et al* [23]. Further, the re-determined crystal structures of the two polymorphic phases are reported as orthorhombic ($Cmcm$) phase by Barrick *et al* [24] and trigonal ($R\bar{3}$) phase by Britton [25]. Differential thermal analysis studies [26] indicate no evidence for temperature induced phase changes between 20°C and 145°C.

Several methods were proposed in the literature to synthesize MF; among them, Howard's recipe for the formation of MF from mercury, nitric acid and ethanol was widely accepted [27–29]. However, MF has been used as a primary explosive for a long time but the determination of its crystal symmetry was controversial until 2007. Since 1931 several investigations have been made to determine the crystal structure of MF using single crystal [2, 30, 31] and powder X-ray diffraction methods [32, 33] but these attempts were unsuccessful to determine correct crystal structure of MF. Recently, Beck *et al* [34] reported the correct crystal structure of this energetic compound. Moreover, Density Functional Theory

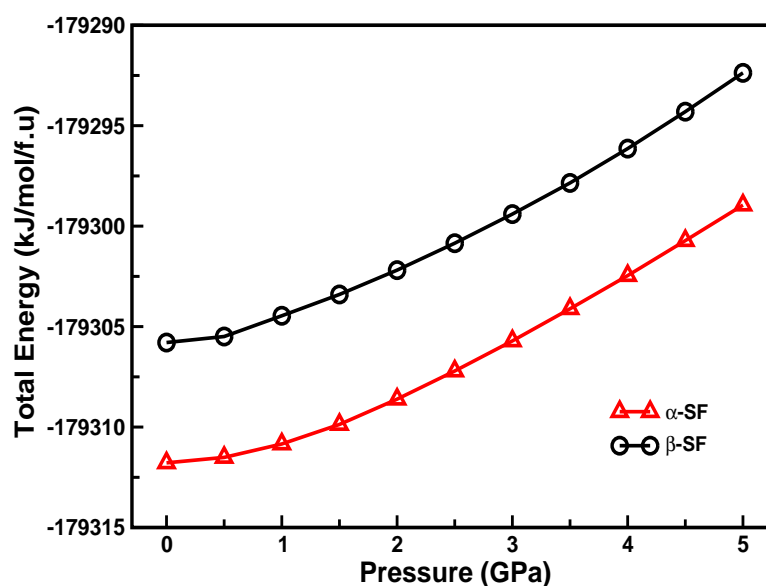


Figure 3.4: Calculated total energy as a function of pressure for α - and β - polymorphic phases of SF within DFT-D2 method.

(DFT) calculations have been carried out for a single molecule of MF at B3LYP level and they predicted bent CNO-Hg-ONC units of molecular structure [35]. Once again Beck et al [12] made a detailed theoretical investigation on molecular structure of MF and they proved that the molecular and Lewis structure of MF is linear in gas phase *i.e.* ONC-Hg-CNO. The molecular structure is in contrast to the previous theoretical prediction [35] but it is in good accord with their recent X-ray diffraction study [34]. In addition, the authors also proposed that Hg-C-N angle is 180° in the isolated molecule, whereas it is 169° in the crystalline solid form which is due to intermolecular interactions and packing effects [12]. Therefore in this chapter, we attempt to explore the phase stability under pressure and temperature, electronic structure, chemical bonding and optical properties of the energetic solids SF polymorphs and MF.

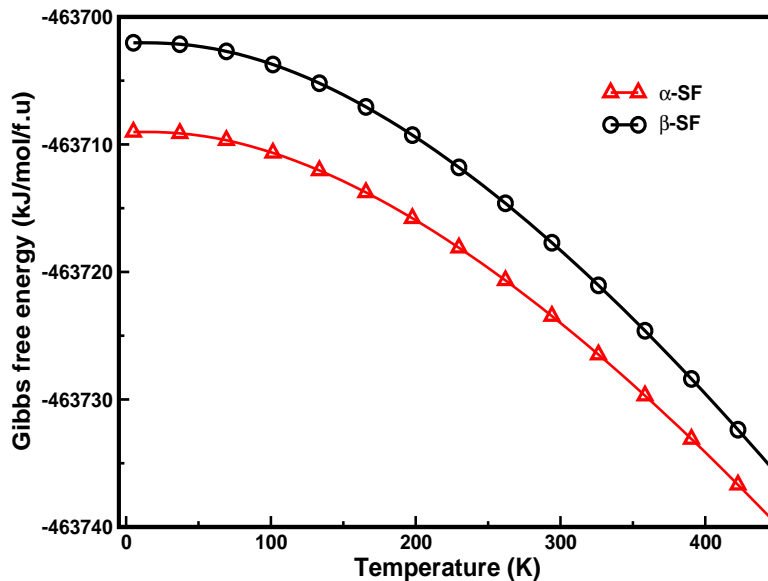


Figure 3.5: Calculated Gibbs free energy as a function of temperature for α - and β - polymorphic phases of SF within DFT-D2 method.

3.2 Methodology of calculation

The polymorphic phases of SF crystals were studied using periodic DFT calculations performed with two different packages namely Plane Wave Self Consistent Field (PWSCF) [36] and Cambridge series of total energy package (CASTEP) [37], which are based on plane wave pseudo potential (PW-PP) approach. We have used Vanderbilt type ultra soft pseudo potentials [38] to treat ion-electron interactions, while electron-electron interactions are treated with the generalized gradient approximation (GGA) developed by Perdew-Burke-Ernzerhof (PBE) [39] and Perdew and Wang [40]. The Broyden-Fletcher-Goldfarb-Shanno (BFGS) minimization scheme [41] was used in geometry optimization. The plane wave cut-off energy was set to 60 Ry (~ 816 eV) and a k-point grid spacing of $2\pi \times 0.025 \text{ \AA}^{-1}$ according to the Monkhorst-Pack grid scheme [42]. The self-consistent energy convergence accuracy was set to 1.0×10^{-6} eV/atom and the force to be 1.0×10^{-4} eV/ \AA .

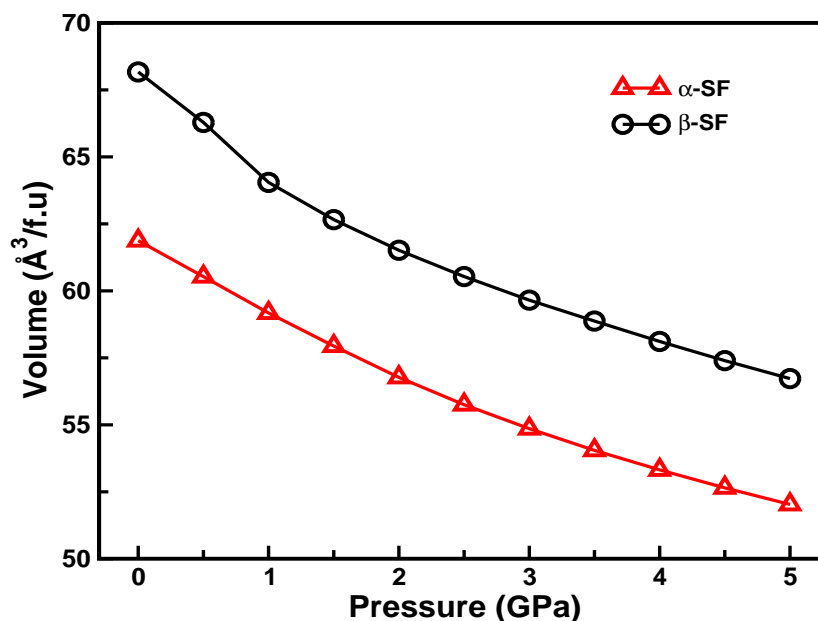


Figure 3.6: Calculated volume as a function of pressure for α - and β - polymorphic phases of SF within DFT-D2 method.

For MF, the calculations were performed using the Vienna ab-initio Simulation Package (VASP) [43] with the all-electron projected augmented wave method. A plane wave cut-off energy of 1000 eV was used. Quasi-Newton algorithm is used to relax the ions and the system was fully relaxed with residual forces smaller than 0.001 eV/Å. To describe the non-covalent interactions in the layered and molecular SF polymorphs and MF crystals, additive pair wise [44–46] and non-local [47, 48] correction methods have been employed.

Tran Blaha-modified Becke Johnson (TB-mBJ) potential [49] has been used to get reliable energy band gaps thereby calculation of electronic structure and optical properties of SF polymorphs and MF. This semi-local potential is implemented through WIEN2K package [50]. To achieve the required convergence of energy eigenvalues, the wave functions in the interstitial region were expanded using plane waves with a cut-off $K_{max} = 7/RMT$ while the charge density was Fourier expanded up to $G_{max} = 14$, where Radius of Muffin Tin (RMT) is the small-

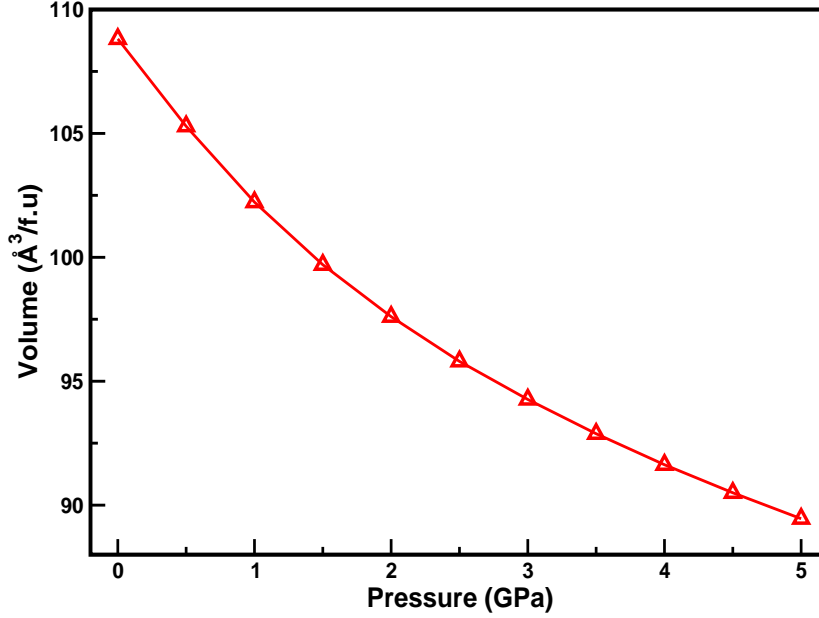


Figure 3.7: Calculated volume as a function of pressure for MF within optB88-vdW method.

est atomic sphere radius and K_{max} denotes the magnitude of the largest K vector in plane wave expansion. The RMT radii are assumed to be 2.0, 1.05, 1.05 and 1.25 Bohrs for Ag/Hg, C, N and O, respectively. The wave functions inside the spheres are expanded up to $l_{max} = 10$. Self-consistency of total energy is obtained by using $9 \times 9 \times 5$ k-mesh in the Irreducible Brillouin Zone (IBZ). The frequency-dependent optical properties were calculated at a denser k-mesh of $20 \times 20 \times 12$, $17 \times 17 \times 17$ and $19 \times 19 \times 12$ for α -, β - phases of SF and MF respectively.

3.3 Results and discussion

3.3.1 Crystal structure and ground state properties

Extreme sensitivity, poor stability and high cost of Silver as a raw material prohibited SF in commercial or military priming and detonating devices [51, 52] but still it finds applications in pyrotechnics, fire works, toy pistols and in the Italian navy. However, the relative stability and conditions necessary for the formation

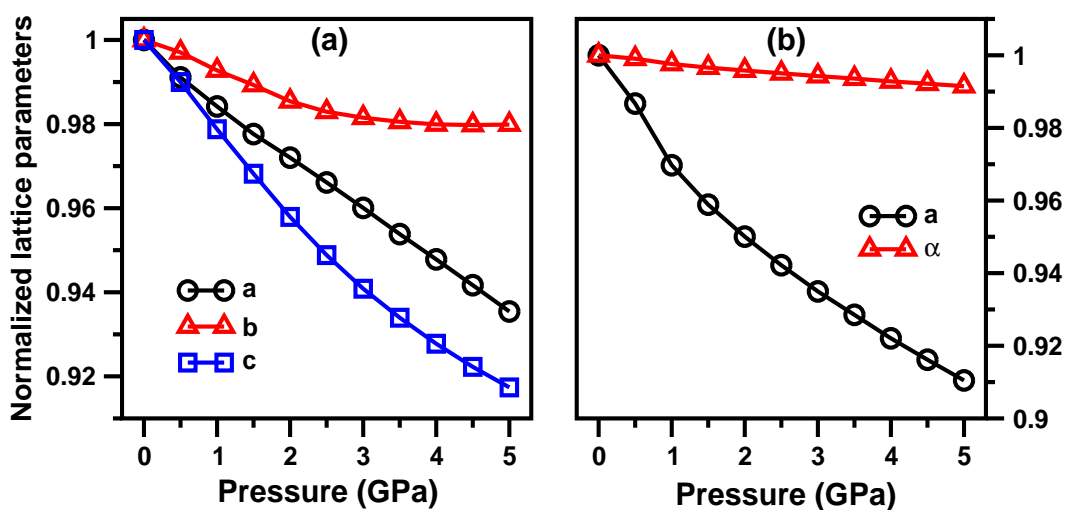


Figure 3.8: Calculated normalized lattice parameters of a) α - and b) β - polymorphic phases of SF as a function of pressure within DFT-D2 method.

of two polymorphic phases are still unknown for this material. On the other hand, MF is a long standing primary explosive but the molecular geometry and crystal structure of MF has been resolved only after more than 300 years of its discovery [34]. As discussed in section 3.1, SF exists in two polymorphic phases at ambient conditions and it is noticed that except the crystal structures [23–25] of both SF polymorphs and MF [34], most of the physical properties are not well understood from experimental and theoretical perspective. The crystal structures of orthorhombic ($Cmcm$) and rhombohedral ($R\bar{3}$) phases of SF are shown in figure 3.1. The crystal structures of the two polymorphic phases mainly differ by planar zig-zag chains (orthorhombic phase in bc plane) and cyclic hexamers (rhombohedral phase in ac plane) [23] (see figure 3.1) and these SF molecules bind through weak vdW forces within the unit cell.

The chemical formula of MF *i.e.* $Hg(CNO)_2$ is analogous to the corresponding Mercury Azide (MA), $Hg(NNN)_2$. Moreover, the fulminate and/or azide single anion is linear and contains 16 valence electrons resulting a negative charge. MF crystallizes in the orthorhombic centro symmetric space group $Cmce$ with $Z = 4$ f.u./cell [34]. While MA crystallizes in non-centro symmetric space group $Pca2_1$

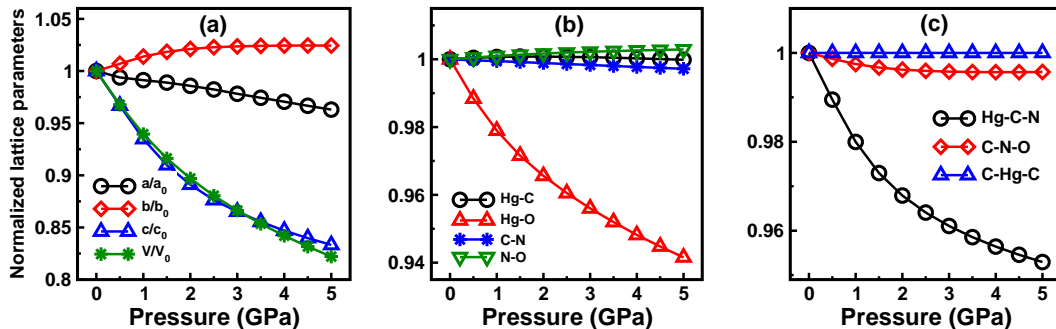


Figure 3.9: Calculated normalized a) lattice parameters b) bond lengths and c) bond angles of MF as a function of pressure within optB88-vdW method.

with $Z = 4$ f.u./cell [53], consequently MA is $\sim 4\%$ more densely packed than MF [34]. As shown in figure 3.2, the crystal structure consists of MF molecule at each corner as well as face centre of the unit cell (see figure 3.2a), the planar MF molecules are located at $x = 0$ and $x = 0.5$ along b-axis [34] and the layers are stacked along a- and c-axes as depicted in figures 3.2b & c, respectively. Apart from this, experimental measurements reveal that the arrangement of MF molecules in b-c plane leads to two non-bonded contacts between Hg and O atoms (see figure 3.2d) with a distance of $\text{Hg}\dots\text{O} = 2.833 \text{ \AA}$ within the unit cell, which is less than the sum of the van der Waals (vdW) radii 3 \AA of Hg and O atoms (vdW radii 1.5 \AA for Hg and O atoms) which causes weak vdW interactions in the crystalline MF [34]. The weak intermolecular interactions play a significant role in predicting the structure and stability of the layered and molecular crystalline solids.

As a first step, we have performed full structural optimization by taking experimental data as a input [24, 25, 34]. The lattice parameters and fractional coordinates are allowed to relax to get the most stable configurations at ambient pressure. The obtained volumes for $Cmcm$ and $R\bar{3}$ phases are overestimated by 22.5% and 13.5% respectively for SF while the same is overestimated by 20.9% within PBE-GGA for MF. This clearly shows that PBE-GGA functional is inadequate to predict the ground state properties of the energetic layered and molecular solids. Therefore, we have used various dispersion corrected (DFT-D) methods

Table 3.1: Calculated ground state lattice parameters (a, b, c, in Å), crystallographic angle (α , in $^\circ$), volume (V, in Å³) and density (ρ , in gr/cc) of α - and β -polymorphic phases of SF using different dispersion corrected DFT-D2, vdW-TS and OBS methods along with the experimental data.

		α - SF				
Package	Method	a	b	c	V	ρ
PWSCF	PBE	4.701	10.765	5.869	297.00	3.35
		(+21.2%)	(+0.03%)	(+1.11%)	(+22.66%)	(-18.5%)
	DFT-D2	3.411	11.467	6.327	247.50	4.02
		(-12.1%)	(+6.6%)	(+9.01%)	(+2.2%)	(-2.2%)
CASTEP	PBE	4.773	10.743	5.847	299.80	3.32
		(+28.0%)	(-0.08%)	(+0.74%)	(+23.8%)	(-19.2%)
	DFT-D2	3.416	11.436	6.340	247.69	4.02
		(-12.0%)	(+6.4%)	(+9.23%)	(+2.3%)	(-2.2%)
	vdW-TS	3.883	11.009	5.872	251.05	3.97
		(+0.07%)	(+2.4%)	(+1.17%)	(+3.7%)	(-3.4%)
	DFT-OBS	4.352	10.749	5.826	272.54	3.65
		(+12.16%)	(-0.02%)	(+0.37%)	(+12.6%)	(-11.2%)
	Expt. ^a	3.880	10.752	5.804	242.13	4.11
		β - SF				
		a	α		V	ρ
PWSCF	PBE	9.571	115.99	-	442.94	3.37
		(+5.3%)	(+0.2%)	-	(+13.4%)	(+11.8%)
	DFT-D2	9.264	115.84	-	409.03	3.65
		(+2.0%)	(+0.09%)	-	(+4.7%)	(+4.5%)
CASTEP	PBE	9.550	116.06	-	436.64	3.42
		(+5.1%)	(+0.3%)	-	(+11.8%)	(+10.5%)
	DFT-D2	9.264	115.86	-	407.76	3.66
		(+2.0%)	(+0.11%)	-	(+4.4%)	(+4.2%)
	vdW-TS	9.223	115.76	-	407.04	3.67
		(+1.5%)	(+0.03%)	-	(+4.2%)	(+4.0%)
	DFT-OBS	9.379	115.90	-	421.24	3.54
		(+3.2%)	(+0.14%)	-	(+7.8%)	(+7.3%)
	Expt. ^b	9.087	115.73	-	390.58	3.82

^a Ref.[24], ^b Ref.[25]

to capture vdW interactions to reproduce the ground state properties which are comparable with the experiments [23–25, 34]. The obtained volumes are overestimated by about 12.6%, 7.8% using DFT-OBS; 3.7%, 4.2% using vdW-TS; and 2.2%, 4.5% using DFT-D2 methods for $Cmcm$, $R\bar{3}$ phases, respectively. On the similar path, the obtained volume with non-local correction methods for MF is overestimated by around 1.7% using vdW-DF; 5.9% using vdW-DF2 and underestimated by around 0.4% using optB88-vdW; 1.1% using optB86b-vdW. Among the studied DFT-D methods, DFT-D2 (vdW-TS) and optB88-vdW dispersion corrected methods apparently work well for SF polymorphs and MF, respectively. The small discrepancies between the theoretical values at 0 K and experimental data at 298 K [23–25, 34] were observed. The order of discrepancies about $\sim 3\text{--}4\%$ are previously reported for secondary explosive molecular crystals with DFT-D methods at 0 K [54–57]. The calculated ground state lattice parameters, unit cell volume and density of SF polymorphs and MF using various DFT-D methods are compared with experimental data and are presented in Tables 3.1 and 3.2 respectively. The obtained ground state properties with and without dispersion correction methods using PWSCF and CASTEP are in good accord with each other for SF polymorphs (see Table 3.1). Further all the calculations were carried out using DFT-D2 method for SF polymorphs whereas optB88-vdW method for MF.

3.3.2 Pressure and temperature effects on the phase stability of SF polymorphs

In general, the energy difference between different polymorphic forms are mostly in the order of 0–10 kJ/mol [58]. The DFT-D2 method is successful in predicting the polymorphs of Benzamide (P1 and P3) with an energy difference of 1.9 kJ/mol [59]. Hence, we have also used the DFT-D2 method for predicting the relative stability of SF polymorphs. The obtained total energy difference for $Cmcm$ phase is lower by ~ 6 kJ/mol per molecule than $R\bar{3}$ phase which implies that $Cmcm$

Table 3.2: Calculated ground state lattice parameters (a , b , c , in \AA), volume (V , in \AA^3), density (ρ , in gr/cc) of orthorhombic MF using standard PBE and various non-local correction methods along with the experimental data.

Parameter	PBE	vdW-DF	vdW-DF2	optB88-vdW	optB86b-vdW	Expt. ^a
a	6.019 (+10.0%)	5.518 (+0.9%)	5.559 (+1.6%)	5.451 (-0.3%)	5.447 (-0.4%)	5.470
b	10.523 (+1.4%)	10.749 (+3.6%)	10.742 (+3.5%)	10.677 (+2.9%)	10.661 (+2.7%)	10.376
c	8.346 (+7.4%)	7.497 (-2.6%)	7.748 (+0.6%)	7.478 (-2.9%)	7.445 (-3.3%)	7.700
V	528.62 (+20.9%)	444.67 (+1.7%)	462.67 (+5.9%)	435.22 (-0.4%)	432.33 (-1.1%)	437.03
ρ	3.576 (-17.4%)	4.251 (-1.8%)	4.086 (-5.6%)	4.343 (+0.3%)	4.372 (-1.0%)	4.33

^a Ref.[34]

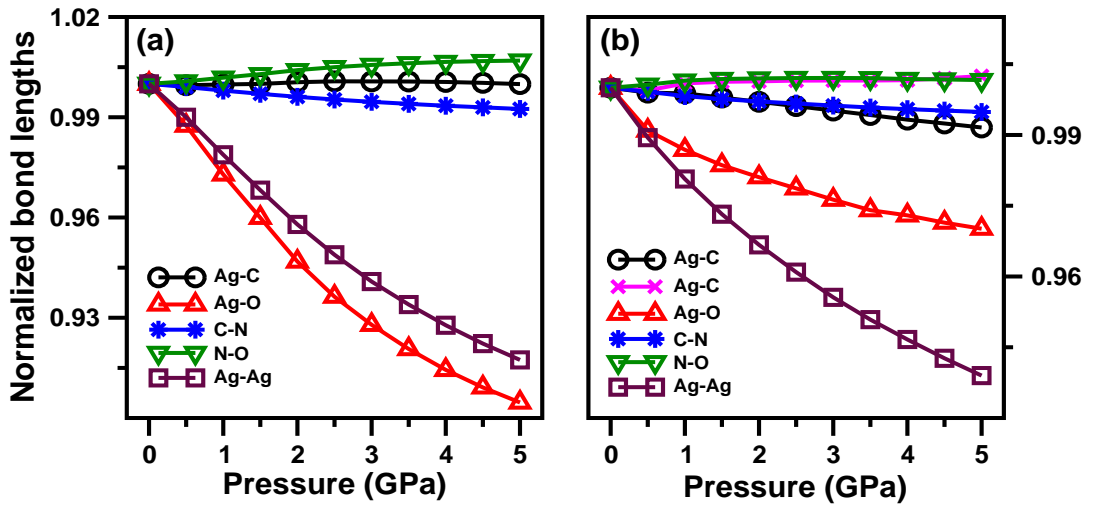


Figure 3.10: Calculated normalized bond lengths of a) α - and b) β - polymorphic phases of SF as a function of pressure within DFT-D2 method.

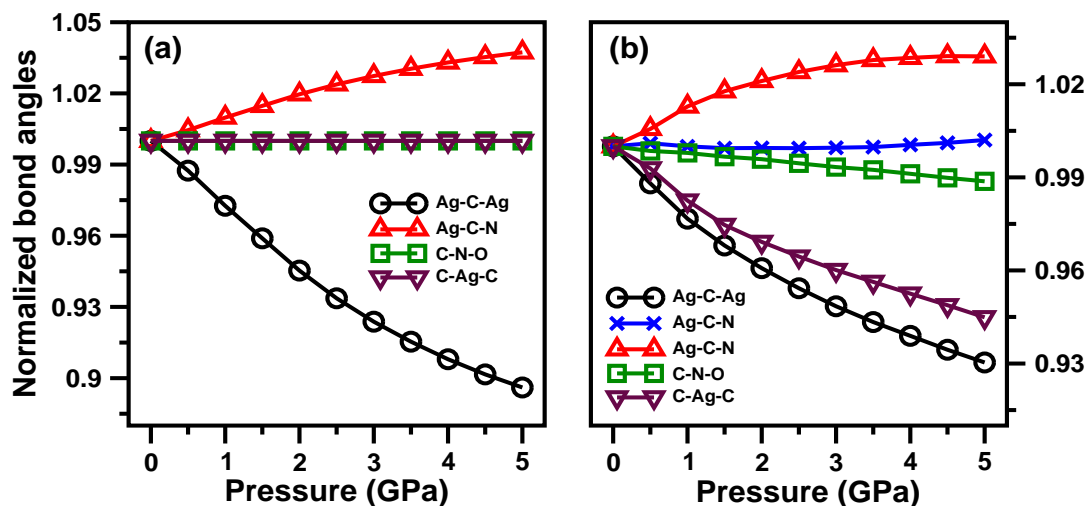


Figure 3.11: Calculated normalized bond angles of a) α - and b) β - polymorphic phases of SF as a function of pressure within DFT-D2 method.

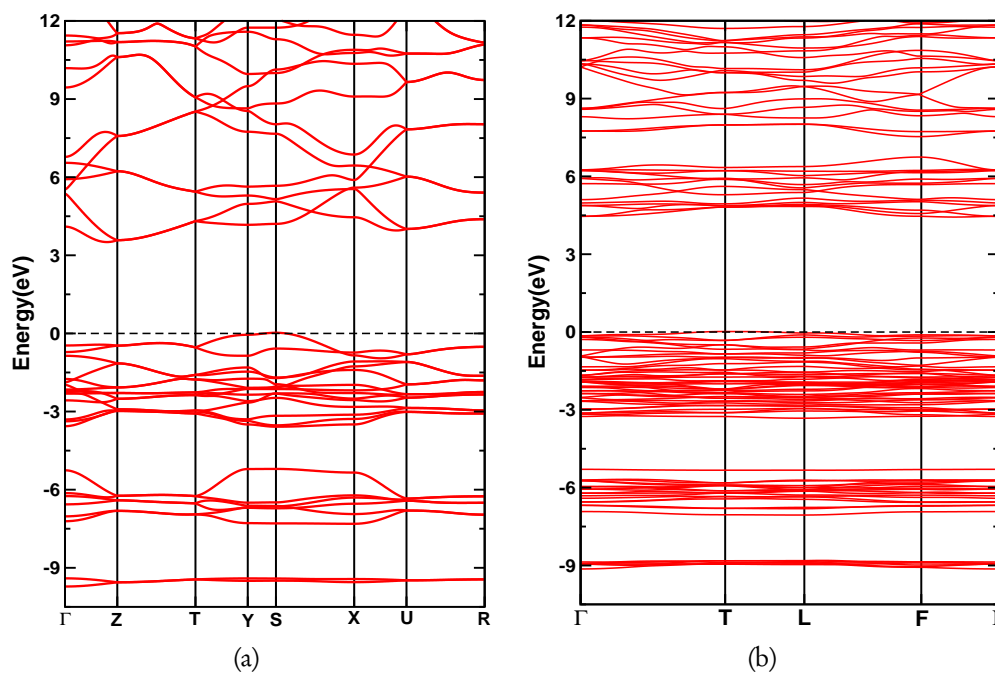


Figure 3.12: Calculated electronic band structures of a) α - and b) β - phases of SF using TB-mBJ potential at the experimental crystal structures [24, 25].

phase is the thermodynamic ground state of SF at ambient pressure. Britton et al [23] proposed that $Cmcm$ is relatively more stable than $R\bar{3}$ phase due to the presence of linear form of CNO anions in its crystal structure [60]. The predicted behavior with DFT-D2 method are in good agreement with the experimental observations [23–25, 60] and this clearly shows the utility of DFT-D2 method in correctly predicting the relative phase stability of the polymorphic phases of SF.

The investigation of energetic materials at extreme conditions is a challenging task due to their sensitivity, complex chemical behavior and risk of decomposition. Several accidents occur during the preparation of SF [3] and hence it is very difficult to perform experiments without any prior knowledge about this kind of energetic materials. Therefore, theoretical modelling and simulations are efficient tools to predict the physical and chemical properties of such complex energetic solids at extreme conditions. DFT is a powerful tool in predicting the behavior of complex solid state systems at extreme conditions. Hence, we attempted to study the relative phase stability and possible polymorphic structural phase transition in SF under hydrostatic pressure up to 5 GPa with a step size of 0.5 GPa. As illustrated in figure 3.3, the calculated enthalpy curves as a function of pressure using standard PBE-GGA functional shows that $R\bar{3}$ phase undergoes a structural polymorphic phase transition to $Cmcm$ phase at around 2.5 GPa using PWSCF and the corresponding transition pressures obtained from CASTEP code is 2.7 GPa (see figure 1 of the Ref. [61]). Overall, we observed similar trends using both of the DFT packages with small deviations in the predicted transition pressures. Above the transition pressures the enthalpy of the $Cmcm$ phase is lower than that of the $R\bar{3}$ phase, indicating that $Cmcm$ structure becomes stable. The $Cmcm$ phase is stable in the pressure range from transition pressure to 5 GPa, which is the highest pressure of the present work. The enthalpy (total energy) difference at 0 GPa is ~ 6 kJ/mol which increases with pressure and it is found to be ~ 21 kJ/mole at 5 GPa within DFT-D2 method. In contrast to LDA/GGA functionals, the DFT-D2 method using both of the packages (PWSCF and CASTEP)

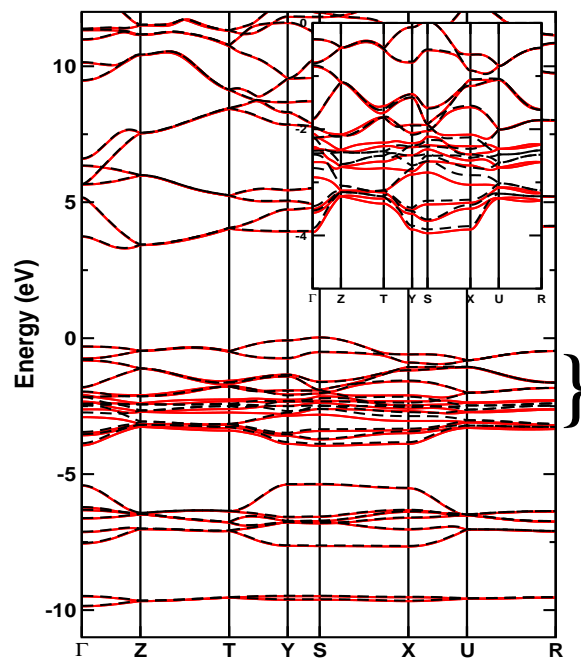
based on PW-PP approach reveals that there is no pressure induced polymorphic phase transition seen in SF polymorphs and the $Cmcm$ phase is found to be the most stable form of SF over the studied pressure range (see figure 3.3). Hitherto, $Cmcm$ and $R\bar{3}$ phases were referred to α - and β -SF, respectively. Our recent high pressure study on $KClO_3$ [62] also revealed that DFT-D2 method is good enough for calculating the transition pressures for molecular solids in opposition to standard LDA/GGA functionals. As shown in figure 3.4 (see figure 2 of the Ref. [61]), the calculated total energies plotted as a function of pressure demonstrates that the DFT-D2 method predicts the α -phase to be the most stable form of SF over the studied pressure range in contrast to usual LDA/GGA functionals.

In addition, the contribution of lattice vibration to the total Gibbs free energy needs to be considered at elevated temperatures. We have used norm-conserving pseudo potentials [63] for calculating the Gibbs free energy as they are well suited for phonon calculations as implemented in CASTEP code. Figure 3.5 shows the calculated Gibbs free energy in the range temperature 0-450 K within DFT-D2 method. The difference in Gibbs free energy (ΔG) is ~ 7 kJ/mol in the low temperature region and it decreases monotonically with increase in temperature between the two α - and β -polymorphs of SF. However, α -SF remains the phase with the lowest free energy throughout the investigated temperature range, despite the contribution of lattice vibration tending to decrease the ΔG gap at elevated temperatures. We have not observed any temperature driven phase transition between the two polymorphs over the studied temperature range and this is consistent with results of differential thermal analysis [26]. Gibbs free energies at temperatures beyond 450 K are not plotted because α -SF phase typically decomposes at higher temperatures between 393-450 K [26]. Present work confirms that the α -phase is the most stable polymorph of SF under the studied pressure and temperature range.

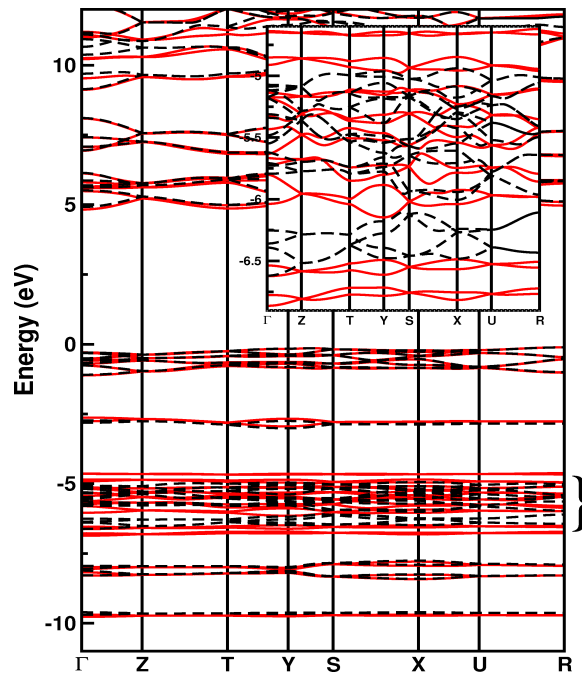
3.3.3 Equation of state and compressibility

The calculated volumes decrease monotonically as a function of pressure using standard LDA/GGA functionals as well as with DFT-D2 method are shown in figure 3.6 (see figure 3 of the Ref. [61]) for SF polymorphs and using optB88-vdW method for MF as shown in figure 3.7. The obtained equilibrium bulk moduli for α - and β -SF are found to be 20.0 (19.4) GPa and 17.8 (19.1) GPa within DFT-D2 method using PWSCF (CASTEP) and 12.2 GPa for MF using optB88-vdW by fitting pressure-volume data to Birch-Murnaghan equation of state [64]. The obtained bulk moduli values reveal that MF is found to be softer than SF polymorphs. In order to understand the behavior of unit-cell parameters and their relative compressibilities under hydrostatic pressure, we have presented the lattice constants as a function of pressure as displayed in figure 3.8. The calculated lattice constant **a** decreases monotonically with pressure whereas the lattice constants **b** and **c** decrease non-monotonically in the pressure range of 2.5 to 5 GPa. As illustrated in figure. 3.8, the **c**- and **b**-axes are the most and least compressible, respectively for α -SF while rhombohedral lattice constant (**a**) and angle (α) decrease with distinct pressure coefficients for β -SF under pressure. Likewise, when the pressure is applied on MF, the lattice constants **a** and **c** decrease whereas **b** increases. Lattice constant **c** is found to be highly compressible as shown in figure 3.9. Lattice constants **b** increases with pressure which is quite interesting and is similar to that of silver azide [65]. This clearly indicates the anisotropic behavior of SF polymorphs and MF under the studied pressure range.

Further, to understand the relative compressibilities of both the polymorphic phases of SF and MF, bond lengths and bond angles are calculated as a function of pressure. As shown in figures 3.9 and 3.10, Ag...O/Hg...O and Ag...Ag intermolecular bonds are more compressible while Ag-C, Hg-C, C-N and N-O intramolecular bonds show similar and less compressible nature over studied pressure range due to strong covalent bonding between Ag/Hg and C as well as



(a)



(b)

Figure 3.13: Calculated electronic band structures of a) α -SF and b) MF with (solid red lines) and without (dotted black lines) inclusion of SO coupling using the TB-mBJ functional at the optimized fractional co-ordinates. Influence of SO coupling is given in the inset for both of the compounds.

within the CNO molecular anion and this can be clearly understood from their electronic structures. This clearly shows that the intermolecular interactions are weaker and are highly compressible over intramolecular interactions in the layered heavy metal fulminates. The bond angle Ag-C-Ag decreases because of the orientation of Ag-C bonds due to high compressible nature of Ag...Ag bonds (see figure 3.10), whereas Ag-C-N bond angle increases under compression. Overall, we observe that Ag-C, Hg-C, C-N and N-O bonds are stiffer whereas Ag...Ag and Ag...O/Hg...O are more compressible under the application of hydrostatic pressure. Further, the compressibility behavior can be clearly understood by analyzing the nature of chemical bonding in the investigated compounds. Hence, we have investigated the electronic structure and chemical bonding in the following section.

3.3.4 Electronic structure and chemical bonding

Inorganic fulminates are iso-electronic with azides, cyanates and cyanamides. Iqbal and co-workers [2] explained that the fulminates are found to be the most sensitive explosives to shock and heat among the energetic materials such as azides, cyanates, thiocyanates and cyanamides due to asymmetric charge distribution in their structures. Also, the heavy metal complex salts are more unstable than alkali metal salts because of the asymmetric inter ionic distances [60]. In order to understand the macroscopic energetic behavior of these sensitive explosives, it is necessary to understand the electronic structure and chemical bonding of these materials at the atomistic level. Iqbal et al [2] carried out a detailed experimental study on the electronic structure and stability of the inorganic fulminates, which reveal that sodium, potassium and thallos fulminates are ionic salts whereas silver and mercury salts are covalent in nature and this will be reflected in the order of stability of the fulminate salts. However, the electronic structure and bonding properties of the SF polymorphs and MF are unknown. Therefore, in this work, we made a detailed analysis of electronic structure and chemical bonding of SF polymorphs

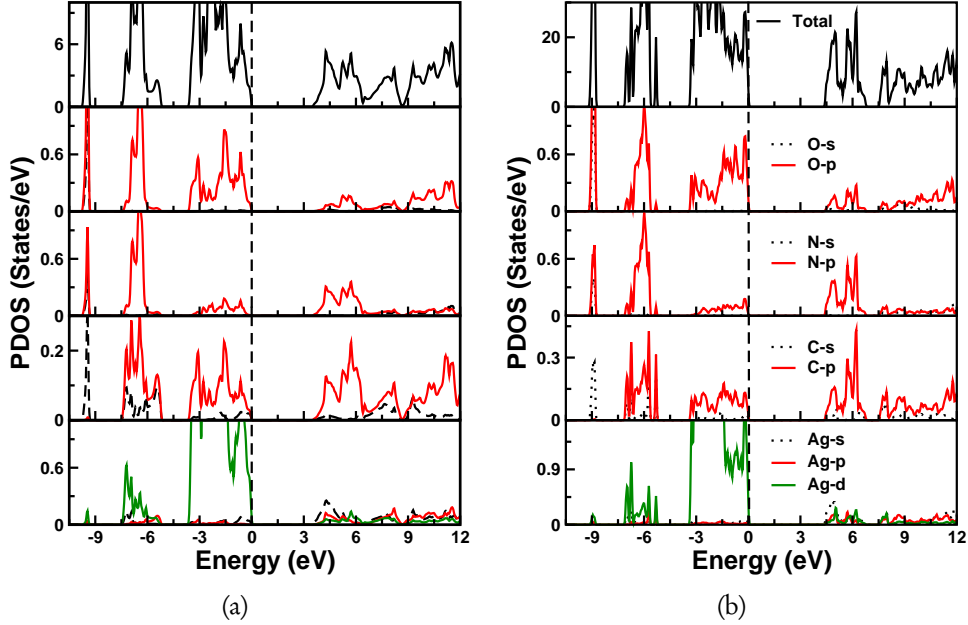


Figure 3.14: Calculated total and PDOS of a) α - and b) β - phases of SF using TB-mBJ potential at the experimental crystal structures [24, 25].

and MF at ambient pressure. The calculated TB-mBJ band gaps at the experimental crystal structures are found to be 3.51 and 4.43 eV for α and β -phases of SF, respectively and the corresponding band gaps using LDA functional are 2.0 and 2.85 eV. The obtained TB-mBJ band gap of 3.51 eV for α -SF is closely comparable with the measured optical energy gap of 4.0 eV [2] over LDA functional. Also, the calculated TB-mBJ band structures show that α and β -SF phases are indirect band gap insulators along S-(Γ -Z) and T-(F- Γ) high symmetry directions of the Brillouin zone as shown in figure 3.12. Since Spin-Orbit (SO) plays a significant role for heavy metals, we attempted to study the electronic structure of thermodynamic ground state of SF polymorph (α -SF) and MF including SO interactions.

We first optimized the fractional co-ordinates of both α -SF and MF at experimental lattice constants using PBE-GGA functional and the respective band gaps are found to be 2.13 and 3.64 eV. The PBE-GGA band gap value is slightly higher than the LDA value of 2.0 eV for α -SF. However, the calculated TB-mBJ band

gap 3.32 eV for α -SF is slightly lowered when compared to the value of 3.51 eV obtained at the experimental crystal structure and the same is found to be 4.92 for MF, which is an indirect band gap insulator along R- Γ directions. When SO is included, the calculated TB-mBJ band gaps are found to be 3.30, 4.82 eV for α -SF and MF, respectively and hence the reduction in the respective band gap values are found to be 0.02 eV and 0.1 eV. We observe a small reduction in the band gap values which is due to occurrence of SO splitting at the lower part of the valence band (VB) for α -SF (between -2 to -4 eV) and for MF (between -4.5 to -7 eV). We have plotted electronic band structures of both the compounds without (black dotted lines) and with (red solid lines) SO on top of each other as presented in figure 3.13. To a large extent the band structures of both the compounds look essentially similar with and without SO coupling except for few bands in the lower part of the VB which are split due to the SO coupling as shown in inset of figure 3.13. The SO is mainly due to $4d$ -states of Ag atom near the top of VB in α -SF while $5d$ -states of Hg atom in the energy range between -4.5 to -7.0 eV in case of MF. From the calculated electronic band structures of α -SF and MF with and without SO, it is found that inclusion of SO is more significant for MF over α -SF.

Further, the inherent characteristics of chemical bonding in SF polymorphs and MF was investigated by examining the total and partial density of states (PDOS) as illustrated in figure 3.14 & 3.15. Apart from the total energy calculations, the relative phase stability of the α and β polymorphs of SF can also be explained on the basis of the electronic structure. As shown in figure 3.14, when compared to β -SF the peaks of the DOS in the valence bands of α -SF have a tendency to shift towards lower energy, indicating better stability of the α -phase over β -phase. Also, it can be seen that total DOS of both phases exhibit some similar features and hence we have also analysed the bonding based on PDOS of α -SF. It is clearly visualized from the PDOS (see figure 3.14 & 3.15) that SF polymorphs and MF have molecular character, which arises from strong overlap contributions

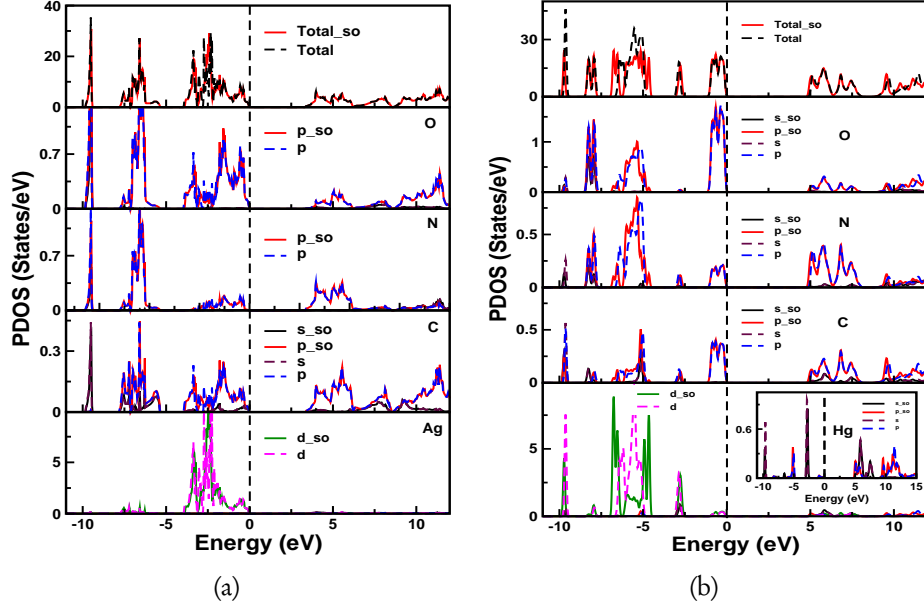


Figure 3.15: Calculated total and PDOS of a) α -SF and b) MF with (solid lines) and without (dotted lines) inclusion of spin-orbit coupling using the TB-mBJ potential at the optimized fractional co-ordinates [24, 34].

of PDOS of Ag/Hg and fulminate anions in the valence and conduction bands and this can be commonly seen in molecular crystalline solids. We have plotted the PDOS of α -SF and MF with and without SO coupling. As illustrated in figure 3.15, the conduction band (CB) is mainly due to p -states of C, N, O and s, p, d -states of metal (Ag/Hg) atoms. The lowest lying states around -10 eV are due to hybridized C- s and s, p states of N and O atoms. The states positioned between -5 to -7 eV are due to hybridization of predominantly $5d$ -states of Hg which are split due to SO splitting and anionic p -states of C, N and O atoms in MF whereas less contribution arises from Ag- $4d$ states in α -SF in this energy range. The states at -2.5 eV below Fermi level are derived from $6s$ -states of Hg atom. The top of the valence band is mainly dominated by anionic states (more contribution from $2p$ -states of oxygen atom) in both α -SF and MF while the $4d$ -states of Ag cation is predominant in α -SF but less contribution from $5d$ -states of Hg. Overall, we ob-

serve *s*, *p*-states of anion and *d*-states of cation are dominant in the VB and strong hybridization between Ag/Hg and C atoms shows the covalent nature of Ag-C and Hg-C bonds in the studied compounds in contrast to the ionic fulminates.

The nature of chemical bond between two atoms can be predicted from their electro-negativity difference. When the differences are greater than or equal to 1.7 and less than 1.7 there is a possibility for the formation of ionic and covalent bonds, respectively. If the difference is greater than 0.5 the covalent bond has some degree of polarity. According to Pauling scale, the electro-negativity values Hg (2.0), Ag (1.9), C (2.5), N (3.0) and O (3.4) show that there exists a covalent bond between N-O, C-N, Ag-C and Hg-C bonds. The electro-negativity difference in N-O (0.4), C-N (0.5), Hg-C (0.5) and Ag-C (0.6) indicate strong and polar covalent nature of N-O, C-N, Hg-C and Ag-C bonds, respectively. There is a strong hybridization between (Hg/Ag)-*d* and *s*, *p*-states of C, N and O atoms leads to strong covalent character consequently the N-O, C-N, Ag-C and Hg-C bonds show less compressibility behavior with increasing pressure (see figures 3.9 and 3.10). Further, this can be clearly understood from electronic charge density plots which are used for accurate description of chemical bonds [66]. The calculated valence charge density using TB-mBJ potential for both the SF polymorphs and MF are as shown in figures 3.16 & 3.17 respectively. It shows anisotropic bonding interactions and the charge cloud is distributed within the CNO molecule indicating covalent character. Overall, the C, N and O atoms are covalently bonded within CNO group and the metal atom is also covalently bonded with CNO group through C atom. X-ray photo electron spectroscopy [67] study on inorganic azides reveals that Heavy Metal azides (HMAs) are more covalent than Alkali metal azides (AMAs), implying that HMAs are more sensitive than AMAs. Similarly, the presence of covalent bonding in SF and MF makes them more sensitive than the above mentioned ionic inorganic fulminates. Therefore, the HMAs and heavy metal fulminates should find applications as initiators for secondary explosives.

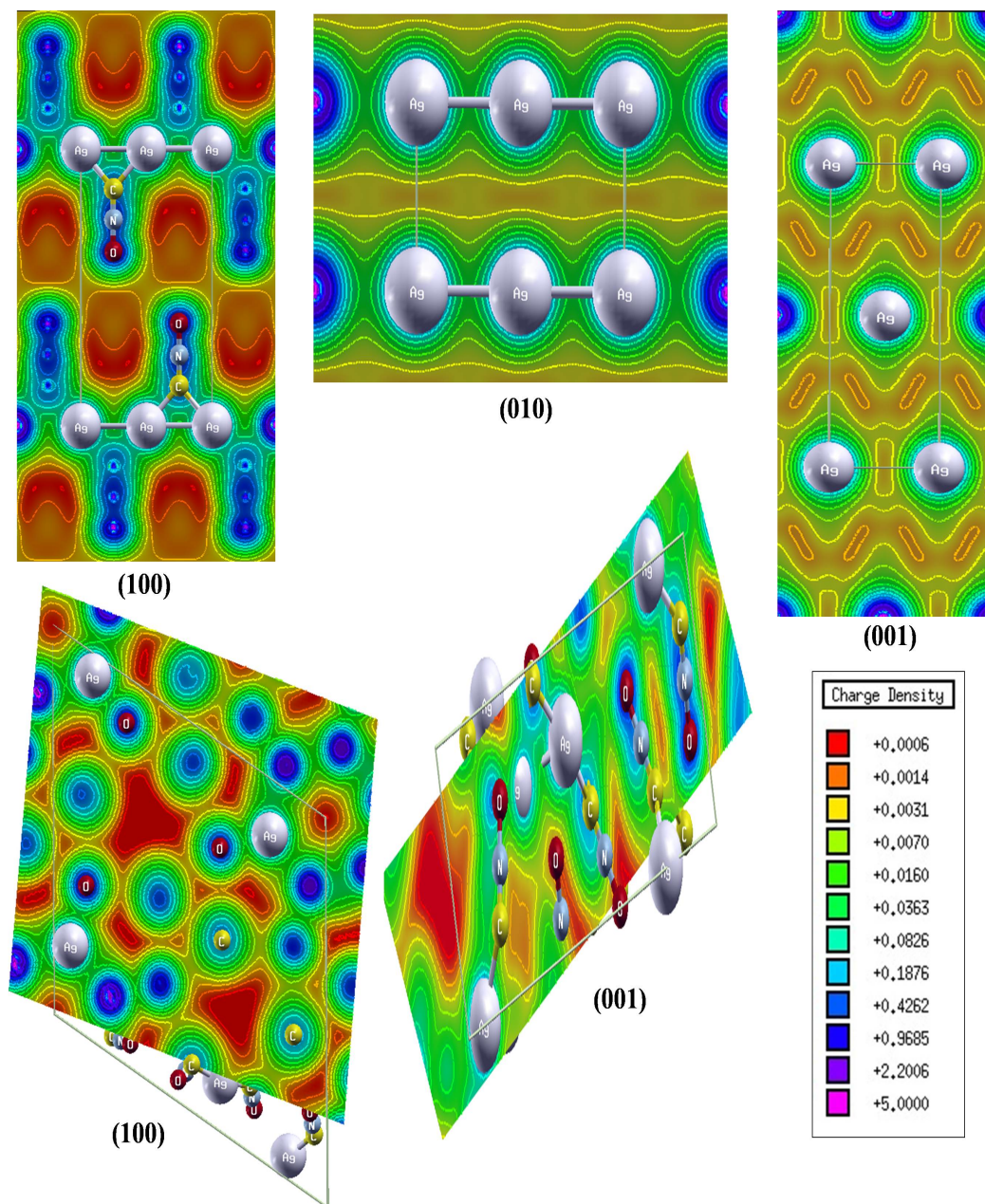


Figure 3.16: Calculated electronic charge densities along (100), (010), (001) planes for α -SF (top) and along (100), (001) planes for β -SF (bottom).

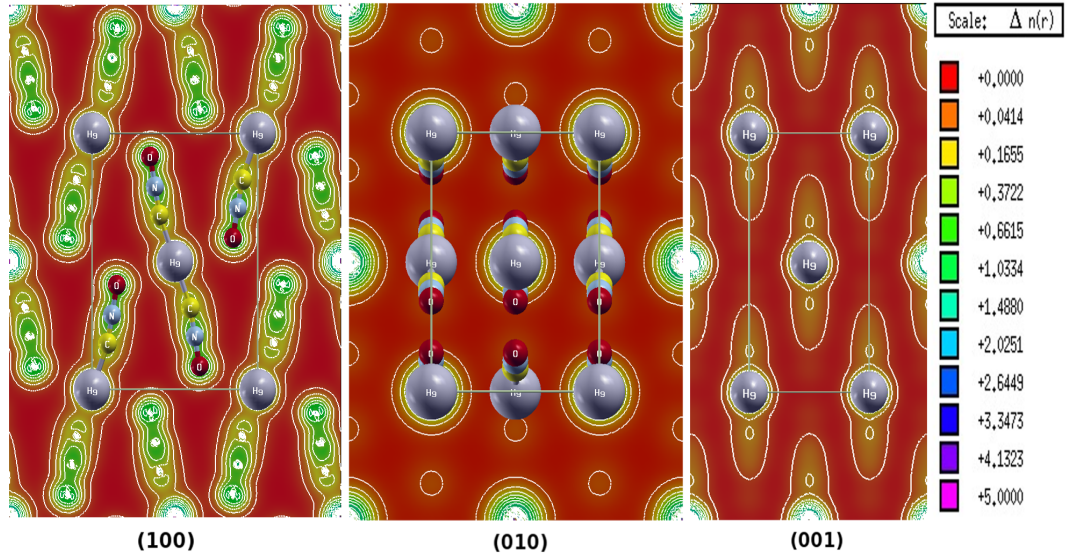


Figure 3.17: Calculated electronic charge densities of MF along crystallographic (100), (010) and (001) planes.

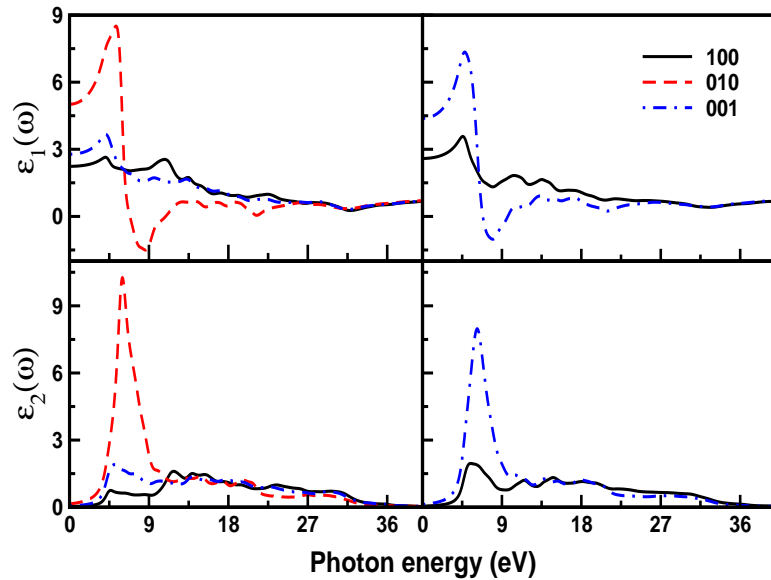


Figure 3.18: Calculated real (top) and imaginary (bottom) parts of dielectric function of α - (left) and β - (right) phases of SF using TB-mBJ potential at the experimental crystal structures [24, 25].

3.3.5 Optical properties

Energetic materials become unstable and they undergo photochemical decomposition under the action of light. Hence it is interesting to study the optical properties of these materials to understand the photo decomposition mechanisms. Electronic structure calculations could provide information about the nature and location of inter band transitions in crystals. The complex dielectric function $\epsilon(\omega) = \epsilon_1(\omega) + i\epsilon_2(\omega)$ can be used to describe the linear response of the system to electromagnetic radiation which is related to the interaction of photons with electrons. The imaginary part of dielectric function $\epsilon_2(\omega)$ is obtained from the momentum matrix elements between the occupied and unoccupied wave functions within selection rules.

As mentioned earlier, the SF polymorphs and MF crystallize in the orthorhombic, hexagonal and orthorhombic symmetries and this allows non zero components of the dielectric tensors three for α -SF and MF, two for β -SF along [100], [010] and [001] directions. Figure 3.18 shows the real $\epsilon_1(\omega)$ and imaginary $\epsilon_2(\omega)$ parts of the dielectric function $\epsilon(\omega)$ as a function of photon energy for both the SF polymorphs. The peaks in $\epsilon_2(\omega)$ mainly arise due to electric-dipole transitions between valence and conduction bands. The major peaks in $\epsilon_2(\omega)$ at 4.57 eV along [100], 5.94 eV along [010], 5.06 eV along [001] in α -phase and 5.45 eV along [100], 6.13 eV along [001] in β -phase arise due to inter band transitions from $\text{Ag}(4d) \rightarrow \text{N}(2p)$ -states. It can be clearly seen from DOS, the top of VB is mainly dominated by $4d$ -states of Silver atom (see Fig. 3.14) in both the polymorphs, which is similar to the case of Silver azide (AgN_3) [68]. As discussed in the section 3.1, SF is iso-electronic and it consists of same chemical species as AgN_3 in addition to C and O atoms, hence one can expect that major optical transitions arise from $\text{Ag}(4d) \rightarrow \text{N}(2p)$ -states in both energetic materials SF and AgN_3 [68]. While the calculated $\epsilon_1(\omega)$ and $\epsilon_2(\omega)$ parts of $\epsilon(\omega)$ for MF with inclusion of SO are as displayed in figure 3.19. The prominent peaks in $\epsilon_2(\omega)$ are as follows: the

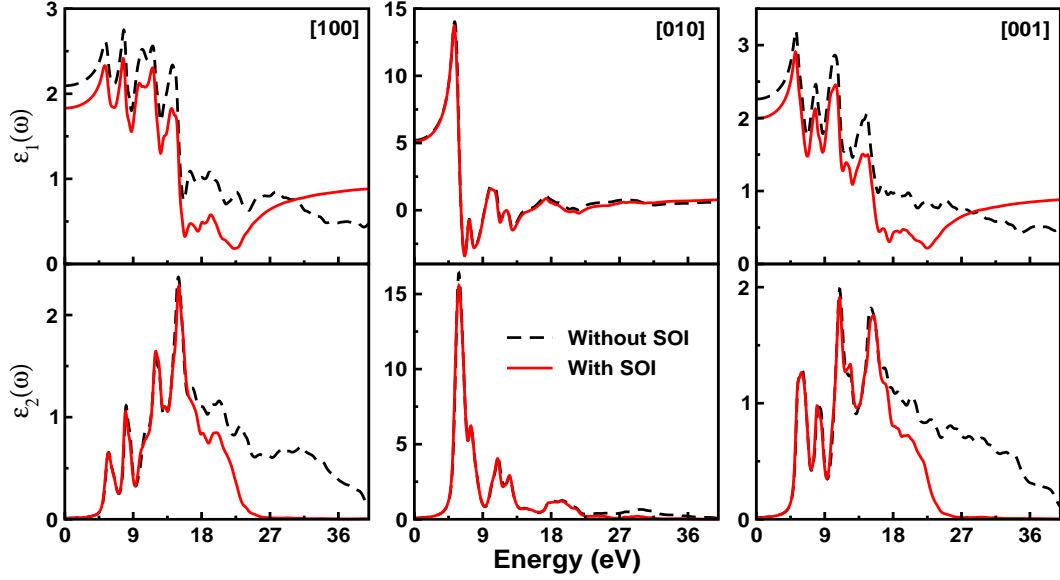


Figure 3.19: Calculated real (top) and imaginary (bottom) parts of complex dielectric function of MF without (dotted black lines) and with (solid red lines) inclusion of spin-orbit interaction (SOI) using the TB-mBJ potential at the experimental lattice constants [34].

peak at 5.9 eV originates from the transition $O(2p) \rightarrow Hg(s)$, the peak at around 8.0 eV arises probably from the transition $Hg(6s) \rightarrow N(p)$, the peaks in energy range 10-16 eV are from the transition $Hg(5d) \rightarrow N/C/O(p)$ and finally the peaks around 19.5 eV are due to the transition between $Hg(5d) \rightarrow Hg(p)$ states along three crystallographic directions.

The real part $\epsilon_1(\omega)$ can be derived from $\epsilon_2(\omega)$ using the Kramer-Kronig relations. The calculated real static dielectric constant along all the crystallographic directions without (with) inclusion of SO are found to be 2.34 (2.00), 5.56 (5.39), 2.96 (2.64) for α -SF, 2.59, 4.38 for β -SF and 2.09 (1.83), 5.21 (5.11), 2.26 (1.99) for MF. The calculated static refractive indices ($n = \sqrt{\epsilon(0)}$) using the dielectric function without (with) inclusion of SO are given by $n_{100} = 1.53$ (1.43), $n_{010} = 2.36$ (2.32), $n_{001} = 1.72$ (1.62) and $n_{100} = 1.61$, $n_{001} = 2.09$ for α and β -phases of SF, respectively while the same are found to be $n_{100} = 1.45$ (1.35), $n_{010} = 2.28$ (2.26), $n_{001} = 1.50$ (1.41) for MF. Iqbal et al [2] proposed that high values for the refractive in-

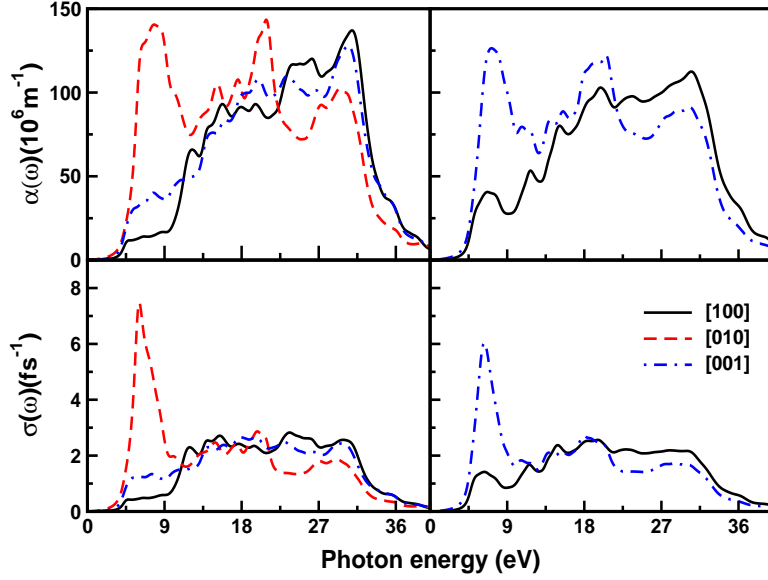


Figure 3.20: Calculated absorption (top) and photoconductivity (bottom) of α - (left) and β - (right) phases of SF using TB-mBJ potential at the experimental crystal structures [24, 25].

dex suggest that directional bonding might be present in the crystal. The authors also observed high refractive index value for SF over MF when the direction of light was parallel to a-axis. From the calculated static refractive indices of both of the compounds, we clearly see that SF has high refractive indices along all the crystallographic directions than MF. Apart from the PDOS, the polarized refractive indices also show that SF has more covalent character when compared to MF which implies that SF is relatively unstable than MF. Also, the obtained refractive indices are distinct in all three crystallographic directions, which indicates the anisotropy of the SF polymorphs. The calculated absorption spectra are shown in figure 3.20 for SF polymorphs (see figure 4 of the Ref. [69] for inclusion SO in case of α -SF) and figure 3.21 for MF and absorption starts after the energy 3.30, 4.43 and 4.82 eV for α -SF, β -SF and MF, respectively which is the energy band gap between the VB maximum and CB minimum. The absorption coefficients are found to have order of magnitude $\sim 10^7 \text{ m}^{-1}$ which shows that absorption of

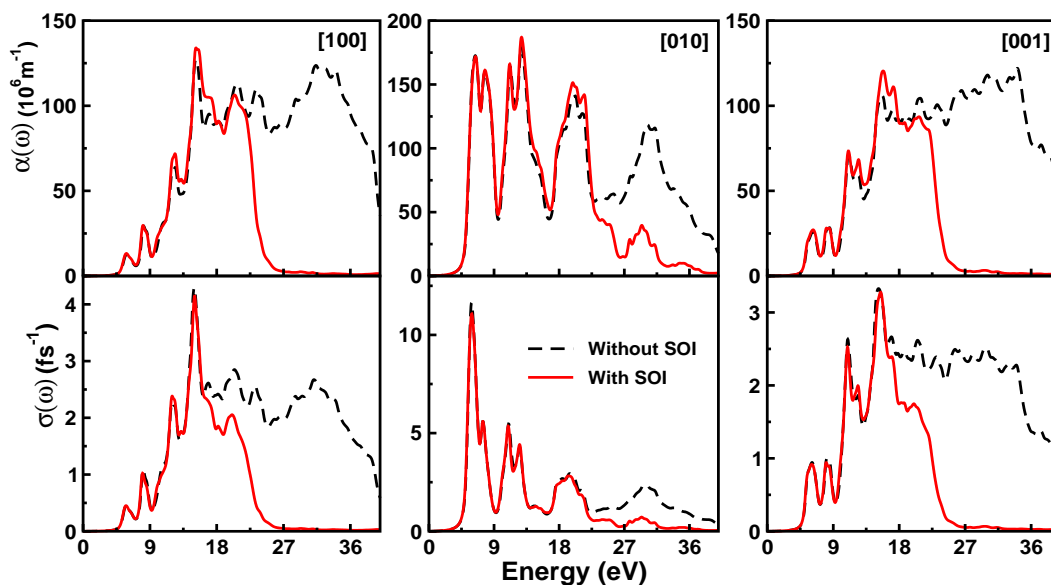


Figure 3.21: Calculated absorption (top) and photoconductivity (bottom) of MF without (dotted black lines) and with (solid red lines) inclusion of spin-orbit interaction (SOI) using the TB-mBJ potential at the experimental lattice constants [34].

the compounds lie in the Ultra-Violet (UV) region. Photo conductivity is due to increase in the number of free carriers when photons are absorbed. The calculated photo conductivity shows a wide photo current response in the absorption region of 3.30-25, 4.43-25 and 4.82-25 eV as shown in figure 3.20 (see figure 4 of the Ref. [69] for inclusion SO in case of α -SF) and figure 3.21 for SF polymorphs and MF, respectively. Overall, we observe that inclusion of SO interactions has significant influence on optical properties of the heavy metal energetic SF (see figures 2, 3 and 4 of the Ref. [69]) and MF salts as shown in figures 3.19 & 3.21. Also, SF polymorphs and MF show strong anisotropy and wide range of absorption. These results may suggest the possible photochemical decomposition of SF/MF into Ag/Hg, CO and N₂ under the action of UV light.

3.4 Conclusions

In summary, *ab-initio* calculations have been performed to investigate the relative phase stability, structural phase transition and compressibilities of both polymorphic orthorhombic ($Cmcm$) and trigonal ($R\bar{3}$) phases of SF and orthorhombic ($Cmce$) MF. The standard DFT functionals are inadequate to predict the relative phase stability and ground state properties of SF polymorphs and MF. From our total energy calculations within DFT-D2 method, $Cmcm$ phase was found to be the preferred thermodynamic equilibrium phase of SF polymorphs under the studied pressure and temperature range. Hence, we confirm that $Cmcm$ and $R\bar{3}$ phases as α and β -SF, respectively. The present study also reveals that there is no structural phase transition observed using DFT-D2 method whereas we could see a pressure induced polymorphic phase transition from $\beta \rightarrow \alpha$ at about 2.5 (2.7) GPa within PBE-GGA using PWSCF (CASTEP) PW-PP approach. Overall, the phase stability and ground state properties obtained from both the PW-PP approaches are in good accord with each other for both of the SF polymorphs. Among the various non-local correction methods used, optB88-vdW method works well for MF in reproducing the experimental trends. MF is found to be softer than SF polymorphs. We have also calculated the electronic structure and optical spectra of both SF polymorphs and MF using TB-mBJ functional at ambient pressure by including SO coupling. It is found that SO is more prominent in MF than α -SF. The calculated electronic band structure show that heavy metal fulminates are indirect band gap insulators. The detailed analysis of electronic charge density maps and PDOS reveal that covalent bonding is predominant in the energetic SF polymorphs and MF. The major peaks in $\epsilon_2(\omega)$ are due to inter band transitions between $Ag(4d) \rightarrow N(2p)$ -states for SF polymorphs whereas $O(2p) \rightarrow Hg(s)$, $Hg(5d) \rightarrow N/C/O(p)$ and $Hg(5d) \rightarrow Hg(p)$ for MF. The calculated absorption spectra reveal that the energetic materials show considerable anisotropy and they may decompose under the action of UV light. Finally, the present study suggests

that the α -form of SF is relatively stable and it can be used in different applications as MF and β -form can be avoided by careful control of the pressure or temperature in the manufacturing process.

References

- [1] P. M. Dickson and J. E. Field, Proc. R Soc. Lond. A, **441**, 359 (1993).
- [2] Z. Iqbal and A. D. Yoffe, Proc. R. Soc. Lond. A, **302**, 35 (1967).
- [3] P. H. Collins and K. J. Holloway, Prop. Explos. Pyrotech., **3**, 159 (1978).
- [4] T. L. Davis, *The chemistry of powder and explosives*, Wiley, New York (1943).
- [5] F. P. Bowden and H. T. Williams, Proc. R. Soc. Lond. A, **208**, 176 (1951).
- [6] T. Urbanski, *Chemistry and Technology of Explosives*, **3**, 157 (1967).
- [7] D. A. Jackson and A. P. Dicks, J. Chem. Educ., **89**, 1267 (2012).
- [8] J. P. Springer, Ger Pat, **953**, 415 (1956).
- [9] F. Martin, *Dber Azide und Fulminate Darmstadt*, (1913).
- [10] L. Wohler and F. Martin, Angezu. Chem., **30**, 33 (1917).
- [11] L. Wohler and F. Martin, Ber. Dtsch. Chem. Ges., **50**, 586 (1917).
- [12] W. Beck and T. M. Klapötke, J. Mol. Struc.-Theochem., **848**, 94 (2008).
- [13] K. Kurzer, J. Chem. Educ., **77**, 851 (2000).
- [14] A. Nobel, J. Soc. Arts., **23**, 611 (1875).
- [15] M. Berthelot and P. Vielle, Comptes rendus, **90**, 946 (1880).
- [16] F. D. Miles, *A history of research in the Nobel Division of ICI*, p.108 (1955).

- [17] M. Meyer, J. Kohler and A. Honburg, *Explosives*, 5th ed. Wiley, Germany, (2002).
- [18] A. M. Peter, *J. Am. Chem. Soc.*, **38**, 486 (1916).
- [19] *Encyclopedia of Explosives and Related Items*, PATR 2700, Vol. 6, Dover, New Jersey, USA, Picatinny Arsenal, (1974).
- [20] J. L. Gay -Lussac, *Ann. Chim. Phys.*, **27**, 199 (1824).
- [21] K. Singh, *Acta Cryst*, **12**, 1053 (1959).
- [22] S. N. Pandey, *Indian J. Phys.*, **36**, 657 (1962).
- [23] D. Britton and J. D. Dunitz, *Acta. Cryst.*, **19**, 662 (1965).
- [24] J. C. Barrick, D. Canfield and B. C. Giessen, *Acta. Cryst.*, **B35**, 464 (1979).
- [25] D. Britton, *Acta Cryst.*, **C47**, 2646 (1991).
- [26] T. Boddington and Z. Iqbal, *Trans. Faraday Soc.*, **65**, 509 (1969).
- [27] H. Wieland, *Ber. Dtsch. Chem. Ges.*, **40**, 418 (1907).
- [28] H. Wieland, *Ber. Dtsch. Chem. Ges.*, **43**, 3362 (1910).
- [29] H. Wöhler, *Ber. Dtsch. Chem. Ges.*, **43**, 754 (1910).
- [30] F. D. Miles, *J. Chem. Soc.*, 2532 (1931).
- [31] A. Suzuki, *J. Ind. Explosives. Soc. Jpn.*, **14**, 142 (1953).
- [32] International Center for Diffraction Data, 12 campus Boulevard, Newton Square, PA, 109073-3273 USA, Powder diffraction File Mercury Fulminate, 00-002-0287.
- [33] M. E. Brown and G. M. Swallowe, *Thermochim. Acta*, **49**, 333 (1981).

- [34] W. Beck, J. Evers, M. Göbel, G. Oehlinger and T. M. Klapötke, *Z. Anorg. Allg. Chem.*, **633**, 1417 (2007).
- [35] L. Türker and S. Erkoç, *J. Mol. Struct. -Theochem.*, **712**, 139 (2004).
- [36] P. Giannozzi et al, *J. Phys.: Condens. Matter*, **21** 395502 (2009).
- [37] M. C. Payne, M. P. Teter, D. C. Allen, T. A. Arias and J. D. Joannopoulos, *Rev. Mod. Phys.*, **64**, 1045 (1992).
- [38] D. Vanderbilt, *Phys. Rev. B*, **41**, 7892 (1990).
- [39] J. P. Perdew, S. Burke and M. Ernzerhof, *Phys. Rev. Lett.*, **77**, 3865 (1996).
- [40] J. P. Perdew and Y. Wang, *Phys. Rev. B*, **45**, 13244 (1992).
- [41] T. H. Fischer and J. Almlof, *J. Phys. Chem.*, **96**, 9768 (1992).
- [42] H. J. Monkhorst and J. D. Pack, *Phys. Rev. B*, **13**, 5188 (1976).
- [43] G. Kresse and D. Joubert, *Phys. Rev. B*, **54**, 11169 (1996).
- [44] F. Ortman, F. Bechstedt and W. G. Schmidt, *Phys. Rev. B*, **73**, 205101 (2006).
- [45] A. Tkatchenko and M. Scheffler, *Phys. Rev. Lett.*, **102**, 073005 (2009).
- [46] S. Grimme, *J. Comp. Chem.* **27**, 1787 (2006).
- [47] M. Dion, H. Rydberg, E. Schroder, D. C. Langreth and B. I. Lundqvist, *Phys. Rev. Lett.*, **92**, 246401 (2004).
- [48] J. Klimes, D. R. Bowler and A. Michaelides, *Phys. Rev. B*, **83**, 195131 (2011).
- [49] F. Tran and P. Blaha, *Phys. Rev. Lett.*, **102**, 226401 (2009).

- [50] P. Blaha, K. Schwarz, G. K. H. Madsen, D. Kvasnicka and J. Luitz, WIEN2K, an Augmented Plane Wave + Local Orbitals Program for Calculating Crystal Properties, Techn. Universitat: Wien, Austria. ISBN: 3-9501031-1-1-2, (2001).
- [51] G. W. C. Taylor and J. M. Jenkins, *Proc. 3rd Symposium on Chemical problems connected with the stability of Explosives*, Ystad, Sweden, May 28-30, 33, (1973).
- [52] C. A. Taylor and E. P. Buxton, *Army Ordnance*, **6**, 118 (1925).
- [53] U. Z. Muller, *Z. Anorg. Allg. Chem.*, **399**, 183 (1973).
- [54] A. C. Landerville, M. W. Conroy, M. M. Budzevich, Y. Lin, C. T. White and I. I. Oleynik, *Appl. Phys. Lett.*, **97**, 251908 (2010).
- [55] F. Shimojo, Z. Wu, R. K. Kalia and P. Vashishta, *J. Chem. Phys.*, **132**, 094106 (2010).
- [56] D. C. Sorescu and B. M. Rice, *J. Phys. Chem. C*, **114**, 6734 (2010).
- [57] Z. Wu, R. K. Kalia, A. Nakano and P. Vashishta, *J. Chem. Phys.*, **134**, 204509 (2011).
- [58] D. Baraga and F. Grepioni, *Making Crystals by Design: Methods, techniques and Applications*, Willey & Sons, (2006).
- [59] P. Ectors and D. Zahn, *Phys. Chem. Chem. Phys.*, **15**, 9219 (2013).
- [60] Z. Iqbal, *Structure and Bonding*, Springer, **10**, 25 (1972).
- [61] ftp://ftp.aip.org/epaps/journ_chem_phys/E-JCPSA6-140-009423/support.pdf
- [62] N. Yedukondalu, Vikas D. Ghule and G. Vaitheeswaran, *J. Chem. Phys.*, **138**, 174701 (2013).
- [63] N. Troullier and J. L. Martins, *Phys. Rev. B*, **43**, 1993 (1991).

- [64] F. D. Murnaghan, Proc. Natl. Acad. Sci. USA, **30**, 244 (1944).
- [65] W. Zhu and H. Xiao, J. Solid State Chem. **180**, 3521 (2007).
- [66] R. Hoffman, Rev. Mod. Phys. **60**, 601 (1988).
- [67] R. J. Colton and J. W. Rabalais. J. Chem. Phys., **64**, 3481 (1976).
- [68] P. Jain, J. Sahariya, H. S. Mund, M. Sharma and B. L. Ahuja, Comput. Mat. Sci., **72**, 101 (2013).
- [69] ftp://ftp.aip.org/epaps/journ_chem_phys/E-JCPSA6-143-029544/support.pdf

Structural stability, vibrational and bonding properties of potassium 1,1'-dinitroamino -5,5' bistetrazolate

In this chapter, a detailed discussion on the crystal structure, equation of state, IR and Raman spectra, electronic structure and absorption spectra of the emerging green primary explosive, potassium 1,1'-dinitroamino -5,5' bistetrazolate (K_2 DNABT) is presented. Influence of weak dispersive interactions on structural and vibrational properties were also discussed through the DFT-D2 method.

4.1 Introduction

Primary explosives are sensitive towards external stimuli such as impact, heat, friction, electric charge [1] showing a very rapid deflagration to detonation transition (*i.e.* reaction front becomes supersonic) by generating a shock wave, which makes the transfer of detonation to a less sensitive secondary explosive [2, 3]. Consequently, the primary explosives can find applications as initiators (in detonators, primers and blasting caps) for secondary booster charges, main charges or propellants. In addition, primary explosives are vital to any military's portfolio and are essential to construction and mining industries [4]. The first primary explosive Mercury (II) Fulminate (MF) adopted by Alfred Nobel is widely used in commercial blasting caps [2]. However, MF is more sensitive, tends to be dead

pressed and its base metal mercury is more expensive. As a result MF finds limited applications in energetic formulations, which calls for a replacement. After an extensive research for about a century, an appropriate replacement for MF was found to be Lead Azide (LA) and Lead Styphnate (LS) which are thermally stable primary explosives. LA is used in detonators due to its high performance ($D = 5.92$ km/s and $P = 33.8$ GPa) and high thermal stability (315°C), whereas LS is used in propellant applications because of its low performance. Although LA and LS find tremendous applications in various fields, the presence of heavy metal severely affects the environment and shows a strong influence on any populations that are in close proximity to areas where explosives are set off or fire arms are employed [4]. The Pb and Hg based explosives cause damage to the central nervous system, kidneys, heart, brain (human memory) and eyes. This impact is not only limited to soldiers in the battle field but also firing ranges ammunition, explosives workers, miners and construction workers are placed at risk [5]. Therefore it is mandatory to search for Hg and Pb free green primary explosives with explosive performance as good as LA and the materials should follow the criterion proposed by Los Alamos national laboratory (LANL) [1, 5–7] as discussed in chapter 1.

Huynh and co-workers [1, 6] synthesized new coordination complex green primary explosives (5-nitro tetrazolate N^2 -ferrate hierarchies) and they replaced the toxic Hg and Pb based primary explosives after about 400 years. Moreover, recently synthesized primary explosives, namely, copper (I) 5-nitro tetrazolate (DBX-1) [8] and potassium 5,7-dinitro [2,1,3] benzoxadiazole 1-4-olate 3-oxide (KDNP) [9] also meet the above mentioned LANL criteria for green primaries [1, 5–7]. Also DBX-1 and KDNP are replacements for LA and LS, respectively. In addition, the KDNP has been qualified by the Department of the Navy, USA as a suitable candidate for use as a primary explosive in weapons development while DBX-1 is under evaluation by the department of Navy [8, 9]. However, high and low concentration of copper (using DBX-1) is harmful to living organisms

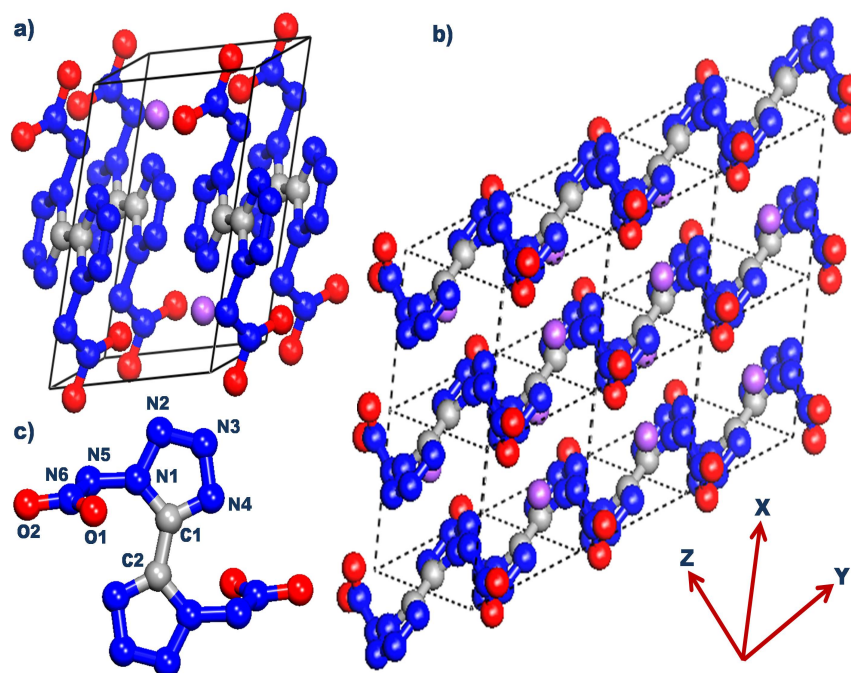


Figure 4.1: (a) Triclinic ($P\bar{1}$) unit cell, (b) Puckered layered structure viewed along xy -plane, (c) Single molecular geometry of tetrazole molecule of K_2 DNABT crystal. Ash, blue, red and violet colour balls represent carbon, nitrogen, oxygen and potassium atoms, respectively.

and ecological systems [5]. Hence optimal copper should be maintained in the DBX-1 explosive. Very recently, a new green primary explosive, potassium 1,1'-dinitroamino -5,5' bistetrazolate (K_2 DNABT) has been synthesized and it exhibits fast detonating characteristics ($D = 8.33$ km/s and $P = 31.7$ GPa) and high initiating power as comparable with LA [10]. The results on structure, equation of state and lattice dynamics would lead to fundamental knowledge of the material in future explosive formulations. Moreover, it is evident that the DFT-D2 method works well for the solid energetic molecular crystals [11]. Therefore, in this chapter, we have systematically investigated the effect of vdW interactions on structural and vibrational properties of the K_2 DNABT layered and molecular crystal under high pressure, electronic and absorption spectra of the newly emerging green primary explosive K_2 DNABT at ambient pressure.

4.2 Method of computation

The accuracy and robustness of density functional theory (DFT) in combination with high computing capacity provide remarkable power to computational experiments at the atomistic level. In the present work, we have used two distinct approaches to perform *ab-initio* calculations. First one, plane wave pseudo potential (PP) approach which is implemented through Cambridge Series of Total Energy Package (CASTEP) [12] in Materials Studio (MS). CASTEP is one of the best modules in MS which can be used to calculate the physical properties of diverse crystalline materials. We have used Vanderbilt [13] ultra-soft (US) and Norm-conserving (NC) [14] PP for electron-ion interactions from the MS database. The USPPs are used to calculate the structural properties at ambient as well as at high pressure while NCPPs have been used to calculate the pressure dependent zone centre IR and Raman spectra of K₂DNABT as they are well suited for lattice dynamical calculations. The local density approximation (LDA) [15, 16] and generalized gradient approximation (GGA) parameterized by Perdew-Burke-Ernzerhof (PBE) [17] were used to treat electron-electron interactions. The Broyden-Fletcher-Goldfarb-Shanno (BFGS) minimization scheme [18] has been used for structural relaxation. The convergence criteria for structural optimization was set to ultra fine quality with a kinetic energy cut-offs of 600 eV for USPPs, 950 eV for NCPPs and a k-point grid spacing of $2\pi \times 0.025 \text{ \AA}^{-1}$ ($5 \times 4 \times 3$) according to the Monkhorst-Pack grid scheme [19]. The self-consistent energy convergence less than 5.0×10^{-6} eV/atom and maximal force between atoms was set to 0.01 eV/Å. The maximum displacement and stress were set to be 5.0×10^{-4} Å and 0.02 GPa, respectively. Semi-empirical dispersion correction (DFT-D2) method of Grimme [20] was applied to treat weak dispersive interactions.

Second one, full potential linearized augmented plane wave (FP-LAPW) method which is implemented in WIEN2K package [21]. Tran-Blaha modified Becke

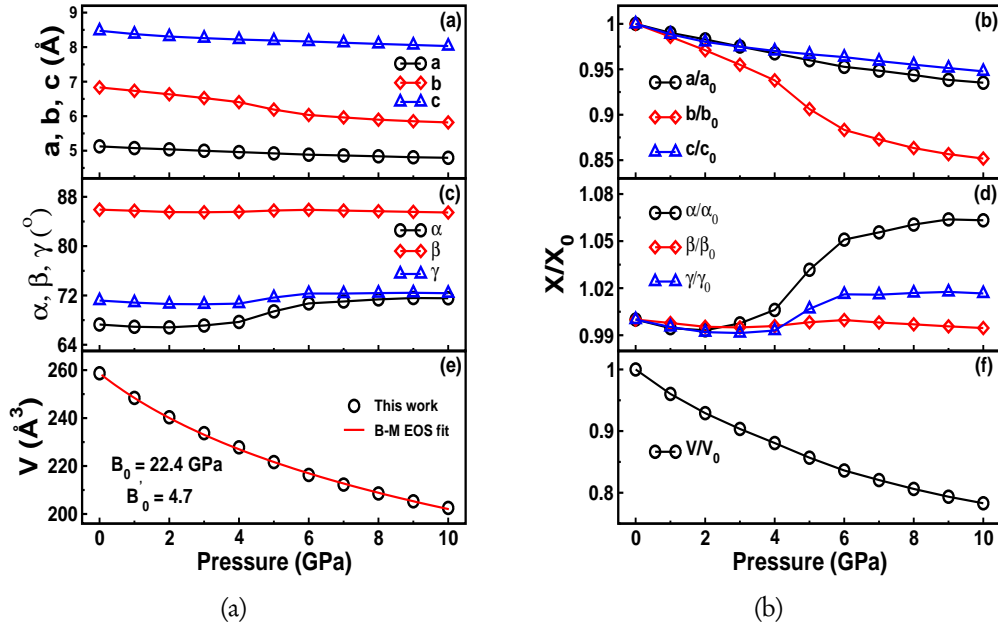


Figure 4.2: Calculated (a) lattice constants (a , b and c), (b) normalized lattice constants (a/a_0 , b/b_0 and c/c_0), (c) lattice angles (α , β and γ), (d) normalized lattice angles (α/α_0 , β/β_0 and γ/γ_0) (e) volume (V) and (f) normalized volume (V/V_0) of K₂DNABT as a function of pressure.

Johnson (TB-mBJ) [22] potential has been used to get reliable band gap thereby calculation of electronic structure and optical properties for the investigated compound. To achieve the required convergence of energy eigenvalues, the wave functions in the interstitial region were expanded using plane waves with a cut-off $K_{max} = 7/RMT$ while the charge density was Fourier expanded up to $G_{max} = 14$, where Radius of Muffin Tin (RMT) is the smallest atomic sphere radius and K_{max} denotes the magnitude of the largest K vector in plane wave expansion. The RMT radii are assumed to be 1.2, 1.12, 1.14 and 1.16 Bohrs for K, C, N and O, respectively. The wave functions inside the spheres are expanded up to $l_{max} = 10$. Self-consistency of total energy is obtained by using $5 \times 4 \times 3$ k-mesh in the Irreducible Brillouin Zone (IBZ). The frequency-dependent optical properties have been calculated using a denser k-mesh of $10 \times 8 \times 6$ in the IBZ.

Table 4.1: Calculated ground state lattice constants (a , b , c , α , β , γ), volume (V) and density (ρ) of K_2 DNABT using standard DFT functionals (LDA, PBE-GGA) and dispersion corrected (DFT-D2) method. Experimental data have been taken from Ref.[10] and the relative errors were given in parenthesis with respect to experimental data.

Parameter	CA-PZ	PBE	DFT-D2	Expt.[10]
a (Å)	4.995 (-2.0%)	5.158 (+1.2%)	5.127 (+0.6%)	5.0963
b (Å)	6.583 (-3.5%)	7.044 (+3.2%)	6.832 (+0.1%)	6.8248
c (Å)	8.224 (-2.4%)	8.746 (+3.8%)	8.474 (+0.5%)	8.4271
α ($^\circ$)	66.60 (-1.4%)	69.46 (+2.8%)	67.29 (+0.4%)	67.56
β ($^\circ$)	85.35 (-0.9%)	87.31 (+1.3%)	85.92 (+0.3%)	86.15
γ ($^\circ$)	70.15 (-1.2%)	72.60 (+2.2%)	71.18 (+0.2%)	71.02
V (Å^3)	233.0 (-8.8%)	283.4 (+10.8%)	258.7 (+1.2%)	255.65
ρ (gr/cc)	2.382 (+9.7%)	1.959 (-9.8%)	2.146 (-1.2%)	2.172

4.3 Results and discussion

4.3.1 Crystal structure and equation of state

K_2 DNABT crystallizes in the triclinic $P\bar{1}$ symmetry with unit cell parameters $a = 5.0963$ Å, $b = 6.8248$ Å, $c = 8.44271$ Å, $\alpha = 67.56^\circ$, $\beta = 86.15^\circ$, $\gamma = 71.02^\circ$ and $Z = 1$ at 100 K [10]. The unit cell of experimental crystal structure is shown in figure 4.1a, in which the two potassium atoms are ionically bonded to two tetrazolate anions through a nitrogen atom, the K_2 DNABT molecule are arranged in a puckered layered manner in xy -plane as shown in figure 4.1b, and a single tetrazolate molecule is shown in figure 4.1c. By considering the experimental structure as an input, we first optimized the lattice geometry by fully relaxing atomic coordinates and lattice constants without treating weak dispersive interactions. The obtained lattice constants using standard DFT functionals are found to differ by ~ 1 -3.5% and ~ 1.2 -3.8% within LDA and PBE-GGA, respectively (see Table 4.1). The predicted equilibrium volume is underestimated by 8.8% within LDA conversely the same is overestimated by 10.8% within PBE-GGA. This clearly shows the poor description of dispersive interactions in this material using the

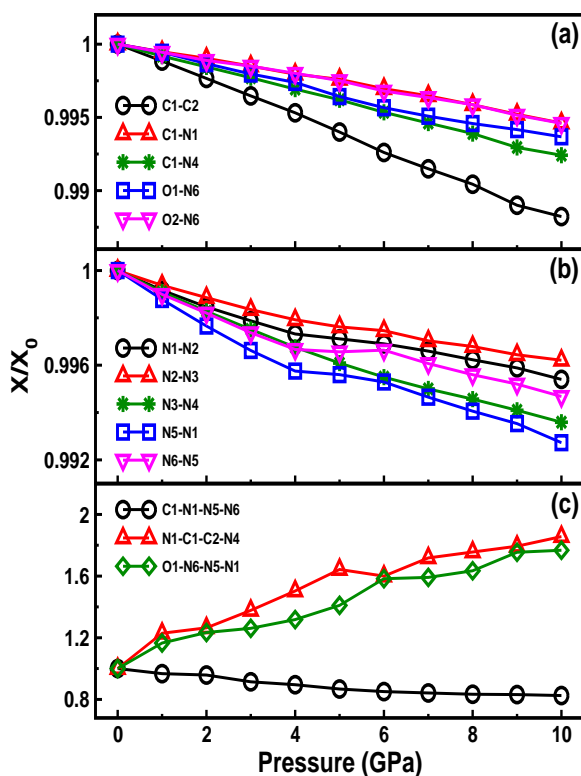


Figure 4.3: Calculated normalized (a, b) bond lengths and (c) torsion angles of K_2DNABT as a function of pressure. X = bond parameter at any instant of pressure and X_0 = bond parameter at ambient pressure.

standard DFT functionals.

Extensive studies have been reported in the literature describing the inability of LDA/GGA functionals in treating these weak dispersive interactions in layered and molecular crystalline solids [Ref. [23] and Refs therein]. In order to capture these weak dispersive forces, semi-empirical dispersion correction methods have been developed and implemented through the standard DFT description. The goal of the dispersion correction methods is to enable DFT to have predictive power for large assemblies of molecules. As discussed in chapter 2, there are two methods of making such corrections; the first one is pairwise additive correction and the second one is non-local correlation and recently both of these methods have shown remarkable success [24]. In the present study, we have used DFT-

Table 4.2: Calculated bond lengths (in, Å) and torsion angles (in, °) of K₂DNABT using standard DFT functionals (LDA, PBE-GGA) and dispersion corrected (DFT-D2) method. Experimental data have been taken from Ref.[10]

Parameter	LDA	PBE	DFT-D2	Expt.[10]
Bond lengths				
C1-C2	1.420	1.438	1.436	1.453
C1-N1	1.352	1.365	1.364	1.352
C1-N4	1.327	1.339	1.338	1.322
O1-N6	1.256	1.269	1.267	1.248
O2-N6	1.264	1.278	1.276	1.261
N1-N2	1.352	1.368	1.366	1.355
N2-N3	1.317	1.327	1.327	1.298
N3-N4	1.349	1.365	1.364	1.361
N5-N1	1.367	1.392	1.389	1.394
N6-N5	1.340	1.359	1.359	1.332
Torsion angles				
C1-N1-N5-N6	70.7	82.6	72.8	75.3
N1-C1-C2-N4	-2.2	-1.6	-1.6	-1.5
O1-N6-N5-N1	3.7	0.05	2.7	1.6

D2 method which is based on pairwise additive correction. The calculated lattice constants deviate by 0.1-0.6% and the corresponding volume is predicted to differ by +1.2%. This is relatively a small deviation in magnitude when compared to standard DFT errors and the results are in good agreement with the experiments [10] as depicted in Table 4.1. There is a significant improvement with DFT-D2 method over standard DFT functionals without dispersion corrections. Also, the obtained intra molecular C-C, C-N (C=N), N-N (N=N) and N-O interactions and torsion angles are now closely comparable with the experimental results [10] as displayed in Table 4.2. Further, the optimized structure at ambient pressure is used to perform high pressure structural and vibrational properties of K₂DNABT.

High pressure studies on structural properties of ionic layered compounds give a good insight into how pressure affects the weak and strong bonds in con-

densed matter. We have systematically investigated the structural properties of K_2DNABT at zero Kelvin temperature under hydrostatic pressure up to 10 GPa in steps of 1 GPa. As illustrated in figure 4.2a, lattice constants **a** and **c** decrease monotonically with increasing pressure while the lattice constant **b** decreases up to 4 GPa and further it shows large compression in the pressure range of 4-10 GPa. Comparison of the calculated lattice constants at 0 and 10 GPa shows the reduction in lattice constants **a**, **b** and **c** by 0.33, 1.01 and 0.44 Å, respectively. It can be clearly noticed that the reduction in **b**-axis is much larger than that of **a** & **c**-axes in the studied pressure range. More precisely, we plotted the normalized lattice constants as a function of pressure as displayed in figure 4.2b; which apparently shows the lattice constants **a**, **b** and **c** shrink with different axial compressibilities 93.52 %, 85.17 % and 94.78 %, respectively. The lattice compressibility along a crystallographic axis can be correlated with the strength of intermolecular interactions observed along that axis. One would expect much lower compressibility for axes that involve strong intermolecular interactions and the corresponding longitudinal elastic stiffness constant is found to be higher along that crystallographic axes [25]. Further, this can be used to correlate with the detonation sensitivity of an explosive material along a particular crystallographic direction. From the calculated axial compressibility, the response of lattice constants to the applied pressure varies as follows $\mathbf{b} < \mathbf{a} < \mathbf{c}$, which clearly indicates that **b**- and **c**- axes are most and least compressible nature respectively. This implies that K_2DNABT is found to be most sensitive to detonate along crystallographic **b**-axis and least sensitive along the **c**-axis. The calculated lattice angles and their normalized values are plotted as a function of pressure as shown in figure 4.2c&d. Variation in the lattice angles is found to be less pronounced with pressures up to 3 GPa for α and γ , and up to 10 GPa for β ; but above 3 GPa, α and γ angles show an increment with application of pressure up to 10 GPa. Also a discontinuity is observed in the lattice constant **b** and lattice angles α , γ in the pressure range of 4-6 GPa.

Moreover, the equations of state are important in describing the properties of

materials. Therefore, we have calculated the volume as a function of pressure and found that it decreases monotonically under studied pressure range as shown in figure 4.2e. We could not see any discontinuity in the P-V curve and the ambient volume is compressed to 21.7 % at 10 GPa (see figure 4.2f). To predict the bulk modulus (B_0) and its pressure derivative (B'_0), the calculated compression data were fitted to the third-order Birch-Murnaghan equation of state [26]. The B_0 and B'_0 are found to be 22.4 GPa and 4.7, respectively. The obtained B_0 value reveals that K_2DNABT is harder than the very sensitive [27] organic primary explosive C_3N_{12} (12.6 GPa) [28] and softer than inorganic primary explosives AgN_3 (39 GPa) [29], $Pb(N_3)_2$ (26 GPa [30] and 41 GPa [31]) and other nitrogen rich energetic salts such as KN_3 (27.2 GPa) [32] and NH_4N_3 (26.34 GPa) [33]. We have also investigated the pressure dependence of intra molecular bond lengths and plotted the normalized bond lengths as shown in figure 4.3a& b. All these bonds are found to stiffen *i.e.* decrease monotonically with progression of pressure, among them C-C bond is the most compressible under the studied pressure range. In addition, we also observe a discontinuity in N5-N1 and N6-N5 bonds in the pressure range of 4-6 GPa as seen previously for the lattice constants of unit cell, which might suggest a structural distortion/transition in the K_2DNABT crystal in this pressure range. Overall, we observe ~ 1 % shortening in the bond lengths when compared at 0 and 10 GPa pressures. Also the calculated torsion angles N1-C1-C2-N4 & O1-N6-N5-N1 are increased by ~ 1.8 times whereas C1-N1-N5-N6 angle is reduced by a factor of 0.8 compared to the values at 0 GPa and highest pressure of the present study as shown in figure 4.3c.

4.3.2 Zone centre IR and Raman spectra at ambient and under high pressure

In addition to the determination of crystal structure of K_2DNABT , Fischer et al [10] also measured IR and Raman frequencies for this material but they have not assigned any of these vibrational modes. Due to the complex crystal structure

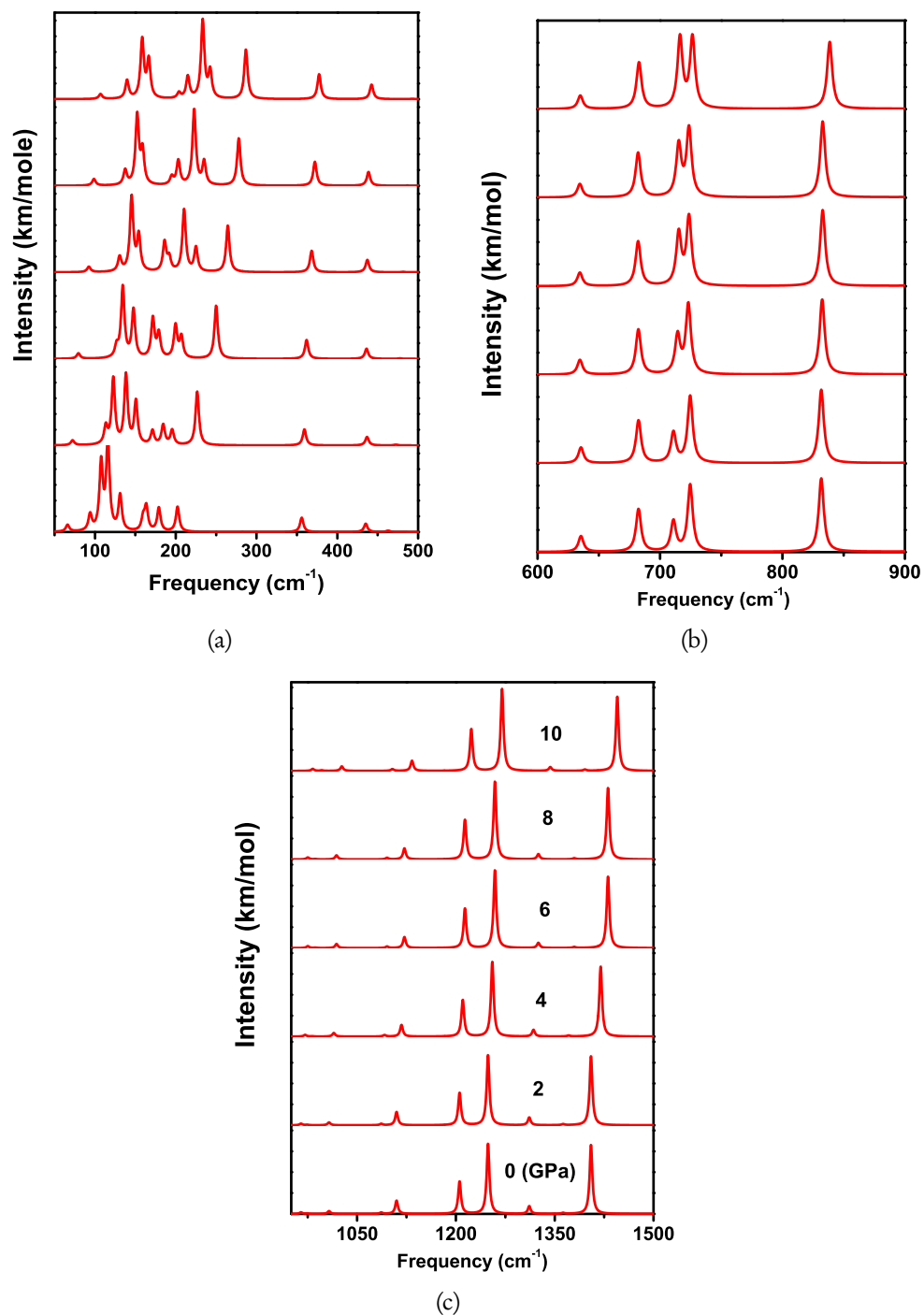


Figure 4.4: Calculated IR spectra (a) 40-500 cm⁻¹, (b) 600-900 cm⁻¹ and (c) 900-1500 cm⁻¹ of K₂DNABT as a function of pressure.

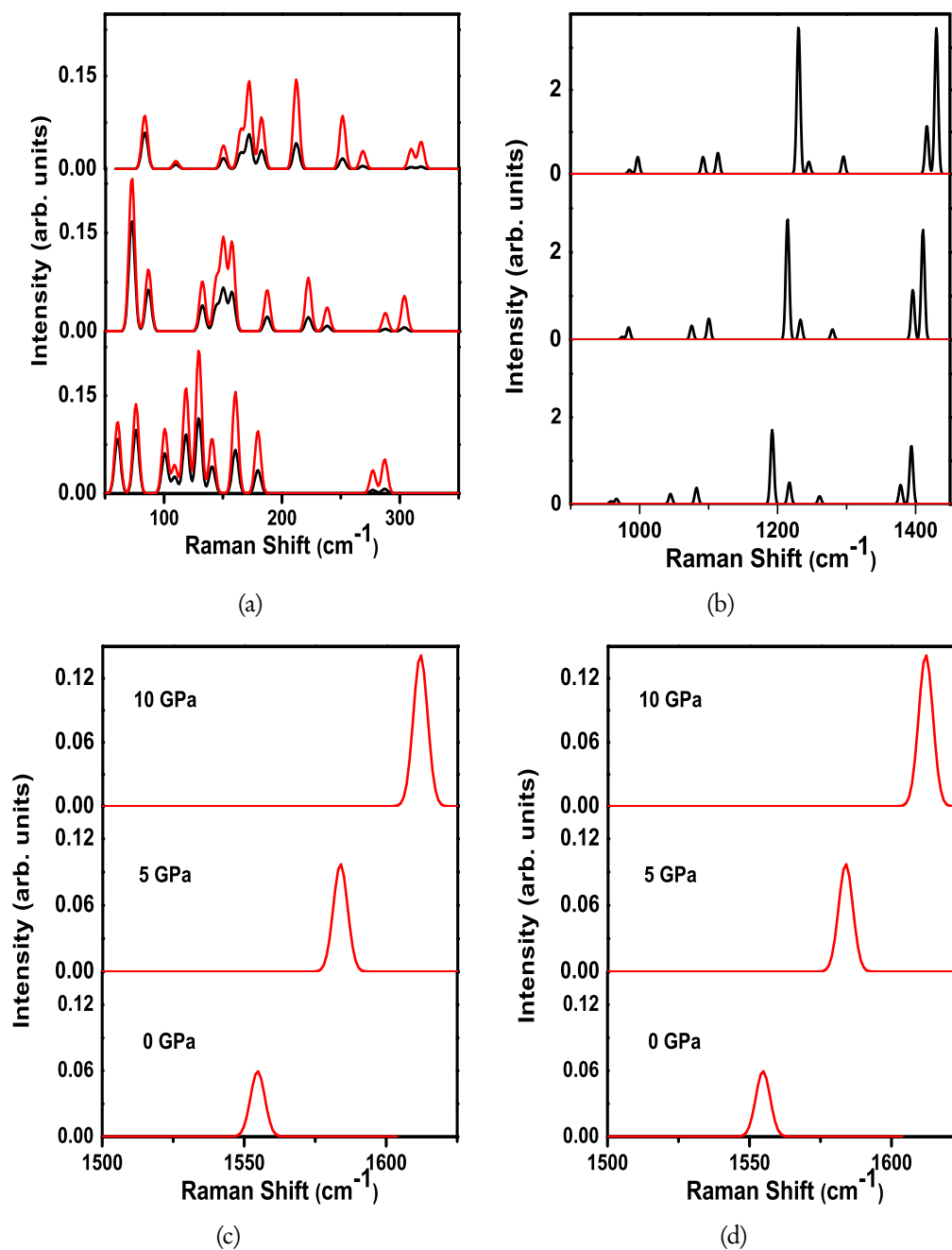


Figure 4.5: Calculated Raman spectra (a) 40-350 cm^{-1} , (b) 900-1450 cm^{-1} and (c,d) 1500-1625 cm^{-1} of K_2DNABT as a function of pressure. Black and red solid lines represent standard Ar (514.5 nm) and Nd:YAG (1064 nm) lasers respectively. The lasers used as an incident light while calculating the Raman spectra of K_2DNABT with Gaussian brodening of 2.5 cm^{-1} .

of K₂DNABT, it becomes a tedious task for experimentalists to assign all the vibrational modes. So, we turn our attention to analyse the complete zone centre vibrational spectrum of K₂DNABT. The zone centre phonon calculations were carried out using linear response approach within density functional perturbation theory. The linear response approach allows one to obtain the effective charges and dielectric tensors directly without any super cell.

Single crystal X-ray diffraction study reveals that K₂DNABT crystallizes in the triclinic $P\bar{1}$ symmetry with one formula unit which includes 20 atoms per unit cell resulting in 60 (3 acoustic + 57 optical) vibrational modes. Using the method of factor group analysis, we determine the distribution of the zone-centre vibrational modes in terms of the representation of C_i point group as $\Gamma_{total} = 30A_u \oplus 30A_g$ ($\Gamma_{acoustic} = 3A_u$; $\Gamma_{optic} = 27A_u \oplus 30A_g$). Since $P\bar{1}$ space group has inversion symmetry, IR and Raman modes do not mix; thus the A_g modes are Raman active whereas A_u modes are IR active, in which g and u represent symmetric and antisymmetric modes with respect to centre of inversion, respectively. The calculated zone centre IR and Raman active vibrational modes and their complete vibrational assignment are given in Tables 4.3 & 4.4. The vibrational spectrum of K₂DNABT can be divided into four regions. 1) The low frequency modes between 60-200 cm⁻¹ which arise due to both potassium cation and tetrazolate anion. 2) The bands from 200-500 cm⁻¹ are mainly due to rotational and translational motions of tetrazole ring and various branches of anion N-N-N, N=N-N, and NO₂ group within and outside the tetrazole ring. 3) Phonon branches in the energy range 500-1090 cm⁻¹ are mainly due to twisting, bending and scissoring motion of C(N)=N-N, N-NO₂, C-C and C-N bands. 4) The bands from 1095-1560 cm⁻¹ are mainly due to symmetric and asymmetric stretching of NO₂, N-N=N, C-N bands as depicted in Tables 4.3 & 4.4.

We also extended our calculations beyond the experiments to investigate IR and Raman spectra under pressure up to 10 GPa. The calculated IR spectra at ambient as well as at high pressure are displayed in figure 4.4. As illustrated in figure

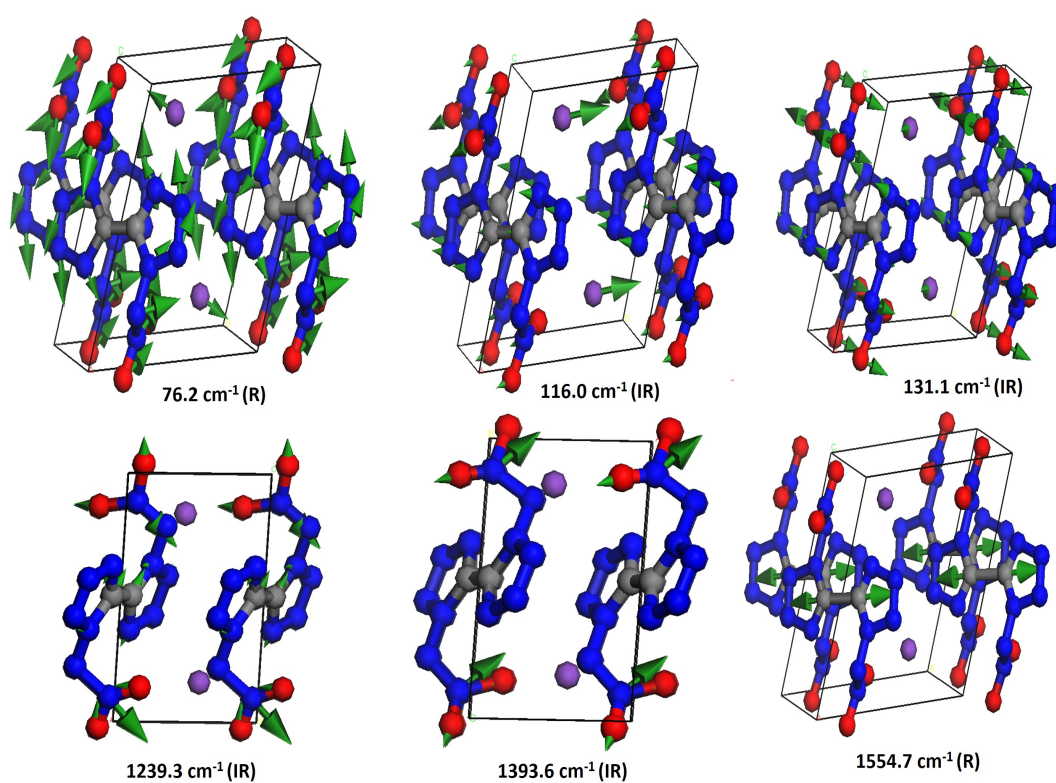


Figure 4.6: The few simulated lattice and internal eigenvectors of K₂DNABT. Here R and IR denote Raman and IR active modes, respectively.

4.4, the frequency and intensity of the IR modes increase with increasing pressure, which shows hardening of the crystal under hydrostatic compression. However, it is clearly seen from figure 4.4a, that as pressure increases, the intensity of two lattice modes with vibrational frequency 116.0 and 131.1 cm^{-1} decreases and the reduction in their intensities is about 58 % and 84 % respectively, when compared to ambient and highest pressure carried out in the present study. The experimental [10] ambient IR data explore that there are strong absorption peaks at 1300 and 1440 cm^{-1} . The corresponding IR peaks from our present calculations (see figure 4.4) are found to be located at 1239.3 and 1393.6 cm^{-1} , which are in close comparison (differ by $\sim 5\%$) with the experimental data [10].

The two absorption bands 1239.3 and 1393.6 cm^{-1} originated from NO_2 symmetric, C-N asymmetric and NO_2 asymmetric stretching, respectively. 1064 nm (Nd:YAG) laser has been used as an incident light to measure Raman data [10] for K_2DNABT single crystals. To compare with the experimentally measured Raman data, we have also calculated the Raman spectra at 298 K using the same laser source as an incident light. Figure 4.5a reveals that the lattice modes are dominant below 300 cm^{-1} and we observed only one strong peak at 1554.7 cm^{-1} in the high frequency region (see figure 4.5c&d) with the 1064 nm laser, which is in good agreement with the experimental value of 1610 cm^{-1} . However, the Raman bands corresponding to twisting, scissoring and bending modes in the frequency range 900-1450 cm^{-1} are displaying very low intensity which complicates the Raman measurements in determining the bending modes of the material with the 1064 nm laser (see figure 1 of the Ref. [34]) Hence we have also calculated the Raman spectra using standard 514.5 nm Ar laser and the calculated Raman bands corresponding to bending modes are as shown in figure 4.5b. Using 514.5 nm laser, the internal modes ($> 900 \text{ cm}^{-1}$) are found to be more intense (see figure 4.5d) while the lattice modes ($< 300 \text{ cm}^{-1}$) are found to have more intensity (see figure 4.5a) using 1064 nm laser. This information could motivate future Raman spectroscopic measurements on this material at ambient as well as at elevated pres-

Table 4.3: Calculated lattice, rotational, translational and liberational modes of K₂DNABT at the DFT-D2 equilibrium volume.

Frequency	IrrRep	Assignment
60.7	A _g	lattice modes
66.0	A _u	
76.2	A _g	
94.0	A _u	
100.7	A _g	
107.7	A _u	
109.1	A _g	
116.0	A _u	
118.6	A _g	
129.6	A _g	
131.1	A _u	
140.8	A _g	
159.6	A _u	
160.6	A _g	
163.5	A _u	
179.1	A _u	Rot. lattice
179.7	A _g	Rot. N-O
202.2	A _u	Rot. lattice
277.2	A _g	Rot. N-N-N
287.3	A _g	Rot. N-N=N
355.9	A _u	Trans. C-C=N-N, N-N-N-O bend
368.9	A _g	Rot. ring, N-O
431.7	A _g	Rot. C-C, N-O, Trans. C-N
435.2	A _u	Rot. ring, N-N-O
463.0	A _u	Trans. ring, Rot. N-O
495.2	A _g	Trans. ring, Rot. N-O
579.6	A _g	Rot. ring, C-C twist.

tures. Furthermore, effect of hydrostatic compression on Raman spectra is also investigated using both of the sources. Our calculations show that the intensity of the lattice modes decreases with pressure and a significant reduction is observed for the lattice mode 76.2 cm^{-1} whereas the frequency as well as intensity of the internal modes grow with application of hydrostatic pressure. However, all these modes keep their identity in the IR and/or Raman spectra up to 10 GPa. The few simulated snapshots of IR and Raman eigenvectors are depicted in figure 4.6. Overall, we predict that the IR and Raman modes exhibit pressure induced blue shift which is due to the inter and intra molecular interactions which stiffen upon compression. This would suggest the dynamical stability of K_2DNABT under the studied pressure range. Our results could be considered as a reference for future experimental or theoretical studies of the green primary explosive at ambient as well as at high pressure.

4.3.3 Electronic structure and absorption spectra

Electronic structure and optical properties of K_2DNABT crystal have been investigated using FP-LAPW method by optimizing the fractional co-ordinates at the experimental lattice constants within PBE-GGA as displayed in Table 4.5. The obtained fractional co-ordinates are in good agreement with the experimental data [10]. The study of microscopic properties like electronic structure and chemical bonding plays a vital role in understanding the macroscopic energetic behavior and stability of explosive materials. Band gap is a fundamental parameter of any semiconducting/insulating material. Zhang and co-workers have explained the correlation between bond dissociation energy, band gap and impact sensitivity for nitro-aromatic compounds [35]. Following this study, Zhu and Xiao [36] have also made a correlation between band gap and impact sensitivity of energetic materials (metal azides and styphanates, pure and K-doped CuN_3 , polymorphs of HMX, CL-20 and TATB) based on the Principle of Easiest Transition (PET), which states that with a smaller band gap it is easier to transfer the electron from

Table 4.4: Calculated liberational and internal modes of K₂DNABT at the DFT-D2 equilibrium volume.

Frequency	IrrRep	Assignment
635.8	A _u	C=N-N bend
664.9	A _g	N=N-N bend
682.4	A _u	C=N-N bend
704.8	A _u	NO2 bend
705.8	A _g	NO2 bend
724.8	A _g	N-C=N, NO2 bend
726.3	A _u	NO2 bend
733.5	A _g	C-C, N-O bend
827.9	A _u	N-N-O twist
842.8	A _g	N-N-O twist
957.6	A _u	N=C-C bend, N-NO2 str
958.2	A _g	N=N-N scissor
966.2	A _u	N-NO2 sym str, N=N-N scissor
966.3	A _g	N-NO2 sym str, N=N-N scissor
996.4	A _u	C=N-N asym str, N=N Scissor
1044.7	A _g	N=N-N asym str, N-N scissor
1078.2	A _u	N=N-N wagg
1082.4	A _g	N=N-N wagg
1098.8	A _u	N=N-N, C-N-N asym str
1192.2	A _g	C-N-N asym str
1197.1	A _u	N-N=N asym str
1217.1	A _g	N-N=N asym str
1239.3	A _u	NO2 sym str, C-N asym str
1260.9	A _g	NO2 sym str
1301.0	A _u	N=C-N asym str
1353.5	A _u	C-N sym str
1378.3	A _g	C-N, N-O asym str
1393.6	A _u	NO2 asym str
1393.9	A _g	C-N, N-O asym str
1554.7	A _g	C-C=N(-N) asym str

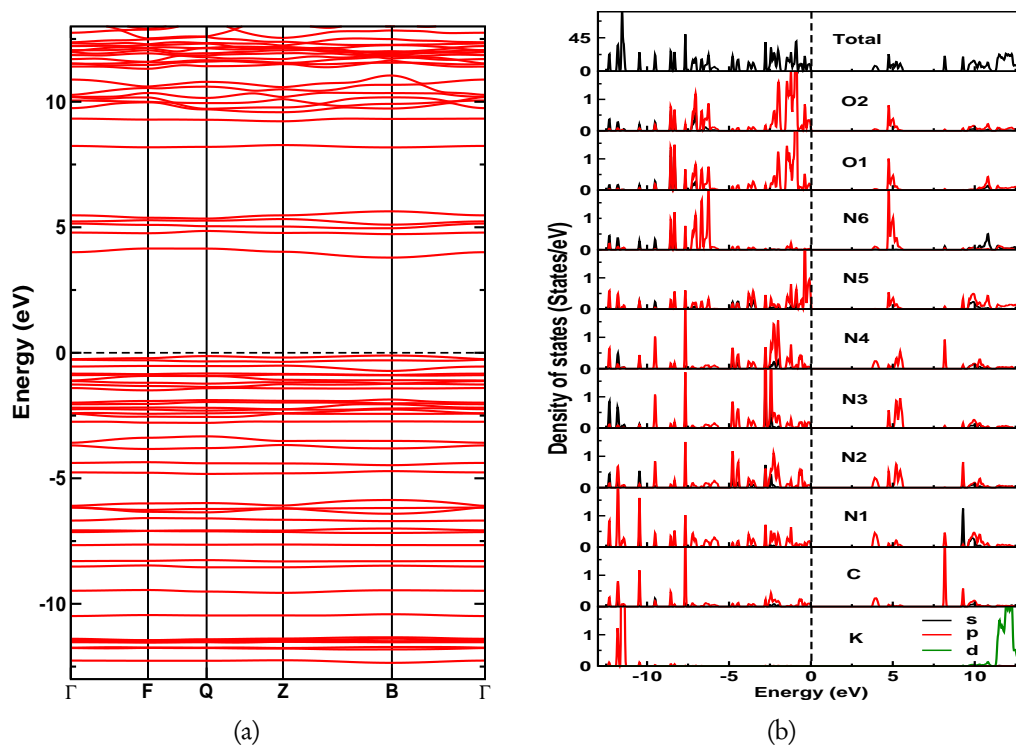


Figure 4.7: Calculated (a) electronic band structure, (b) partial density of states, (c) electron charge density of K_2DNABT using TB-mBJ potential.

Table 4.5: Optimized fractional co-ordinates of K_2DNABT using FP-LAPW method within PBE-GGA functional at the experimental lattice constants. Experimental data have been taken from Ref. [10].

Atom	Wyckoff	This work	Expt.[10]
K	$2i$	(0.4231, 0.7112, 0.1596)	(0.4225, 0.71168, 0.15855)
C	$2i$	(0.0661, 0.0790, 0.4986)	(0.0667, 0.0796, 0.4992)
N1	$2i$	(0.2113, 0.1753, 0.3673)	(0.2098, 0.1747, 0.3679)
N2	$2i$	(0.3140, 0.3061, 0.4140)	(0.3128, 0.3063, 0.4141)
N3	$2i$	(0.2312, 0.2894, 0.5670)	(0.2319, 0.2895, 0.5667)
N4	$2i$	(0.0751, 0.1527, 0.6229)	(0.0748, 0.1515, 0.6233)
N5	$2i$	(0.2821, 0.1397, 0.2175)	(0.2830, 0.1373, 0.2170)
N6	$2i$	(0.0579, 0.2320, 0.1061)	(0.0600, 0.2316, 0.1073)
O1	$2i$	(-0.1775, 0.3411, 0.1341)	(-0.1748, 0.3404, 0.1355)
O2	$2i$	(0.1039, 0.1955, -0.0307)	(0.1033, 0.1968, -0.03031)

^aRef.[10]

valence band to conduction band [36]. The calculated band gap for K_2DNABT crystal is found to be 2.87 eV within PBE-GGA, which is 0.45 eV less than that of the band gap value 2.42 eV [37] of α -LA. According to PET criteria, K_2DNABT should be less sensitive than LA but the experimental measurements disclose that K_2DNABT is more sensitive than LA. This clearly indicates the band gap and impact sensitivity criteria will be helpful to make correlation within a group of materials and/or between the polymorphs. In order to make this correlation, one has to predict accurate band gaps for the energetic materials. Therefore, in the present study, we have used TB-mBJ potential to calculate the electronic band gap of the material. The obtained band gap using TB-mBJ potential is 3.57 eV which is improved by 0.7 eV when compared to PBE-GGA value of 2.87 eV and the predicted band gap serves as a reference for future experiments. The TB-mBJ band structure is plotted along high symmetry directions Γ (0.0, 0.0, 0.0) \rightarrow F (0.0, 0.5, 0.0) \rightarrow Q (0.0, 0.5, 0.5) \rightarrow Z (0.0, 0.0, 0.5) \rightarrow B (0.5, 0.0, 0.0) \rightarrow Γ (0.0, 0.0, 0.0) as shown in figure 4.7a; K_2DNABT is a direct band gap insulator along the B direction of the Brillouin zone.

In order to understand the contribution of each atom to the electronic band

structure, we have plotted the partial density of states (PDOS) for each inequivalent atom of the unit cell. As illustrated in figure 4.7b, the states near the Fermi level are mainly dominated by more electronegative oxygen (O1 & O2) and nitrogen (N5) atoms. The $2p$ -states in the energy range -6 to -8 eV are derived from nitrogen (N6) and oxygen (O1 & O2) atoms and they have strong hybridization between N6 and O1(O2) which shows the covalent nature of NO_2 group within the unit cell. It is also seen from the PDOS and charge density map (see figures 4.7b & c), there is a charge sharing between C-N1, C-N4, N1-N2, N2-N3 & N3-N4 atoms which implies a covalent bonding between these atoms within the tetrazolate anion. However, there is no charge sharing between potassium cation and tetrazolate anion which clearly indicates that the bonding in this material is strongly ionic. Overall, we observed mixed bonding nature in K_2DNABT crystal; strong ionic bonding between potassium and tetrazolate ions and also covalent bonding within the tetrazolate anion. X-ray electron spectroscopic study [38] on inorganic metal azides reveals that Alkali metal azides (AMAs) possess more ionic character than Heavy Metal azides (HMAs), implying that AMAs are relatively more stable than HMAs. On the similar path the presence of ionic bonding in K_2DNABT crystal makes it relatively more stable and insensitive when compared to covalently bonded primary explosives (cyanuric triazide [27]). The calculated absorption spectra of the K_2DNABT crystal along three crystallographic directions using the TB-mBJ potential is shown in figure 4.8. The computed absorption spectra shows that the strong optical anisotropy and absorption starts at the band gap value. As the optical edge starts at 3.57 eV, we confirm that K_2DNABT crystal is expected to undergo decomposition by the irradiation of Ultra-Violet (UV) light with a wavelength of 347.3 nm. The excitonic peak may lie below the calculated absorption edge (347.3 nm) and these excitonic effects can be obtained by solving the Bethe-Salpeter equation using quasi particle energies which is a future direction emerging from this study.

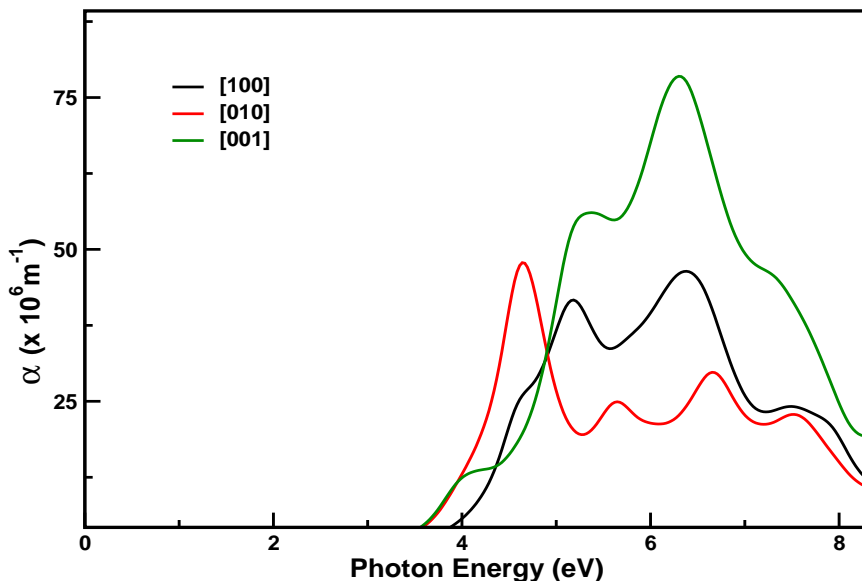


Figure 4.8: Calculated absorption spectra of K_2DNABT as function of photon energy using TB-mBJ potential.

4.4 Conclusions

In conclusion, we have investigated the pressure dependent structure, the equation of state and vibrational spectra of the emerging green primary explosive K_2DNABT . The calculated ground state properties using DFT-D2 are in good agreement with the experiments in contrast to standard LDA/GGA functionals. The anisotropic compressibility ($b < a < c$) of K_2DNABT crystal implies that the material is found to be most sensitive to detonate along crystallographic b-axis and least sensitive along the c-axis. The obtained equilibrium bulk modulus reveals that K_2DNABT is softer than the toxic lead azide and harder than the most sensitive cyanuric triazide. A complete assignment of all vibrational modes has been made according to their molecular vibrations and compared with the available experimental data. The computed IR and Raman spectra show hardening of the lattice under compression. In addition, we also calculated electronic structure and bonding properties using recently developed TB-mBJ potential and

it is found that the compound is a direct band gap insulator with band gap value 3.87 eV. K₂DNABT possesses mixed bonding nature with strong ionic bonding between potassium cation and tetrazolate anion and also covalent bonding within the tetrazolate anion. The existence of ionic bonding may suggest that the material is stabler than covalent primary explosives. The computed absorption spectra indicate that the present investigated compound is sensitive to UV light. The present study could be helpful when this material finds applications in energetic formulations as a green primary explosive.

References

- [1] M. H. V. Huynh, M. A. Hiskey, T. J. Meyer and M. Wetzler, PNAS, **103**, 5409 (2006).
- [2] T. M. Klapötke, Prop. Explos. Pyrotech., **39**, 7 (2014).
- [3] K. D. Oyler, *Green Energetic Materials*, John Willey & Sons, (2014).
- [4] J. Giles, Nature, **427**, 580 (2004).
- [5] M. A. Ilyushin, I. V. Tselinsky and I. V. Shugalei, Cent. Eur. J. Energ. Mater., **9**, 293 (2012).
- [6] M. H. V. Huynh, M. D. Coburn, T. J. Meyer and M. Wetzler, PNAS, **103**, 10322 (2006).
- [7] T. M. Klapötke, *Chemistry of High-Energy Materials*, 2nd ed. Walter de Gruyter Berlin, p.19, (2012).
- [8] J. W. Fronbarger, M. D. Williams, W. B. Sanborn, J. G. Bragg, D. A. Parrish and M. Bichay, Prop. Explos. Pyrotech., **36**, 541 (2011).
- [9] J. W. Fronbarger, M. D. Williams, W. B. Sanborn, D. A. Parrish and M. Bichay, Prop. Explos. Pyrotech., **36**, 459 (2011).

- [10] D. Fischer, T. M. Klapötke and J. Stierstorfer, *Angew. Chem. Int. Ed.*, **53**, 8172 (2014).
- [11] G. Vaitheeswaran, K. Ramesh Babu, N. Yedukondalu and S. Appalakondiah, *Curr. Sci.*, **106**, 1219 (2014).
- [12] M. C. Payne, M. P. Teter, D. C. Allen, T. A. Arias and J. D. Joannopoulos, *Rev. Mod. Phys.*, **64**, 1045 (1992).
- [13] D. Vanderbilt, *Phys. Rev. B*, **41**, 7892 (1990).
- [14] N. Troullier and J. L. Martins, *Phys. Rev. B*, **43**, 1993 (1991).
- [15] D. M. Ceperley and B. J. Alder, *Phys. Rev. Lett.*, **45**, 566 (1980).
- [16] J. P. Perdew and A. Zunger, *Phys. Rev. B*, **23**, 5048 (1981).
- [17] J. P. Perdew, S. Burke and M. Ernzerhof, *Phys. Rev. Lett.*, **77**, 3865 (1996).
- [18] T. H. Fischer and J. Almlof, *J. Phys. Chem.*, **96**, 9768 (1992).
- [19] H. J. Monkhorst and J. D. Pack, *Phys. Rev. B*, **13**, 5188 (1976).
- [20] S. Grimme, *J. Comput. Chem.*, **27**, 1787 (2006).
- [21] P. Blaha, K. Schwarz, G. K. H. Madsen, D. Kvasnicka and J. Luitz, *WIEN2K, an Augmented Plane Wave + Local Orbitals Program for Calculating Crystal Properties*, Techn. Universitat: Wien, Austria. ISBN: 3-9501031-1-1-2, (2001).
- [22] F. Tran and P. Blaha, *Phys. Rev. Lett.*, **102**, 226401 (2009).
- [23] D. C. Sorescu and B. M. Rice, *J. Phys. Chem. C*, **114**, 6734 (2010).
- [24] Y. Cho, W. J. Cho, I. S. Youn, G. Lee, N. J. Singh and K. S. Kim, *Acc. Chem. Res.*, **47**, 3321 (2014).
- [25] J. J. Haycraft, *J. Chem. Phys.*, **131**, 214501 (2009).

- [26] F. D. Murnaghan, Proc. Natl Acad. Sci. USA, **30**, 244 (1944).
- [27] J. P. Agrawal and R. Hodgson, *Organic Chemistry of Explosives*, John Wiley & Sons, (2007).
- [28] S. Appalakondaiah, G. Vaitheeswaran and S. Lebégue, Chem. Phys. Lett., **605-606**, 10 (2014).
- [29] D. Hou, F. Zhang, C. Ji, T. Hannon, H. Zhu, J. Wu, V. I. Levitas and Y. Ma, J. Appl. Phys., **110**, 023524 (2011).
- [30] D. I. A. Millar, *Energetic materials at extreme conditions*, Springer theses, Springer-Verlag, Berlin Heideberg (2012).
- [31] C. E. Weir, S. Block and G. J. Piermarini, J. Chem. Phys., **53**, 4265 (1970).
- [32] K. Ramesh Babu and G. Vaitheeswaran, Chem. Phys. Lett., **533**, 35 (2012).
- [33] N. Yedukondalu, Vikas D. Ghule and G. Vaitheeswaran, J. Phys. Chem. C, **116**, 16910 (2012).
- [34] ftp://ftp.aip.org/epaps/journ_chem_phys/E-JCPSA6-143-055528/support.pdf
- [35] H. Zhang, F. Cheung, F. Zhao and X. -L. Cheng, Int. J. Quantum Chem., **109**, 1547 (2009).
- [36] W. Zhu and H. Xiao, Struct. Chem., **21**, 847 (2010).
- [37] W. Zhu and H. Xiao, J. Phys. Chem. B, **110**, 18196 (2006).
- [38] R. J. Colton and J. W. Rabalais, J. Chem. Phys., **64**, 3481 (1976).

Pressure induced structural phase transitions in potassium based oxidizers

In this chapter, pressure induced polymorphic phase transitions and vibrational spectra of potassium chlorate (PC) and potassium nitrate (PN) have been discussed extensively.

5.1 Introduction

An explosive usually contains a mixture of fuel and oxidizer in appropriate proportions to enhance the combustion and to release large amount of energy at the expense of chemical reactions occurring in the system. Oxidizers such as metal or ammonium-based nitrates, chlorates, perchlorates, permanganates, chromates, peroxides are frequently used in the explosives and pyrotechnic systems [1, 2]. Explosives undergo decomposition and lead to high energy release via oxidation process. Most of the secondary explosives have negative oxygen balance (oxygen deficiency) and their heat release is restricted due to incomplete oxidation reactions [3]. Hence, oxidizers are mixed with energetic materials to make the oxidation reactions more complete and reduce the demand of oxygen from air [4-7]. It is a well-known fact that oxidizer composites respond easily to an external stimulus such as impact or friction due to their sensitivity to mechanical energies [8, 9].

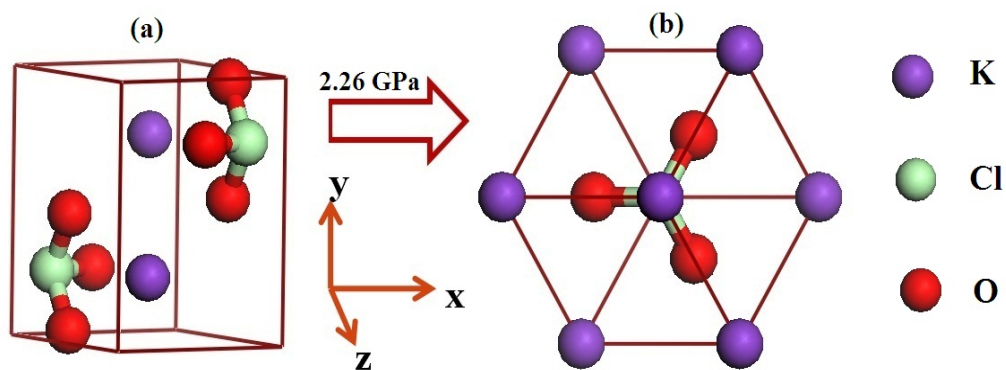


Figure 5.1: Crystal structures of a) phase I (monoclinic, $P2_1/m$) and b) phase II (rhombohedral, $R3m$) of KClO_3 .

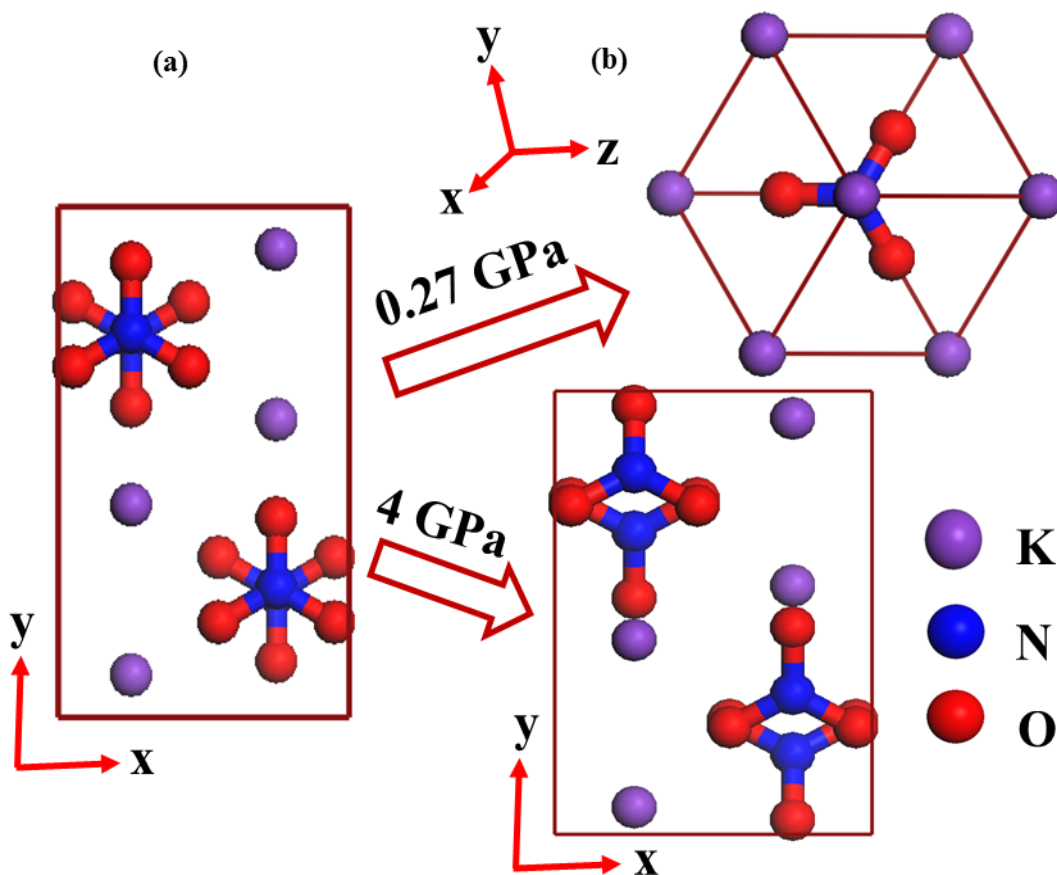


Figure 5.2: Crystal structures of a) phase II (Orthorhombic, $Pmcn$) and b) phase III (rhombohedral, $R3m$) of KNO_3 .

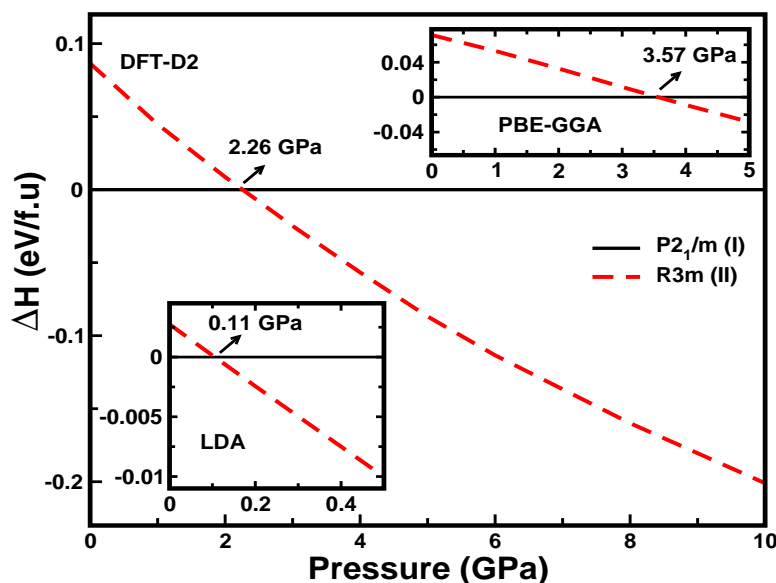
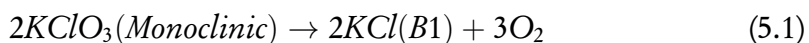


Figure 5.3: Calculated enthalpy difference of phase I ($P2_1/m$, black solid line) and phase II ($R3m$, red dotted line) of $KClO_3$ as a function of pressure using dispersion corrected DFT-D2 method. The lower and upper inset figures correspond to LDA and PBE-GGA functionals, respectively.

The explosive properties of chlorate-based energetic compositions were reported at the end of 18th century on mixtures of PC with sugar and sulfur [10, 11]. PC would be an ideal choice as oxidizer because of its ability to sustain at low reaction temperatures, kinetic stability at its melting point and compatibility with energetic materials [12–14]. It is more appropriate to use PC in pyrotechnic mixtures due to its lower energy content and combustion behavior. Dong and Liao et al [7, 15] investigated the thermal decomposition process of the $KClO_3$ -RDX and $KClO_3$ -HMX composite materials and proved that energy release of mixtures exceeded that of pure RDX and HMX, respectively by 10% and 40%. In addition, their study also revealed that the presence of PC increases the gaseous products in the decomposition mechanism. The decomposition process of PC takes place in two different mechanisms [7, 16–18].



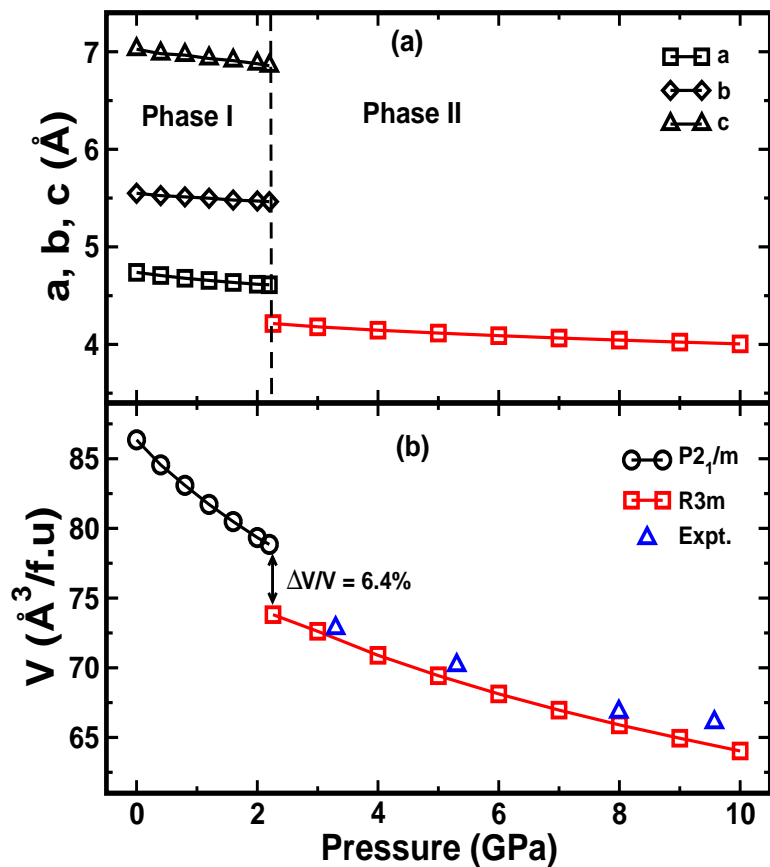
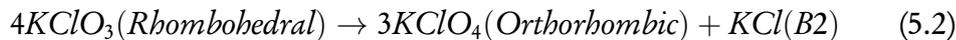


Figure 5.4: Calculated a) lattice constants b) volume of phase I and II of PC as a function of pressure using dispersion corrected DFT-D2 method. The experimental data points are taken from Ref. [31] for the phase II ($R3m$).



At high pressures, the first mechanism is almost inoperative, but the second mechanism is actually favored, since the mixture of the decomposition products is denser than PC itself. This process is relatively simple and the reaction mechanism is also easy to obtain. PC provides a large amount of free oxygen radicals in its thermolysis process which is used to oxidize the energetic intermediates produced by thermal decomposition of explosives. PC is an ionic molecular solid, which crystallizes in the primitive monoclinic ($P2_1/m$) structure at ambient con-

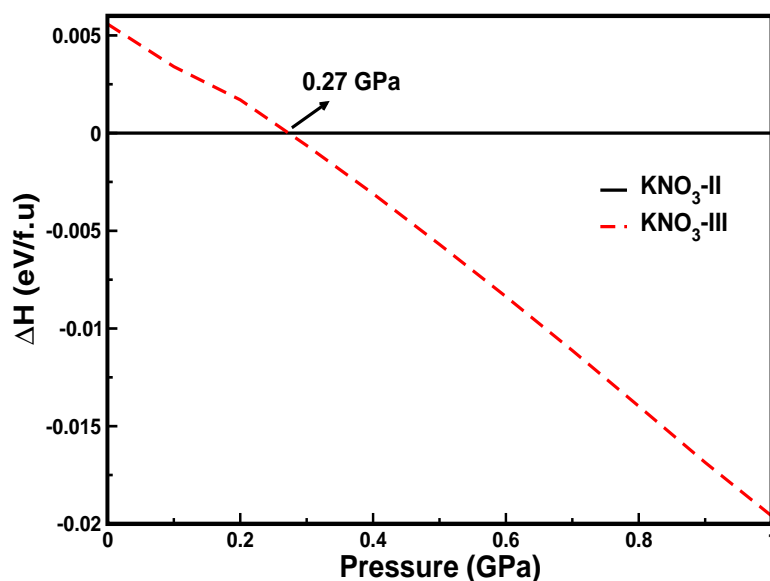


Figure 5.5: Calculated enthalpy difference of phase II and III of PN polymorphs as a function of pressure.

ditions [19]. High pressure studies on molecular crystals are interesting because the effect of pressure on intermolecular bonds is predominant over intramolecular bonds [20]. Several Raman and IR measurements have been performed on PC at ambient as well as at extreme conditions [19–27]. The Raman studies reveal that PC undergoes a pressure induced structural phase transition from ambient monoclinic (phase I) to rhombohedral (phase II) structure about 0.7 GPa [24], or above 1 GPa [28, 29]. Moreover, recent high pressure X-ray diffraction study (XRD) [30, 31] shows that PC undergoes a rapid decomposition below 2 GPa, and it slowdown above 2 GPa because of structural phase transformation from phase I to II (see figure 5.1).

PN is one of the most frequently used oxidizer in pyrotechnics. PN is the major ingredient in black powder and also it serves as an oxidizer with sorbitol in rocket propulsion applications. PN can exist in several polymorphic phases depending up on temperature and pressure conditions. PN crystallizes in the primitive orthorhombic structure ($Pm\bar{c}n$, phase II) at room temperature [32]. Later

Adiwidjaja et al [33] reported a super-structure of phase II with crystal symmetry $Cmc2_1$ which consists of a $2 \times 2 \times 1$ super cell of the $Pm\bar{c}n$ unit cell. When heated phase-II transforms to phase I with disordered nitrate anions at around 128 °C [34], and it passes through a ferroelectric phase III between 124 and 110 °C upon cooling [35]. The crystal structures of PN polymorphs are shown in figure 5.2. On the other hand, high pressure X-ray [36] Neutron powder [37] diffraction and Raman spectroscopic [38] studies revealed that phase II of PN transforms to phase IV around 0.36 GPa under compression. However, most of the fundamental properties such as structural and dynamical stability are still not fully understood due to lack of theoretical data at ambient as well as at high pressures for both the investigated compounds. Further, these properties will be helpful in understanding the decomposition mechanisms. Therefore, in the present chapter, we have systematically investigated the effect of pressure on crystal structure and lattice dynamics of PC and PN by means of the first principles calculations based on the density functional theory (DFT).

5.2 Methodology of calculations

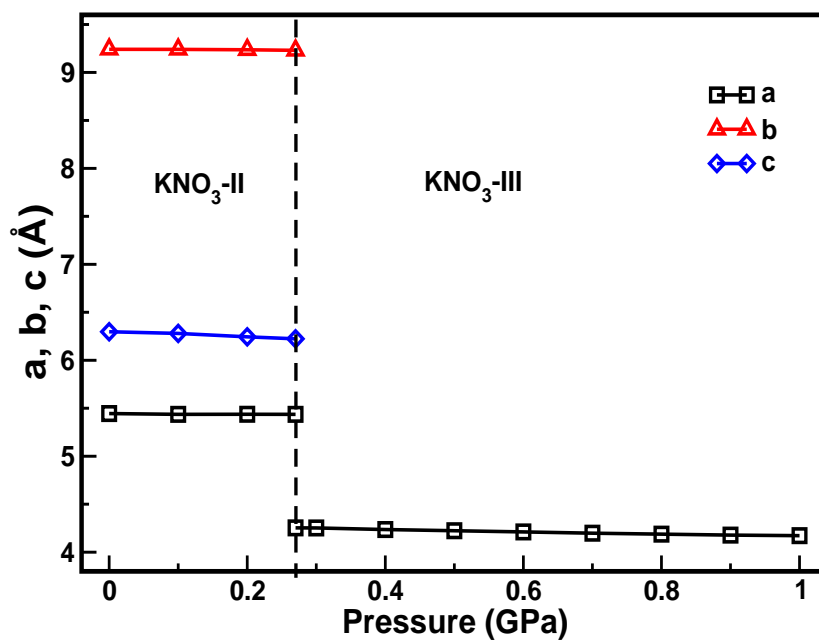
Cambridge Series of Total Energy Package (CASTEP) [39] has been used to perform the first-principles calculations of PC and PN using plane wave pseudo potential (PW-PP) approach based on DFT [40, 41]. We used Norm conserving pseudo potentials [42] for electron-ion interactions. The local density approximation (LDA) [43, 44] and generalized gradient approximation (GGA) [45] were used to treat electron-electron interactions. The Broyden-Fletcher-Goldfarb-Shanno (BFGS) minimization scheme [46] has been used for structural relaxation. The plane wave basis orbitals used in the calculations are $3s^2, 3p^6, 4s^1$ for K; $3s^2, 3p^5$ for Cl; $2s^2, 2p^4$ for O; and $2s^2, 2p^3$ for N. The convergence criteria for structural optimization was set to ultra-fine quality with a kinetic energy cutoff of 1000 eV for PC and 950 eV for PN and $2\pi \times 0.04 \text{ \AA}^{-1}$ separation of k-mesh according to the

Monkhorst-Pack grid scheme [47]. The self-consistent energy convergence was set to 5.0×10^{-6} eV/atom. The convergence criterion for the maximum force between atoms was 0.01 eV/Å. The maximum displacement and stress were set to be 5.0×10^{-4} Å and 0.02 GPa, respectively. In the present study, we have systematically studied the effect of DFT-D2 method [48] on the structural and vibrational properties of PC and PN at ambient as well as at high pressure.

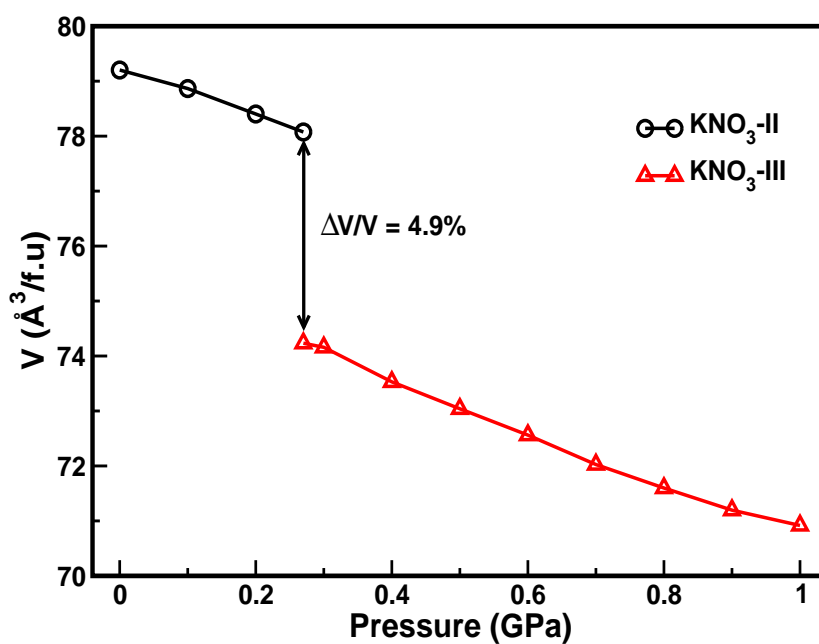
5.3 Results and discussion

5.3.1 Pressure induced polymorphic phase transitions in PC

Theoretical modeling and simulations are efficient tools to predict physical and chemical properties of complex energetic solids at high pressure as a complement to experiments in modern physics, chemistry and materials science. XRD studies on single crystals of PC reveal that the phase I of PC possesses distorted NaCl-type structure with low symmetry, crystallizing in the primitive monoclinic crystal structure with $P2_1/m$ space group. Raman spectroscopic measurements and high pressure XRD studies reveal that PC undergoes a pressure induced phase transition from phase I \rightarrow II about 0.7 GPa [24], 1.0 GPa [28, 29] and around 2.0 GPa [31]. There is an inconsistency between the various experiments [24, 28, 29, 31] with regard to the transition pressure of PC. In order to resolve this issue, total energy calculations were performed based on DFT, which is a powerful tool in predicting the behavior of solid state systems at ambient as well as at high pressures. As illustrated in figure 5.3, the calculated enthalpy difference shows that phase I transforms to phase II at around 0.11 and 3.57 GPa using LDA and PBE-GGA, respectively. It is well known from the literature [49–52] that the LDA functional usually underestimates transition pressures, whereas the GGA overestimates the same. The same trend is observed in our present calculations for PC, where the LDA functional severely underestimates the transition pressure, whereas the PBE-GGA functional overestimates when compared to the experi-



(a)



(b)

Figure 5.6: Calculated (a) lattice constants and (b) volume as a function of pressure for both polymorphic phases II and III of PN.

mental transition pressure *i.e.* above 2 GPa [31]. However, the dispersion corrected DFT-D2 method provides reliable transition pressures for molecular solids [53–55]. In the present study, the DFT-D2 method reproduces the transition pressure accurately in contrast to the standard LDA and PBE-GGA functionals, and this in very good agreement with the experimental transition pressure of around 2 GPa [31]. The calculated lattice parameters a , b and c of phase I and lattice parameter a of phase II are shown in figure 5.4a as a function of pressure. It is clearly observed that all lattice parameters in both phases decrease monotonically with increasing pressure. But, the angles of both phases (β in phase I and α in phase II) increase monotonically over the studied pressure range. Figure 5.4b shows the pressure dependence of volume and there is a 6.4% volume collapse at 2.26 GPa. This is consistent with the experimental results [28, 29] as the ambient phase transforms to a $\sim 6\%$ denser phase II of PC, which indicates the first order nature of phase transition. We also predicted the cell parameters of phase II at 3 GPa, which crystallizes in the rhombohedral structure with $R3m$ ($Z = 1$) space group (see figure 5.1b). The calculated lattice parameters $a = 4.179 \text{ \AA}$ and $\alpha = 84.95^\circ$ are in good agreement with experimental data at ~ 3.5 GPa, $a = 4.201 \text{ \AA}$ and $\alpha = 84.80^\circ$ [29, 31]. All the structural parameters of phase II are presented in Table 5.1 along with experimental data [29]. In addition, the pressure-volume data of phase II are consistent with high pressure XRD data [31].

As discussed in section I, the first decomposition mechanism (see section I) of PC is as follows: phase I of PC undergoes a rapid decomposition [30, 31] to give B1 form of KCl and oxygen (O_2) as the decomposition products at lower pressures (< 2 GPa) and this is ineffective at high pressures. The present study reveals that phase I transforms to phase II at 2.26 GPa, which is in good agreement with experimental transition pressure and the structural transition is responsible for the slowdown of the decomposition process of PC above 2 GPa [30, 31]. Since PC transforms from phase I to II above 2 GPa, the second decomposition mechanism (see section I) is favorable at high pressures. Johnson et al [18] reported the detailed

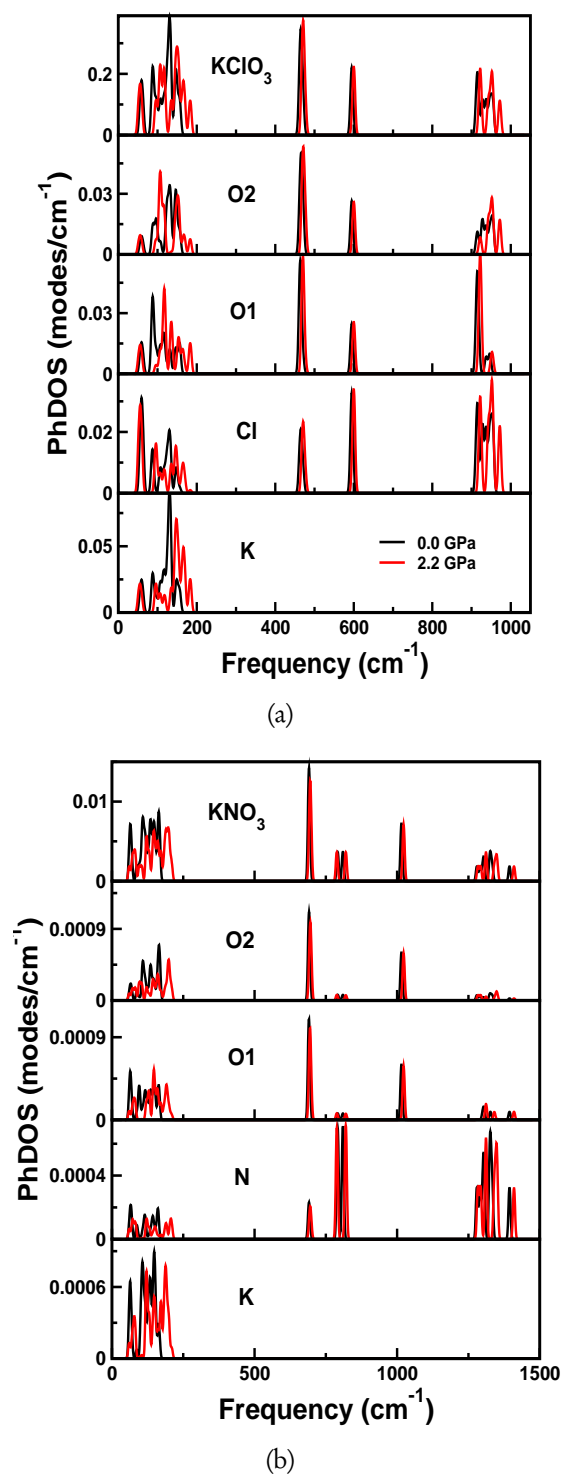


Figure 5.7: Calculated phonon density of states (PhDOS) for phase I and phase II of a) PC and b) PN, respectively using DFT-D2 method.

Table 5.1: Calculated lattice parameter (a), rhombohedral angle (α), volume (V) and fractional coordinates for phase II of PC at 3.0 GPa using DFT-D2 method along with the experimental data [29, 31].

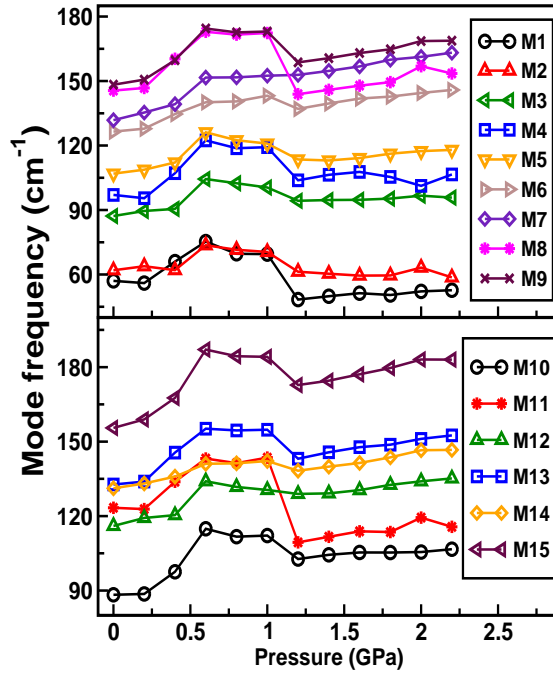
Parameter	Wyckoff	DFT-D2	Expt.
$a(\text{\AA})$		4.179	4.201 ^a
α ($^\circ$)		84.95	84.80 ^a
$V(\text{\AA}^3)$		72.17	73.28 ^a , 77.873 ^b
K	1a	(0.0000, 0.0000, 0.0000)	(0.0000, 0.0000, 0.0000) ^a
Cl	1a	(0.4747, 0.4747, 0.4747)	(0.5000, 0.5000, 0.5000) ^a
O	3b	(0.5434, 0.5434, 0.1176)	(0.6250, 0.6250, 0.1250) ^a

^aRef.[29], ^bRef.[31]

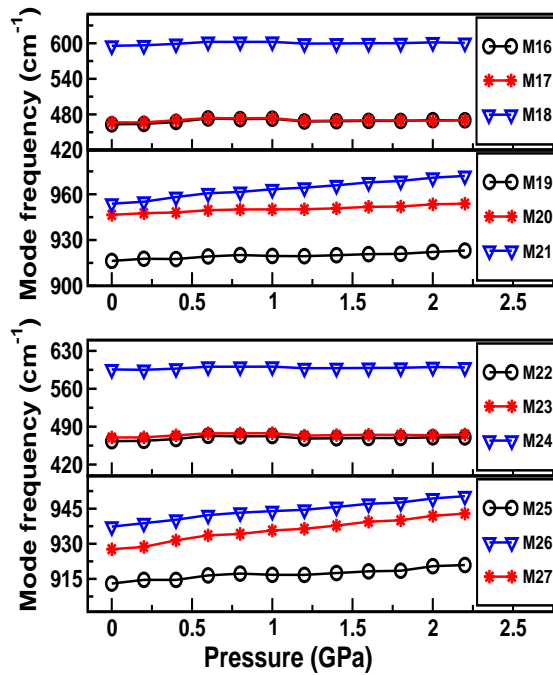
thermal decomposition of phase II of PC, which produces B2 form of KCl and oxygen (O_2) via orthorhombic $KClO_4$.

5.3.2 Pressure induced polymorphic phase transitions in PN

We have also attempted to study the phase stability of PN polymorphs. As discussed in section 5.1, PN exists in multiple polymorphic phases. The previous calculations show that the volume of α -phase is severely underestimated when compared to the experiments [32] by around 34.7 % [56] and 15.3 % [57] within LDA and the volume of $Cmc2_1$ super structure is overestimated by 4.5 % within PBE-GGA functional even at higher plane wave cut-off energies [58]. Thus the standard LDA/GGA functionals are unsuccessful in reproducing the geometries thereby predicting the phase stability of PN polymorphs [56]. Hence, we turn our attention to reproduce the experimental geometries thereby predicting the phase stability of the polymorphs using DFT-D2 method. In contrast to the above reports, the obtained equilibrium volume using DFT-D2 method is in excellent agreement (~ 0.003 - 0.2 %) with experimental results [32, 33]. Also our total energy calculations show that $Pm\bar{c}n$ and $Cmc2_1$ structures are differ by ~ 1 meV/f.u., and this is consistent with the previous theoretical calculations and it is due to very similar local bonding environment between the two structures [58].



(a)



(b)

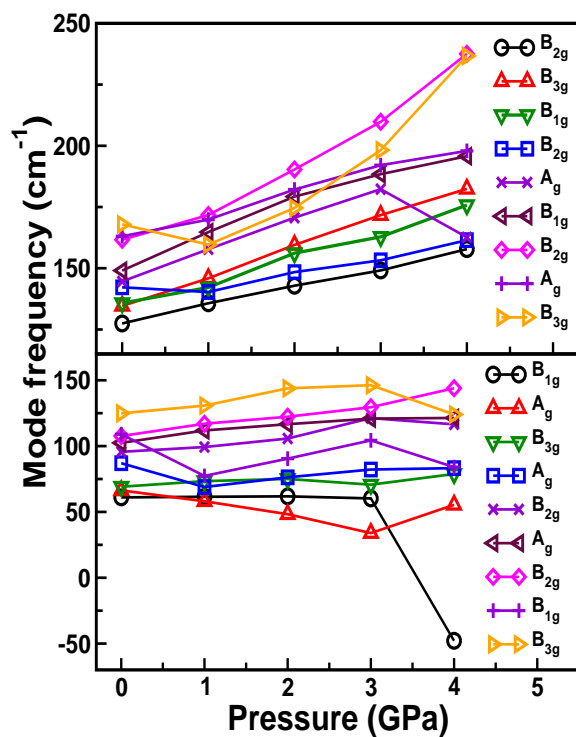
Figure 5.8: Calculated Raman (top) and IR (bottom) active (a) lattice and (b) internal modes of phase I of PC as a function of pressure using DFT-D2 method.

Since the two structures differ by a very small energy (~ 1 meV/f.u.), we have used *Pmcn* unit cell for further calculations to reduce the computational time. It is also found from our present calculations that the total energy of α -phase is lowered by ~ 7 meV/f.u when compared to γ -phase which shows the stability of α -phase over γ -phase, which is in good agreement with experiments in contrast to previous calculations [56].

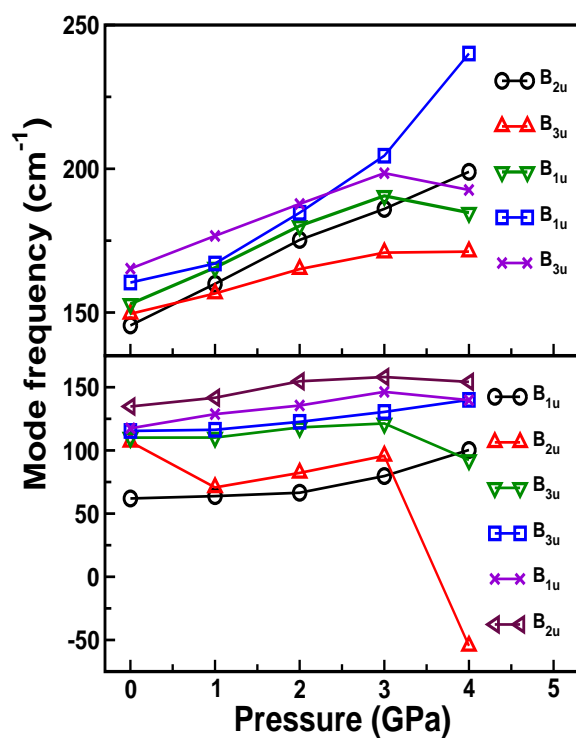
In addition, we have investigated the effect of hydrostatic pressure on the phase stability of PN polymorphs. Interestingly from our total energy calculations, we found that phase-II undergoes a pressure induced polymorphic structural phase transition to phase-III around 0.27 GPa as illustrated in figure 5.5. We also calculated lattice constants as a function of pressure which are decreasing monotonically with increasing pressure as shown in figure 5.6a. In order to figure out the order of transition, we have presented the volume as a function of pressure as shown in figure 5.6b. This clearly shows that there is a discontinuity at the transition with a volume collapse of 4.9% which indicates that the transition is of first order type similar to the case of PC. We also observed change in the orientation of nitrate group from ab-plane as shown in figure 5.2 up on further compression to 4 GPa. The obtained structure at 4 GPa (see figure 5.2) is analogous to phase IV of PN determined by using the X-ray and powder diffraction and Raman spectroscopic measurements [36–38]. Therefore, we confirm that PN (< 0.3 GPa) and PC (< 2.3 GPa) can be used as an oxidizers at low pressure region due to rapid release of O_2 as one of its decomposition products for oxygen deficient energetic materials like TNT (-74.00%), HNS (-67.60%), HMX (-21.62%) and RDX (-21.60%) [3].

5.3.3 Zone center phonon frequencies at ambient pressure

A detailed vibrational spectra analysis of PC and PN has been carried out at ambient as well as at high pressures. Single crystal XRD studies reveal that the phase I and II of PC and PN consist of 10 and 20 atoms with two and four formula units



(a)



(b)

Figure 5.9: Calculated a) Raman and b) IR active lattice modes of phase II of PN as a function of pressure using DFT-D2 method.

Table 5.2: Calculated Raman and IR active lattice modes (in cm^{-1}) of phase I of PC at ambient pressure using LDA, PBE-GGA functionals and dispersion corrected DFT-D2 method along with experimental data [21, 24, 25]. (T = Translational and R = Rotational).

	Mode	Symmetry	LDA	PBE-GGA	DFT-D2	Expt.	Assignment
Raman	M1	A_g	58.12	55.68	57.06	53 ^a	T
	M2	B_g	54.63	47.06	61.96	57, ^a 55 ^b	T
	M3	A_g	90.23	78.70	87.21	86, ^a 90, ^b 87 ^c	T
	M4	B_g	86.07	66.77	97.02	78, ^a 83 ^c	R
	M5	A_g	119.68	90.76	106.93	100, ^a 102, ^b 109 ^c	T
	M6	B_g	144.54	104.34	126.48	125, ^a 134, ^b 132 ^c	T
	M7	A_g	159.80	113.55	131.80	—	T
	M8	B_g	156.79	126.23	145.56	146, ^b 144 ^c	R
	M9	A_g	179.63	130.40	148.30	145, ^a 161 ^c	R
IR	M10	A_u	83.86	49.74	88.28	—	R
	M11	A_u	133.24	104.73	123.34	—	R
	M12	B_u	137.77	101.53	116.02	—	T
	M13	A_u	150.69	109.31	132.73	131 ^b	T
	M14	B_u	146.85	115.35	131.17	—	T
	M15	B_u	194.60	137.83	155.52	—	R

^a Ref.[25], ^bRef.[24], ^cRef.[21]

per unit cell, respectively. This results in 30 and 60 vibrational modes, which are further classified into 3 acoustic and 27 (57) optical modes for PC (PN). According to the group theory analysis, the group symmetry decomposition into irreducible representations of the modes for the two compounds are given as follows:

$$\Gamma_{tot}^{PC} = 9A_g \oplus 6A_u \oplus 6B_g \oplus 9B_u$$

$$\Gamma_{tot}^{PN} = 9B_{1u} \oplus 6B_{2u} \oplus 9B_{3u} \oplus 6B_{1g} \oplus 9B_{2g} \oplus 6B_{3g} \oplus 9A_g \oplus 6A_u$$

Due to the centre of symmetry of the crystal structure [19], the vibrational modes of phase I of PC are summarized as $6A_u \oplus 9B_u \oplus 9A_g \oplus 6B_g$. A_g and B_g modes possess inversion symmetry and hence they are Raman active, while A_u and B_u modes are IR active due to change of sign under inversion symmetry for PC. A_g , B_{1g} , B_{2g} and B_{3g} are Raman active, B_{1u} , B_{2u} , B_{3u} are IR active and A_u is forbidden in both for PN.

We have calculated zone center vibrational frequencies at ambient pressure using LDA, PBE-GGA functionals and DFT-D2 method (see Tables 5.2 & 5.3) for PC. The calculated lattice modes ($< 200 \text{ cm}^{-1}$) using LDA and PBE-GGA functionals show large deviation from the experimental results [21, 24, 25] as the LDA and PBE-GGA functionals are inadequate to treat intermolecular interactions in molecular solids [59–61]. The non-bonded interactions can be treated very well with dispersion corrected DFT-D2 [48] method and thus, the calculated lattice modes using DFT-D2 method are found to be in good agreement with the experimental data [21, 24, 25]. The obtained internal (high frequency) modes using LDA, PBE-GGA functionals and DFT-D2 method are also in close comparison with the experimental results [21, 24, 25]. Further, the optical modes are classified into 15 external ($< 200 \text{ cm}^{-1}$) and 12 internal ($> 400 \text{ cm}^{-1}$) modes. Among the 15 external (lattice) modes, there are 9 Raman active and 6 IR active modes and these lattice modes are mutually exclusive [22, 23]. The lattice modes assigned to translational ($4A_g \oplus 2B_u \oplus 2B_g \oplus A_u$) and rotational ($A_g \oplus B_u \oplus 2B_g \oplus 2B_u$) motion of phase I of PC are shown in Table 5.2.

It is well known that the chlorate ClO_3^- ion in free state possesses four fun-

Table 5.3: Calculated Raman and IR active internal modes (in cm^{-1}) of phase I of PC at ambient pressure using LDA, PBE-GGA functionals and dispersion corrected DFT-D2 method along with experimental data [21, 24, 25].

	Mode	Symmetry	LDA	PBE-GGA	DFT-D2	Expt.	Assignment
Raman	M16	B_g	477.75	456.51	463.24	487 ^a	Twist. + def. of Cl-O
	M17	A_g	480.69	460.07	466.45	488, ^a 490 ^b	Scissor of Cl-O
	M18	A_g	614.84	591.79	595.77	619, ^c 620 ^{a,b}	Wagg. + Bend. of Cl-O
	M19	A_g	955.01	915.14	916.28	940, ^{a,b} 939 ^c	Symm. Str. of Cl-O
	M20	A_g	987.53	952.00	946.49	979, ^{a,b} 978 ^c	Asymm. Str. of Cl-O
	M21	B_g	996.16	938.81	953.81	982, ^{a,c} 983 ^b	Asymm. Str. of Cl-O
	M22	A_u	478.25	456.05	463.08	484 ^a	Twist. + def. of Cl-O
IR	M23	B_u	485.02	462.73	470.07	493 ^a	Scissor. Cl-O
	M24	B_u	614.17	590.89	594.14	620 ^a	Wagg. + Bend. of Cl-O
	M25	B_u	952.62	911.92	913.00	939 ^a	Symm. Str. of Cl-O
	M26	B_u	979.78	935.45	937.33	1000 ^a	Asymm. Str. of Cl-O
	M27	A_u	967.82	913.28	927.69	992 ^a	Asymm. Str. of Cl-O

^aRef.[21], ^bRef.[24], ^cRef.[25]

Table 5.4: Calculated asymmetric (ν_{Asym}), symmetric (ν_{Sym}) stretching and bending (ν_{Bend}) vibrational frequencies (in cm^{-1}) of PN using DFT-D2 method. Experimental data is taken from the Refs. [62, 63].

IrrRep	Freq	Assignment
B _{2g}	1391.8	ν_{Asym}
B _{1g}	1335.9 (1348 ^a)	
B _{2u}	1327.3	
B _{1u}	1324.9	
A _g	1302.9 (1360 ^a)	
B _{3u}	1298.3	
A _u	1282.9	
A _g	1015.2 (1050 ^b , 1054 ^a)	ν_{Sym}
B _{3u}	1014.9	
B _{2g}	1013.8	
B _{1u}	1013.6	
B _{1u}	812.3	ν_{Bend}
B _{2g}	811.9	
A _g	793.9	
B _{3u}	793.4	
B _{3u}	691.6	
B _{2u}	690.9	
B _{1g}	690.7	
A _u	690.6	
B _{2g}	690.6	
B _{3g}	690.2	
B _{1u}	690.1	
A _g	689.2 (718 ^a)	

^aRef.[62], ^bRef.[63]

damental Raman active vibrations 478 (E), 615 (A_1), 930 (A_1) and 975 (E) with degeneracies 2, 1, 1 and 2, respectively [22, 23]. The degeneracy is removed due to the presence of K^+ ion in the unit cell of PC, which results in six Raman and six IR active non-degenerate internal vibrations. These two sets are mutually exclusive as PC possesses a center of symmetry [22, 23]. The calculated internal (Raman and IR active) modes using DFT-D2 along with the LDA and PBE-GGA functionals and their vibrational assignment are presented in Table 5.3. The vibrational assignment of internal modes are explained by considering the DFT-D2 modes: the M16 (463.24 cm^{-1}) and M22 (463.08 cm^{-1}) modes correspond to twisting and deformation of the lattice. The scissoring of Cl-O bond corresponds to M17 (466.45 cm^{-1}) and M23 (470.07 cm^{-1}) bands, whereas the bending motion of ClO_3^- corresponds to M18 (595.77 cm^{-1}) and M24 (594.14 cm^{-1}) modes. The modes M19 (916.28 cm^{-1}) and M25 (913.00 cm^{-1}) correspond to symmetric stretching of Cl-O bonds, while M20 (946.49 cm^{-1}), M26 (937.33 cm^{-1}) and M21 (953.81 cm^{-1}), M27 (927.69 cm^{-1}) modes arise due to asymmetric stretching of ClO_3^- ion along yz-plane of the PC lattice. Since, the intra molecular bond lengths (Cl-O and N-O) within the $\text{ClO}_3^-/\text{NO}_3^-$ group are almost unchanged by the inclusion of dispersion corrected DFT-D2 to the standard PBE-GGA functional, the corresponding ClO_3^- internal vibrations using PBE-GGA and DFT-D2 method are found to be comparable with each other (see Table 5.3 and figure 5.8b). A similar kind of behavior is observed for energetic molecular crystals such as RDX and HMX at ambient pressure [64, 65]. The dispersion corrected methods are successful in predicting the lattice vibrations thus enabling comparison with the experiments.

The analysis of vibrational spectrum of PN were made using DFT-D2 method alone to reduce the computational time. NO_3^- anion also consists of four internal vibrations (are given in cm^{-1}) in its free state such as Raman active 1050 (A_1), IR active 820 (A_2), and both Raman and IR active 1385 (E), 725 (E) degenerate modes. The presence of K^+ cation with NO_3^- anion in PN crystal removes the degeneracy

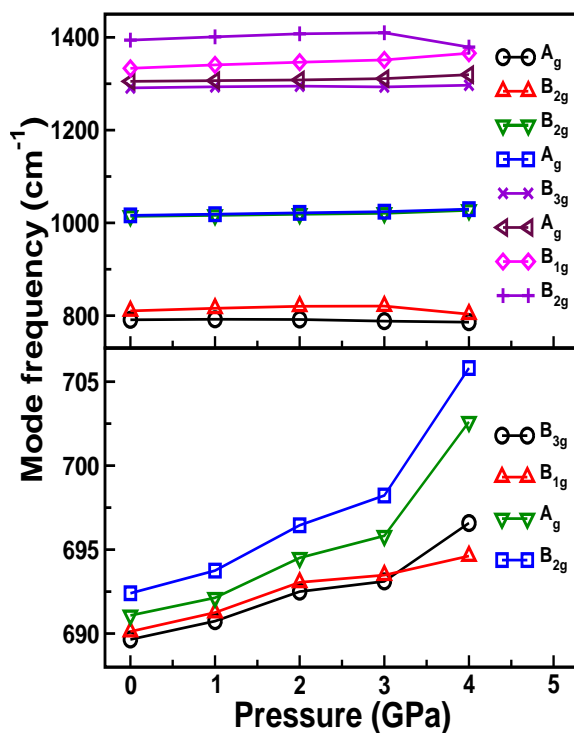
Table 5.5: Calculated lattice modes and their vibrational assignment of PN using DFT-D2 method. The letters T, Tw, R, Roc correspond to Translational, Rotational, Twisting, Rocking modes, respectively. The experimental data in parenthesis is taken from Ref. [62].

IrrRep	Freq	Assignment	IrrRep	Freq	Assignment
B_{3u}	160.2	TK, Tw NO ₃	B_{2u}, B_{3g}	131.6, 126.0(124)	R NO ₃
B_{2g}, B_{1g}	155.3, 154.1	TK, NO ₃	B_{2g}, B_{2g}	127.6, 125.1	TK, NO ₃
B_{1u}	152.6	T NO ₃	B_{3u}, B_{2g}, A_g	109.1, 105.6, 102.3(108)	TK, NO ₃
B_{3g}, A_g, A_u	151.9, 151.1(159), 150.6	Roc NO ₃	B_{3u}	95.3	T NO ₃
B_{2u}, B_{2u}, B_{3g}	148.0, 146.8, 138.3	TK, NO ₃	B_{1g}, B_{3u}, B_{2g}	89.7, 87.5, 86.6(84)	Tw NO ₃
B_{3u}, A_g	144.7, 140.5(142)	TK, Tw NO ₃	A_u, B_{3g}, B_{1g}	82.6, 82.0(83), 77.2	TK, NO ₃
A_u, B_{1g}, A_u	136.52, 129.8, 116.5	TK, R NO ₃	A_g, B_{1u}, A_g	76.2(76), 53.5, 53.0(53)	TK, NO ₃

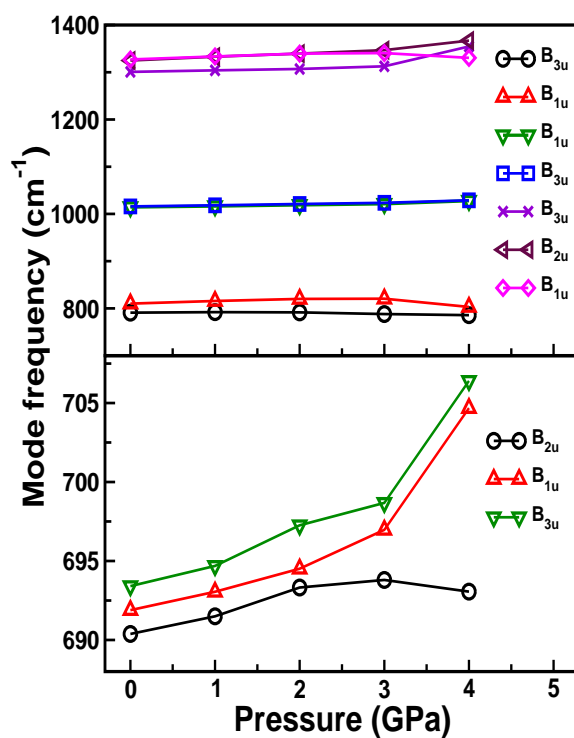
of NO_3 ion internal vibrations from 4 \rightarrow 24 non-degenerate modes due to four molecules in the PN crystal as presented in Table 5.4. We have also made lattice vibrational mode assignment (33 in number) and compared them with the available experimental data [62] as depicted in Table 5.5. The calculated frequency of internal modes with and without dispersion correction are underestimated when compared to the experimental data, which may be due to the fact that the linear response approach used in the present study is based on the harmonic approximation. Further, we turn our attention to understand the high pressure vibrational spectra of both of the compounds PC and PN.

5.3.4 Zone center phonon frequencies under high pressure

To investigate the dynamical stability under hydrostatic pressure, we have systematically studied the effect of pressure on zone center external (lattice) and internal phonon modes using DFT-D2 method to complement the high pressure Raman and IR measurements of PC [24] and PN [38]. The calculated phonon density of states (PhDOS) at ambient as well as at high pressure 2.2 GPa for PC and 3.0 GPa for PN are shown in figure 5.7. The low frequency modes (below 250 cm^{-1}) are due to both potassium and chlorate/nitrate ions, whereas modes above 400 cm^{-1} are due to the chlorate/nitrate anion alone. The vibrational modes shift towards high frequency region under compression as displayed in figure 5.7. As illustrated in figure 5.8a, the low frequency Raman (M1-M9) and IR (M10-M15) active lattice modes soften under hydrostatic pressure, except M7 lattice mode which is hardening under pressure for PC. While the lattice modes are hardening with pressure except few lattice modes soften above 3 GPa, in particular the Raman active B_{1g} and IR active B_{1u} modes are found to be imaginary around 3.5 GPa for PN as depicted in figure 5.9a, which clearly indicates that phase-II of PN becomes dynamically unstable above 3.5 GPa. This is due to change in the orientation of nitrate group in the ab-plane. The optical modes in the frequency range between $450\text{-}620 \text{ cm}^{-1}$ *i.e.* M16-M18 and M22-M24 are found to be slightly modified with



(a)



(b)

Figure 5.10: Calculated (a) Raman and (b) IR active internal modes of phase II of PN as a function of pressure using DFT-D2 method.

the application of pressure, whereas the high frequency internal modes such as M19-M21 and M25-M27 are found to increase linearly with pressure for both of the compounds PC and PN, which can be clearly seen from figures 5.8b & 5.10.

Overall, we observe that all lattice modes of PC increase with pressure up to 0.6 GPa and remain almost constant between 0.6-0.8 GPa. We also find a sudden decrease in all the Raman and IR active lattice modes from 1.0 to 1.2 GPa, which may result in the dynamical instability of phase I of PC under pressure. As evident from figure 5.8, all the Raman and IR active lattice modes do not vary significantly with pressure after 1.2 GPa, which might be the reason for coexistence of the two phases from 1.0 GPa up to transition pressure (2.26 GPa). Hence, we confirm that the transition starts at about 1.0 GPa due to softening of lattice and completes at 2.26 GPa (see figure 5.3). Thus the low symmetry phase I ($P2_1/m$) undergoes a pressure induced structural phase transition to high symmetry phase II ($R3m$), which agrees quite well with the recent experimental results using X-ray diffraction technique [31]. Similarly, the lattice B_{1g} and B_{1u} modes drive the instability in the thermodynamic ground state *i.e.* phase-II of PN around 3.5 GPa due to change in the orientation of nitrate group. Raman spectroscopy and single crystal X-ray diffraction studies reveal that phase-II transforms to phase-IV around 0.36 GPa. Our results also support this phase transformation but the transition pressure will be well below the dynamical instability obtained from zone centre phonons for phase-II of PN.

5.4 Conclusions

In summary, first principles calculations were performed to investigate the high pressure behavior of PC and PN. Standard DFT functionals are unable to account for the non-bonded interactions in the molecular solids. However, the calculated ground state properties using DFT-D2 method are in excellent agreement with the experiments. It is found that PC undergoes a pressure induced structural

phase transition from phase I to II and the calculated transition pressures using LDA and PBE-GGA functionals are 0.11 and 3.57 GPa, respectively. The LDA severely underestimates the transition pressure whereas PBE-GGA overestimates it. However, the calculated transition pressure using DFT-D2 method is 2.26 GPa, which is in good accord with a recent high pressure X-ray diffraction study. The transition is associated with a volume contraction of 6.4% and this is found to be consistent with experimental reduction of $\sim 6\%$ which indicates a first order type phase transition. We have also observed that PN encounter a polymorphic structural phase transition from orthorhombic ($Pm\bar{c}n$) \rightarrow rhombohedral ($R\bar{3}m$) structure at 0.27 GPa with a volume collapse of 4.9% similar to that of PC. We also calculated the zone center phonon frequencies at ambient as well as at high pressures up to 2.2 GPa and 4 GPa to investigate the dynamical stability of phase I of PC and phase II of PN, respectively. We observe the softening in the Raman and IR active lattice modes under pressure. Overall, the present study reveals that the softening of lattice of phase I starts after 1.0 GPa and it completely transforms to phase II at 2.26 GPa, which agrees quite well with recent experimental results for PC. While the lattice B_{1g} and B_{1u} modes drives the instability in PN around 3.5 GPa due to change in the orientation of nitrate group from ab-plane. Finally, the present study confirms that the pressure induced phase transition leads to a change in the decomposition mechanisms of PC which also supports the recent experimental observations.

References

- [1] G. Steinhauser and T. M. Klapötke, *Angew. Chem. Int. Ed.*, **47**, 3330 (2008).
- [2] N. Kubota, *Propellants and Explosives: Thermochemical Aspects of Combustion*, 2nd Ed., Wiley-VCH, (2007).
- [3] J. Akhavan, *The Chemistry of Explosives*, Royal Society of Chemistry, Cam-

- bridge, UK, (2004).
- [4] M. Hemmila, M. Hihkio and K. Linnainmaa, *Prop. Explos. Pyrotech.*, **32**, 415 (2007).
- [5] J. A. Conkling and C. Mocella, *Chemistry of Pyrotechnics: Basic Principles and Theory*, 2nd Ed., CRC Press, (2010).
- [6] B. Berger, *Prop. Explos. Pyrotech.*, **30**, 27 (2005).
- [7] X. F. Dong, Q. L. Yan, X. H. Zhang, D. L. Cao and C. L. Xuan, *J. Anal. Appl. Pyrol.*, **93**, 160 (2012).
- [8] K. Takita, K. Shiraki, A. Miyake and T. Ogawa, *Prop. Explos. Pyrotech.*, **24**, 291 (1999).
- [9] J. A. Conkling, *Chemistry of Pyrotechnics*, Marcel Dekker, New York, (1985).
- [10] M. Comet and H. Fuzellier, *L'Act. Chim.* **4**, 7 (2000).
- [11] J. C. Oxley, *Terrorism and Political Violence*, **5**, 30 (1993).
- [12] D. P. Dolata, *Prop. Explos. Pyrotech.*, **30**, 63 (2005).
- [13] M. M. Markowitz and D. A. Boryta, *J. Phys. Chem.*, **68**, 2282 (1964).
- [14] P. G. Urban, *Bretherick's Handbook of Reactivity Chemical Hazards*, 5th ed., Butterworth-Heinemann, London, (1995).
- [15] L. Q. Liao, Q. L. Yan, Y. Zheng, Z. W. Song, J. Q. Li and P. Liu, *Ind. J. Eng. Mater. Sci.*, **18**, 393 (2011).
- [16] W. W. Wendlandt, *Thermal Methods of Analysis*, 2nd ed., Wiley, New York, (1974).
- [17] C. Otto and H. Fry, *J. Am. Chem. Soc.*, **46**, 272 (1924).

- [18] M. C. Johnson, D. Walker, S. M. Clark and R. L. Jones, *Am. Mineral.*, **86**, 1367 (2001).
- [19] J. Danielsen, A. Hazel and F. K. Larsen, *Acta cryst.*, **B37**, 913 (1981).
- [20] W. F. Shearman, *J. Phys. C*, **13**, 4601 (1980).
- [21] J. B. Bates, *J. Chem. Phys.*, **55**, 494 (1971).
- [22] C. S. Kumari, *Proc. Ind. Acad. Sci.*, **32A**, 177 (1950).
- [23] A. K. Ramdas, *Proc. Ind. Acad. Sci.*, **35A**, 249 (1952); **36A**, 55 (1952); **37A**, 451 (1953).
- [24] A. M. Heyns and J. B. Clark, *J. Raman Spectrosc.*, **14**, 342 (1983).
- [25] M. H. Brooker and J. G. Shapter, *J. Phys. Chem. Solids*, **50**, 1087 (1989).
- [26] D. A. Adams, A. E. Heath, M. Pogan and P. W. Ruff, *Spectrochem. Acta. Part A*, **47**, 1075 (1991).
- [27] P. W. Bridgman, *Collected Experimental Papers*, Harvard University Press, Mass., **5**, p.119 (1964).
- [28] C. W. F. T. Pistorius, *J. Chem. Phys.*, **52**, 1009 (1970).
- [29] C. W. F. T. Pistorius, *J. Chem. Phys.*, **56**, 6263 (1972).
- [30] M. Pravica, C. Park, L. Bai, Y. Liu and J. Robinson, *Rev. Sci. Instrum.*, **45**, 106102 (2011).
- [31] M. Pravica, L. Bai and N. Bhattacharya, *J. Appl. cryst.*, **45**, 48 (2012).
- [32] J. K. Nimmo and B. W. Lucas, *J. Phys. C*, **6**, 201 (1973).
- [33] G. Adiwidjaja and D. Pohl, *Acta Crystllogr. C*, **59**, i139 (2003).

- [34] J. K. Nimmo and B. W. Lucas, *Acta Crystllogr.*, **B32**, 968 (1976).
- [35] J. K. Nimmo and B. W. Lucas, *Nature*, **237**, 61 (1972).
- [36] D. A. Adams, P. D. Hatton, A. E. Heath and D. R. Russell, *J. Phys. C: Solid State Phys.* **21**, 505 (1988).
- [37] T. G. Worlton, D. L. Decker, J. D. Jorgensen and R. Kleb, *Physica B*, **136**, 503 (1986).
- [38] Z. X. Shen and W. F. Sherman, *J. Mol. Struct.*, **247**, 397 (1991).
- [39] M. D. Segall, P. L. D. Lidan, M. J. Probert, C. J. Pickard, P. J. Hasnip, S. J. Clark and M. C. Payne, *J. Phys.: Condens. Matter*, **14**, 271 (2002).
- [40] P. Hohenberg and W. Kohn, *Phys. Rev. B*, **136**, 384 (1964).
- [41] W. Kohn and L. J. Sham, *Phys. Rev. A*, **140**, 1133 (1965).
- [42] N. Troullier and J. L. Martins, *Phys. Rev. B*, **43**, 1993 (1991).
- [43] D. M. Ceperley and B. J. Alder, *Phys. Rev. Lett.*, **45**, 566 (1980).
- [44] J. P. Perdew and A. Zunger, *Phys. Rev. B*, **23**, 5048 (1981).
- [45] J. P. Perdew, S. Burke and M. Ernzerhof, *Phys. Rev. Lett.*, **77**, 3865 (1996).
- [46] T. H. Fischer and J. Almlof, *J. Phys. Chem.*, **96**, 9768 (1992).
- [47] H. J. Monkhorst and J. D. Pack, *Phys. Rev. B*, **13**, 5188 (1976).
- [48] S. Grimme, *J. Comput. Chem.*, **27**, 1787 (2006).
- [49] A. R. Oganov and S. Ono, *Nature*, **430**, 445 (2004).
- [50] A. R. Oganov and J. P. Brodholt, *Phys. Chem. Miner.*, **27**, 430 (2000).
- [51] J. Kang, E. -C. Lee and K. J. Chang, *Phys. Rev. B*, **68**, 054106 (2003).

- [52] J. E. Jaffe, J. A. Snyder, Z. Lin and A. C. Hess, *Phys. Rev. B*, **62**, 1660 (2000).
- [53] G. I. G. Griffiths, A. D. Fortes, C. J. Pickard and R. J. Needs, *J. Chem. Phys.*, **136**, 174512 (2012).
- [54] G. I. G. Griffiths, A. J. Misquitta, A. D. Fortes, C. J. Pickard and R. J. Needs, *J. Chem. Phys.*, **137**, 064506 (2012).
- [55] O. Kambara, K. Takahashi, M. Hayashi and J. -L. Kuo, *Phys. Chem. Chem. Phys.*, **14**, 11484 (2012).
- [56] M. K. Aydinol, J. V. Mantese and S. P. Alpay, *J. Phys.: Condens. Matter*, **19**, 496210 (2007).
- [57] H. M. Lu and J. R. Hardy, *Phys. Rev. B*, **44**, 7215 (1991).
- [58] O. M. Lovvik, T. L. Jensen, J. F. Moxnes, O. Swarg and E. Unneberg, *Comput. Mat. Sci.*, **50**, 356 (2010).
- [59] B. Santra, J. Klimes, D. Alfe, A. Tktchenko, B. Slater, A. Michaelides, R. Car and M. Scheffler, *Phys. Rev. Lett.*, **107**, 185701 (2011).
- [60] D. Lu, Y. Li, D. Rocca and G. Galli, *Phys. Rev. Lett.*, **102**, 206411 (2009).
- [61] M. Dion, H. Rydberg, E. Schroder, D. C. Langreth and B. I. Lundqvist, *Phys. Rev. Lett.*, **92**, 246401 (2004).
- [62] D. Liu, F. G. Ullman and J. R. Hardy, *Phys. Rev. B*, **45**, 2142 (1992).
- [63] D. W. James and W. H. Leong, *J. Chem. Phys.*, **49**, 5089 (1968).
- [64] F. Shimojo, Z. Wu, K. Nakano, R. K. Kalia and P. Vashishta, *J. Chem. Phys.*, **132**, 094106 (2010).
- [65] Z. Wu, R. K. Kalia, A. Nakano and P. Vashishta, *J. Chem. Phys.*, **134**, 204509 (2011).

High pressure structural, elastic, vibrational and detonation properties of ammonium based oxidizers

In the present chapter, structural, equation of state, hydrogen bonding, mechanical, IR spectra and detonation properties of ammonium nitrate (AN), ammonium perchlorate (AP) and ammonium dinitramide (ADN) have been discussed broadly.

6.1 Introduction

Investigation and development of low toxic and eco-friendly green energetic (primary, secondary explosives, oxidizers and propellants) materials is an active field of research over the last decade. Especially, usage of green oxidizers and propellants for pyrotechnic formulations prevents the environmental pollution [1]. AP has widespread applications in munitions, primarily as oxidizers for solid rocket and missile propellants, as an air-bag inflater in the automotive industry in fireworks and as a component of agricultural fertilizer [2]. However, AP produces HCl as a combustion product, 503 tonnes propellant liberates 100 tonnes of HCl and other chlorine containing compounds during its burning, thereby polluting the atmosphere and hence it could cause “Ozone layer depletion” in the stratosphere [3]. The large amount of HCl could cause “acid rain” and high concen-

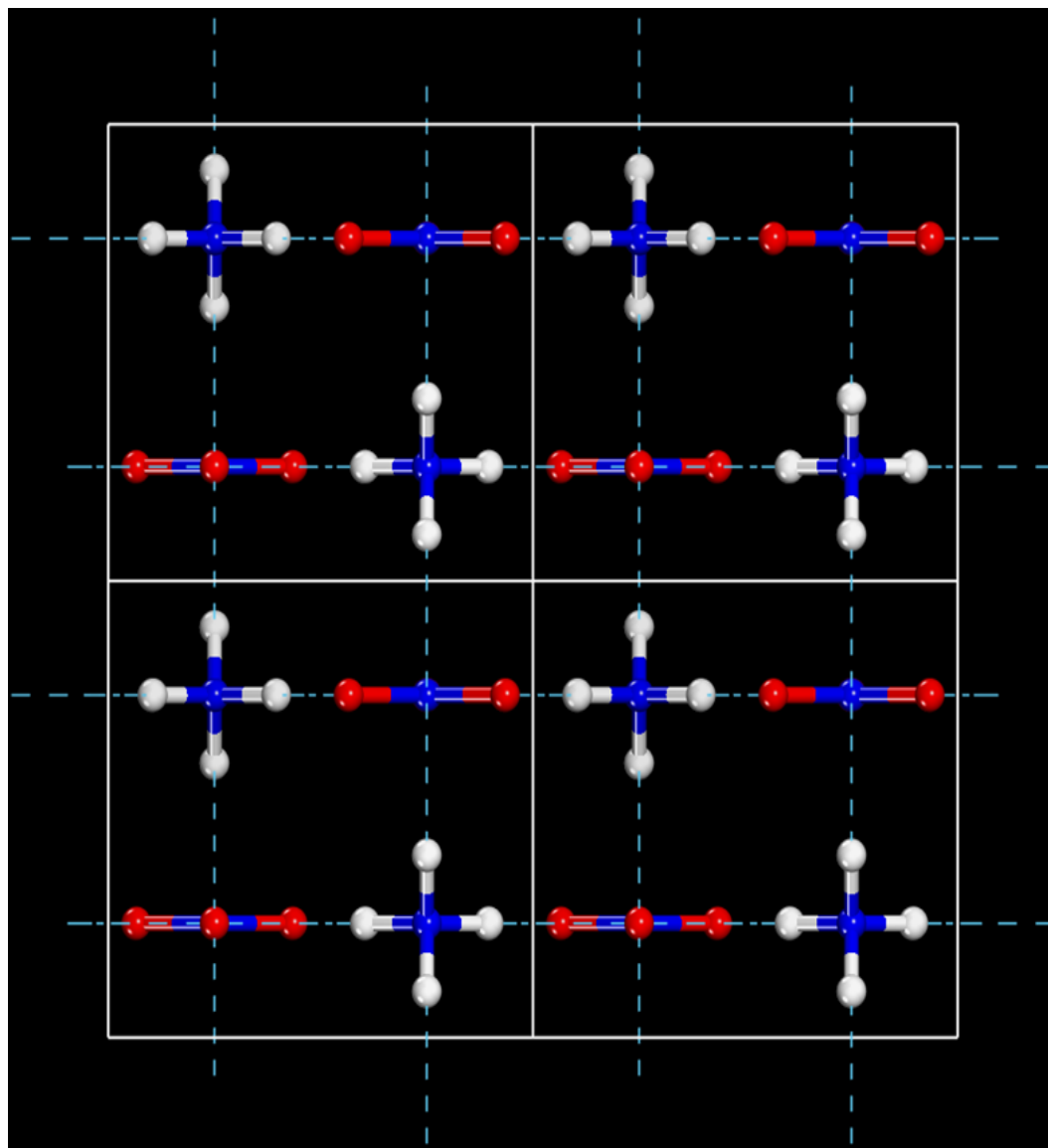


Figure 6.1: Two dimensional hydrogen bonding network in AN as viewed along ab-plane. White, blue and red color balls represent hydrogen, nitrogen and oxygen atoms, respectively.

trations of perchlorate can affect thyroid gland function [3]. An effective replacement for AP is AN. AN was considered to be an environment-friendly alternative to AP. AN has been widely used as fertilizer, blasting agent, solid oxidizer for rocket propulsion and military applications [4, 5]. Pure AN is used as an oxidizer rather than an explosive before it causes major explosive accidents. For instance, Cargo ship explosion at Texas city in 1947 and recently at a storage facility, AZF factory, Toulouse, France in 2001 [6]. AN is classified as a weak group II explosive [7]. AN has high oxygen balance, ecologically clean combustion products, very accessible, cheap and thermally stable. However, its extreme low enthalpy of formation and relatively low density prevents AN usage in solid composite propellants (SCP) [8]. Therefore, there is a considerable interest in finding environmentally benign replacements for the extensively used AP and AN. ADN has been identified as a promising new oxidizer for solid propellants because of its desirable properties namely low sensitivity of ammonium salts, high performance characteristics of nitramine compounds [9], high oxygen balance and free from chlorine atoms. Apart from this, a space shuttle can lift 8% more mass into orbit by using ADN as a propellant in comparison to AP [10].

High pressure/temperature polymorphs and structural phase transitions have wide ranging consequences on the fundamental properties of energetic molecular solids such as intermolecular interactions, chemical bonding, crystal structures and thermo-elastic properties [11]. Two different energetic polymorphs display distinct energetic performance attributing such as crystal density thereby changes in the detonation characteristics. Extensive reports are available in the literature on high temperature behavior and thermal decomposition of AN [Ref. [12] and Refs. therein], AP [13–15] and ADN [16–21]. At ambient pressure, AN exists in five different polymorphic phases in the temperature range 0–442 K. The detailed structural information of all the polymorphs is given in the Ref. [22] and the multiple structural phase transitions at low temperature precluded its usage in SCP applications [23]. Surprisingly very limited studies are available on high

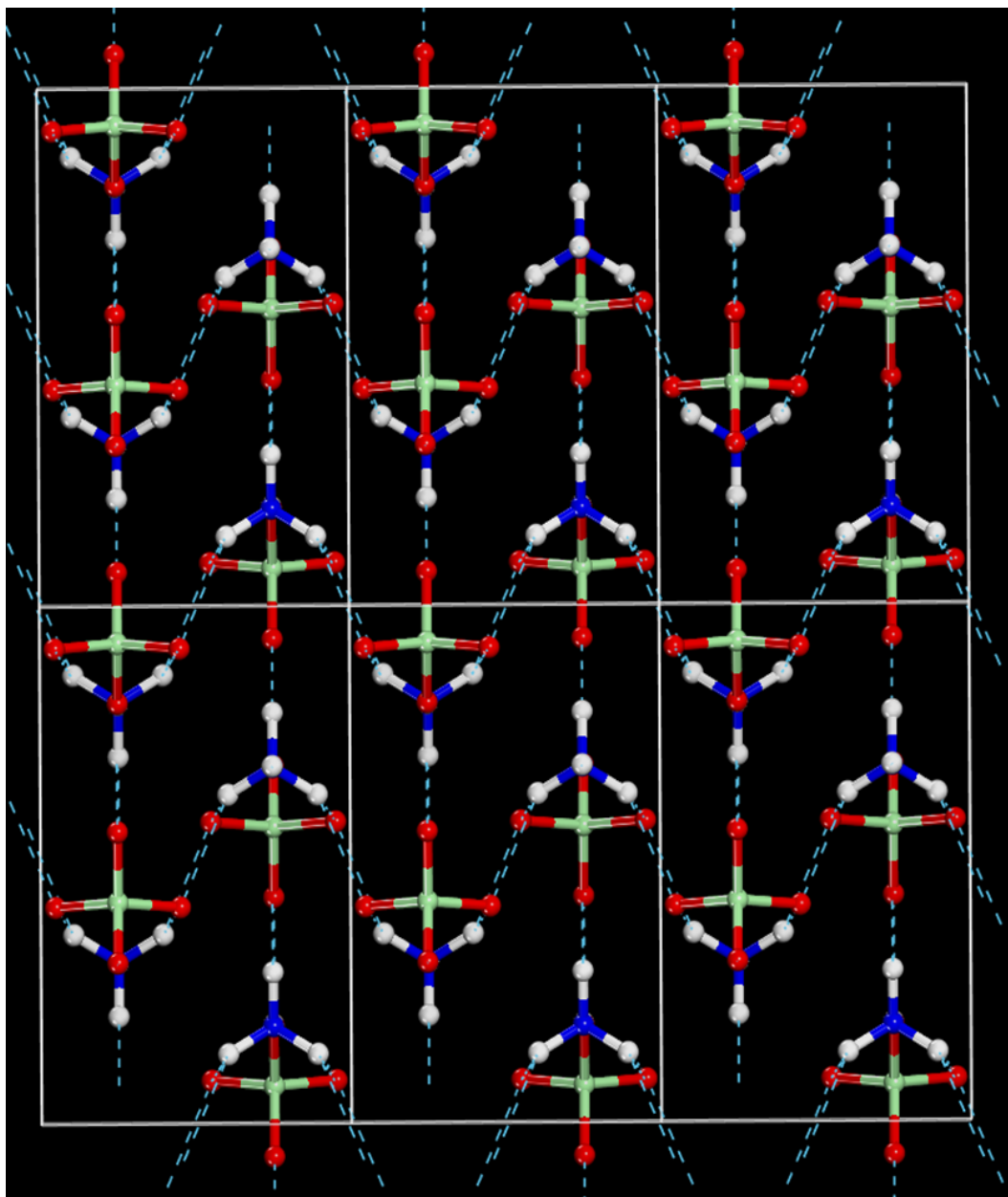


Figure 6.2: Periodic wave type hydrogen bonding network in AP as viewed along ab -plane. White, blue, red and light green color balls represent hydrogen, nitrogen, oxygen and chlorine atoms, respectively.

pressure-temperature (P-T) phase diagram of AN. Among all the low temperature polymorphs of AN, room temperature phase (AN-IV) is found to be stable up to 40 GPa under hydrostatic pressure and it undergoes a phase transition from phase IV \rightarrow IV' meta-stable phase between 17 and 28 GPa under non-hydrostatic conditions [11]. This work was further extended by Chellappa et al [24] up to 45 GPa and 467 K but no phase transition were observed under the studied hydrostatic pressure range. For AP, the most thorough studies to date are by Peiris et al [25] who investigated the pressure effects up to 5.6 GPa using X-ray diffraction, IR and Raman spectroscopy. They observed two first order phase transitions to occur at around 0.9 and 2.9 GPa pressures. But a recent neutron diffraction study revealed that AP undergoes a first order iso-structural phase transition to a more closely packed structure (phase-II) at 3.98 GPa and phase-II is stable up to 8.1 GPa *i.e.* highest pressure of the study [26]. In case of ADN, Russell et al [27] reported the P-T diagram up to 10 GPa and temperatures between 198-398 K, in which a reversible phase transition is observed from $\alpha \rightarrow \beta$ at about 2.0 GPa. In contrast to the previous measurements [27], α -ADN is found to be stable up to 4.03 GPa using powder X-ray diffraction study [28].

To complement the experimental studies, atomistic simulations are an effective way to model the crystal structures, physical and chemical properties of materials. Sorescu et al [22, 29] investigated structural and electronic properties of the polymorphic phases of AN (0-600 GPa) and ADN (0-300 GPa) using plane wave pseudo potential (PW-PP) approach at ambient as well as at high pressure without treating the intermolecular interactions. They found that the volume of AN-IV is compressed to 71 % when compared at 0 and 600 GPa and AN-IV ($Pm\bar{m}n$) transformed to monoclinic ($P2_1/m$) symmetry above 75 GPa [22]. While in the case of ADN, the ambient phase ($P2_1/c$) undergoes a structural transformation to triclinic ($P\bar{1}$) structure above 10 GPa [29]. Apart from this, Zhu et al [30] also made a comparative study of electronic, vibrational and thermodynamic properties between AP and ADN at ambient pressure. Further, they also investigated the effect

of hydrostatic pressure on structure, electronic and vibrational properties of AP [31]. However, the authors used incorrect crystal symmetry $Pna2_1$ rather than the correct crystal symmetry $Pnma$ in their calculations for AP [31]. The three examined compounds are ionic molecular solids, hence contribution towards intermolecular interactions from dispersion may be quite low but the ammonium cations and nitrate/perchlorate/dinitramide anions are linked through hydrogen bonding networks (see figures 6.1, 6.2 & 6.3). Therefore, it is worth while to investigate the structural, mechanical and dynamical stability for these materials by treating weak intermolecular interactions at ambient as well as at high pressure. With this motivation, in the present chapter, we have investigated the pressure dependent structural, elastic, vibrational and detonation properties of three compounds using dispersion corrected DFT-D methods as discussed in chapter 2.

6.2 Computational details

The first principles calculations were carried out with the projector augmented wave (PAW) method implemented in VASP package [32]. The generalized gradient approximation (GGA) in the Perdew-Burke-Ernzerhof parametrization was considered as the exchange-correlation functional [33]. Structural optimizations were achieved by setting the convergence criteria below 1.0×10^{-8} eV for total energies, residual forces to be less than 1.0×10^{-4} eV/Å and stresses are limited to 0.02 GPa. To correct the missing dispersion interactions, we have used several recently proposed methods such as PBE functional with atomic pair-wise potential methods D2 [34], TS [35], TS-SCS [36] and non-local density functional (vdW-DF) [37] methods as implemented in the VASP code. The density functional perturbation theory (DFPT) calculations are performed using plane wave pseudo potential (PW-PP) approach incorporated through CASTEP package [38]. Norm-conserving [39] PW-PPs were used to calculate the lattice dynamical properties. A kinetic energy cutoff of 950 eV and $2\pi \times 0.04$ Å⁻¹ separation of k-mesh according

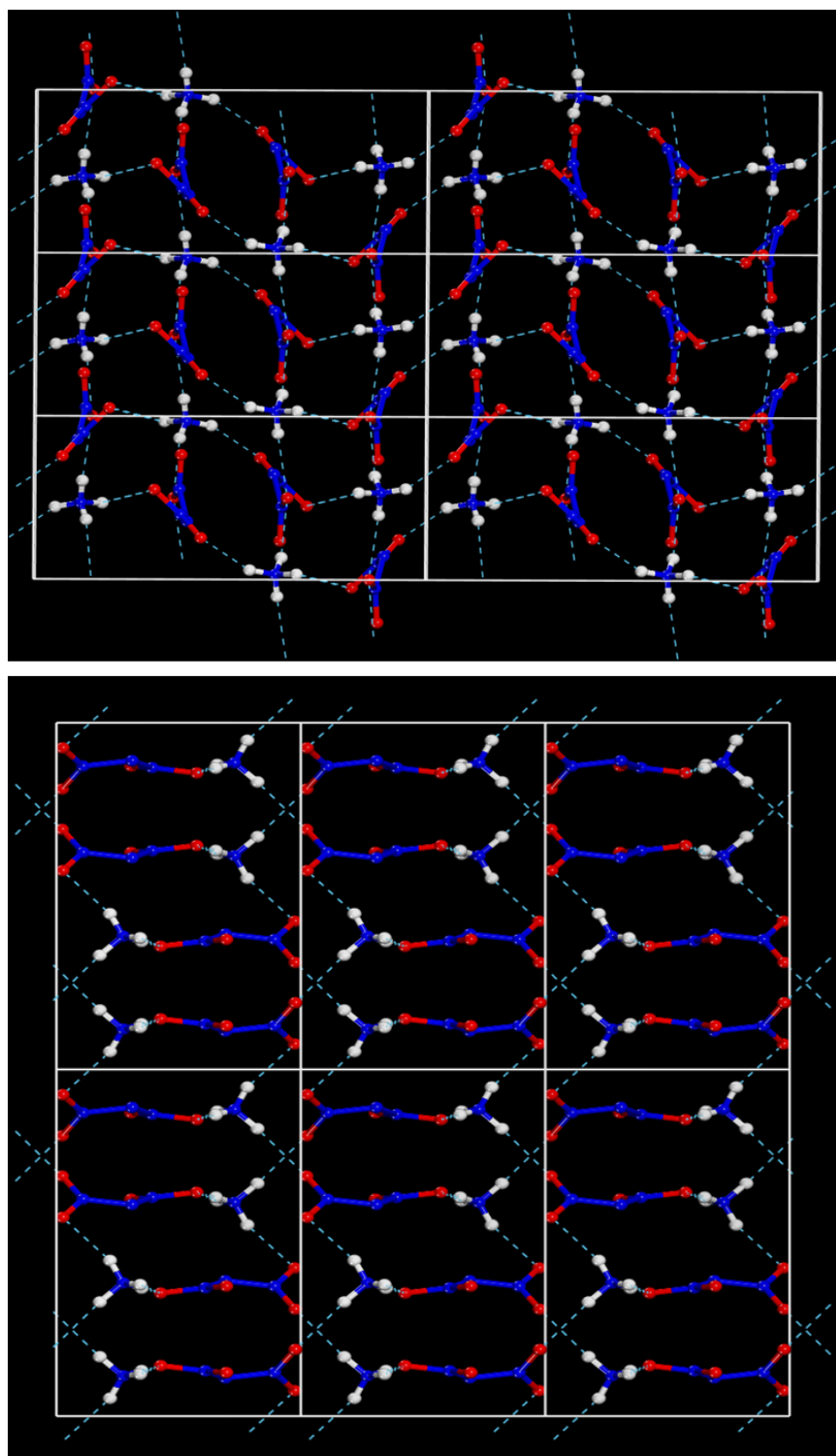


Figure 6.3: Three dimensional hydrogen bonding network in ADN as viewed along bc (top) and ab (bottom)-planes. White, blue and red color balls represent hydrogen, nitrogen and oxygen atoms, respectively.

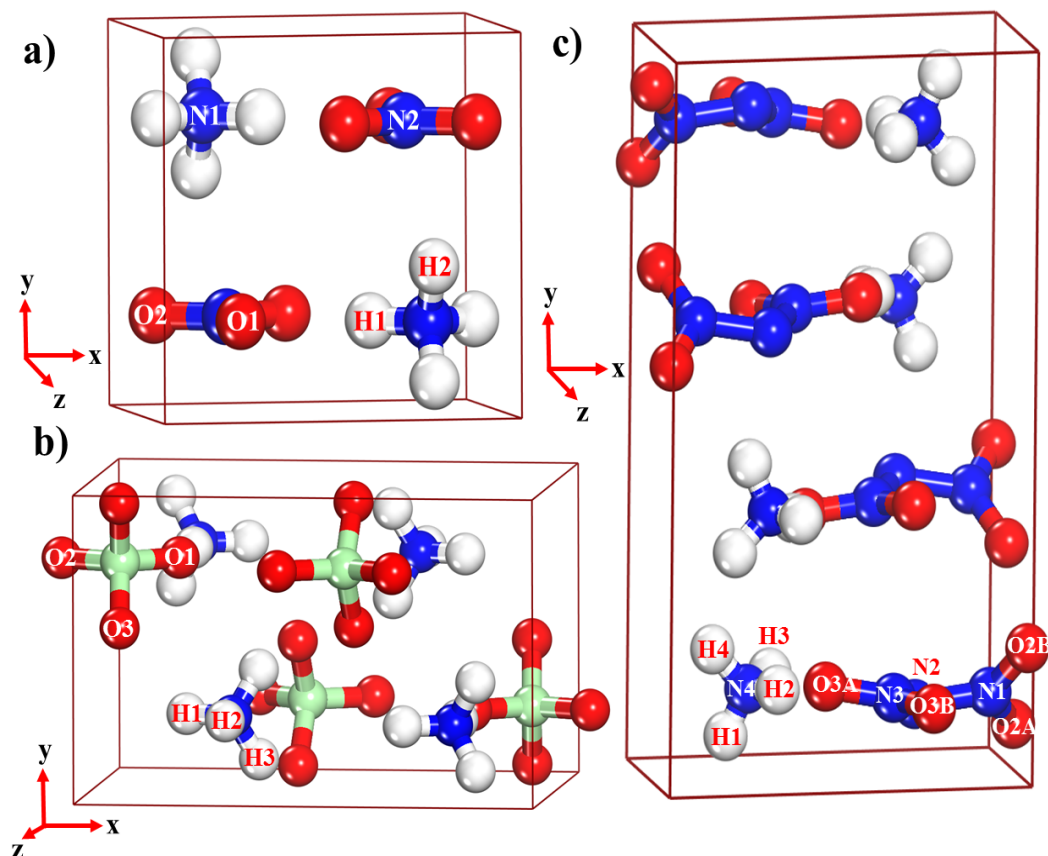


Figure 6.4: Crystal structures of a) AN b) AP and c) ADN.

to the Monkhorst-Pack grid scheme were used in the calculations [40]. The self-consistent energy convergence was set to 5.0×10^{-6} eV/atom. The convergence criterion for the maximum force between atoms was 0.01 eV/Å. The maximum displacement and stress were set to be 5.0×10^{-4} Å and 0.02 GPa, respectively.

6.3 Results and discussion

6.3.1 Crystal structure and equation of state

As discussed in section 6.1, AN exhibits rich polymorphism below its melting temperature (442 K). In particular, among the five polymorphs, the ordered room

temperature phase-IV has received much attention recently. AN-IV (hereafter denoted as AN) crystallizes in the orthorhombic $Pm\bar{m}n$ symmetry with $Z=2$ at ambient conditions [41]. The crystal structure of AN consists of infinite parallel chains $N1-H1...O1...H1-N1$ with $H1...O1 = 2.05 \text{ \AA}$ and these chains are linked by weaker hydrogen bonds $N1-H2...O1$ with $H2...O1 = 2.16 \text{ \AA}$ to form infinite sheets bound together by van der Waals forces parallel to (001) plane by forming a two dimensional hydrogen bonding network as shown in figure 6.1. Also, the bond length $N2-O1 = 1.266 \text{ \AA}$ is longer than $N2-O2 = 1.223 \text{ \AA}$, which is due to the fact that O1 is involved in four strong hydrogen bonds whereas O2 is in one weaker hydrogen bond [41]. Peyronel et al [42] determined the crystal structure of AP as orthorhombic with space group $Pna2_1$ which is in contrast to the previously reported space group $Pnma$ [43]. Later, Chio et al [44] re-determined the crystal symmetry of AP and they observed that AP crystallizes in the $Pnma$ space group with four molecules per unit cell which is in contradiction to the previously determined space group $Pna2_1$ [42] at ambient conditions. Recently, Davidson et al [26] revisited the crystal structure of AP using X-ray and Neutron powder diffraction techniques and they confirmed that AP crystallizes in the $Pnma$ orthorhombic crystal symmetry. In $Pnma$ symmetry, the four oxygen atoms attached to the chlorine atom are involved in the hydrogen bonding through three inequivalent hydrogen atoms; H1 and H2 atoms form a single hydrogen bond whereas H3 atoms are involved in two hydrogen bonds by forming a periodic wave type hydrogen bonding network with neighboring oxygen atoms as depicted in figure 6.2.

Gilardi et al [45] reported that ADN crystallizes in the primitive monoclinic structure having space group $P2_1/c$ with $Z=4$ at ambient conditions. In contrast to AN and AP, the hydrogen bonds in ADN are directed tetrahedrally to form a three dimensional network. ADN contains two independent three dimensional networks of hydrogen bonds [45]. The first one involves a hydrogen bonding chain propagating along c-axis by connecting one of the nitro group ($N3-O3A-$

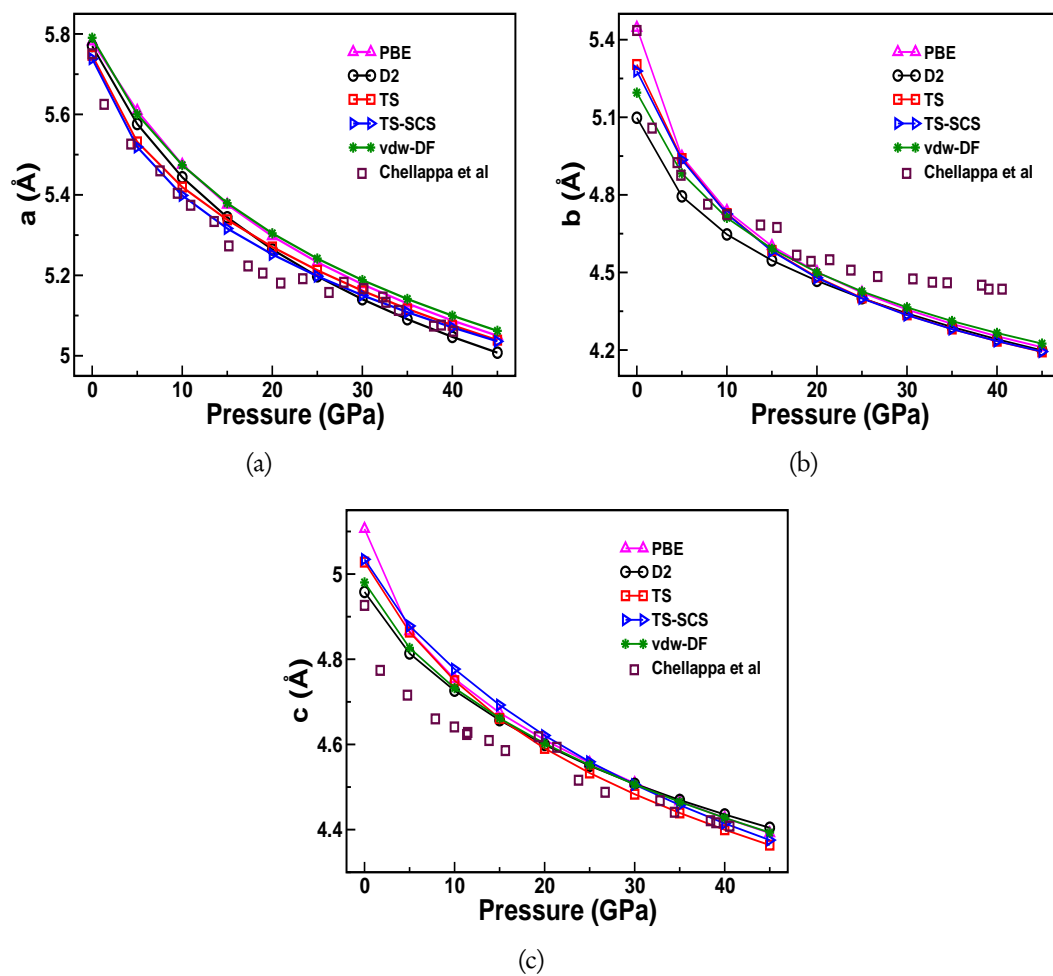


Figure 6.5: Calculated lattice constants of AN as a function of pressure up to 45 GPa using various dispersion correction methods. Experimental data is taken from the Ref. [24]

O3B) of the anion via O3A to hydrogen atoms H2 and H3 of the NH_4 cation. The second one, other nitro group of the anion consists of twisted O2A which is out of plane for first nitro group of the anion to form hydrogen bonding through H1 and H4 atoms and the adjacent layers of cation form an helical structure along b-axis. The two inter-penetrating patterns form two independent three dimensional hydrogen bonding networks as presented in figure 6.3. Also, the crystal structures and atomic labels corresponding to each in equivalent atom in the unit cell of AN, AP and ADN were given in figure 6.4.

By considering the experimental data as an input, we performed full structural optimization of both lattice constants and fractional co-ordinates within PBE-GGA and various dispersion correction (DFT-D2, vdW-TS, TS-SCS and vdW-DF) methods. The obtained equilibrium volumes without dispersion correction (DC) methods are overestimated by around 4.4, 7.5 and 13.2 % for AN, AP and ADN, respectively. While the predicted volumes using empirical and non-empirical DC methods are found to differ by -5.3, -3.5 and +0.01 % using DFT-D2; -0.5, +0.2 and +4.0 % using vdW-TS; -1.0, +0.1 and +5.1 % using TS-SCS; and -2.7, -2.2 and +0.003 % using vdW-DF, for AN, AP and ADN, respectively. Here '-' and '+' represent under and overestimation of equilibrium volume when compared to the experiments [26, 41, 45]. Cancellation of errors by under and overestimating the lattice constants lead to the prediction of equilibrium volume closely comparable with the experiments for AN, AP and ADN using vdW-TS, TS-SCS and DFT-D2 methods, respectively as previously reported for AP using various DC methods [26].

Further the optimized ground state structures at ambient pressure were used to perform high pressure calculations for AN (0-45 GPa insteps of 5 GPa), AP (0-4 GPa insteps of 0.5 GPa) and ADN (0-5 GPa insteps of 0.5 GPa). For AN, the high pressure behavior of lattice constant 'a' is in good accord with experimental results whereas lattice constants 'b' and 'c' show low and high compressible nature above and below 20 GPa, respectively as shown in figure 6.5. The 'b' and 'c' lat-

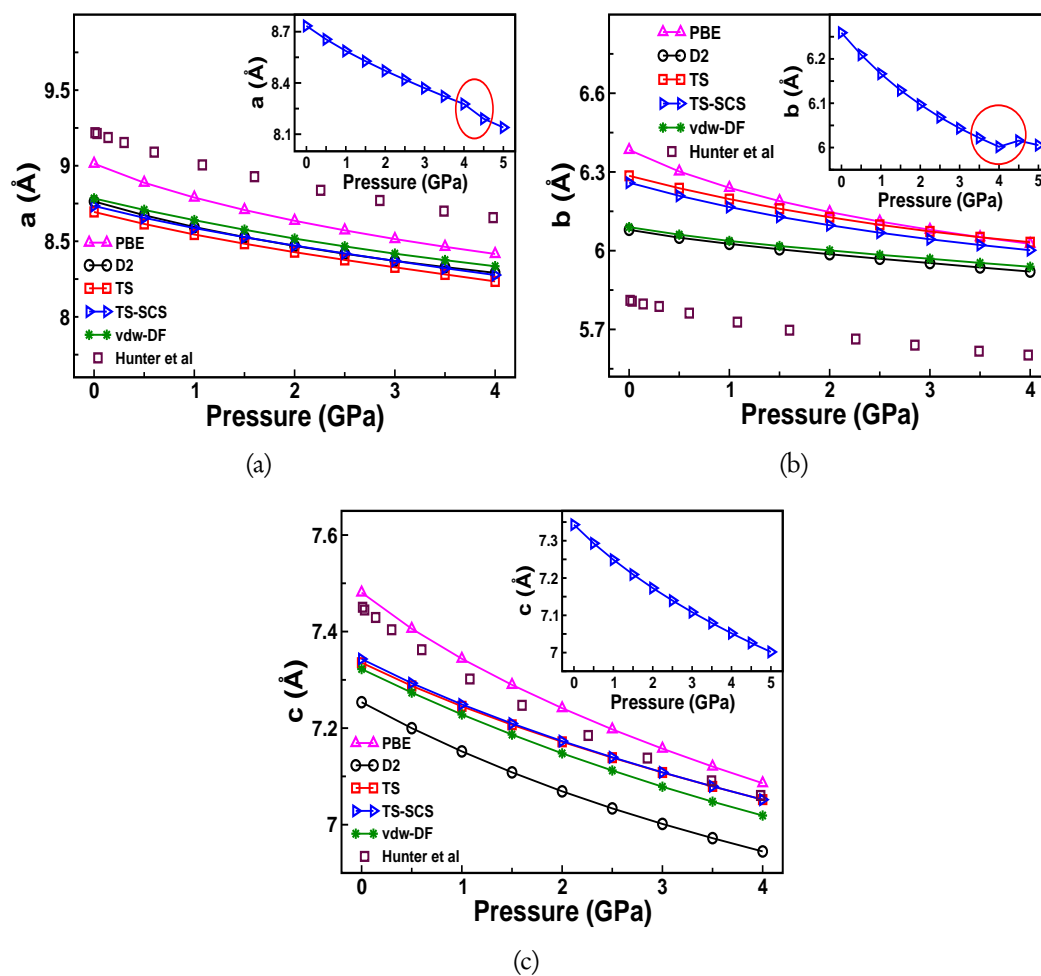


Figure 6.6: Calculated lattice constants of AP as a function of pressure up to 4 GPa using various dispersion correction methods. Inset figures show the obtained lattice constants under pressure up to 5 GPa using TS-SCS method. Experimental data is taken from the Ref. [26].

tice constants are converging at around 10 GPa and then start diverging up to the maximum studied pressure range, this behavior is not seen in the powder X-ray diffraction study by Davidson et al [11] up to 20 GPa. Using synchrotron X-ray diffraction measurements, Chellappa and co-workers [24] observed that the lattice parameters converge in length and remain close to each other beyond 20 GPa. In case of AP, the lattice constants ‘a’ and ‘b’ are strongly over- and under-binded, respectively whereas lattice constant ‘c’ follows the behavior of PBE curve (see figure 6.6) throughout the studied pressure range. The observed trends are consistent with the recent theoretical calculations by Davidson et al [26]. Apart from this, we could see a discontinuity in the lattice parameters ‘a’ and ‘b’ as a function of pressure *i.e.* lattice constant ‘a’ further decreases whereas lattice constant ‘b’ increases with pressure which supports a first order structural phase transition in AP as observed in the experiments [26].

Also, the computed lattice constants for ADN are found to decrease monotonically with pressure up to 5 GPa. Overall, the calculated lattice constants are decreasing monotonically below transition pressure for all these compounds (except the monoclinic angle (β) of ADN which is increasing with pressure as depicted in figure 6.7) in the above mentioned pressure range. Russell et al [27] reported the P-T phase diagram of ADN using Energy dispersive X-ray diffraction and Raman spectroscopic measurements under pressure up to 10 GPa and they claimed that ambient phase of ADN (α -ADN) transforms to β -ADN phase through a first order polymorphic phase transition around 2 GPa. However, Davidson and co-workers [28] revisited the high pressure behavior of ADN using a combination of X-ray and Neutron powder diffraction techniques and found that ADN is quite stable up to 4.03 GPa. From the theoretical perspective, without treating intermolecular interactions, Sorescu et al [29] predicted that ADN is stable up to 10 GPa and it transforms from monoclinic ($P2_1/c$) to triclinic symmetry ($P\bar{1}$) above 10 GPa. There exists an inconsistency between various studies regarding the high pressure behavior of ADN. In order to resolve this issue, we have extended our

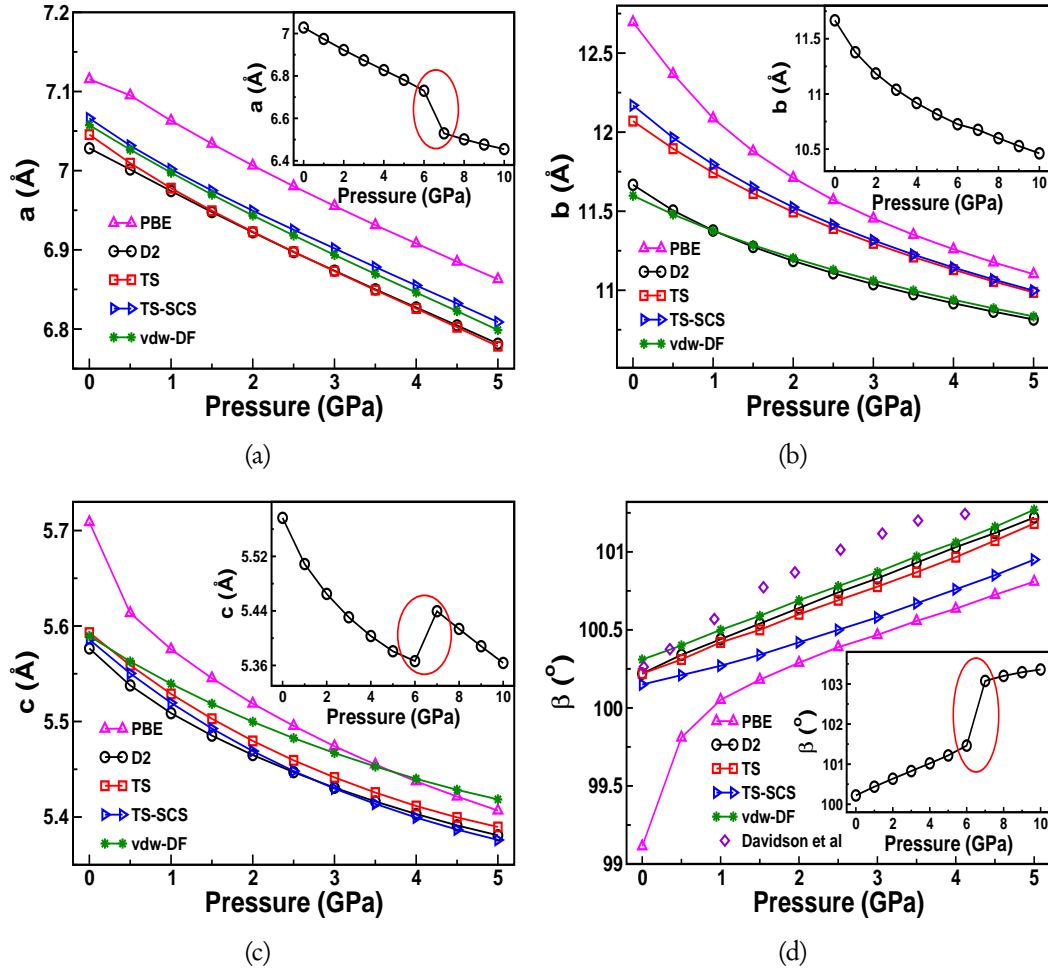


Figure 6.7: Calculated lattice constants of ADN as a function of pressure up to 5 GPa using various dispersion correction methods. Inset figures show the obtained lattice constants under pressure up to 10 GPa using DFT-D2 method. Experimental data is taken from the Ref. [28].

pressure range from 5-10 GPa for ADN using DFT-D2 method. As illustrated in the inset of figure 6.7, we could see a discontinuity in the lattice constants ‘a’, ‘c’ and monoclinic angle β whereas lattice constant ‘b’ exhibits monotonic behavior as a function of pressure up to 10 GPa. These results may suggest first order structural phase transition in ADN around 6 GPa.

Apart from this, we have also calculated the normalized lattice constants and presented the same in figure 6.8; the lattice constants **a**, **b** and **c** shrink with different compressibilities 87.7, 79.0 and 86.7 % for AN (0-45 GPa), 94.8, 95.9 and 96.0 % for AP (0-4 GPa) and 96.5, 92.70 and 96.49 % for ADN (0-5 GPa), respectively. The calculated axial compressibilities for ADN are found to be consistent with the X-ray powder diffraction study [28]. Also, the axial compressibilities show that b-axis is the most compressible over a- and c-axes for both AN and ADN compounds whereas a-axis is the most compressible one for AP, which are due to weaker intermolecular interactions (van der Waals and/or hydrogen bonding) along the b- and a-axes for AN, ADN and AP, respectively. As illustrated in figure 6.9, the volume is decreasing with pressure and we observe a discontinuity in the pressure-volume curve in the pressure range 6-7 GPa for ADN. In addition, we have also calculated the equilibrium bulk modulus (B_0) and its pressure derivative (B'_0) by fitting the pressure-volume data of AN (0-45 GPa), AP (0-4 GPa) and ADN (0-5 GPa) to 3rd order Birch-Murnaghan equation of state [46]. The obtained B_0 and B'_0 values using PBE and various DC methods are presented in Table 6.1 along with the experimental results [11, 24–26, 28, 47]. It is found that the obtained B_0 and B'_0 values fall in the range of experiments and are also consistent with the available theoretical calculations [22, 26, 29]. These results reveal that the three investigated compounds are soft materials but harder than the conventional secondary explosives [48–50].

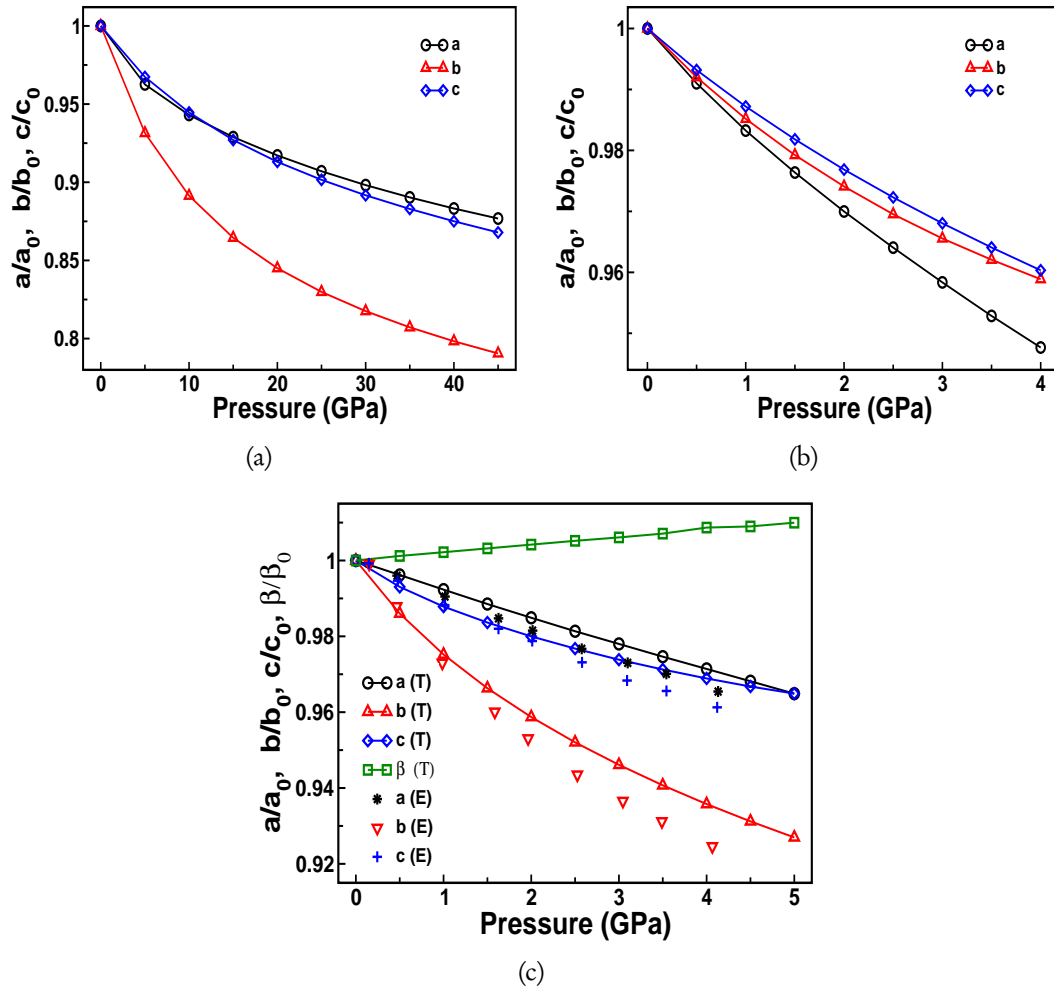


Figure 6.8: Calculated normalized lattice constants of (a) AN (0-45 GPa), (b) AP (0-5 GPa) (c) (0-5 GPa) ADN as a function of pressure. Experimental data is taken from the Ref. [28]. Here T and E represent theory and experiment, respectively.

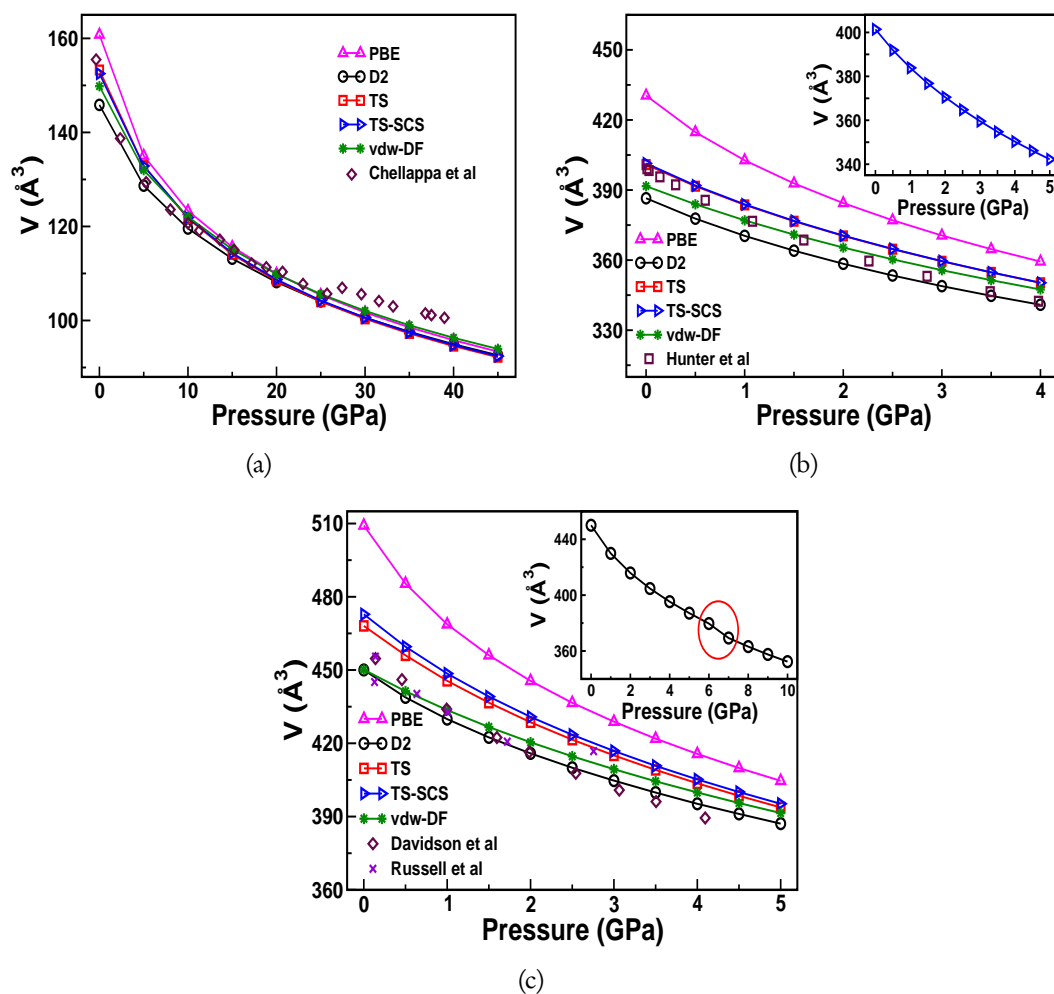


Figure 6.9: Calculated volume of (a) AN (0-45 GPa), (b) AP (0-5 GPa) (c) (0-5 GPa) ADN as a function of pressure. Inset shows the obtained volume under pressure up to 5 and 10 GPa using TS-SCS and DFT-D2 method for AP and ADN, respectively. Experimental data is taken from the Refs. [24, 26, 28].

Table 6.1: Calculated structural properties volume (V_0 , in \AA^3), bulk modulus (B_0 , in GPa) and its pressure derivative (B'_0) of AN, AP and ADN using standard PBE-GGA functional and various dispersion corrected DFT-D methods.

Compound	Method	V_0	B_0	B'_0
AN	PBE	160.78	17.96	5.68
	D2	145.85	30.89	5.11
	TS	153.26	23.76	5.06
	TS-SCS	152.51	25.11	5.03
	vdW-DF	149.82	29.05	5.10
	Expt.	154.3955 ^a , 153.89 ^b	15.7 ^a , 14.0 ^a , 20.1 ^a , 10.69 ^b , 16.6 ^c	9.4 ^a , 10.8 ^a , 4.55 ^a , 7.7 ^{b,c}
AP	Others	152.9 ^c	23.6 ^d	5.0 ^d
	PBE	154.4 ^d	11.93	7.07
	D2	430.46	20.03	7.63
	TS	386.46	19.69	5.81
	TS-SCS	401.42	20.08	5.82
	vdW-DF	400.87	23.45	5.91
ADN	Others	391.67	11.96 ^e , 19.91 ^e , 20.5 ^e	7.12 ^e , 5.96 ^e , 7.53 ^e
	Expt.	426.87 ^e , 397.53 ^e , 382.50 ^e	14.91 ^e , 12.2 ^g	7.32 ^e , 12.1 ^h
	PBE	399.33 ^e , 400.48 ^f	8.54	8.91
	D2	509.48	18.48	8.20
	TS	450.03	17.70	5.70
	TS-SCS	468.09	16.20	6.14
Others	vdW-DF	472.83	24.13	5.67
	Others	450.15	20.65 ^b	4.03 ^b
	Expt.	450.0 ⁱ , 456.6 ^c	16.4 ^c	6.5 ^c

^aRe.[24], ^bRef.[11], ^cRef.[28], ^dRef.[22], ^eRef.[26], ^fRef.[47], ^gRef.[25], ^hRef.[29], ⁱRef.[45]

6.3.2 Hydrogen bonding under pressure

As discussed in the above section, hydrogen bonding plays a vital role in the structural properties of all the three examined compounds. In order to understand the effect of pressure on hydrogen bonding, we have plotted the intermolecular normalized hydrogen bond parameters (bond lengths and angles) as a function of pressure as depicted in figure 6.10. As illustrated in figure 6.10a&b, H2...O1 bond of AN is found to be relatively more compressible when compared to H1...O1 and H1...O2 bonds and the corresponding bond angle N1-H2...O1 is increasing whereas remaining two bond angles namely N1-H1...O1 and N1-H1...O2 are decreasing with pressure. Also, the more compressible nature of H2...O1 bond (see figure 6.10a) is responsible for high compressibility of AN lattice along the crystallographic **b**-direction (see figure 6.8a). In case of AP, the intermolecular hydrogen bonds are found to decrease monotonically with pressure. As pressure increases, a new H3...O3' intermolecular hydrogen bond has been established to form a rectangular periodic wave type hydrogen bonding network with the neighboring hydrogen bonds, H3...O3 along the **b**-axis (see figure 6.2). The high compressibility of AP lattice along **a**-direction is due to the large compressible nature of H1...O2 and H3...O3 intermolecular hydrogen bonds. While the intermolecular hydrogen bond angles N-H1(2)...O1(2) increases with pressure towards forming a linear hydrogen bonding. However, N-H1...O2 bond angle decreases in the pressure range 3-5 GPa. The N-H3...O3(3') bond angle decreases whereas N-H3...O3 bond angle increases above 3 GPa as shown in figure 6.10c&d. In case of ADN, H3...O3A and H4...O2B intermolecular bonds are more compressible over H1...O2A and H2...O3A bonds. Similar to AN lattice, ADN lattice is found to be more compressible along crystallographic **b**-direction which is due to large compressibility (mainly arises from H4...O2B) of helical structured hydrogen bonding network along the **b**-axis (see figure 6.3). In addition, we also observe sharp discontinuities in the hydrogen bond lengths and angles in the pressure range between 6-7 GPa

for ADN. The sharp increase in hydrogen bond lengths lead to weakening of hydrogen bonding which may further drives structural instability in this pressure range.

6.3.3 Elastic constants and mechanical stability

Elasticity is a fundamental property of materials to examine mechanical response to the applied stress. Quantifying and understanding the elastic properties of energetic materials is important to have a basic knowledge about the intermolecular interactions thereby stiffness of the materials. It has been previously reported [51] that stiffer the lattice less sensitive it becomes to detonation from a mechanical shock initiation. Several investigations were carried out to measure the elastic stiffness constants for the well known secondary explosives namely RDX [51], HMX [52, 53], PETN [54] and CL-20 [55]. These studies reveal that overall RDX is the stiffest lattice which indicates the relative insensitiveness of RDX when compared to HMX, PETN and CL-20. On the similar path, to understand the mechanical response and stiffness of the three examined solid energetic oxidizers, in the present work, we have calculated the elastic stiffness constants for AN, AP and ADN. It is well known from single crystal X-ray diffraction measurements [26, 41, 45], that AN, AP and ADN crystallize in the orthorhombic and monoclinic structure at ambient conditions, respectively. Correspondingly AN, AP and ADN have nine and thirteen independent elastic constants. The obtained elastic constants at ambient pressure are given in Table 6.2 along with the available experimental data for AP [56, 57]. There is a good agreement between the calculated ones and experimental results [56, 57]. Also the calculated elastic constants meet the well known Born's stability criteria indicating that the investigated compounds are mechanically stable at ambient pressure. In addition, the three diagonal elements can be used to correlate with the intermolecular interactions along three crystallographic directions. Based on the measured stiffness constants, Haycraft [55] reported that CL-20 should be most sensitive to detona-

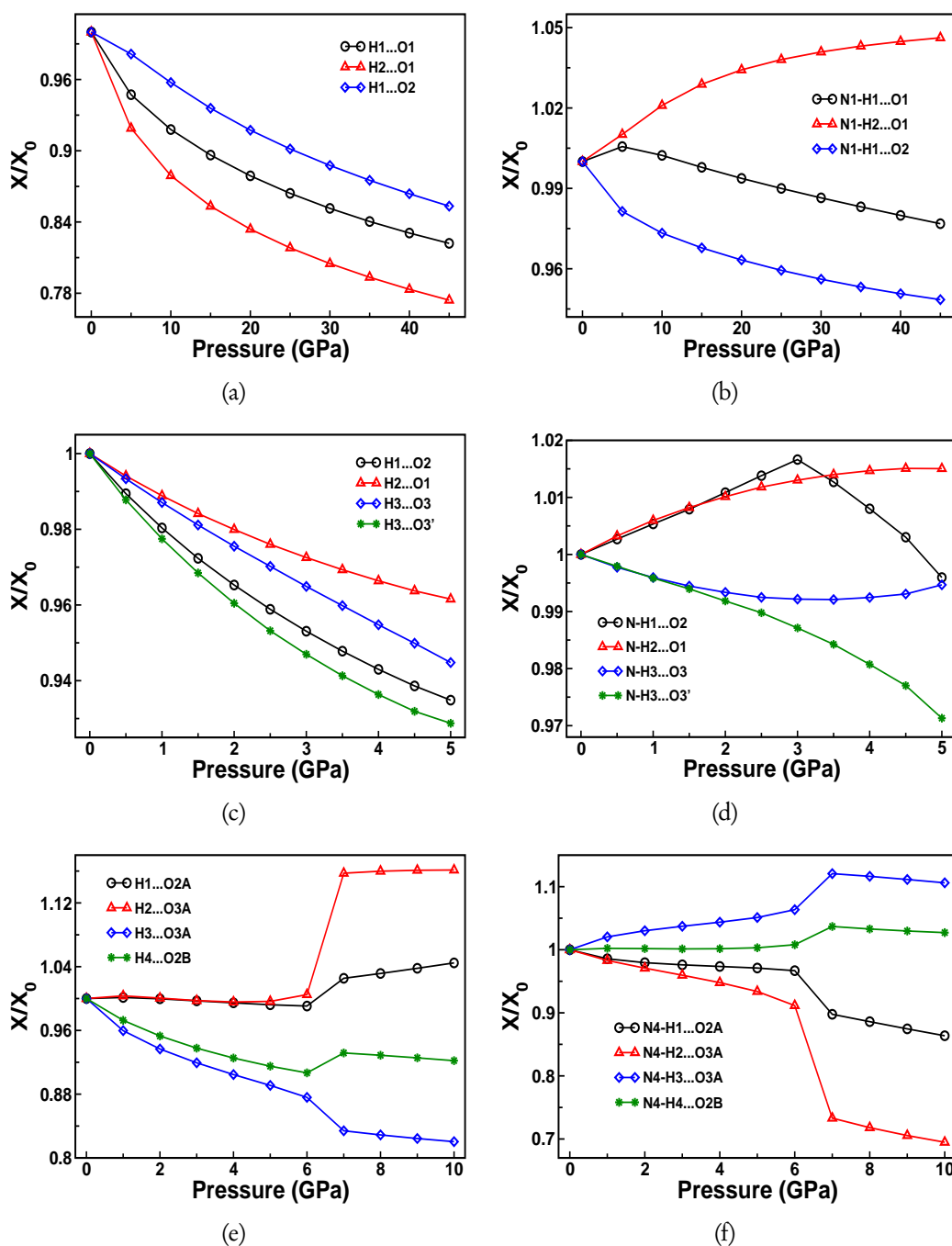


Figure 6.10: Calculated intermolecular hydrogen bond lengths (a, c, e) and angles (b, d, f) of (a,b) AN, (c,d) AP and (e,f) ADN as a function of pressure. Where X_0 and X represent obtained bond parameters at ambient and as a function of pressure, respectively.

tion along a-axis and least sensitive along b-axis. Also it is observed that C_{11} is the stiffest elastic constant for PETN which makes PETN to be least sensitive along [100] direction [54]. Similarly the calculated ordering of diagonal elastic constants for the three investigated compounds as follows; $C_{33} > C_{11} > C_{22}$ for AN, $C_{33} > C_{22} > C_{11}$ for AP and $C_{11} > C_{33} > C_{22}$ for ADN. The elastic constant C_{33} is much higher than C_{11} & C_{22} , while C_{11} & C_{22} differ by ~ 2 GPa for AN. The experimental [57] trend $C_{33} > C_{22} > C_{11}$ is followed for AP which is in contrast to the trend $C_{33} > C_{11} > C_{22}$ followed by other experimental work of Vazquez et al [56]. However, the difference in the order is only for C_{11} & C_{22} which are closely comparable in magnitude with each other. C_{11} is found to be the stiffest elastic constant for ADN whereas C_{33} for AN and AP, which is due to strong intermolecular interactions along a-axis for ADN and along c-axis for AN and AP. This implies that ADN is less sensitive to detonation along [100] direction similar to that of PETN [54] while AN and AP are found to be least sensitive along [001] direction. The lower elastic moduli and high compressibilities reveal that AN, ADN and AP are most sensitive to detonation along **b**- and **a**-axis, respectively.

Furthermore to understand the mechanical stability under hydrostatic pressure, we have also calculated the elastic constants as a function pressure and are depicted in figure 6.11 for the three examined compounds. The nine independent elastic constants are increasing with progression of pressure for AN and AP, with an exception C_{11} which increases up to 4 GPa and it becomes softer in the pressure range of 4-5 GPa for AP. This may be due to the structural transition observed around 4 GPa in the experiments [26]. As illustrated in figure 6.11c, 11 out of 13 elastic constants are increasing with pressure while the remaining two C_{66} and C_{46} are softening under compression for ADN. In addition, we also observe the discontinuities in the elastic stiffness constants for C_{11} and C_{33} as a function of pressure which are reflected from the pressure dependent lattice constants and bond parameters. These results indicate a possible structural phase transition in ADN around 6 GPa.

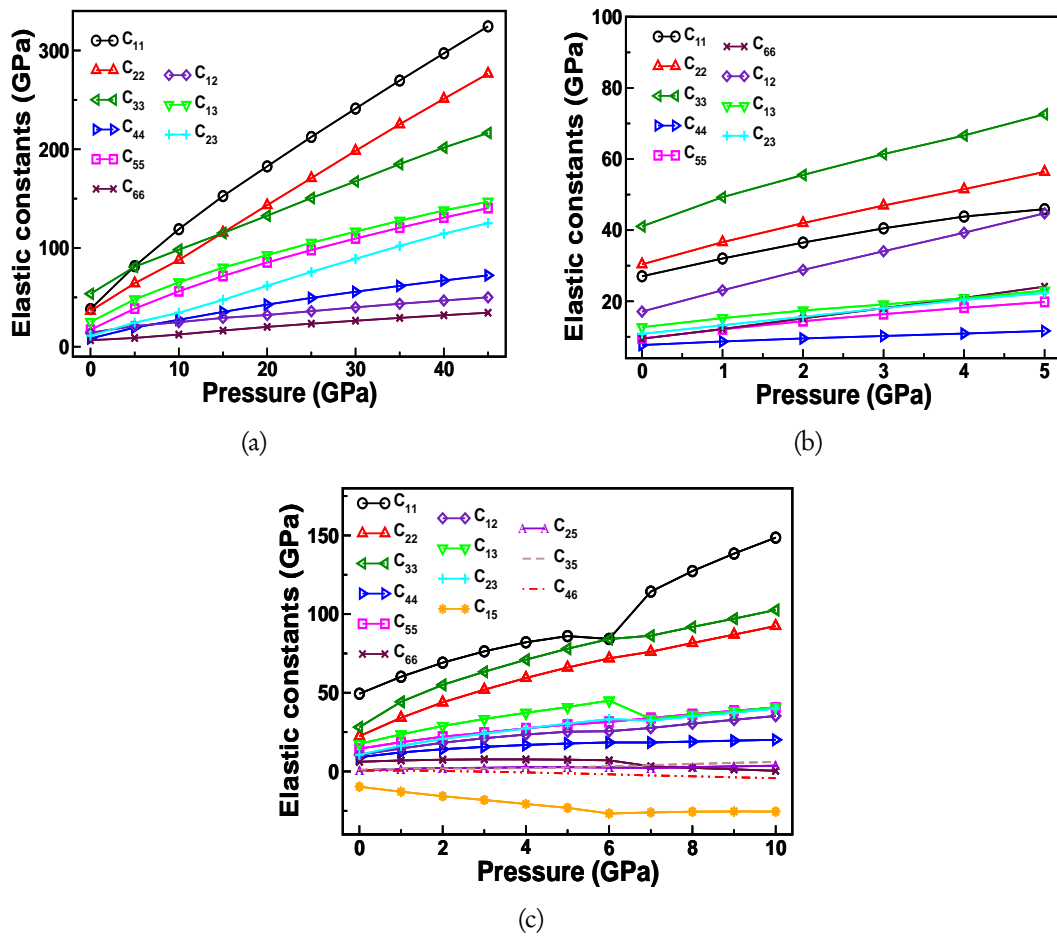


Figure 6.11: Calculated elastic constants of a) AN (0-45 GPa) b) AP (0-5 GPa) and c) ADN (0-10 GPa) as a function of pressure.

Table 6.2: Calculated elastic constants (C_{ij} , in GPa) of AN, AP and ADN using TS, TS-SCS and D2 equilibrium volume, respectively. Experimental data is taken from Refs. [56, 57] for AP.

Parameter	AN	AP	ADN
C_{11}	38.1	27.0 (25.1 ^a , 22.97 ^b)	49.4
C_{22}	36.2	30.4 (24.6 ^a , 23.56 ^b)	22.4
C_{33}	53.6	41.1 (31.5 ^a , 30.12 ^b)	28.2
C_{44}	8.4	7.7 (6.6 ^a , 4.69 ^b)	9.1
C_{55}	17.2	9.5 (4.7 ^a , 5.84 ^b)	14.4
C_{66}	6.6	9.5 (10.3 ^a , 9.64 ^b)	6.2
C_{12}	14.2	17.1 (16.3 ^a , 16.60 ^b)	10.6
C_{13}	25.1	12.7 (11.5 ^a , 7.35 ^b)	17.6
C_{23}	11.2	10.8 (7.6 ^a , 10.33 ^b)	10.7
C_{15}	-	-	-9.7
C_{25}	-	-	0.6
C_{35}	-	-	1.0
C_{46}	-	-	0.6

^aRe.[56], ^bRef.[57]

6.3.4 Zone center phonons at ambient pressure

In order to explore the dynamical stability, we have first calculated the zone center phonon frequencies for the three investigated compounds. AN, AP and ADN possess orthorhombic ($Pmnm$ for AN and $Pnma$ for AP) and monoclinic ($P2_1/c$) symmetries with 2, 4 and 4 molecules per unit cell respectively, which result in 54, 120 and 144 vibrational modes at center of the Brillouin zone. The symmetry decomposition of the vibrational modes for the studied compounds is as follows:

$$\Gamma_{tot}^{AN} = 9B_{1u} \oplus 7B_{2u} \oplus 8B_{3u} \oplus 3B_{1g} \oplus 8B_{2g} \oplus 7B_{3g} \oplus 9A_g \oplus 3A_u$$

$$\Gamma_{tot}^{AP} = 18B_{1u} \oplus 12B_{2u} \oplus 18B_{3u} \oplus 12B_{1g} \oplus 18B_{2g} \oplus 12B_{3g} \oplus 18A_g \oplus 12A_u$$

$$\Gamma_{tot}^{ADN} = 36A_u \oplus 36B_u \oplus 36A_g \oplus 36B_g$$

The first two optical phonon modes of AN are found to be imaginary with $Pmnm$ crystal symmetry and are consistent with the previously reported calculations of Witko et al [58] and they proposed that AN (phase-IV) actually crystallizes in the $Pmn2_1$ space group rather than $Pmnm$. Later on, Bourahla et al [59] reported

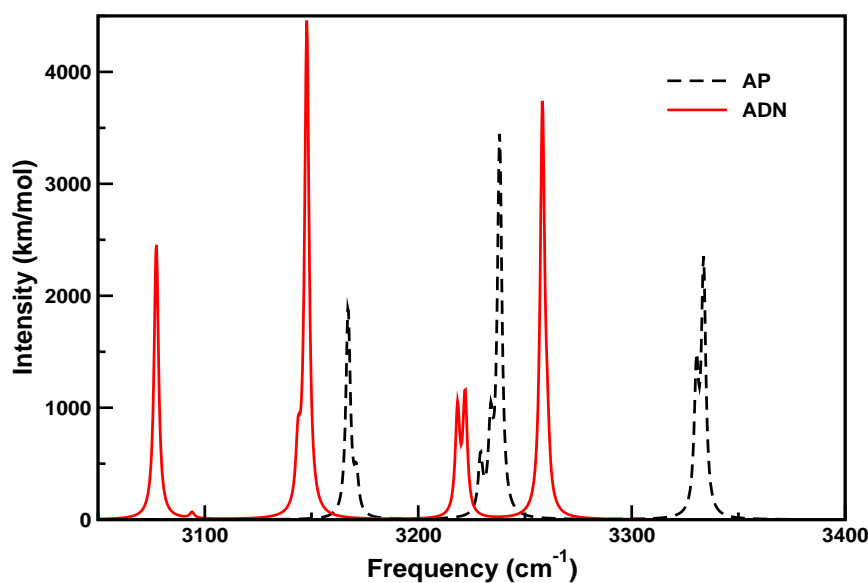


Figure 6.12: Calculated IR spectra of AP and ADN in the near IR region at ambient pressure.

all the optical phonon modes to be positive by indicating the dynamical stability of AN at Γ -point using CRYSTAL package. Therefore, the results impose a question, regarding the stability of the $Pm\bar{m}n$ crystal symmetry, which further warrants a detailed structural analysis from both experiments and theory. All the optical phonon modes are found to be real for both AP and ADN. Earlier, Zhu et al [30, 31] made a detailed vibrational analysis of each vibrational mode for AP (using different space group *i.e.* $Pna2_1$) and ADN compounds. In the present calculations, we have used the correct space group $Pnma$ for AP. The detailed vibrational spectra analysis of ADN at ambient pressure can be found in the Ref. [30].

6.3.5 IR spectra under high pressure

To understand the hydrogen bonding and possible structural phase transformations in AP and ADN, we have calculated the IR spectra at ambient as well as at high pressure. We compared the calculated high frequency asymmetric and

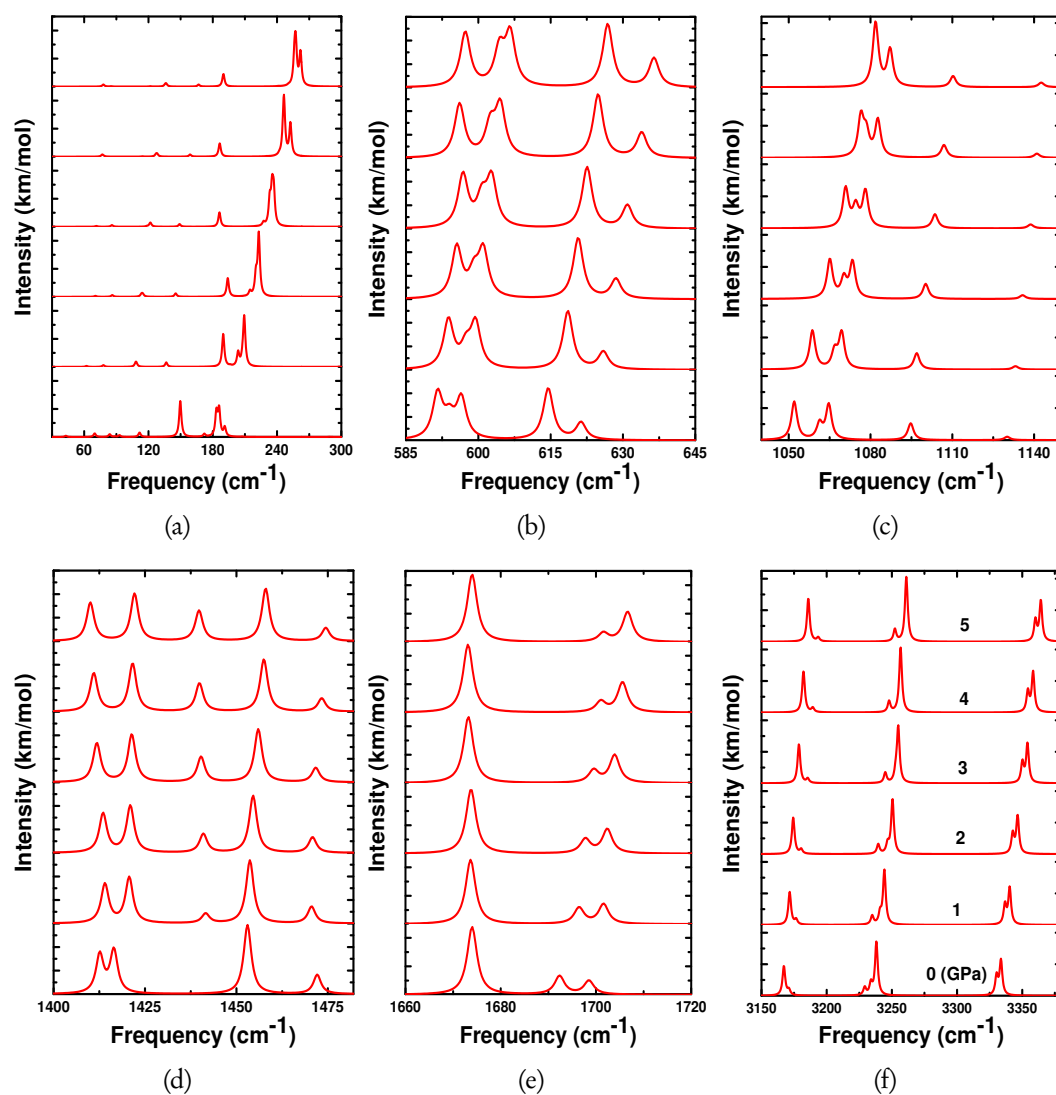


Figure 6.13: Calculated IR spectra (a) lattice modes (b) torsional and bending modes of NH₄ and ClO₄ ions (c) N-H wagging, rocking and scissoring modes (d) ClO₄ asymmetric modes (e, f) N-H symmetric and asymmetric stretching modes of AP as a function of pressure.

symmetric stretching bands of AP and ADN in the near IR region as presented in figure 6.12. Stronger the hydrogen bonding is, the more displacement towards low frequency (red-shift) region occurs. As illustrated in figure 6.12, the high frequency N-H stretching modes of ADN show red-shift in comparison to the N-H stretching frequencies of AP which is consistent with the Fourier transform IR experiments [9]. This clearly indicates that ADN has stronger hydrogen bonding over AP due to which ADN can bind large amounts of water by forming strong hydrogen bonding networks with water. This could be the reason why ADN has more hygroscopic nature when compared to AP [9].

For AP, the lattice mode frequencies which arise from both NH_4 and ClO_4 oscillations, rotation and translation motion of NH_4 cations are increasing with pressure indicating that lattice is hardening up on compression as depicted in figure 6.13a. The bending, symmetric and asymmetric stretching modes of ClO_4 anions show blue-shift under pressure (see figures 6.13b & c). The vibrational modes correspond to N-H bending, rocking, scissoring, symmetric and asymmetric modes show blue-shift as a function of pressure, except B_{2u} (1416 cm^{-1}) mode which exhibits blue-shift below 2 GPa and then shows a red-shift up to 5 GPa as shown in figure 6.13d, e & f. Overall, most of the N-H bending and stretching modes show blue-shift with increasing in pressure which leads to weakening of hydrogen bonding in AP. This may be a suggestive of structural phase transformation in AP under high pressure which is consistent with the recent X-ray and Neutron diffraction study [26].

In addition, we have also calculated IR spectra of ADN up to 10 GPa. As illustrated in figure 6.14a, the far IR lattice frequencies which include both NH_4 and $\text{N}(\text{NO}_2)_2$ oscillations, NO_2 twisting, NH_4 translation and rotation of NH_4 and N-NO_2 fragments of the ADN molecules are increasing with pressure below 5 GPa and these vibrational modes show red-shift above 5 GPa. The IR vibrational modes corresponding to bending and stretching of N-N and NO_2 bands exhibit a blue-shift with pressure as depicted in figures 6.14b & c. As illustrated in figures

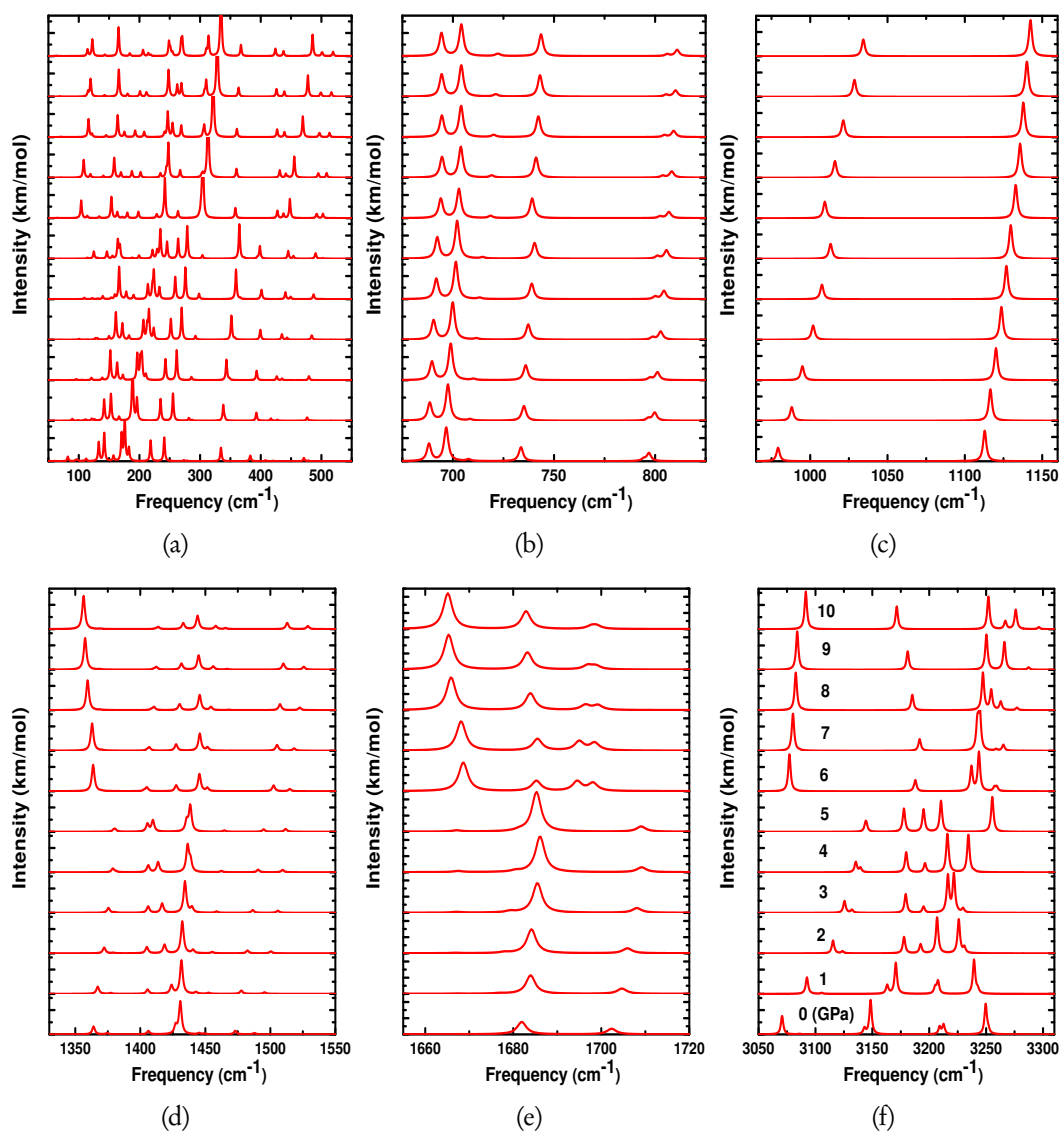


Figure 6.14: Calculated IR spectra (a) lattice modes (b) torsional and bending modes of NH₄ and N(NO₂)₂ ions (c) N-H wagging, rocking and scissoring modes (d) N(NO₂)₂ asymmetric modes (e, f) N-H symmetric and asymmetric stretching modes of ADN as a function of pressure.

6.14d, e& f, the N-H bending, symmetric and asymmetric stretching bands show a blue-shift as a function of pressure up to 5 GPa which indicates the weakening of hydrogen bonding below 5 GPa. However, the N-H bending and symmetric bands show abrupt red-shift and sharp increase in intensity when compared to the IR spectra between the pressure range 0-5 and 6-10 GPa. The features of computed IR spectra under pressure is different below and above 5 GPa (see figures 6.14a, d, e& f). This is a clear spectroscopic indication for the weakening and strengthening of hydrogen bonding in ADN below and above 5 GPa, respectively. The results strongly suggest that ADN undergoes a structural transformation around 6 GPa due to weakening of hydrogen bonding under pressure similar to that of ammonium azide [60]. ADN is found to be stable up to 5 GPa which is in good accord with the recent X-ray and Neutron diffraction study [28]. Strengthening of hydrogen bonding above 5 GPa reveal that the high pressure phase has strong hydrogen bonding nature when compared to ambient phase of ADN.

6.3.6 Detonation properties

The detonation characteristics namely detonation velocity and pressure are estimated using EXPLO5 program [61]. The obtained densities from *ab-initio* calculations with dispersion correction methods and heat of formation (HOF) from isodesmic reactions with Gaussian09 package in the solid phase were used in the prediction of detonation properties. The calculated crystal density, HOF, detonation velocity and pressure are presented in Table 6.3 along with the available experimental and theoretical results [17, 62-64]. The calculated detonation velocity and pressure at Chapman-Jouguet (CJ) point for the AN, AP and ADN oxidizers are relatively low ($D_{CJ} = \sim 6-7$ km/s and $P_{CJ} = \sim 17-25$ GPa) when compared to the high performance ($D_{CJ} = \sim 8-10$ km/s and $P_{CJ} = \sim 30-50$ GPa) conventional secondary explosives such as RDX, HMX, PETN and ONC etc. Relatively high detonation parameters of ADN reveal that ADN is a powerful energetic oxidizer among the three investigated ammonium based compounds.

Table 6.3: Calculated heat of formation (HOF, in kJ/mol), density (ρ , in gr/cc), detonation velocity (D_{CJ} , in km/s) and pressure (P_{CJ} , in GPa) of AN, AP and ADN.

Compound	Method	HOF	ρ	D_{CJ}	P_{CJ}
AN	Present	-336	1.734	7.28	18.71
	Expt.	-326 ^a , -354.6 ^b	1.72 ^b		
AP	Present	-236	1.946	6.50	17.64
	Expt.	-295 ^a , -283.1 ^b , -298 ^c	1.95 ^b , 1.9 ^c		
ADN	Present	-116	1.831	8.09	25.54
	Expt.	-125.3 ^b , -151 ^c , -149.7 ^d , -122.7 ^d	1.81 ^b , 1.8 ^c	8.074 ^b	23.72 ^b

^aRef.[17], ^bRef.[62] ^cRef.[63], ^dRef.[64]

6.4 Conclusions

High pressure structural, mechanical and vibrational properties of AN, AP and ADN have been calculated using dispersion correction methods to capture weak vdW interactions. The obtained ground state lattice parameters and equilibrium bulk moduli for the investigated compounds are in good agreement with the experimental results. The calculated compressibility curves and elastic moduli reveal that AN, ADN and AP are found to be more compressible along b- and a-axes respectively which are due to weak intermolecular interactions along that axes. We also observe a discontinuity in the lattice constants as a function of pressure which might be suggestive of structural phase transitions in AP and ADN under high pressure. The calculated zone center phonon frequencies reveal that AN has two imaginary optical phonon modes whereas AP and ADN possess all real optical phonon modes at Γ -point. In addition, we have also calculated IR spectra of AP and ADN at ambient as well as at high pressure. ADN is found to have more hygroscopic nature over AP due to strong hydrogen bonding at ambient pressure. Calculated Pressure dependent IR spectra show that weakening of hydrogen bonding which further leads to structural phase transitions in AP and ADN and also the high pressure phase of ADN has stronger hydrogen bonding

than the ambient phase. The calculated detonation properties reveal that ADN is a powerful energetic oxidizer when compared to AN and AP.

References

- [1] G. Steinhauser and T. M. Klapötke, *Angew. Chem. Int. Ed.*, **47**, 3330 (2008).
- [2] E. Gökcinar and T. M. Klapötke, *Turk. J. Chem.*, **34**, 953 (2010).
- [3] S. Venkatachalam, G. Santhosh and K. N. Ninan, *High Energy Oxidisers for Advanced Solid Propellants and Explosives, Advances in Solid Propellant Technology*, 1st International HEMS1 Workshop, Ranchi, India, pp.87-106 (2002).
- [4] Kirk-Othmer Encyclopedia of Chemical Technology, 4th ed. (Wiley, New York), Vol. 2, p.698–705 (1992).
- [5] C. Oomen and S. R. Jain, *J. Hazard. Mater.*, **67**, 253 (1999).
- [6] K. D. Shah, *Ammonium nitrate production, storage and distribution: accidents and investigations, in Proceedings of the International Fertiliser Society, International Fertiliser Society*, New York, UK, Vol. **629**, p.1 (2008).
- [7] D. Price, *Contrasting patterns in the behavior of high explosives, in Proceedings of the International Symposium on Combustion*, Vol. **11**, p.693 (1967).
- [8] G. B. Manelis and D. B. Lempert, *Progress in Propulsion Physics*, **1**, 81 (2009).
- [9] J. Cui, J. Han, J. Wang and R. Huang, *J. Chem. Eng. Data*, **55**, 3229 (2010).
- [10] D. M. Badgular, M. B. Talawar, S. N. Asthana, P. P. Mahulikar, *J. Hazard. Mater.*, **151**, 289 (2008).
- [11] A. J. Davidson, R. S. Chellappa, D. M. Dattelbaum and C. -S. Yoo, *J. Phys. Chem. A*, **115**, 11889 (2011).

- [12] S. Chaturvedi and P. N. Dave, *J. Ener. Mat.*, **31**, 1 (2013).
- [13] A. G. Keenan and R. F. Siegmund, *Quart. Rev. Chem. Soc.*, **23**, 4303 (1969).
- [14] V. V. Boldyrev, *Thermochimica Acta*, **443**, 1 (2006).
- [15] Y. -L. Zhua, H. Huangab, H. Rena and Q. -J. Jiao, *J. Ener. Mat.*, **32**, 16 (2014).
- [16] A. S. Tompa, *Thermochimica Acta*, **357-358**, 177 (2000).
- [17] R. Yang, P. Thakre and V. Yang, *Cobust. Explo. Shock waves*, **41**, 657 (2005).
- [18] J. C. Oxley, J. L. Smith, W. Zheng, E. Rogers and M. D. Coburn, *J. Phys. Chem. A*, **101**, 5646 (1997).
- [19] S. Libbecke, T. Keicher, H. Krause and A. Pfeil, *Solid State Ionics*, **101-103**, 945 (1997).
- [20] H. Matsunaga, H. Habu and A. Miyake, *J. Therm. Anal. Calorim.* **111**, 1183 (2013).
- [21] H. Matsunaga, H. Habu and A. Miyake, *J. Therm. Anal. Calorim.* **116**, 1227 (2014).
- [22] D. C. Sorescu and D. L. Thompson, *J. Phys. Chem. A*, **105**, 720 (2001).
- [23] S. Venkatachalam, G. Snathosh and K. N. Ninan, *Prop. Explos. Pyrotech.*, **29**, 178 (2004).
- [24] R. S. Chellappa, D. M. Dattelbaum, N. Velisavljevic and S. Sheffield, *J. Chem. Phys.*, **137**, 064504 (2012).
- [25] S. M. Peiris, G. I. Pangilinan and T. P. Russell, *J. Phys. Chem. A*, **104**, 11188 (2000).

- [26] S. Hunter, A. J. Davidson, C. A. Morrison, C. R. Pulham, P. Richardson, M. J. Farrow, W. G. Marshall, A. R. Lennie and P. J. Gould, *J. Phys. Chem. C*, **115**, 18782 (2011).
- [27] T. P. Russell, C. J. Piermarini, S. Block and P. J. Miller, *J. Phys. Chem.*, **100**, 3248 (1996).
- [28] C. R. Pulham, A. J. Davidson, I. D. H. Oswald, D. I. A. Millar, F. P. A. Fabbiani, D. J. Francis, W. G. Marshall, A. S. Cumming, D. R. Allan, A. R. Lennie and T. J. Prior, *24th European Crystallographic Meeting, ECM24, Marrakech, Acta Cryst.*, **A63**, S44 (2007).
- [29] D. C. Sorescu and D. L. Thompson, *J. Phys. Chem. A*, **105**, 7413 (2001).
- [30] W. Zhu, T. Wei, W. Zhu and H. Xiao, *J. Phys. Chem. A*, **112**, 4688 (2008).
- [31] W. Zhu, X. Zhang, W. Zhu and H. Xiao, *Phys. Chem. Chem. Phys.*, **10**, 7318 (2008).
- [32] G. Kresse and D. Joubert, *Phys. Rev. B*, **54**, 11169 (1996).
- [33] J. P. Perdew, S. Burke and M. Ernzerhof, *Phys. Rev. Lett.*, **77**, 3865 (1996).
- [34] S. Grimme, *J. Comput. Chem.*, **27**, 1787 (2006).
- [35] A. Tkatchenko and M. Scheffler, *Phys. Rev. Lett.*, **102**, 073005 (2009).
- [36] A. Tkatchenko, R. A. DiStasio Jr., R. Car and M. Scheffler, *Phys. Rev. Lett.*, **108**, 236402 (2012).
- [37] M. Dion, H. Rydberg, E. Schroder, D. C. Langreth and B. I. Lundqvist, *Phys. Rev. Lett.*, **92**, 246401 (2004).
- [38] M. C. Payne, M. P. Teter, D. C. Allen, T. A. Arias and J. D. Joannopoulos, *Rev. Mod. Phys.*, **64**, 1045 (1992).

- [39] N. Troullier and J. L. Martins, *Phys. Rev. B*, **43**, 1993 (1991).
- [40] H. J. Monkhorst and J. D. Pack, *Phys. Rev. B*, **13**, 5188 (1976).
- [41] C. S. Choi and J. E. Mapes, *Acta Cryst.*, **B28**, 1357 (1972).
- [42] G. Peyronel and E. A. Pignedoli, *Acta Cryst.*, **B31**, 2052 (1975).
- [43] C. S. Choi, H. J. Prask and E. Prince, *J. Chem. Phys.*, **61**, 3523 (1974).
- [44] C. S. Choi and H. J. Prask, *Acta Cryst.*, **B32**, 2919 (1976).
- [45] R. Gilardi, J. F. Anderson, C. George and R. J. Butcher, *J. Am. Chem. Soc.*, **119**, 9411 (1997).
- [46] F. D. Murnaghan, *Proc. Natl. Acad. Sci. USA*, **30**, 244 (1944).
- [47] L. Kotai, G. Argay, S. Holly, A. Keszler, B. Pukanszky and K. K. Banerji, *Z. Anorg. Allg. Chem.*, **627**, 114 (2001).
- [48] F. Shimojo, Z. Wu, R. K. Kalia and P. Vashishta, *J. Chem. Phys.*, **132**, 094106 (2010).
- [49] Z. Wu, R. K. Kalia, A. Nakano and P. Vashishta, *J. Chem. Phys.*, **134**, 204509 (2011).
- [50] S. Appalakondaiah, G. Vaitheeswaran and S. Lebégue, *J. Phys. Chem. A*, **119**, 6574 (2015).
- [51] J. J. Haycraft, L. L. Stevens and C. J. Eckhardt, *J. Chem. Phys.*, **124**, 024712 (2006).
- [52] L. L. Stevens and C. J. Eckhardt, *J. Chem. Phys.*, **122**, 174701 (2005).
- [53] B. Sun, J. M. Winey, Y. M. Gupta and D. E. Hooks, *J. Appl. Phys.*, **106**, 053505 (2009).

- [54] J. M. Winey and Y. M. Gupta, *J. Appl. Phys.*, **90**, 1669 (2001).
- [55] J. J. Haycraft, *J. Chem. Phys.*, **131**, 214501 (2009).
- [56] F. Vazquez, R. S. Singh and J. A. Gonzalo, *J. Phys. Chem. Solids*, **37**, 451 (1976).
- [57] S. Haussühl, *Z. Anorg. Allg. Chem.*, **192**, 137 (1990).
- [58] E. M. Witko, W. D. Buchanan and T. M. Korter, *J. Phys. Chem. A*, **115**, 12410 (2011).
- [59] S. Bourahla, A. A. Benamara and S. K. Moustefai, *Can. J. Phys.*, **92**, 216 (2014).
- [60] N. Yedukondalu, G. Vaitheeswaran, P. Anees and M. C. Valsakumar, *Phys. Chem. Chem. Phys.*, **17**, 29210 (2015).
- [61] M. Sucéska, EXPLO5 program, Zagreb, Croatia (2005).
- [62] H. H. Kraue, "Energetic Materials" WILEY-VCH Verlag, Weinheim, ISBN:3-527-30240-9 (2005).
- [63] U. R. Nair, S. N. Asthana, A. Subhananda Rao and B. R. Gandhe, *Defence Sci. Journal*, **60** 137 (2010).
- [64] Z. Zeng, R. Wang, B. Twamley, D. A. Parris and J. M. Shreeve, *Chem. Mater.*, **20**, 6176 (2008).

Phase stability, lattice dynamics, electronic, optical and detonation properties of ammonium azide

The main focus of this chapter is towards understanding the phase stability of four hydro-nitrogen (N_4H_4) solids. Among them, Ammonium Azide (AA) is found to be the thermodynamic ground state of N_4H_4 compounds. Structural, elastic and lattice dynamical properties of AA have been carried out at ambient as well as at high pressure. In addition, electronic structure, optical and detonation properties of AA are discussed in detail.

7.1 Introduction

AA has been attracting considerable interest as a precursor for synthesis of polymeric nitrogen due to its high nitrogen content of 93.3% by weight and also the fact that it gives out environment friendly decomposition products [1]. It also exhibits extensive hydrogen bonding between the ammonium cation and terminal nitrogen atoms of azide anions [2, 3]. Unlike the alkali, alkaline-earth and transition metal azides which are either ionic or covalent [4], AA is found to have mixed bonding nature [5] with unique properties. It has got much attention recently as a gas generator due to its weak explosive characteristics [6]. Using Kamlet-Jacobs equations, the calculated detonation properties, namely, detonation velocity and pressure are found to be 6.45 km/s and 15.16 GPa, respectively [5]. AA used in in-

flate safety cushions for auto-mobiles with a suitable oxidizer and also as a solid rocket propellant in photochemical micro-rockets for altitude control [7]. In order to address its potential applications, one has to understand the crystal structure and physical properties of AA at the microscopic level. Several experimental studies have been reported in the literature exploring fundamental properties at ambient conditions. Frevel [8] first reported the crystal structure of AA which was re-determined later using single crystal [2] and powder [3] X-ray diffraction techniques. The infra-red (IR) vibrational spectra were reported [9], which was followed by a combined IR and Raman study [10]. It was further refined and extended by Iqbal et al [11] who analyzed the vibrational modes of azide ion and the low frequency lattice modes using far-IR and Raman spectroscopic techniques at ambient pressure and low temperatures. From the theoretical perspective, the structural, mechanical, electronic and optical properties of AA were reported at ambient pressure from first principles calculations at 0 K [5, 12].

Inorganic azides undergo a series of phase transitions involving lattice distortions coupled with changes in the orientation of the linear azide anions thereby forming polymeric nitrogen networks under pressure. Therefore, high pressure study of these materials has become an active field of research during the last decade [13]. Synthesis of polymeric nitrogen from molecular nitrogen ($\text{N}\equiv\text{N}$ is the strongest bond, 954 kJ/mol) has been achieved [14–16] and it consists of individual nitrogen atoms connected by single bonded (N-N) networks. It is the best green high energetic density material (HEDM) known till date [15, 16]. The azides consist of linear-rod-shaped N_3^- ions with quasi double bonds (N=N bond is weaker than $\text{N}\equiv\text{N}$ with 418 kJ/mol energy). Hence, it can be expected that the $(\text{N}=\text{N}=\text{N})^-$ ions of metal azides may form polymeric nitrogen networks more readily than molecular nitrogen ($\text{N}\equiv\text{N}$) [14]. Among the inorganic azides, AA is quite interesting due to modification in the strength of hydrogen bonding under compression. Raman spectroscopic studies [1, 17, 18] revealed that it undergoes a polymorphic phase transition around ~ 3 GPa due to weakening of the hydro-

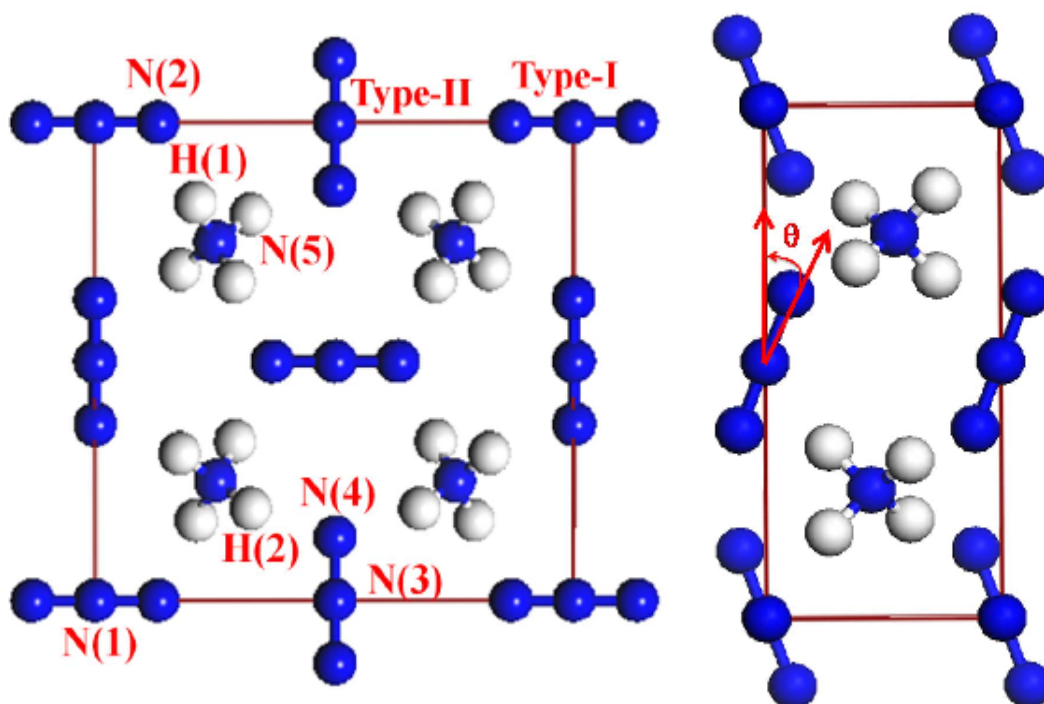


Figure 7.1: Crystal structure of AA viewed in a-c (left) b-c (right) planes. Azide (N_3) ion parallel and perpendicular to a-axis named as Type I and Type-II, respectively. Angle θ is defined as orientation of Type-II azides w.r.t. to c-axis.

gen bonding under pressure. This is reinforced by recent high pressure X-ray and Neutron powder diffraction studies on AA and the transition pressure is found to be ~ 2.6 GPa [19] and ~ 2.9 GPa [1, 20, 21], respectively but still the crystal structure of high pressure phase has remained elusive until now. Hu and Zhang [22] proposed that AA and Trans-Tetrazene (TTZ) could be precursors for the high-pressure synthesis of hydro-nitrogen solid (HNS-1) with $P2_1/m$ crystal symmetry and it can be obtained at 36 and 75 GPa from AA and TTZ, respectively using standard Generalized Gradient Approximation parameterized by Perdew-Burke-Ernzerhof (PBE-GGA) functional.

In our previous study [5] we systematically studied the effect of semi-empirical dispersion correction methods on structural properties of AA along with standard DFT functionals. The dispersion corrected PBE functional (vdW-TS) developed

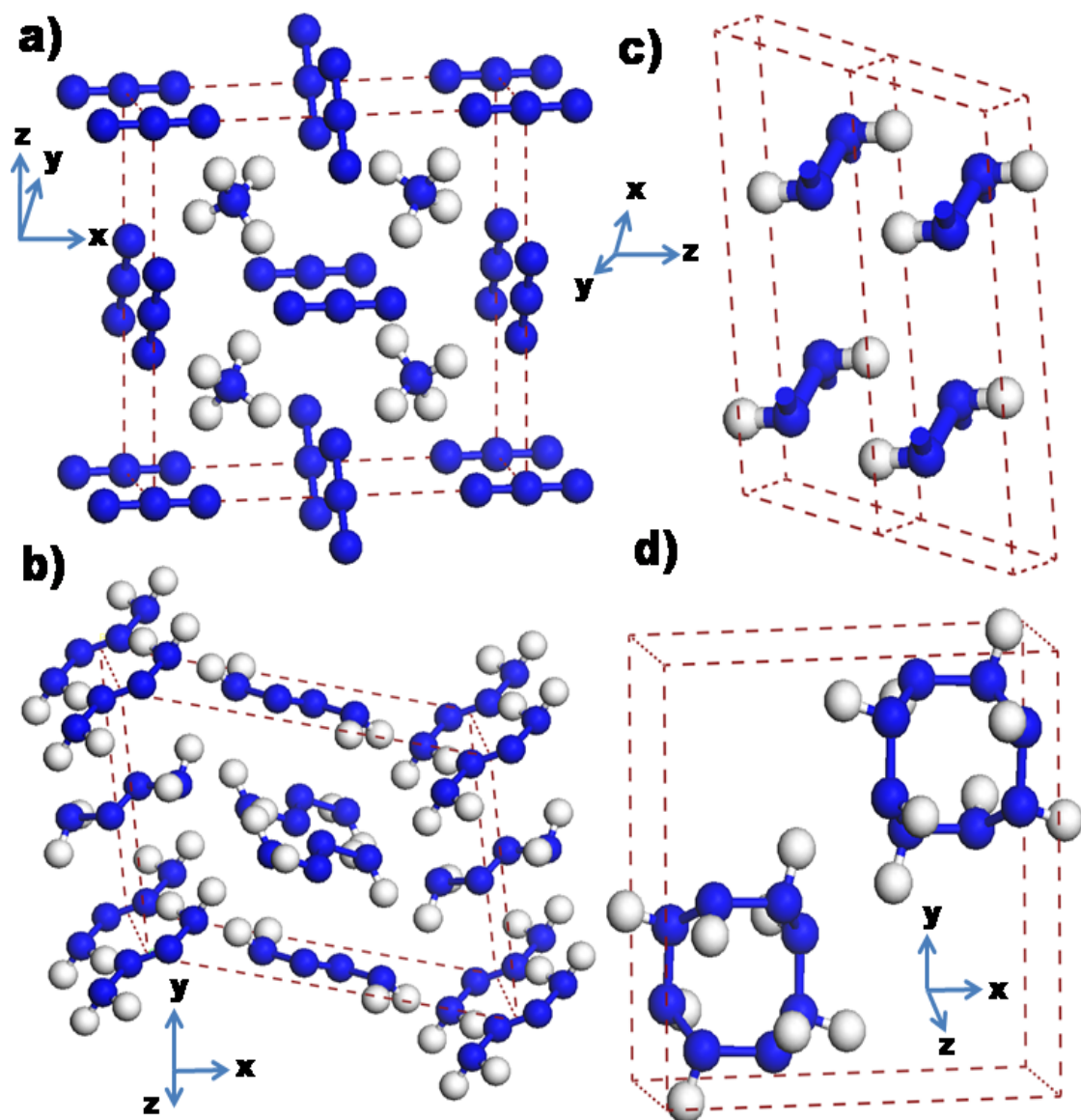


Figure 7.2: Crystal structures of hydro-nitrogen solids; (a) AA, (b) T'TZ, (c) HNS-1 (super cell) and (d) HNS-2.

by Tkatchenko and Scheffler [23] works better for the molecular crystalline solid AA in contrast to conventional DFT functionals. Following this study, Liu and co-workers predicted the phase stability of N_4H_4 compounds at ambient [24] as well as under pressure up to 80 GPa [25] using the vdW-TS method. They proposed a new tetragonal phase (HNS-2) with crystal symmetry $P4_2/n$. The order of stability of the four phases at ambient pressure is as follows: $AA > \text{TTZ} > \text{HNS-2} > \text{HNS-1}$ and they also encounter a series of phase transitions from $AA \rightarrow \text{HNS-2}$ at 5.6 GPa, $\text{HNS-2} \rightarrow AA$ at 15 GPa, $AA \rightarrow \text{TTZ}$ at 30 GPa and $\text{TTZ} \rightarrow \text{HNS-1}$ at 69.2 GPa. Crowhurst et al [21] revisited these phase transitions for three (AA, TTZ, HNS-1) phases and are found to occur between $AA \rightarrow \text{TTZ}$ at 41.4 GPa and $\text{TTZ} \rightarrow \text{HNS-1}$ at 89.4 GPa, respectively using DFT-D2 method. There is an inconsistency between theoretical calculations in predicting the phase transition pressures using various dispersion corrected approaches and the dependence of phase stability on temperature of N_4H_4 compounds is unknown. With this motivation, we have investigated relative phase stability of N_4H_4 compounds, crystal structure and lattice dynamics of AA at ambient as well as at high pressure using dispersion corrected density functional calculations. The rest of the chapter is organized as follows: in section 7.2, we briefly describe the methodology of computation. Results and discussion concerning phase stability of hydro-nitrogen solids as well as structural and lattice dynamics of AA under high pressure are presented in section 7.3. Finally section 7.4 summarizes the conclusions of the chapter.

7.2 Method of computation

Cambridge Series of Total Energy Package (CASTEP) [26] is used to calculate the structural and vibrational spectrum of the N_4H_4 compounds. We have used Norm-conserving (NC) pseudo potentials (PP) for electron-ion interactions, as they are well suited for phonon calculations [27] while PBE-GGA [28] was used

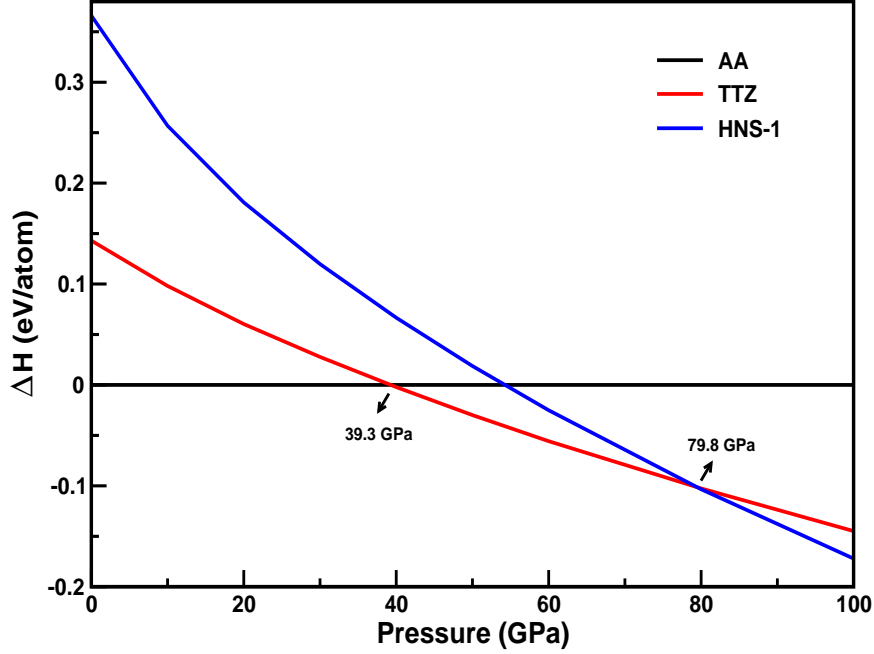


Figure 7.3: Calculated relative enthalpies of TTZ and HNS-1 with respect to AA using NCPP approach as a function of pressure.

to treat electron-electron interactions. The Broyden-Fletcher-Goldfarb-Shanno (BFGS) minimization scheme [29] has been used for the structural relaxation. The convergence criteria for structural optimization was set to ultrafine quality with a kinetic energy cutoff of 850 eV and $2\pi \times 0.025 \text{ \AA}^{-1}$ separation of k-mesh according to the Monkhorst-Pack grid scheme [30]. The self-consistent energy convergence less than 5.0×10^{-6} eV/atom and maximal force between atoms was set to 0.01 eV/Å. The maximum displacement and stress were set to be 5.0×10^{-4} Å and 0.02 GPa, respectively.

The elastic constants and phonon dispersion curves of AA are computed using density functional perturbation (DFPT) [31] theory as implemented in the Vienna ab-initio Simulation Package (VASP) [32]. The initial geometry is further relaxed, and ensured a force convergence of the order 10^{-5} eV/atom with zero external pressure. The calculated phonon dispersion using the unit cell shows imaginary frequencies. Since VASP code computes the dynamical matrix in real space, we

have to use a sufficiently large super cell to incorporate the long range nature of the dynamical matrix. To compute the phonon dispersion curves a super cell of size $1 \times 2 \times 1$ (64 atoms) has been used. The force constant matrix is computed and the dynamical matrix is obtained from its Fourier transform. The eigenvalues and eigenvectors of the dynamical matrix will yield the square of the phonon frequencies and polarization of each mode. The DFPT calculations will give the phonon frequencies and polarization at the zone center ($q=0$). In order to obtain the phonon dispersion in the entire Brillouin zone, we used an auxiliary post process package PHONOPY [33]. All the CASTEP and VASP calculations were performed using vdW-TS [23] and TS-SCS [34] schemes, respectively.

7.3 Results and discussion

7.3.1 Phase stability of N_4H_4 compounds

At ambient conditions, AA crystallizes in the orthorhombic structure with space group $Pmna$ [1–3, 19]. It possesses a distorted CsCl-type structure because of strong hydrogen bonding between NH_4^+ and N_3^- ions and the arrangement of azide ion is similar to that in the ambient structures of heavy metal (Ag, Tl) azides. Due to the presence of hydrogen bonding one half of the azide anions lie parallel to a-axis (Type-I) and the other half lie perpendicular to a-axis (Type-II) as depicted in figure 7.1 by allowing a tetrahedral arrangement around a single ammonium cation [19]. TTZ is a molecular crystal, which consists of non-linear arrangement of four N-atoms in a chain with two hydrogen atoms each attached to both ends of the N_4 molecule and four such molecules are arranged with $P\bar{1}$ symmetry in the unit cell [35]. HNS-1 contains similar molecular structure as TTZ with a hydrogen atom attached to each nitrogen atom in each $(NH)_2$ unit and the two units are separated by a distance within the unit cell of $P2_1/m$ symmetry [22]. Recently a new tetragonal phase has been predicted with $P4_2/n$ symmetry [25], where two $(NH)_4$ units form a distorted cyclic octagon within the unit cell, in

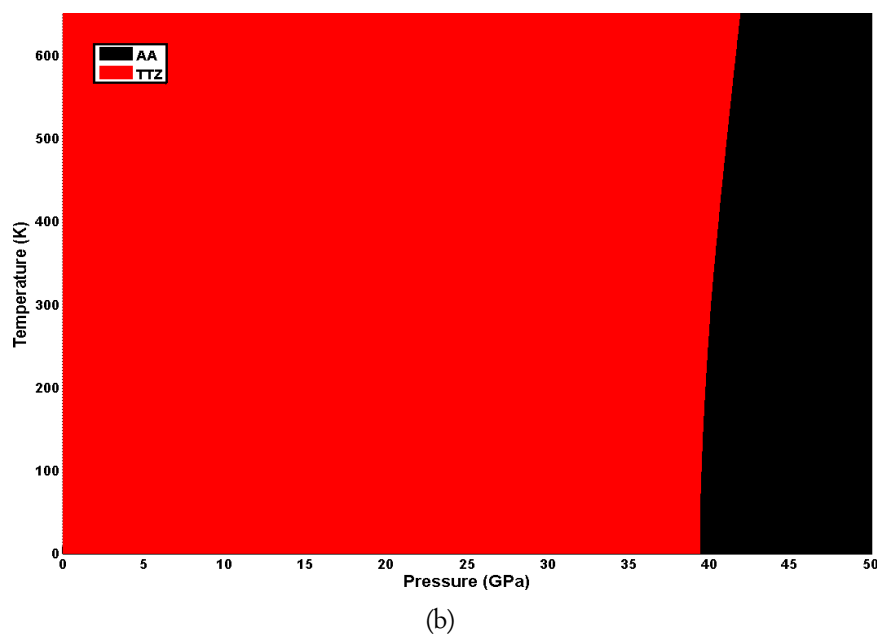
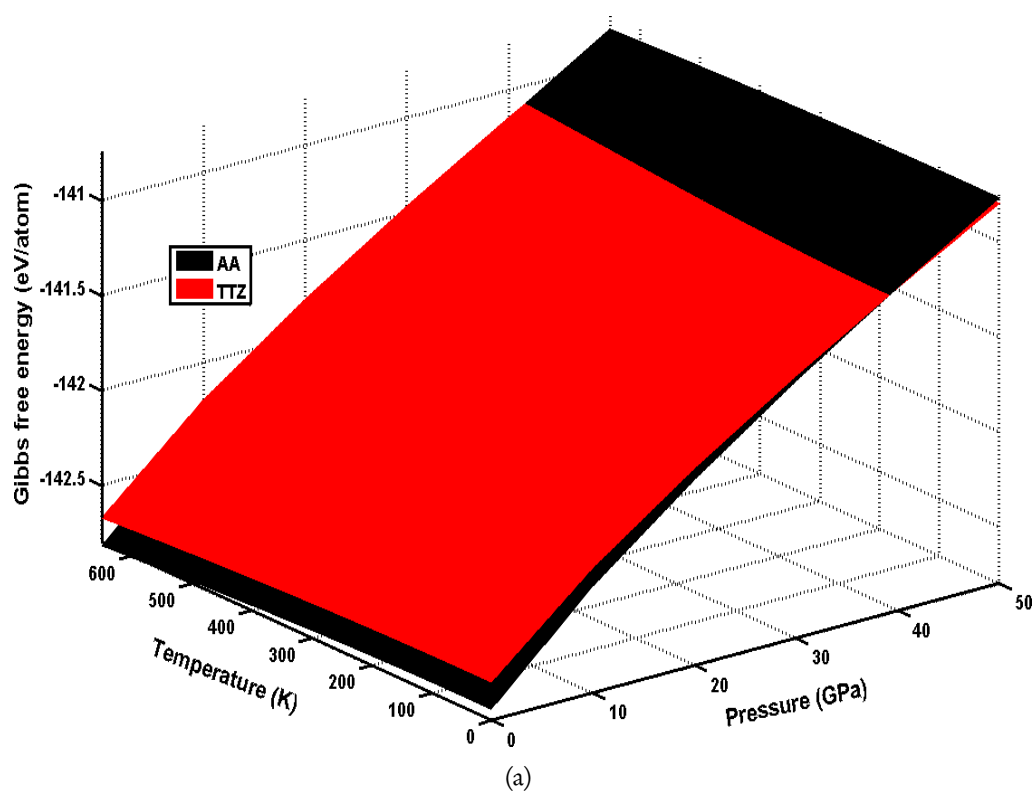


Figure 7.4: Calculated phase diagram (G, P, T) of (a) AA and TTZ (b) viewed in P-T plane for AA and TTZ using NCPP approach.

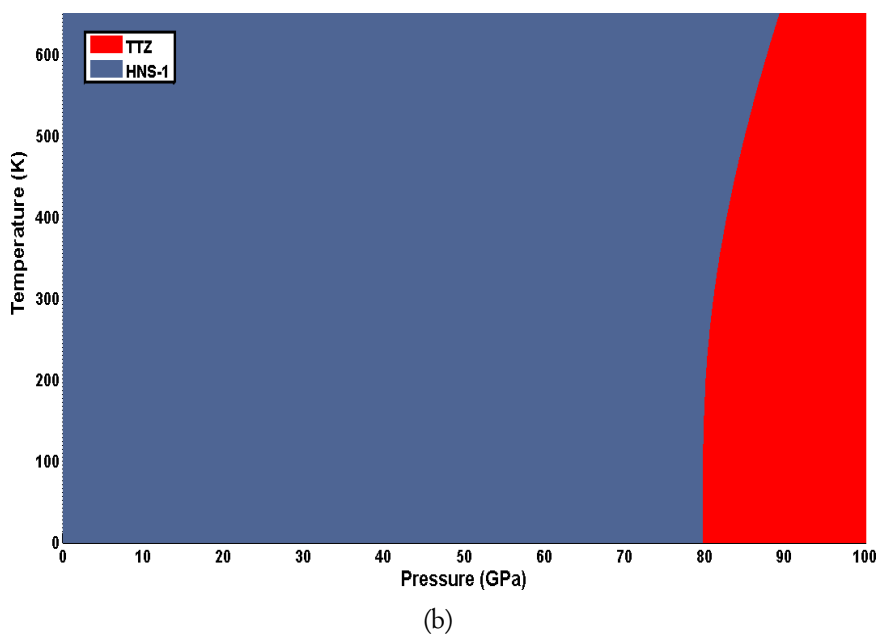
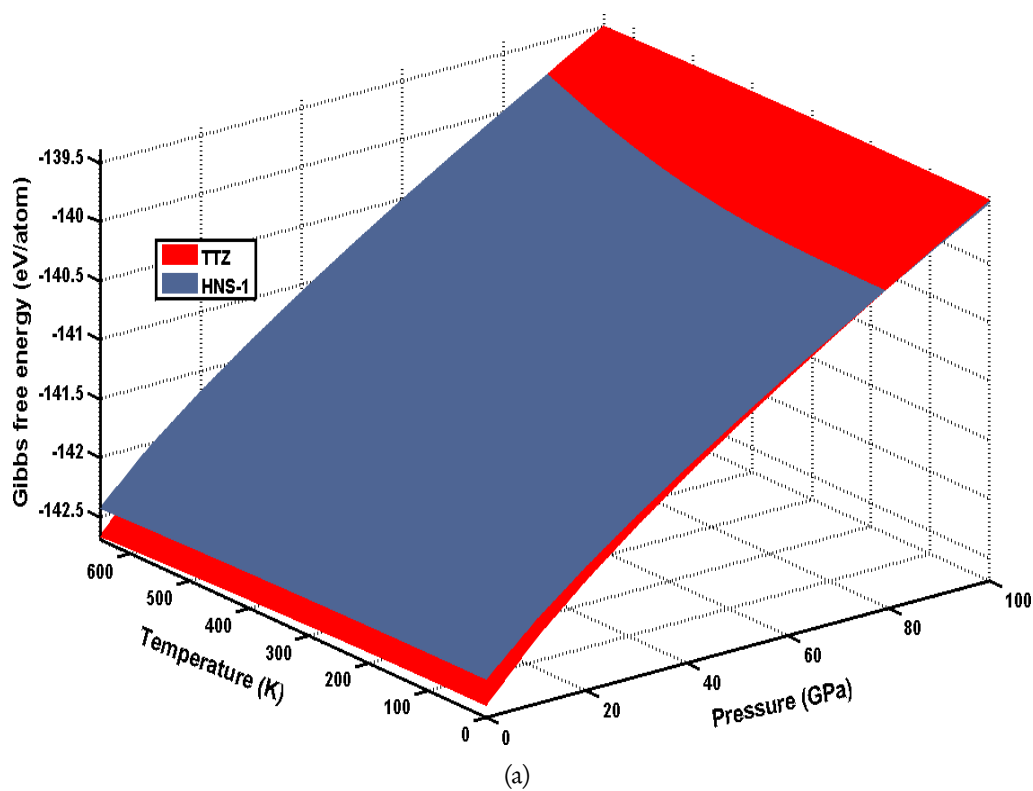


Figure 7.5: Calculated phase diagram (G, P, T) of (a) TTZ and HNS-1 (b) viewed in P-T plane for TTZ and HNS-1 using NCPP approach.

which each nitrogen atom is attached to one hydrogen atom. The crystal structures of the four N_4H_4 compounds are shown in figure 7.2 and all these phases are molecular crystalline solids. However, most of the energetic systems such as primary (Fulminates, Azides, Styphanates, etc.) and secondary (RDX, HMX, TNT, PETN, etc.) explosive molecular crystals are bonded through weak dispersive interactions. The non-covalent weak interactions such as hydrogen bonding and dispersive interactions play a significant role in determining the stability of these molecular solids. As discussed in the previous section, we also show that the vdW-TS method is successful in predicting the ground state properties of AA over DFT-D2 method [5, 36]. Hence, we have used the dispersion corrected vdW-TS and TS-SCS methods for all the calculations. As a first step, we have performed full structural optimization including lattice geometry and fractional coordinates of the four N_4H_4 compounds. The calculated unit cell parameters for these compounds are consistent with the available experimental data [1–3, 19] and other theoretical calculations [22, 24, 25] which are presented in Table 7.1.

From our first principles calculations, we found that total energies of the N_4H_4 compounds increase in the following order; $E_0^{AA} < E_0^{TTZ} < E_0^{HNS-2} < E_0^{HNS-1}$ at ambient pressure. The total energy of the AA is lowered by 0.15, 0.36 and 0.38 eV/atom when compared to TTZ, HNS-2 and HNS-1, respectively and the order of stability is consistent with the previous calculations [22, 24, 25]. This clearly shows that AA is the relatively stable phase among the studied N_4H_4 compounds at ambient pressure. What happens to the order of stability at higher pressures for these four phases? We made an attempt to investigate the phase transitions and the possibility for the formation of hydro-nitro solid under high pressure. As illustrated in figure 7.3, we predict a series of phase transitions $AA \rightarrow TTZ$ at 39.3 GPa, $TTZ \rightarrow HNS-1$ at 79.8 GPa using NCPP approach, which are in good agreement with recent theoretical calculations [21] using dispersion corrected DFT-D2 method. Also the transition pressures obtained using ultra-soft pseudo-potential (USPP) approach are found to be $AA \rightarrow TTZ$ at 27.5 GPa, $TTZ \rightarrow HNS-1$ at

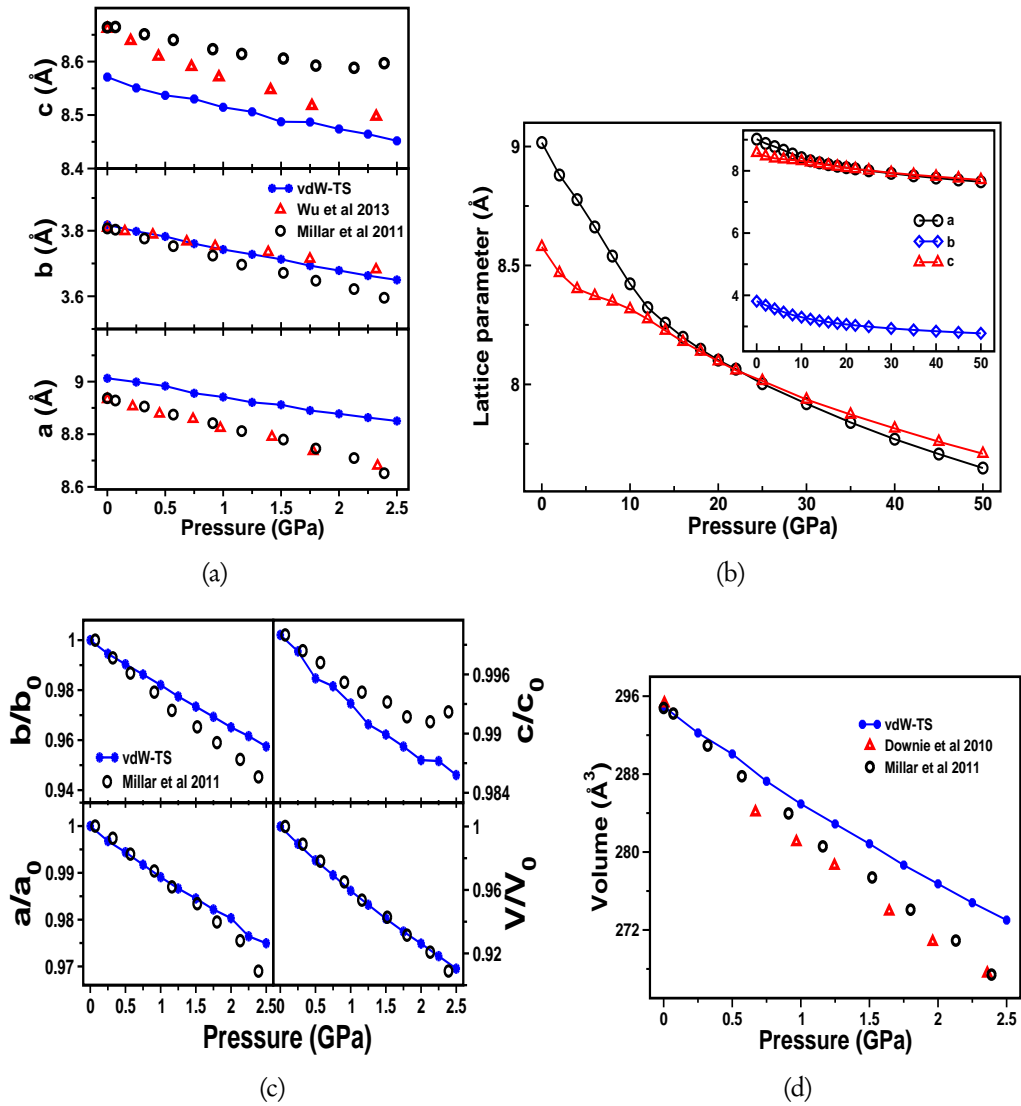
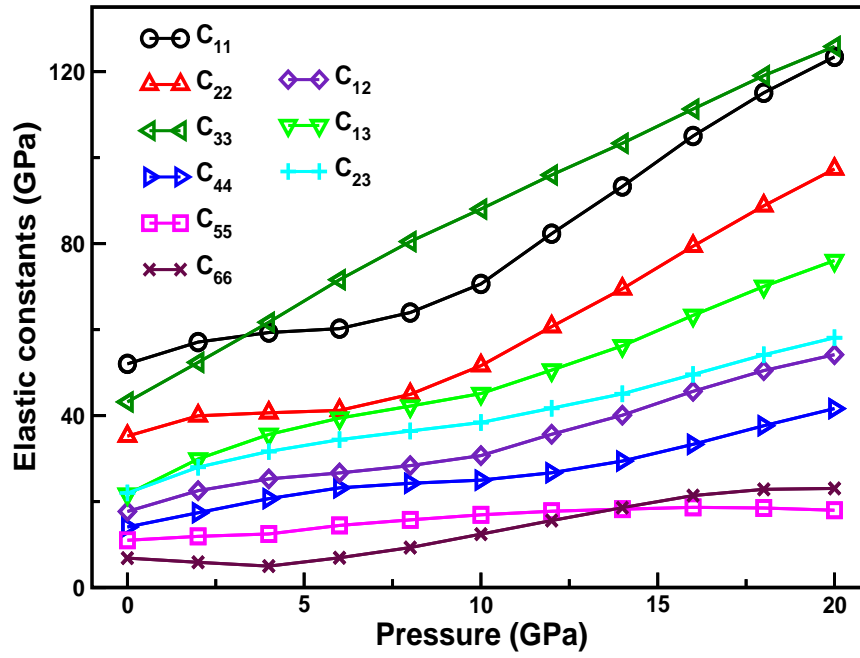


Figure 7.6: Calculated (a, b) lattice constants a , b and c ; (c) relative compressibility of unit cell parameters a , b and c ; (d) volume of AA as a function of pressure up to 2.5 GPa (except figure 7.6b which is up to 50 GPa). The experimental data is taken from Refs.[1, 19, 38]

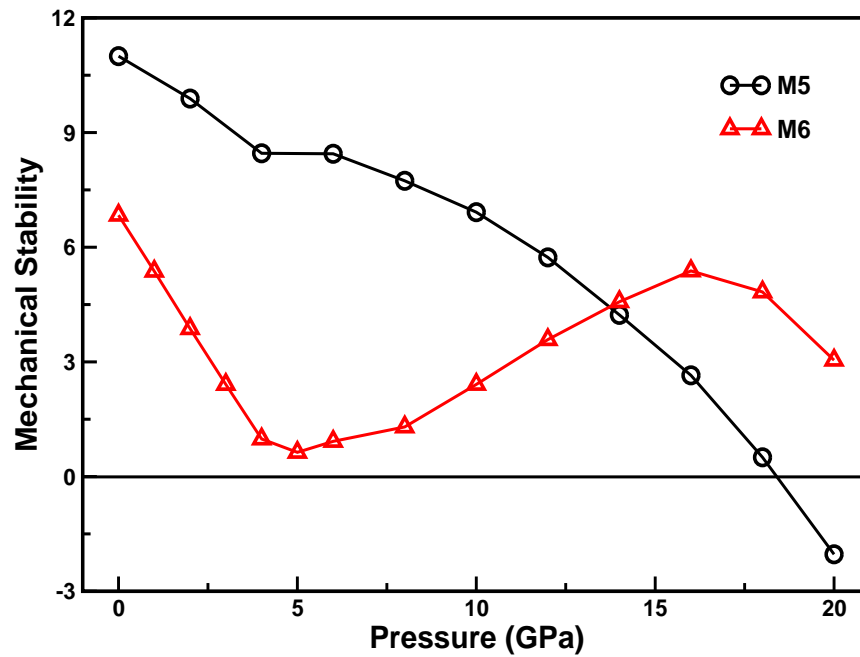
Table 7.1: Calculated and experimental ground state lattice parameters (a, b, c, in Å), crystallographic angles (α , β , γ , in $^\circ$), volume (V, in Å³) and total energy (E₀, in eV/atom) of N₄H₄ compounds. USPP and NCPP were used in the vdW-TS calculations implemented in CASTEP package and PAW pseudo potentials were used within dispersion corrected TS-SCS method incorporated through VASP package.

Phase	Parameter	This work			Other calculations		Experiment
		USPP	NCPP	PAW			
(Pmna, Z=4)	a	9.015	9.012	9.021	9.0247 ^a , 8.7539 ^b	8.93283 ^f , 8.948 ^g , 8.937 ^h	
	b	3.809	3.816	3.837	3.8089 ^a , 3.6363 ^b	3.80848 ^f , 3.808 ^g , 3.807 ^h	
	c	8.551	8.574	8.482	8.5460 ^a , 8.3560 ^b	8.66147 ^f , 8.659 ^g , 8.664 ^h	
TTZ (P1, Z=4)	V	293.66	294.89	293.57	275.9 ^c , 285.4 ^c	294.45 ^f , 295.05 ^g , 294.79 ^h	
	E ₀	-143.51	-142.75	-5.99	-143.512 ^a		
	a	10.469	10.498	10.391	10.5752 ^a	10.23 ⁱ	
	b	6.888	6.904	7.030	6.8631 ^a	7.12 ⁱ	
HNS-1 (P2 ₁ /m, Z=2)	c	4.081	4.127	4.122	4.0264 ^a	4.19 ⁱ	
	α	102.63	102.37	102.27	102.599 ^a	102.0 ⁱ	
	β	87.94	88.19	88.16	87.463 ^a	90.0 ⁱ	
	γ	104.22	103.79	104.89	104.248 ^a	106.5 ⁱ	
HNS-2 (P4 ₂ /n, Z=4)	V	278.29	283.72	284.27		285.66 ⁱ	
	E ₀	-143.39	-142.60	-5.83	-143.392 ^a		
	a	8.395	8.472	8.307	8.1850 ^a , 8.5935 ^d		
	b	2.312	2.339	2.306	2.3114 ^a , 2.3167 ^d		
HNS-2 (P4 ₂ /n, Z=4)	c	3.051	3.076	3.054	3.0641 ^a , 3.0021 ^d		
	β	107.34	107.46	107.24	107.38 ^a , 105.74 ^d		
	V	56.53	58.15	55.88			
	E ₀	-143.19	-142.37	-5.58	-143.158 ^a		
HNS-2 (P4 ₂ /n, Z=4)	a	8.183	8.209	8.204	8.2348 ^e		
	c	4.211	4.367	4.290	4.1338 ^e		
	V	281.96	294.28	288.77			
	E ₀	-143.16	-142.39	-5.60	-143.191 ^e		

^a Ref.[12]; ^b Ref.[24]; ^c Ref.[36]; ^d Ref.[22]; ^e Ref.[25]; ^f Ref.[1]; ^g Ref.[2]; ^h Ref.[3]; ⁱ Ref.[35]



(a)

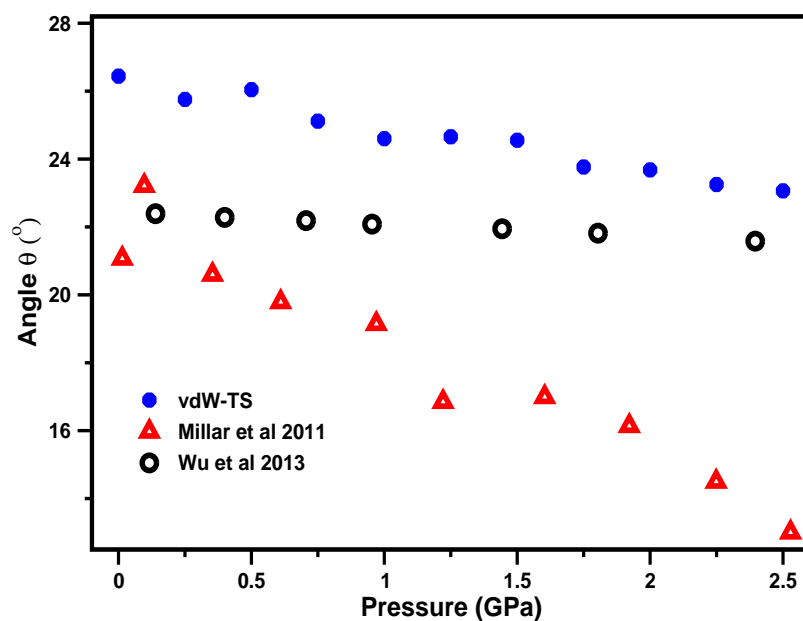


(b)

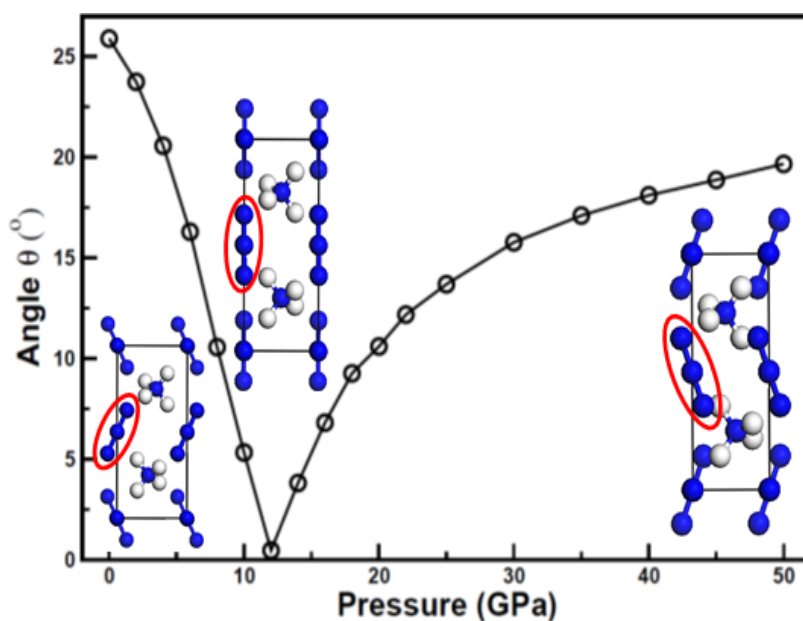
Figure 7.7: Calculated (a) elastic constants (C_{ij}) (b) mechanical stability criteria of AA as a function of pressure up to 20 GPa.

74.2 GPa (see figure 1 of the Ref. [37]) and are comparable with the ones obtained in the study by Liu et al [25]. The inconsistency between transition pressures of the examined compounds are due to various pseudo-potentials used in the calculations. Recent Raman spectroscopic measurements reveal that the HNS-1 will be formed even at much higher pressures (> 71 GPa) and hence the transition pressures obtained using NCPP including dispersive interactions are in good agreement with the experimental observations [21]. Medvedev et al [17] determined the pressure at which polymorphic structural phase transition from phase I to II occurs at around 3 GPa and phase II consists of NH_4 and N_3 ions similar to phase I with a difference that both of the azide groups must occupy equivalent crystallographic positions to be consistent with observations from Raman spectroscopic study [17]. This is further confirmed by the single crystal X-ray diffraction study and the phase II is temporarily assigned as tetragonal phase [1]. Recently Liu et al [25] predicted the crystal structure of the tetragonal phase with $P4_2/n$ symmetry and it possesses a distorted cyclic structure which is in contrast to the structure proposed by the Raman spectroscopic measurements [17]. In addition, they also find structural transitions from AA \rightarrow HNS-2 at 5.6 GPa and HNS-2 \rightarrow AA at 15 GPa. In order to resolve the above issues we systematically investigated the high pressure behavior of AA and HNS-2 phases and we found that AA does not undergo a transition to HNS-2 phase below 20 GPa (see figure 2 of the Ref. [37]). Therefore, prediction/determination of crystal structure of phase II is still an open challenge for both theoreticians and experimentalists.

In addition, we also considered the contribution of lattice vibration at elevated pressure and temperatures. Since AA decomposes at 673 K (400 °C) [6], we have plotted Gibbs free energy as a function of pressure (0-100 GPa) and temperature (0-650 K) within the vdW-TS method. AA undergoes a structural transition to TTZ around 39.3 GPa at 0 K (see figure 7.3) and the transition pressure increases to 42.6 GPa with increasing temperature up to 650 K as illustrated in figure 7.4. Further, TTZ transforms to HNS-1 around 79.8 GPa at 0 K (see figure 7.3) and



(a)



(b)

Figure 7.8: Calculated angle θ that a Type-II azide ion makes with c-axis (see figure 7.1) in AA up to (a) 0-2.5 GPa and (b) 0-50 GPa. The optimized structures of AA are given in inset at 0, 12 and 50 GPa pressures (from left to right) in order to show change in the orientation of azide ions with c-axis in figure (b) as highlighted in ellipse for one Type-II azide and it is also applicable for Type-II azides which are aligned along c-axis. The experimental data is taken from Ref. [1].

the transition pressure increases from 79.8 to 89.7 GPa when the temperature raises from 0 to 650 K as shown in figure 7.5. Overall, we observe that AA is the thermodynamic ground state of N_4H_4 compounds which is consistent with the previous theoretical calculations [20, 24, 25]. Also AA transforms to TTZ around $\sim 39-43$ GPa followed by transformation of TTZ to HNS-1 around $\sim 80-90$ GPa under the studied temperature range 0-650 K.

7.3.2 Structural properties of AA under high pressure

We have also studied the structural properties of the thermodynamic ground state of N_4H_4 compounds (AA) under pressure up to 0-2.5 GPa, 0-20 GPa and 20-50 GPa in steps of 0.25, 2 and 5 GPa, respectively. The pressure dependent unit cell parameters obtained using vdW-TS method are in good accordance with the experimental data [1, 19] within 0-2.5 GPa with an exception for lattice parameter c , which shows a larger contraction due to over binding within the studied pressure range (see figure 7.6a). As shown in figure 7.6b, we observe that there is a strong anisotropy between the lattice constants a , b and c in the low pressure region (0-3 GPa). The lattice constants a and c approach towards each other because of accelerated and decelerated compression of a and c lattice constants respectively and they merge between 18-22 GPa. This is due to rotation of Type-II azide ions and reduction in the hydrogen bond energy [20], consequently the anisotropic phase I undergoes transition to phase II under compression. This will be further confirmed by lattice dynamical calculations under pressure in the up coming section. In addition, we have also compared the calculated normalized lattice parameters (a , b , c and V) at ambient pressure (0 GPa) with the experimental data (0.07 GPa is experimental ambient pressure) [19]. The calculated relative compressibilities of unit cell axes are presented in figure 7.6c along with the experimental results [19]. The reduction of b lattice parameter is larger under compression which is clearly seen from the study of the first order pressure coefficients $\gamma(X) = \frac{1}{X} \frac{dX}{dP}$ ($X = a, b, c$). The calculated first order pressure coefficients (in GPa^{-1}) using vdW-TS

scheme are found to be 8.9×10^{-3} , 20.4×10^{-3} and 6.6×10^{-3} for lattice parameters a , b and c , respectively. This clearly shows that b -axis is the most compressible due to flattening of the wave-like planes of N_3^- anions under compression which further reveals that AA is sensitive to impact along the b -axis. Crystallographic c -axis is the least compressible because of Type-II azide anions align parallel to c -axis with increasing pressure as shown in figure 7.6c, resulting in an excellent agreement with the experimental observation [1, 19] as well as with our recent theoretical prediction from the longitudinal elastic constants [5]. The ordering of the calculated elastic constants ($C_{33} > C_{11} > C_{22}$) further confirm that b -axis is the most and c -axis is the least compressible axes for AA [5, 24]. As illustrated in figure 7.6d, the calculated pressure-volume (P-V) data is consistent with the experiments [19, 38] especially in the low pressure region. This might be due to fact that the dispersion coefficients C_6 used for the chemical species N and H are kept constant over the studied pressure range. Overall, the experimental trends are well reproduced by the vdW-TS method up to 2.5 GPa. We also calculated equilibrium bulk modulus (B_0) and it is found to be 27.6 GPa by fitting pressure-volume data to 2nd order Birch-Murnaghan equation of state [39]. The obtained B_0 value of 27.6 GPa is slightly higher when compared to the experimental values of 24.5 [1], 20.2 [19] and 19.8 [38] GPa and it is consistent with our previously calculated value of 26.34 GPa using USPP [5]. The B_0 of AA lies between the B_0 values of Alkali Metal Azides (AMA) and Heavy Metal Azides (HMA) indicating that AA is relatively harder than AMA and softer than HMA.

7.3.3 Mechanical properties of AA under high pressure

In order to get more insight on structural phase transition in AA, we have also calculated the elastic constants at ambient as well as at high pressure up to 20 GPa. The calculated elastic constants at ambient pressure are consistent with our previous [5] and other [24] theoretical calculations. A crystalline lattice is mechanically stable at zero pressure only if the Born stability criteria [40] are

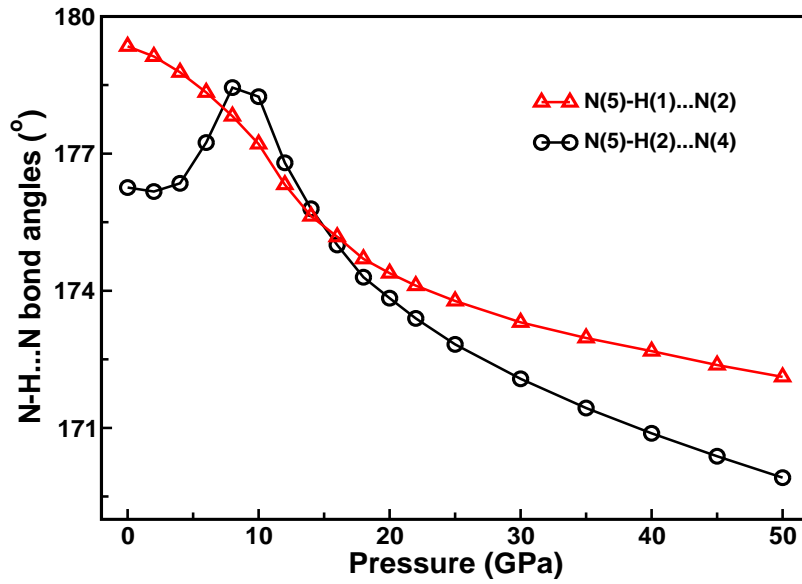


Figure 7.9: Calculated hydrogen bond angles (N-H...N) as a function of pressure up to 50 GPa. Atomic labels are given in figure 7.1.

fulfilled. In case of orthorhombic systems the stability criteria are [41]

$$\begin{aligned}
 C_{11} &> 0, C_{11}C_{22} > C_{12}^2, \\
 C_{11}C_{22}C_{33} + 2C_{12}C_{13}C_{23} - C_{11}C_{23}^2 - C_{22}C_{13}^2 - C_{33}C_{12}^2 &> 0, \\
 C_{44} &> 0, C_{55} > 0, C_{66} > 0
 \end{aligned} \tag{7.1}$$

The obtained elastic constants satisfy the Born stability criteria indicating that AA is mechanically stable at ambient pressure. When a non-zero uniform stress is applied to the crystal, the above criteria to describe the stability limits of the crystal at finite strain are not adequate. Hence, the Born stability criteria must be modified under pressure [42]. Sin'ko and Smirnov proposed the theoretical conditions of elasticity under pressure [43, 44] and the modified elastic constants for an orthorhombic crystal under pressure are $C_{ii} = C_{ii} - P$, (for $i = 1-6$), $C_{12} = C_{12} + P$, $C_{13} = C_{13} + P$ and $C_{23} = C_{23} + P$. Hence new stability criteria are obtained by replacing the elastic constants in eqn-7.1 by the modified elastic constants. Therefore, AA is mechanically stable under hydrostatic pressure when the generalized

Born stability criteria are:

$$\begin{aligned}
M1 &= C_{11} - P > 0, M2 = C_{11}C_{22} - P(C_{11} + C_{22}) > 2PC_{12} + C_{12}^2, \\
M3 &= C_{11}C_{22}C_{33} + 2C_{12}C_{13}C_{23} - C_{11}C_{23}^2 - C_{22}C_{13}^2 - C_{33}C_{12}^2 \\
&\quad + P(C_{12}^2 + C_{13}^2 + C_{23}^2 - C_{11}C_{22} - C_{22}C_{33} - C_{33}C_{11}) \\
&\quad + 2P(C_{12}C_{13} + C_{12}C_{23} + C_{13}C_{23} - C_{11}C_{23} - C_{22}C_{13} - C_{33}C_{12}) \\
&\quad + 4P^2(C_{12} + C_{13} + C_{23}) + 4P^3 > 0, \\
M4 &= C_{44} - P > 0, M5 = C_{55} - P > 0, M6 = C_{66} - P > 0 \quad (7.2)
\end{aligned}$$

are simultaneously satisfied. As depicted in figure 7.7a, the calculated elastic constants show a non-monotonic variation with pressure. The pressure dependent elastic constants obey the generalized Born stability criteria as given in eqn-7.2 except M5 and it is plotted as a function of pressure along with M6. As illustrated in figure 7.7b, M6 decreases up to 5 GPa and later it increases up to 16 GPa and then starts decreasing with pressure, which indicates that the applied pressure drives shear instability in the system up to 5 GPa and then stabilizing above 5 GPa. Also M5 violates the stability criteria between 18-20 GPa, which clearly indicates the mechanical instability of AA under high pressure. Softening of the shear elastic moduli M5 and M6 suggests a shear instability of AA under pressure. Karki et al [45] reported that elastic instability bounds the transition pressure and determines the transition pressure precisely for first and second order phase transitions, respectively. Mechanical stability criteria, M6 and M5 bounds the transition pressure for AA and hence one can expect that the phase transition in AA is of first order type.

7.3.4 Hydrogen bonding in AA under pressure

As discussed in section 7.1, Raman spectroscopic measurements on AA [17, 18] revealed that it undergoes a polymorphic structural phase transition about 3.0 GPa due to weakening of the hydrogen bonding under pressure. They also pro-

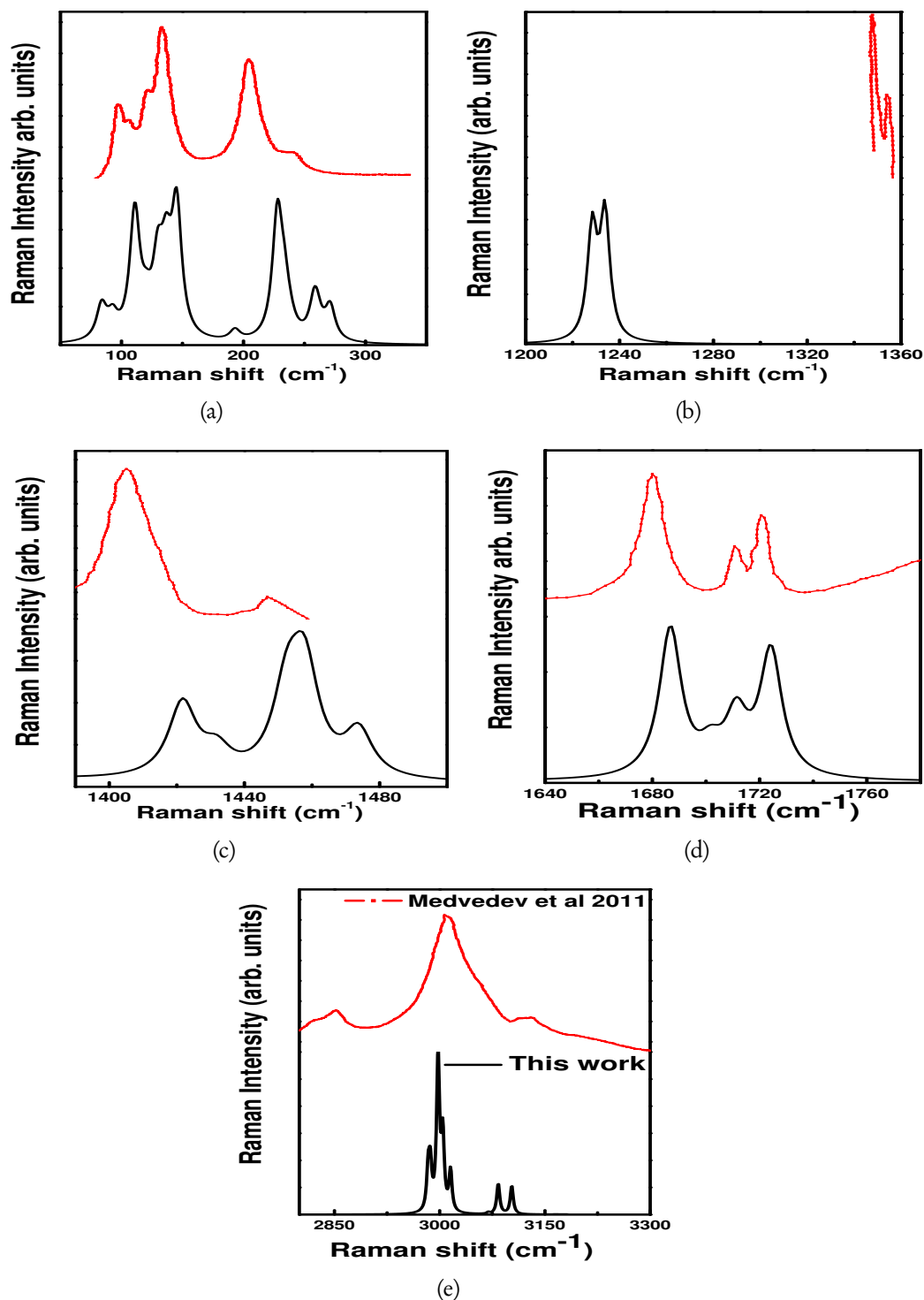


Figure 7.10: Calculated (bottom, solid black line) and experimental (top, solid red line) Raman spectra of AA at ambient pressure. The experimental data is taken from Ref. [17]

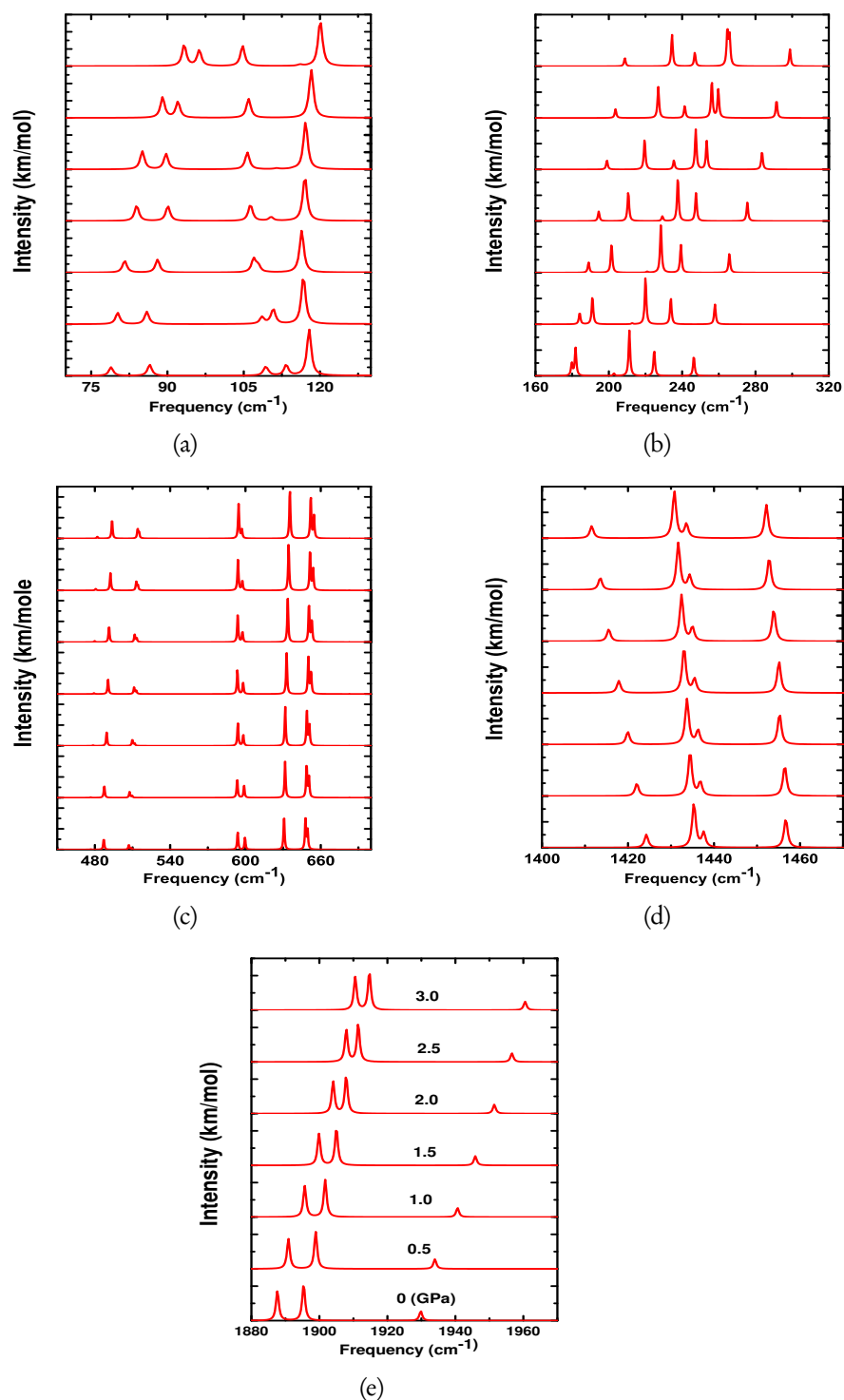
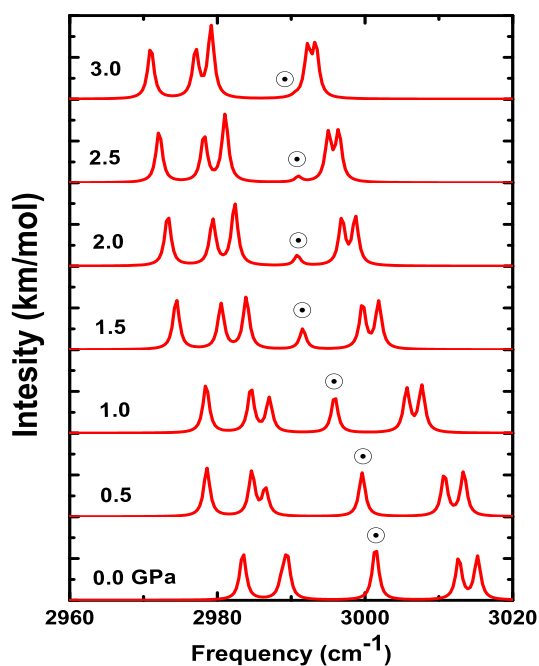
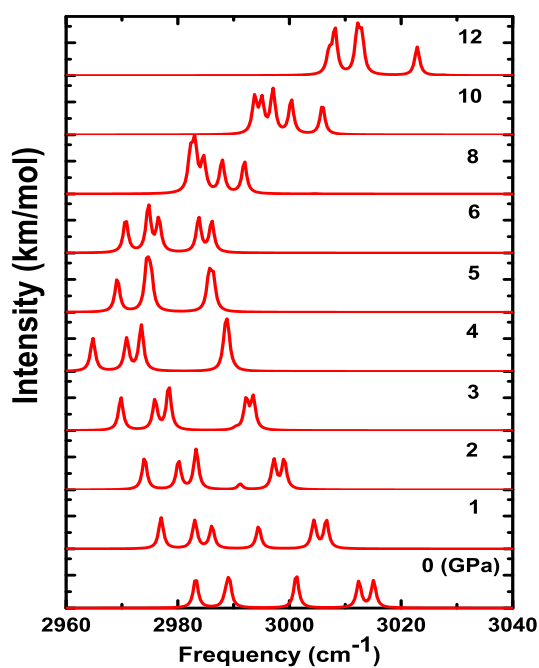


Figure 7.11: Calculated IR spectra (a, b) lattice modes (c) torsional and bending modes of NH₄ and N₃ ions (d) N-H wagging, rocking and scissoring modes of NH₄ ions (e) N₃ asymmetric modes of AA as a function of pressure. Calculated lattice, N-H torsional + N₃ bending and azide stretching modes show blue shift with pressure.

posed two possible reasons for weakening of hydrogen bonding [17] which are 1) elongation of N...N distance due to the rotation of azide (N_3^-) ion, which leads to increment of the N-H bond length. 2) Reorientation of NH_4^+ ions leading to bending of N-H...N bond [17]. A recent experimental study [1] on AA shows that N-H...N bond decreases with pressure and the weakening of hydrogen bonding is only because of the bending of N-H...N bond, which is possibly due to movement of ammonia cation and rotation of azide (Type-II) ions. In order to confirm this, we made an attempt to investigate the high pressure behavior of intermolecular hydrogen bonds. The angle made by Type-II azides with c-axis (see figure 7.1), *i.e.* angle θ , is plotted in the pressure range 0-2.5 GPa. As seen from figure 7.8a, the angle θ decreases with pressure, which is consistent with the experimental data [1] whereas the Neutron powder diffraction data shows a much rapid decrease of the angle in the pressure range of 0-2.5 GPa [19]. Further, we investigated the angle θ beyond 2.5 GPa and observe a rapid decrease below 12 GPa, it reaches a minimum value at 12 GPa and then it starts increasing with pressure up to 50 GPa as shown in figure 7.8b which is due to re-orientation of Type-II azide ions with respect to c-axis under compression. The calculated hydrogen bond lengths (N(5)...N(2) and N(5)...N(4)) and the corresponding bond angles (N(5)-H(1)...N(2) and N(5)-H(2)...N(4)) under pressure are shown in figure 4 of the Ref. [37]. The calculated N(5)...N(2) and N(5)...N(4) bond lengths decrease with pressure and are in good agreement with the experimental data up to 2.5 GPa [1]. The reorientation of NH_4^+ ions leads to bending of N-H...N hydrogen bond and this can be analyzed by calculating the intermolecular hydrogen bond angles of N-H...N bonds under compression. The calculated hydrogen bond angles show a significant variation (~ 176 - 178) between 4-10 GPa and the N(5)-H(2)...N(4) reaches a maximum value at 10 GPa due to orientation of Type-II azide ions as shown in figure 7.9.



(a)



(b)

Figure 7.12: Calculated IR spectra (a, b) N-H symmetric and asymmetric stretching modes of AA as a function of pressure. Calculated N-H stretching modes show red shift with pressure. In particular the N-H stretching modes show red shift up to 4 GPa thereafter show blue-shift between 5-12 GPa.

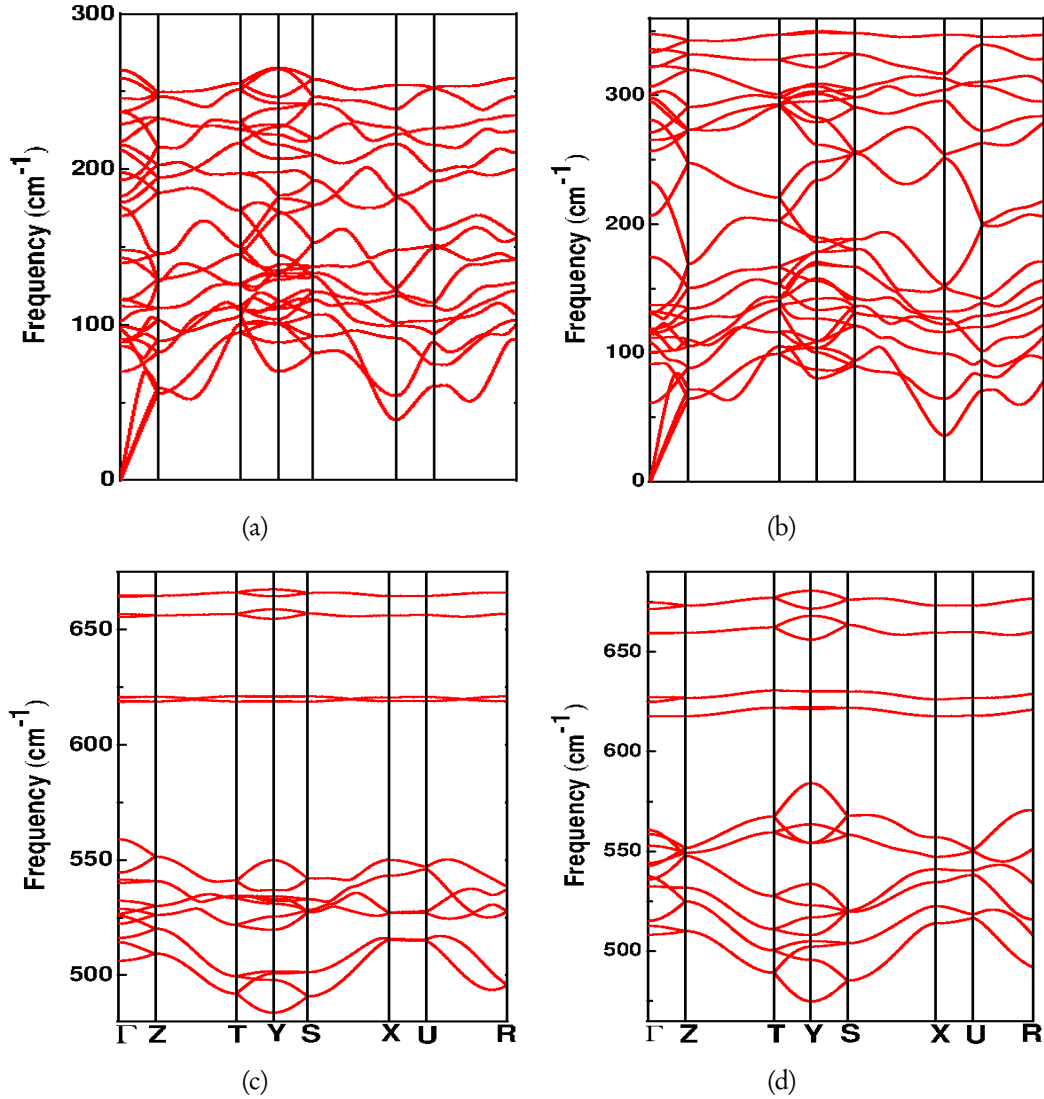


Figure 7.13: Calculated phonon dispersion curves in the low frequency region ($< 700 \text{ cm}^{-1}$) of AA at 0 GPa (left) as well as at 6 GPa (right) along high symmetry directions Γ (0.0, 0.0, 0.0) \rightarrow Z (0.0, 0.0, 0.5) \rightarrow T (0.0 0.5, 0.5) \rightarrow Y (0.0 0.5 0.0) \rightarrow S (0.5, 0.5, 0.0) \rightarrow X (0.5, 0.0, 0.0) \rightarrow U (0.5, 0.0, 0.5) \rightarrow R (0.5, 0.5, 0.5) in the Brillouin zone.

7.3.5 Zone centre phonons of AA at ambient pressure

IR and Raman spectroscopic techniques have been used for the identification and characterization of energetic materials [46]. The vibrational properties of a molecular solid provide information about the intra- and inter-molecular bonding. Therefore, the changes in vibrational properties are important indicators for understanding physical and chemical changes in the molecular crystals. The quantum mechanical DFT methods have proven themselves as essential tools for interpretations and predicting vibrational spectra of materials [47, 48]. In the present study, the vibrational spectrum of AA is calculated using linear response method within DFPT and a detailed analysis of the vibrational spectra and their complete assignment have been made at ambient as well as at high pressure. Single crystal X-ray and Neutron powder diffraction studies [1–3, 19] revealed that AA crystallizes in the orthorhombic structure with $Pmna$ space group; NH_4^+ and N_3^- ions occupy the sites of symmetry C_2 and C_{2b} , respectively. It consists of four molecules per unit cell (or 32 atoms per cell) resulting in the 96 vibrational modes, which are further classified into 3 acoustic and 93 optical modes. According to the group theory analysis of $Pmna$ space group, the symmetry decomposition of the modes as follows.

$$\Gamma_{acoustic} = B_{1u} \oplus B_{2u} \oplus B_{3u}$$

$$\Gamma_{optical} = 15B_{1u} \oplus 14B_{2u} \oplus 11B_{3u} \oplus 11B_{1g} \oplus 10B_{2g} \oplus 11B_{3g} \oplus 10A_g \oplus 11A_u$$

The optical modes B_{1u} , B_{2u} and B_{3u} are IR active, whereas B_{1g} , B_{2g} , B_{3g} and A_g are Raman active. A_u mode vibrations are silent as they do not cause change in polarizability or dipole moment and therefore these modes are neither Raman nor IR active. The calculated optical modes and their vibrational assignment at ambient pressure are given in Table I of the Ref. [37]. The modes from M96 to M89 and M88 to M81 are due to asymmetric and symmetric stretching of N-H bonds, respectively. This is consistent with Dows et al [9] assignment of the absorption between 2800 and 3200 cm^{-1} . The strongest Raman mode frequency

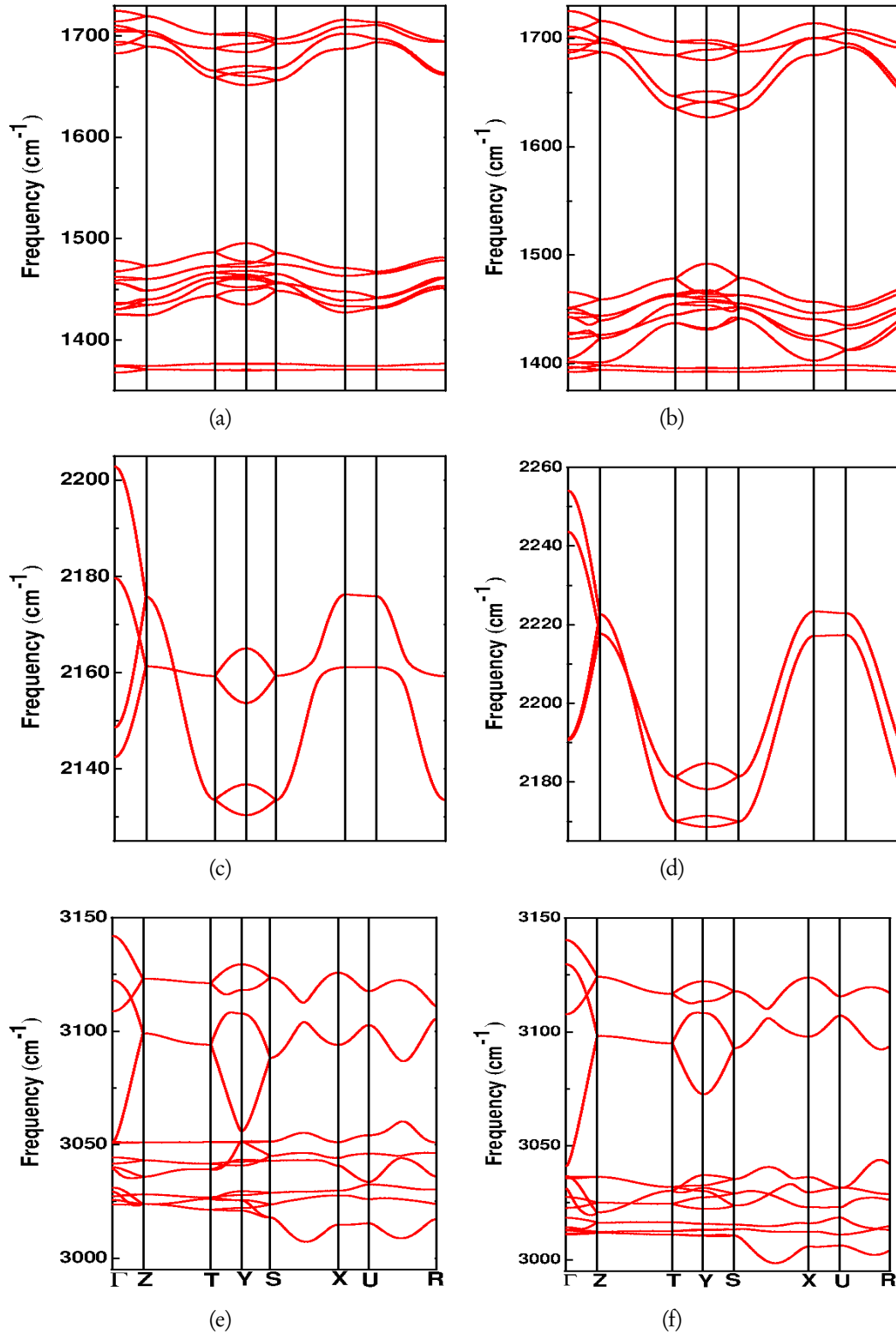


Figure 7.14: Calculated phonon dispersion curves in the high frequency region ($> 700 \text{ cm}^{-1}$) of AA at 0 GPa (left) as well as at 6 GPa (right) along high symmetry directions (notations have same representation as in figure 7.13) in the Brillouin zone.

2998.2 cm^{-1} (see figure 7.10e) in N-H symmetrical stretching region is in excellent agreement with the experimental value of 3000 cm^{-1} [17]. Modes from M80 to M77 originate from N=N=N asymmetric stretching of azide (Type-I & II) ions are in good accord with measured value of 2030 cm^{-1} [9]. Most of the vibrational modes for NH_4^+ ion in AA are assigned based on the vibrational modes of well-known ammonium halides (NH_4Cl and NH_4Br). Bending motion of NH_4^+ ion lies between M76 to M69, and the analogous frequencies in case of NH_4Cl [49] and NH_4Br [50] are 1712 and 1686 cm^{-1} , respectively. Apart from N-H...N short distance from the crystal structure [1-3, 19], the clear spectroscopic indications of hydrogen bonding in AA [17, 51] are due to shift of bending mode frequency above 1400 cm^{-1} , torsional and bending motion of NH_4^+ ion about 1830 and 2080 cm^{-1} , respectively. This is also seen from our present calculations, where N-H wagging, rocking and scissoring vibrations arise from M68 to M57 modes and are consistent with measured values of 1400 [9] and 1430 [17] cm^{-1} and also these vibrations are comparable with ammonium halides, 1402 for NH_4Cl [49] and 1401 cm^{-1} for NH_4Br [50]. The calculated N=N=N symmetric stretching (M56 to M53) modes (doublet is due to presence of Type-I & II azide ions) of azide ions are consistent with the calculated values for LiN_3 (1269.5 cm^{-1}) [52] and KN_3 (1228.5 cm^{-1}) [53]. However, the calculated values are smaller than the experimental values of 1345 [9] and ~ 1350 [17] cm^{-1} but the splitting of the doublet is ~ 5.5 cm^{-1} which is in good agreement with experimental value of ~ 5 cm^{-1} [17].

The calculated N=N=N bending and N-H rotational motion of (M52 to M45) modes are consistent with measured values of 664 and 652 cm^{-1} [9]. The modes from M44 to M33 (525.1 to 476.5 cm^{-1}) arise from NH_4^+ torsional motion and this can be clearly seen from figure 7.11c and the obtained torsional mode frequencies are in good agreement with recent theoretical calculations at ambient pressure [20]. Infrared Spectroscopy [9] and Inelastic Neutron Scattering [54] studies revealed that the torsional mode of NH_4^+ ion is located at 420 ± 20 cm^{-1} and the

free rotational motion of NH_4^+ ion is prevented by the existence of this torsional motion due to the hydrogen bonding between the nitrogen of NH_4^+ ion and the closest nitrogens of azide ions (N-H...N), whereas the torsional motion of Raman bands are very weak, therefore these modes were not observed in the Raman spectroscopic studies at ambient as well as at high pressure [11, 17]. The torsional frequency (in cm^{-1}) of ammonium azide and halides decreases in the following order: [9, 55] NH_4F (523) < NH_4N_3 (420) < NH_4Cl (359) < NH_4Br (319) < NH_4I (297) and this shows that the rotational motion of NH_4^+ ion is hindered in both NH_4F and NH_4N_3 than other mentioned ammonium halides due to the strong hydrogen bonding. The mode M32 is purely from the rotation of both NH_4^+ and N_3^- ions, whereas M31 and M30 arise from translation motion of NH_4^+ ion, which agrees well with the observed Raman mode value of 240 cm^{-1} [11]. The modes from M29 to M4 originate from rotational or translation, or a combined rotational and translation motion of NH_4^+ and N_3^- ions and the vibrational assignment for each mode is given in Table I of the Ref. [37]. The calculated Raman and IR vibrational modes at ambient pressure are shown in figures 7.10, 7.11 and 7.12 respectively. As illustrated in figure 7.10, the calculated Raman spectra at ambient pressure is in close agreement with measured spectra from Raman spectroscopic studies at 0.25 GPa [17].

7.3.6 IR spectra of AA under pressure

In general, structural transformation in materials under compression is experimentally probed by IR and Raman spectroscopy by monitoring the changes in the vibrational spectra under compression [36]. Therefore, we have calculated the IR spectra under pressure up to 12.0 GPa and it can be divided into five parts as shown in figure 7.11. As illustrated in figures 7.11a and b, as pressure increases the frequency of lattice modes (M4-M52) are found to increase, especially the modes in the Far-IR region (below 300 cm^{-1}) which implies hardening of the lattice under pressure. The lattice modes include NH_4^+ , N_3^- translation,

rotational (see figure 7.11a & b), NH_4^+ torsion and N_3^- bending (see figure 7.11c) vibrational modes. The $\text{N}=\text{N}=\text{N}$ asymmetric modes (M77-M80) show a blue-shift under compression (see figure 7.11e) whereas the N-H scissoring, rocking (M57-M68) and N-H stretching (M81-M96) modes exhibit a red-shift under compression (see figures 7.12a and b). Due to the presence of hydrogen bonding it can be expected that the N-H stretching frequency decreases with increase in pressure [56] and this compression leads to strengthening of hydrogen bonding. Joseph et al [57] have given an unified explanation for strengthening of hydrogen bonding (X-H...Y) based on red/blue-shift of IR frequency and its corresponding intensity. The contraction of hydrogen donor bond (X-H) due to electron affinity of X atom, which associated with the blue-shift and decrease in the intensity of respective IR bands. The elongation of hydrogen donor bond (X-H) due to attraction between the positive H and electron rich Y atom, which is associated with the red-shift and increase in the intensity of corresponding IR bands. As shown in figures 7.11d & 7.12a, the N-H scissoring, rocking and stretching mode frequencies show a red-shift and an increase in the intensity of the corresponding vibrational modes up to 4 GPa, which clearly indicates strengthening of the hydrogen bonding under compression below 4.0 GPa. Also, the N-H stretching frequencies show a blue-shift between 5-12 GPa which shows weakening of the hydrogen bonding as shown in figure 7.12b. As displayed in figure 7.12a & b, two N-H asymmetric stretching B_{2u} (2988.6 cm^{-1}) and B_{3u} (2989.2 cm^{-1}) degenerate modes lift the degeneracy whereas the B_{1u} (3012.4 cm^{-1}) and B_{3u} (3015.1 cm^{-1}) non-degenerate modes become degenerate under pressure. This is due to strong and weak coupling between N-H band of NH_4 and terminal nitrogens of type-I and II azide ions which strengthens and weakens the hydrogen bonding, respectively in the pressure range 0-4 GPa. In addition, we also observe the intensity of asymmetric N-H stretching mode B_{2u} (3001.2 cm^{-1}) decreases with pressure and it diminishes between 3-4 GPa. Weakening of hydrogen bonding and disappearance of B_{2u} mode might be the driving force for the structural transition from

phase I \rightarrow II as seen in the experiments [1, 17].

7.3.7 Phonon dispersion curves of AA under high pressure

In order to get more insight into the dynamical stability of crystalline AA under high pressure, the phonon dispersion curves are calculated at 0 and 6 GPa with $1 \times 2 \times 1$ super cell (64 atoms). The computed phonon dispersion curves are plotted along Z-T-Y-S-X and U-R high symmetry directions of the Brillouin zone. As depicted in figure 7.13, all the lattice modes ($< 700 \text{ cm}^{-1}$) shift towards high frequency region except a phonon branch that shows softening (from 38.8 to 35.5 cm^{-1}) along the high symmetry S-X-direction when compared at 0 and 6 GPa pressures (see figures 7.13a & b). It is also found that the lattice phonon branches become dispersive at 6 GPa. However, the phonon frequencies are still real along X-direction at 6 GPa which shows the dynamical stability of AA at this pressure. The degenerate N_3 bands around $\sim 620 \text{ cm}^{-1}$ at 0 GPa become non-degenerate modes at 6 GPa (see figures 7.13 c & d). As illustrated in figure 7.14a, the lowest lying Raman bands correspond to symmetric stretching of Type-I & II azide ions at 0 GPa which persist even at high pressure 6 GPa, but the Raman measurements [1, 17] have only one stretching band in this region above 3 GPa because the two azides occupy equivalent Wyckoff positions in the high pressure phase (see 7.14a & b). The present and recent theoretical calculations [58] are unsuccessful in reproducing the Raman spectral evolution under high pressure as observed in the experiments [1, 17]. The middle and top phonon bands correspond to N-H bending modes which show a red shift when compared at 0 and 6 GPa pressures as displayed in figures 7.14a & b. The N=N=N asymmetric phonon bands show a blue-shift with pressure as depicted in figures 7.14c & d. The high frequency N-H symmetric and asymmetric stretching bands show a red-shift as presented in figures 7.14e & f. However, the high frequency modes show a red shift up to 4 GPa and later on they exhibit blue-shift as shown in figure 7.12b.

We also observe that there is a deviation in the calculated phonon frequencies

using NC (see figures 7.10, 7.11 and 7.12) and PAW (see figures 7.13 and 7.14) pseudo potentials, especially for N=N=N symmetric and asymmetric stretching phonon modes. Overall, we observe that all the vibrational modes are real for the ambient phase (I) of AA at 0 and 6 GPa. This implies that AA is found to be dynamically stable at ambient as well as at high pressure (6 GPa) as depicted in figures 7.13 and 7.14 and also suggest that the structural transition might be due to the weakening of the hydrogen bonding under high pressure.

7.3.8 Electronic structure and chemical bonding

Electronic structure of inorganic azides have been investigated by X-ray electron spectroscopy [4] to understand the chemical bonding. This study reveals that the ionic character intensifies in AMAs as follows, $\text{LiN}_3 < \text{NaN}_3 < \text{KN}_3 < \text{RbN}_3 < \text{CsN}_3$; this is in very good agreement with recently reported [59] trend for the AMAs, while the same in HMAs, $(\text{AgN}_3, \text{CuN}_3, \text{Cu}(\text{N}_3)_2, \text{Hg}(\text{N}_3)_2, \text{Hg}_2(\text{N}_3)_2) < (\text{TlN}_3, \alpha\text{-Pb}(\text{N}_3)_2) < \text{Cd}(\text{N}_3)_2$, which indicates that AMAs are more ionic than HMAs, implying that AMAs are relatively more stable than HMAs. In order to understand the relative stability of AA when compared to the mentioned inorganic azides, it is necessary to have a knowledge about the electronic structure and chemical bonding of AA. The electronic structure determines the fundamental physical and chemical properties such as initiation, decomposition and detonation of an energetic material. Electronic band gap is an important property for energetic materials, which can be used to predict the relative stability and sensitivity [60]. We have used the TB-mBJ potential to calculate electronic structure and optical properties of AA at ambient pressure. Previous theoretical studies [60–63] revealed the relationship between band gap and impact sensitivity for the metal azides and C-H-N-O based energetic materials within the framework of periodic DFT calculations. Further, Kuklja et al [64, 65] investigated the excitonic mechanism of detonation initiation in explosives and clarified that pressure inside the impact wave front reduces the band gap. It can be expected that the smaller the

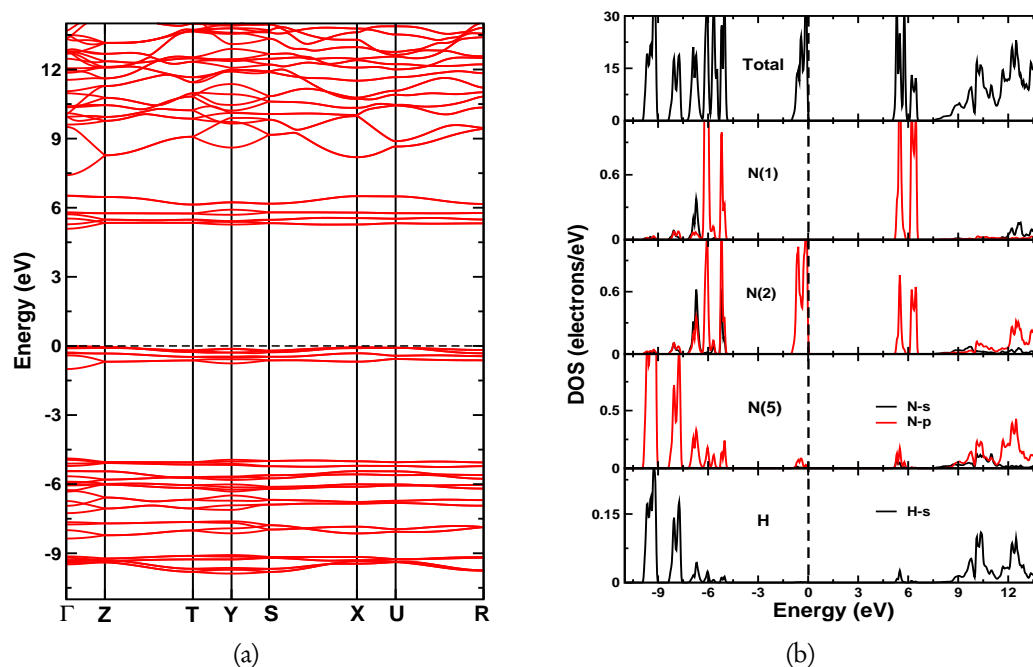


Figure 7.15: Calculated electronic band structure along high symmetry directions in the Brillouin zone (notations have same representation as in figure 7.13) and PDOS of AA using the TB-mBJ potential at the experimental crystal structure. N(M) and N(T) represent middle and terminal nitrogen atoms of azide anions, respectively.

band gap, the easier the electron transfers from valence band to conduction band; thus, the energetic system becomes more and more sensitive to external stimuli such as light, heat, friction and impact. The calculated band structure of AA along high symmetry directions is as follows, Γ -point at 5.08 eV; Z, T, U, R-points at 5.29 eV; Y-point at 5.21 eV and S, X-points at 5.24 eV in the first Brillouin zone as shown in figure 7.15a. The top of valence band and bottom of the conduction band occur along Γ - Γ direction, indicating that this material is a direct band gap insulator with a minimum separation of 5.08 eV. The corresponding band gap value using PBE-GGA functional is 4.10 eV. Experimental band gap value when available could be compared with our theoretical band gap.

In order to explain the chemical bonding in AA, we have calculated total and

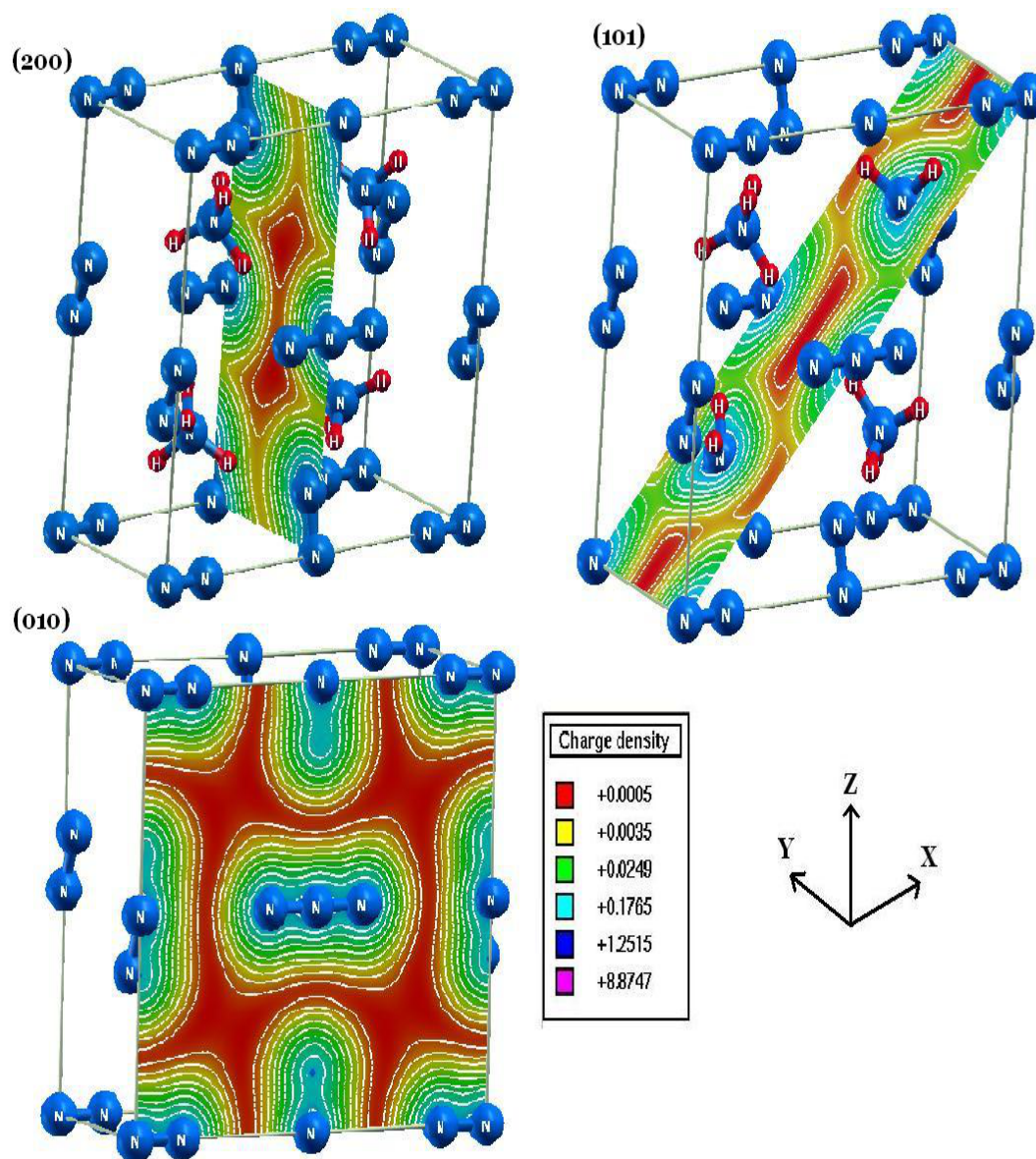


Figure 7.16: Calculated electronic charge densities of AA plotted along (200), (101) and (010) planes.

partial density of states (PDOS) (see figure 7.15b). The conduction band is mainly dominated by $2p$ -states of nitrogen atoms (N(1/3), N(2/4), N(5)) and $1s$ -states of hydrogen (H) atom. The top of valence band is completely dominated by $2p$ -states of terminal nitrogen N(2/4) of azide ion, which implies that these states might be responsible for initiation of decomposition process in AA. The relatively less contribution from $2p$ -states of NH_4 ion, when compared to azide ion in the valence band region upto -4.5 eV from Fermi level, indicates a degree of non directional (ionic) bonding between ammonium (NH_4^+) and azide (N_3^-) ions. There is a considerable overlap between $2p$ -states of terminal N(2/4) (or N(T)) and middle N(1/3) (or N(M)) nitrogens of azide ion as well as $2p$ -states of nitrogen from NH_4 and s -states of nitrogen atoms of azide ion in the energy range from -7.5 to -5 eV. Similarly, in the energy range from -10.5 to -7.5 eV, $2p$ -states of nitrogen atom from NH_4 overlap with $1s$ -states of the hydrogen atom. This does suggest that there is hybridization between N(T)-N(M) of azide ion and H-N(5), implying directional (covalent) bonding in N-N (nitrogen atoms of azide anion) and N-H bonds (within ammonium cation). The Pauling scale has been used as measure of the attraction ability of an atom for electrons in a covalent bond [66]. The difference in Pauling electro-negativities of nitrogen (3.0) and hydrogen (2.1) is used to predict the nature of the N-H bond in the ammonium ion. The electronegativity difference is 0.9, which points to a polar covalent bond character of N-H bond. In ammonium ion, the unit positive charge of the complex might be residing more on nitrogen atom, as a consequence of polar covalent character of N-H bond. This can be clearly understood from the electronic charge density contours along (200), (101) and (010) planes of AA crystal as shown in figure 7.16. The charge density along N(T)-N(M) is pronounced due to the hybridization between terminal and middle nitrogens of azide anion, suggesting directional bonding in the azide ion. However, there is very less charge sharing between NH_4^+ and N_3^- (see figure 7.15b) ions which indicates that ionic bonding is predominant in AA.

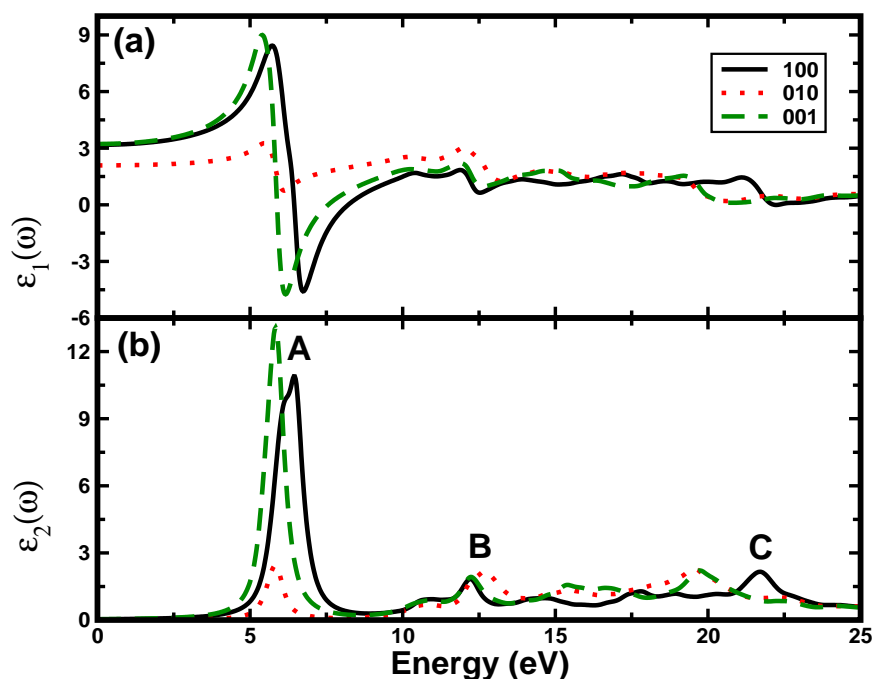


Figure 7.17: The real $\epsilon_1(\omega)$ and imaginary $\epsilon_2(\omega)$ parts of dielectric function of AA along three crystallographic axes as a function of photon energy at ambient conditions. Black solid line (along [100]), red dotted line (along [010]) and green thick dotted line (along [001]).

The nature of bonding in AA is interpreted through bulk modulus, Colton *et al* [4] determined ionic character (in %) for the AMAs and HMAs and found that AMAs are ionic solids while the HMAs are covalent solids. Also, the bulk moduli of AMAs are lower when compared to HMAs (see section 7.3.2), which reveals that the covalent azides have higher bulk modulus than ionic azides due to strong directional bonding. The bulk modulus value of AA is found to lie between AMAs and HMAs. Therefore, we confirm from the calculated electronic band structure, PDOS, charge density distributions and bulk modulus, thus, AA exhibits predominantly ionic bonding along with partial covalent nature from the N-H and N-N bonds of NH_4^+ and N_3^- ions, respectively.

7.3.9 Optical properties

The linear response of a system to electromagnetic radiation can be described by means of the dielectric function. In general, there are two contributions to dielectric function, namely; intra- and inter band transitions. The intra band transitions occur only in metals. Further, the inter band transitions are classified into direct and indirect transitions. The indirect inter band transitions arise from scattering of phonons, which are neglected in our calculations because their contribution is negligible to the dielectric function when compared to direct inter band transitions. The contribution of direct inter band transitions to the imaginary $\epsilon_2(\omega)$ part of the dielectric function in the random phase approximation [67] without local field effects can be calculated by summing all the possible transitions between the occupied and unoccupied states for a set of k-vectors over the Brillouin zone. The real $\epsilon_1(\omega)$ part of dielectric function can be derived from the imaginary $\epsilon_2(\omega)$ part of dielectric function by using Kramers-Kronig relations [68].

The linear optical properties of AA have been calculated using TB-mBJ electronic structure with denser k-mesh of 735 k-points in the IBZ. AA crystallizes in the orthorhombic *Pmna* space group; this symmetry has three independent components of dielectric function. Hence, the real and imaginary parts of dielectric function are determined as a function of photon energy along three crystallographic ([100], [010] and [001]) directions as shown in figure 7.17. The imaginary part of dielectric function $\epsilon_2(\omega)$ has three prominent peaks due to inter band transitions between valence band maximum (VBM) and conduction band minimum (CBM) along three crystallographic axes. The peaks in $\epsilon_2(\omega)$ (see figure 7.17b) are divided into three energy regions, named as A, 5-7.5 eV; B, 11.5-13.5 eV; and C, 17.5-23.5 eV. The peaks in the region A are due to interband transitions between $2p$ states of terminal nitrogen N(T) of azide ion to s-states of H/N of NH_4 , while the peaks in region B arise from transitions between N- $2p$ of NH_4 to H- $1s$ states. Finally, the peaks in region C originate from H- $1s$ to N- $2p$ states of NH_4 and vice

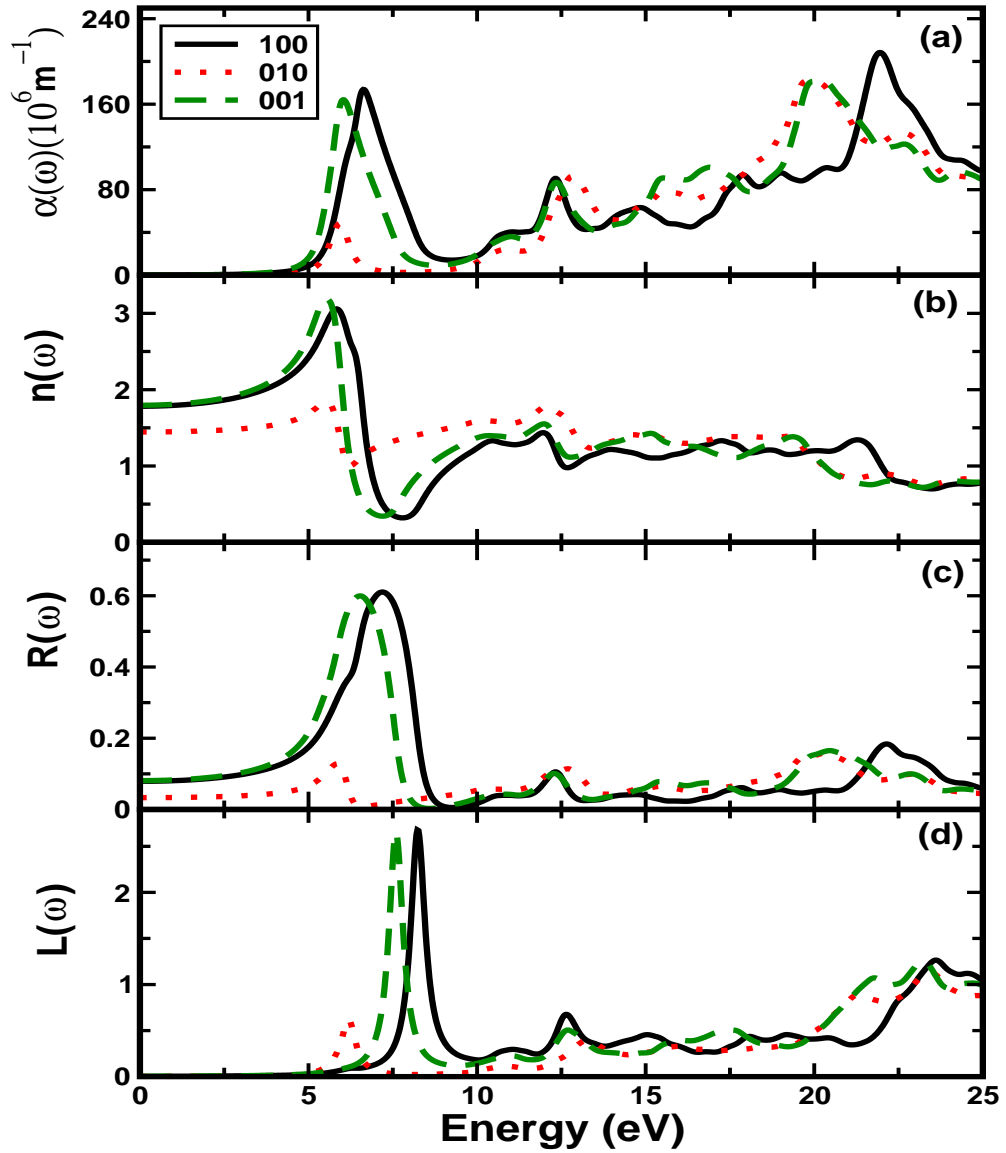


Figure 7.18: The calculated absorption spectra $\alpha(\omega)$, refractive index $n(\omega)$, reflectivity $R(\omega)$ and loss function $L(\omega)$ of AA as a function of photon energy at ambient conditions. Black solid line (along [100]), red dotted line (along [010]) and green thick dotted line (along [001]).

versa. It should be noted that most of the optical transitions are mainly from $2p$ (N) \rightarrow $1s$ (H) states. The static real part of dielectric function $\epsilon_1(\omega)$ along three crystallographic directions is found to be 3.18 (along [100]), 2.09 (along [010]), and 3.22 (along [001]). Further, we have derived the four important optical constants absorption spectra $\alpha(\omega)$, refractive index $n(\omega)$, reflectivity $R(\omega)$, and loss function $L(\omega)$ of AA as a function of photon energy from the calculated real and imaginary parts of dielectric function using the formulations given in the Ref. [68]. They have been displayed in figure 7.18. As shown from figure 7.18a, the absorption starts from 5.08 eV, which is a fundamental energy gap between VBM and CBM known as fundamental absorption edge for AA. The first absorption peaks along three crystallographic directions [100], [010] and [001] are at 6.64, 5.94 and 6.03 eV and the corresponding absorption coefficients $1.7 \times 10^8 \text{ m}^{-1}$, $4.7 \times 10^7 \text{ m}^{-1}$ and $1.6 \times 10^8 \text{ m}^{-1}$, respectively. This result reveals that AA decomposes under the action of UV light. The absorption takes place from 5.08 (fundamental absorption edge) to 25 eV and then it decreases in the high energy region because the crystal becomes transparent above 25 eV.

The calculated static refractive index of AA along the crystallographic axes is 1.78 (along [100]), 1.45 (along [010]) and 1.80 (along [001]). The distinct static refractive index values in each crystallographic direction indicates that AA is an optically anisotropic crystal (see figure 7.18b). The electron energy-loss function $L(\omega)$ describes the energy loss of a fast electron traversing in a material. The peaks in the $L(\omega)$ spectra represent the characteristics associated with the plasma resonance, and the corresponding frequency is the so-called plasma frequency, above which the material is a dielectric ($\epsilon_1(\omega) > 0$) and below which the material behaves like a metallic compound ($\epsilon_1(\omega) < 0$). As illustrated in figure 7.18d, the prominent peaks in $L(\omega)$ correspond to trailing edges in the reflection spectra (see figure 7.18c) are observed at 8.2 eV (along [100]), 6.1 eV (along [010]) and 7.6 eV (along [001]) directions and about 23.5 eV in all the three directions corresponding to abrupt reduction in the reflection spectra $R(\omega)$.

7.3.10 Detonation properties

For an explosive, detonation velocity (D_v) and detonation pressure (D_p) are the most important factors to evaluate its performance. The Kamlet-Jacobs equations [69, 70] based on the reported density and heat of formation (HOF) were chosen for the prediction of detonation performance. Values for D_v (in km/s) and D_p (in GPa) were calculated according to the following equations:

$$D_v = 1.01(NM^{0.5}Q^{0.5})^{0.5}(1 + 1.30\rho_0) \text{ and } D_p = 1.55\rho_0^2NM^{0.5}Q^{0.5}$$

In the above equations, N is moles of gaseous detonation products per gram of explosives, M is average molecular weights of gaseous products, Q is chemical energy of detonation (kJ/mol) defined as the difference of the HOFs between products and reactants, and ρ_0 is the density of explosive (gr/cc). We have calculated the D_v and D_p using calculated density (1.357 g/cc) and reported HOF (112.8 kJ/mol) [71, 72] and the corresponding values are found to be 6.45 km/s and 15.16 GPa, respectively which indicates that AA is a moderate explosive.

7.4 Conclusions

In summary, we made a detailed study of phase stability of N_4H_4 compounds, structural, mechanical and vibrational properties of AA under hydrostatic compression with dispersion correction methods. The calculated ground state parameters at ambient as well as at high pressure using vdW-TS and TS-SCS methods are in good agreement with experimental data and this study shows the importance of semi-empirical dispersion correction methods to capture dispersive interactions in molecular solids. The calculated compression curves are consistent with the trend followed by the elastic constants as well as with high pressure experimental data. Softening of the shear elastic moduli is suggestive of mechanical instability of AA under high pressure. AA is found to be the thermodynamic ground state of N_4H_4 compounds and it undergoes a series of phase transitions

from AA \rightarrow TTZ at around ~ 39 -43 GPa and TTZ \rightarrow HNS-1 at 80-90 GPa under the studied temperature range of 0-650 K which are consistent with the recent theoretical calculations. The anisotropic compressibility of a and c lattice constants suggests that the ambient phase of AA undergoes a transition to tetragonal phase. We predict a rapid decrease in the angle that Type-II azides make with c-axis (θ) till 12 GPa and then an increase up on further compression. In addition to that we have also calculated the zone centre phonon frequencies and IR spectra using DFPT at ambient and under high pressure. The calculated vibrational frequencies at ambient pressure and their complete vibrational assignment are consistent with experimental observations. AA is found to be dynamically stable at ambient pressure and no soft phonon mode is observed beyond the experimental transition pressure from phonon dispersion curves. Also the calculated IR spectra show that the N-H stretching frequencies get a red and blue-shift below and above 4 GPa, respectively. The intensity of the B_{2u} mode is found to diminish gradually and the weak coupling between NH_4 and N_3 ions makes B_{1u} and B_{3u} modes to be degenerate with progression of pressure up to 4 GPa which causes weakening of hydrogen bonding and these effects may lead to a structural phase transition in AA around 4 GPa and this is in good agreement with the experimental observations. As an explosive, AA shows moderate performance from the predicted detonation velocity and pressure of 6.45 km/s and 15.16 GPa, respectively.

References

- [1] X. Wu, H. Cui, J. Zhang, R. Cong, H. Zhu and Q. Cui, *Appl. Phys. Lett.*, **102**, 121902 (2013).
- [2] E. Prince and C. S. Choi, *Acta Crystallogr. B*, **34**, 2606 (1978).
- [3] H. S. D. Amorim, M. R. D. Amaral Jr, P. Pattison, I. P. Ludka and J. C. Mendes, *J. Mex. Chem. Soc.*, **46**, 313 (2002).

- [4] R. J. Colton and J.W. Rabalais, *J. Chem. Phys.*, **64**, 3481 (1976).
- [5] N. Yedukondalu, Vikas D. Ghule and G. Vaitheeswaran, *J. Phys. Chem. C*, **116**, 16910 (2012).
- [6] G. S. Yakovleva, R. K. Kurgangalina and L. N. Stestik, *Combustion, Explosion and Shock Waves*, **13**, 405 (1977).
- [7] J. N. Maycock and V. R. Pai Verneker, *J. Spacecr. Rockets*, **6**, 336 (1969).
- [8] L. K. Frevel, *Z. Krist.*, **94**, 197 (1936).
- [9] D. A. Dows, E. Whittle and G. C. Pimentel, *J. Chem. Phys.*, **24**, 1475 (1955).
- [10] P. Gray and T. C. Waddington, *Trans. Faraday Soc.*, **53**, 901 (1957).
- [11] Z. Iqbal and M. L. Malhotra, *Spectrochim. Acta. A*, **27**, 441 (1971).
- [12] Q. -J. Liu, W. Zneg, F. -S. Liu and Z. -T. Liu, *Comput. Theor. Chem.*, **1014** 37 (2013).
- [13] C. Ji, R. Zheng, D. Hou, H. Zhu, J. Wu, M. -C. Chyu and Y. Ma, *J. Appl. Phys.*, **111**, 112613 (2012).
- [14] M. I. Eremets, M.Y. Popov, I. A. Trojan, V. N. Denisov, R. Boehler and R. J. Hemley, *J. Chem. Phys.*, **120**, 10618 (2004).
- [15] M. I. Eremets, A. G. Gavriiliuk, I. A. Trojan, D. A. Dzivenko and R. Boehler, *Nat. Matter.*, **3**, 558 (2004).
- [16] M. I. Eremets, R. J. Hemley, H. K. Mao and E. Gregoryanz, *Nature*, **411** 170 (2001).
- [17] S. A. Medvedev, M. I. Eremets, J. Evers, T. M. Klapötke, T. Palasyuk and I. A. Trojan, *Chem. Phys.*, **386**, 41 (2011).

- [18] S. A. Medvedev, T. Palasyuk, I. A. Trojan, P. G. Naumov, J. Evers, T. M. Klapötke and M. I. Eremets, *Vibrational Spectroscopy*, **58**, 188 (2012).
- [19] D. I. A. Millar, *Energetic materials at extreme conditions*, Springer Theses, Springer-Verlag, Berlin Heidelberg, (2011).
- [20] X. Wu, F. Ma, C. Ma, H. Cui, Z. Liu, H. Zhu, X. Wang and Q. Cui, *J. Chem. Phys.*, **141**, 024703 (2014).
- [21] J. C. Crowhurst, J. H. Zaug, H. B. Radousky, B. A. Steele, A. C. Landerville and I. I. Oleynik, *J. Phys. Chem. A*, **118**, 8695 (2014).
- [22] A. Hu and F. Zhang, *J. Phys.: Condens. Matter*, **23**, 022203 (2011).
- [23] A. Tkatchenko and M. Scheffler, *Phys. Rev. Lett.*, **102**, 073005 (2009).
- [24] Q. -J. Liu, N. -C. Zhang, J. Eu, Y. -Y. Sun, M. -J, Zhang, F. -S. Liu, H. -Y. Wang and Z. -T. Liu, *Comput. Mat. Sci.*, **81**, 582 (2014).
- [25] Q. -J. Liu, N. -C. Zhang, Y. -Y. Sun, M. -J, Zhang, F. -S. Liu and Z. -T. Liu, *Phys. Lett. A*, **378**, 1333 (2014).
- [26] M. C. Payne, M. P. Teter, D. C. Allen, T. A. Arias and J. D. Joannopoulos, *Rev. Mod. Phys.*, **64**, 1045 (1992).
- [27] N. Troullier and J. L. Martins, *Phys. Rev. B*, **43**, 1993 (1991).
- [28] J. P. Perdew, S. Burke and M. Ernzerhof, *Phys. Rev. Lett.*, **77**, 3865 (1996).
- [29] T. H. Fischer and J. Almlof, *J. Phys. Chem.*, **96**, 9768 (1992).
- [30] H. J. Monkhorst and J. D. Pack, *Phys. Rev. B*, **13**, 5188 (1976).
- [31] S. Baroni, S. de Gironcoli A. Del Corso and P. Giannozzi, *Rev. Mod. Phys.*, **73**, 515 (2001).

- [32] G. Kresse and D. Joubert, Phys. Rev. B, **54**, 11169 (1996).
- [33] A. Togo, F. Oba and I. Tanaka, Phys. Rev. B, **78**, 134106 (2008).
- [34] A. Tkatchenko, R. A. DiStasio Jr., R. Car and M. Scheffler, Phys. Rev. Lett., **108**, 236402 (2012).
- [35] V. M. Veith and G. Schlemmer, Z. Anorg. Allg. Chem. **494**, 7 (1992).
- [36] A. C. Landerville, B. A. Steele and I. I. Oleynik, J. Phys.: Conf. Ser., **500**, 162006 (2014).
- [37] <http://www.rsc.org/suppdata/c5/cp/c5cp04294a/c5cp04294a1.pdf>
- [38] L.E. Downie, *Pathways to Recovering Single-Bonded Nitrogen at Ambient Conditions: High Pressure Studies of Molecular and Ionic Azides*. University of Ottawa, Canada (2010).
- [39] F. D. Murnaghan, Proc. Natl. Acad. Sci., **30**, 244 (1944).
- [40] M. Born and K. Huang, *Dynamical Theory of Crystal Lattices*; Oxford University Press: Oxford, U.K., (1998).
- [41] F. Mouhat and F. -X. Coudert, Phys. Rev. B, **90**, 224104 (2014).
- [42] V. Monteseuro, P. Rodríguez-Hernández, H. M. Ortiz, V. Venkatramu, F. J. Manjón, C. K. Jayasankar, V. Lavín and A. Muñoz, Phys. Chem. Chem. Phys., **17**, 9454 (2015).
- [43] G. V. Sin'ko, N. A. Smirnov, J. Phys. Condens. Matter, **14**, 6989 (2002).
- [44] G. V. Sin'ko, N. A. Smirnov, J. Phys. Condens. Matter, **16**, 8101 (2004).
- [45] B. B. Karki, G. J. Ackland and J. Crain, J. Phys.: Condens. Matter, **9**, 8579 (1997).

- [46] N. F. Fell Jr, J. A. Vanderho, R. A. Pesce-Rodriguez and K. L. J. McNesby, *J. Raman Spectrosc.*, **29**, 165 (1998).
- [47] B. A. Hess Jr, J. Schaad, P. Carsky and R. Zaharaduick, *Chem. Rev.*, **86**, 709 (1986).
- [48] V. Krishnakumar, N. Jayamani and R. Mathammal, *J. Raman Spectrosc.*, **40**, 936 (2009).
- [49] E. L. Wagner and D. F. Hornig, *J. Chem. Phys.*, **18**, 296 (1950).
- [50] E. L. Wagner and D. F. Hornig, *J. Chem. Phys.*, **18** 305 (1950).
- [51] J. T. Dunsmuir and A. P. Lane, *Spectrochim. Acta A*, **28**, 45 (1972).
- [52] K. Ramesh Babu, Ch. Bheema Lingam, S. P. Tewari and G. Vaitheeswaran, *J. Phys. Chem. A*, **115**, 4521 (2011).
- [53] K. Ramesh Babu and G. Vaitheeswaran, *Chem. Phys. Lett.*, **533**, 35 (2012).
- [54] H. Boutin, S. Trevino and H. Prask, *J. Chem. Phys.*, **45**, 401 (1966).
- [55] D. N. Satyanarayana, *Vibrational Spectroscopy: Theory and Applications*. New Delhi: New Age International (P) limited Publishers) 2nd ed., p.474 (2004).
- [56] J. Reynolds and Ss. Sternste, *J. Chem. Phys.*, **41**, 47 (1964).
- [57] J. Joseph and E. D. Jemmis, *J. Am. Chem. Soc.*, **129**, 4620 (2007).
- [58] <http://meetings.aps.org/link/BAPS.2014.MAR.J26.7>
- [59] D. Hou, F. Zhang, C. Ji, T. Hannon, H. Zhu, J. Wu and Y. Ma, *Phys. Rev. B*, **84**, 064127 (2011).
- [60] W. H. Zhu and H. M. Xiao, *Struct. Chem.*, **21**, 847 (2010).
- [61] W. H. Zhu and H. M. Xiao, *J. Comput. Chem.*, **29**, 176 (2008).

- [62] W. H. Zhu, J. J. Xiao, G. F. Ji, F. Zhao and H. M. Xiao, *J. Phys. Chem. B*, **111**, 12715 (2007).
- [63] X. J. Xu, W. H. Zhu and H. M. Xiao, *J. Phys. Chem. B*, **111**, 2090 (2007).
- [64] M. M. Kuklja, E. V. Stefanovich and A. B. Kunz, *J. Chem. Phys.*, **112**, 3417 (2000).
- [65] M. M. Kuklja and A. B. Kunz, *J. Appl. Phys.*, **87**, 2215 (2000).
- [66] L. Pauling, *The Nature of the Chemical Bond*, 3rd ed.; Cornell University Press: Ithaca, NY, (1960).
- [67] H. Ehrenreich and M. H. Cohen, *Phys. Rev.*, **115**, 786 (1959).
- [68] M. Fox, *Optical Properties of Solids*; Oxford University press: Newyork, (2001).
- [69] M. J. Kamlet and S. J. Jacobs, *J. Chem. Phys.*, **48**, 23 (1968).
- [70] M. J. Kamlet and J. E. Ablard, *J. Chem. Phys.*, **48**, 36 (1968).
- [71] L. O. Williams, US Patent 5081930 (1992).
- [72] P. Gray and T. C. Waddington, *Proc. R. Soc. Lond. A*, **235**, 481 (1956).

Summary & Future scope

Finally, this chapter summarizes the outcome of the entire thesis. In addition, we have also outlined some future research directions which have emerged naturally during the course of the current thesis work.

First principles calculations have been extensively employed to study the structure, phase stability, equation of state, compressibility and lattice dynamics under hydrostatic compression while the electronic structure, chemical bonding and optical properties are analyzed at ambient pressure for the diverse classes of energetic materials namely primary explosives (silver fulminate, mercury fulminate and potassium 1,1-dinitramino 5,5-bistetrazolate), solid oxidizers (potassium nitrate, potassium chlorate, ammonium nitrate, ammonium perchlorate, ammonium dinitramide) and a nitrogen rich salt or gas generator (ammonium azide). The standard LDA/GGA functionals are inadequate to predict the ground state properties of the energetic layered and/or molecular crystalline solids. In contrast to standard DFT functionals, additive pair-wise and non-local correction methods are quite successful in describing the weak intermolecular interactions (vdW forces and/or hydrogen bonding). Hence the predicted ground state properties are closely comparable with experimental results which is the first objective of the current thesis. Subsequently, we have presented a detailed study of structure, polymorphic phase stability, possible structural phase transitions and dynamical stability from ambient to high pressures using various dispersion correction methods.

We resolved the issue of polymorphic phase stability between two $Cmcm$ and $R\bar{3}$ polymorphs of SF at ambient as well as at high pressure and temperature. Using DFT-D2 method, $Cmcm$ phase is found to be the thermodynamic

ground state of SF under the studied pressure (0-5 GPa) and temperature (0-650 K) range. Hence, $Cmcm$ and $R\bar{3}$ phases are represented as α -SF and β -SF, respectively. We observe a pressure induced polymorphic phase transition from $\beta \rightarrow \alpha$ at 2.5 (2.7) GPa within PBE-GGA functional using PWSCF (CASTEP) package and the same was not observed using DFT-D2 method. Non-local correction optB88-vdW method works well for MF. In addition, the high compressibility of weak Ag..O/Hg..O intermolecular interactions along c-axis leads to high sensitivity along the c-crystallographic direction for SF/MF, which enables a directional sensitivity in explosive materials. We have investigated the structural stability, bonding and vibrational properties of the emerging green primary explosive, K_2DNABT . We found that K_2DNABT is relatively softer than well-known primary explosive, lead azide. We have also calculated and assigned all the vibrational modes of K_2DNABT and it is found to be dynamically stable up to 10 GPa at the center of Brillouin zone. The computed TB-mBJ electronic structure show that SF-polymorphs, MF and K_2DNABT are indirect and direct band gap insulators, respectively. Inclusion of spin-orbit coupling is found to be more predominant for $4d$ - and $5d$ -states of Ag and Hg atoms of α -SF and MF, respectively below the valence band. The presence of ionic bonding in K_2DNABT suggests that it is relatively stable when compared to covalent primary explosives. The most probabilistic electric-dipole transitions are found to occur between Ag/Hg $\rightarrow N/(N/C/O)(p)$ -states for SF and MF respectively. The calculated absorption spectra reveal that the SF-polymorphs, MF and K_2DNABT are found to decompose under the irradiation of ultra-violet light.

PC undergoes a pressure induced structural phase transition from monoclinic ($P2_1/m$) \rightarrow rhombohedral ($R3m$) structure at around 2.26 GPa, which is in good accord with a recent high pressure X-ray diffraction study. The transition is associated with a volume contraction of 6.4% and it is consistent with experimental reduction of $\sim 6\%$, which indicates a first order type transition. In contrast, the calculated transition pressures 0.11 GPa and 3.57 GPa using LDA and PBE-GGA functionals are severely under- and over-estimated, respectively for PC. We have also seen that PN encounters a polymorphic structural phase transition from orthorhombic ($Pmcn$) \rightarrow rhombohedral ($R3m$) structure at 0.27 GPa with a volume

collapse of 4.9% similar to that of PC. We observe the softening of lattice modes for PC whereas the lattice modes drive the instability in PN around 3.5 GPa. The computed compressibility curves and elastic moduli reveal that AN, ADN and AP are found to be more compressible along **b**- and **a**-axes respectively which are due to weak intermolecular interactions along the corresponding axes. The calculated zone center phonon frequencies reveal that AN (phase-IV) has two imaginary optical phonon modes with $Pm\bar{m}n$ crystal symmetry whereas AP and ADN possess all real optical phonon modes at the centre of Brillouin zone. In addition, we have also calculated IR spectra of AP and ADN at ambient as well as at high pressure. ADN is found to have more hygroscopic nature over AP due to strong hydrogen bonding at ambient pressure and blue-shift in the near IR frequencies as a function of pressure. The abrupt changes in the lattice constants and weakening of the hydrogen bonding might be the reasons for possible pressure induced structural phase transitions in AP and ADN. The calculated detonation properties disclose that ADN is a powerful energetic oxidizer when compared to AN and AP.

AA is found to be the thermodynamic ground state of N_4H_4 compounds and it undergoes a series of phase transitions from AA \rightarrow TTZ at around ~ 39 -43 GPa and TTZ \rightarrow HNS-1 at 80-90 GPa under the studied temperature range of 0-650 K which are consistent with the recent theoretical calculations. Softening of the shear elastic moduli is suggestive of mechanical instability in AA under high pressure. The calculated vibrational frequencies at ambient pressure and their complete vibrational assignment are consistent with experimental observations. AA is found to be dynamically stable at ambient pressure and no soft phonon mode is observed beyond the experimental transition pressure from phonon dispersion curves which suggests a first order structural phase transition. Also the calculated IR spectra show that the N-H stretching frequencies display red- and blue-shift below and above 4 GPa, respectively. The intensity of the B_{2u} mode is found to diminish gradually and the weak coupling between NH_4 and N_3 ions makes B_{1u} and B_{3u} modes to be degenerate with progression of pressure up to 4 GPa which cause weakening of the hydrogen bonding and these effects may lead to a structural phase transition in AA around 4 GPa and this is in good agreement with

the experimental observations. AA exhibits moderate energetic performance as inferred from the predicted detonation velocity and pressure of 6.45 km/s and 15.16 GPa, respectively.

Besides the consequences of the present thesis, there is a still room for improvement of the present work in various aspects. Understanding the stability of the energetic solids under non-hydrostatic and high temperature conditions is very crucial, which will be considered as a future work. As discussed in section 1, the crystal structure prediction packages will be employed to predict the polymorphic phases of energetic solids. This will provide a valuable information to the experimentalists towards synthesis of high performance and low sensitive energetic materials. In addition, it is essential to understand the defects in these materials because defects can serve as hotspots for energetic materials.

Statement of Plagiarism statistics



Computational Study of Energetic Materials
under Hydrostatic Compression by Neelam
Yedukondalu

From Ph. D. Thesis (Thesis)

Similarity Index 15%	Similarity by Source	
	Internet Sources:	13%
	Publications:	8%
	Student Papers:	4%

Processed on: 19-Feb-2016 9:15 PM IST

ID: 634067904

Word Count: 61224

